Title

Fault-Controlled Patterns of Uplift in the Central California Coast Range and Laser-Ablation Depth-Profile Analysis of Zircon

Author
Steely, Alexander Newton

Publication Date
2016

UNIVERSITY OF CALIFORNIA
SANTA CRUZ

FAULT-CONTROLLED PATTERNS OF UPLIFT IN THE CENTRAL CALIFORNIA COAST RANGE AND LASER-ABLATION DEPTH-PROFILE ANALYSIS OF ZIRCON

A dissertation submitted in partial satisfaction
of the requirements for the degree of

DOCTOR OF PHILOSOPHY

in

EARTH SCIENCES

by

Alexander Newton Steely

December 2016

The Dissertation of Alexander Newton Steely is approved:

____
Professor Jeremy Hourigan, Chair

____
Professor Emily Brodsky

____
Professor Noah Finnegan

____
Tyrus Miller
Vice Provost and Dean of Graduate Studies

TABLE OF CONTENTS

LIST OF FIGURES

LIST OF TABLES

ABSTRACT

FAULT-CONTROLLED PATTERNS OF UPLIFT IN THE CENTRAL CALIFORNIA COAST RANGE AND LASER-ABLATION DEPTH-PROFILE ANALYSIS OF ZIRCON

Alexander Newton Steely

The spatial pattern of uplift and long-term exhumation of the Santa Lucia range in central California is defined and the major structures responsible for this deformation are elucidated using low-temperature thermochronometry (44 apatite and 39 zircon (U-Th)/He cooling ages), geomorphic metrics of erosion, deformed late Quaternary marine terraces, geologic constraints, and a basin-subsidence analysis. Thermochronometers indicate rapid late Miocene cooling along the entire 90 km-long southwest flank of the range; a ~6 Ma onset of rapid exhumation is most consistent with available constraints. Exhumation rates are greatest NE of the San Gregorio-Hosgri fault (SGHF), decrease away from it, and are low across its trace to the SW. Deformed marine terraces also indicate a strong fault control on uplift; terrace elevations are 3–5 times higher directly NE of the SGHF and decay to baseline values over a ~5 km-wide zone; elevations drop rapidly across the fault to the SW. A geomorphic analysis using range-wide normalized channel steepness and river-profile plots of χ indicates higher rates of uplift NE of the SGHF, even when controlled for changes in lithology. Together, these data indicate that the SGHF has focused uplift and exhumation along its NE side since the late Miocene, has continued to do so in the late Quaternary, and is the primary driver of high topography and relief in the Santa Lucia range. A basin analysis indicates a cyclic pattern of uplift and subsidence over the last 80 m.y. that may be related to the emplacement of underplated schist during late Cretaceous crustal restructuring.

A multi-pulse method for single-collector ICP-MS laser ablation systems is presented that interrogates isotopic variation as a function of sample depth. The method resolves U-Pb ages in zircon with ~0.55 μm depth resolution and ~6% 2σ uncertainty. Metrics of radiation damage, crystal-lattice distortion, and ablation depth indicate that crystal structure exerts a fundamental control on elemental fractionation and must be matched between standards and unknowns for ultimate age precision.

ACKNOWLEDGMENTS

The work of one is always the work of many. My sincerest thanks goes to my primary advisor, Dr. Jeremy Hourigan, who spurred me on to achieve things I did not think I was capable of—sometimes by directly suggesting projects, but more often through subtle hints and a healthy dose of allowing me to explore the world and find my own path to a greater truth; I have forged bonds of knowledge far greater than those of any classroom because of you.

Committee members Dr. Noah Finnegan and Dr. Emily Brodsky provided the inspiration to learn MATLAB by introducing me to a world where every geoscience question seems to be answerable by ‘this little MATLAB script I wrote’. The Geomorphology Seminar class of 2014, led by Dr. Finnegan, was instrumental in developing some of the initial insight into the wealth of information encoded in the topography of the Santa Lucia range.

I would also like to thank Rob Franks, Laboratory Manager for the UCSC Plasma Analytical Facility and Dr. Terry Blackburn, Director of the W.M. Keck Isotope Lab, both of whom provided much training and analytical support during my research. This thesis relies heavily on data produced in their labs. Quentin Williams and Elise Knittle provided access to their Raman Spectroscopy Laboratory for which I am very grateful. Earl O’Bannon III helped me to figure out what to do once I was in the door.

Several undergraduates helped with this work. Andre Mere collected and processed 7 apatite and 8 zircon (U-Th)/He ages that proved most useful. Sam Anderson helped survey marine terraces in Big Sur and separated zircon and apatite from field samples. Jonathan Ooms and Chris Gallagher explored remote and brushy parts of the Ventana Wilderness and produced 6 apatite (U-Th)/He ages in the process. Devon Orme produced the first seven zircon cooling ages in the Santa Lucia range and her initial results prompted the development of all subsequent work. Erik Juel helped immensely in the data collection of Chapter 4.

Finally, I would like to thank the many friends and family members who helped make this time possible, if not enjoyable. An especial sense of gratitude goes to my partner in graduate school and in life, Chelsea Gustafson. Without her moral support throughout, and financial support at the end, this would remain a pile of spreadsheets and half-written computer code.

Funding for this project was provided in part by grants to A. Steely from the Northern California Geological Society Richard Chambers Memorial Scholarship, the Casey Moore Foundation, and a Graduate Student Grant from the Geological Society of America. Funding for instrumentation was provided in part by National Science Foundation grants OCE-0821303, EAR 0949322, and EAR 1214745.

The text of Chapter 4 is a reprint of the following previously published material:

Steely, A.N., Hourigan, J.K., Juel, E., 2014, Discrete multi-pulse laser ablation depth profiling with a single-collector IC-PMS: Sub-micron U-Pb geochronology of zircon and the effect of radiation damage on depth-dependent fractionation. Chemical Geology, v. 372, p. 92-108. DOI: 10.1016/j.chemgeo.2014.02.021

Within this manuscript, A. Steely performed the data acquisition for U-Pb ages, software development, data collection for raman spectroscopy and vertical-scanning interferometric measurements of ablation depth, and the majority of the writing. E. Juel assisted with sample preparation and measurement of ablation pit depths. J. Hourigan supervised the research and provided extensive feedback on the mathematical description of the data-reduction process.

CHAPTER 1

PUNCTUATED CYCLES OF RAPID UPLIFT AND SUBSIDENCE OVER 80 MILLION YEARS IN THE SANTA LUCIA RANGE, CENTRAL CALIFORNIA: THE ROLE OF UNDERPLATED SCHIST IN STRAIN LOCALIZATION

ABSTRACT

The Santa Lucia range of central California exposes a nearly 8-km-thick composite section of late Cretaceous to late Miocene basin fill deposited on Salinian bedrock. Basin analysis techniques, in combination with geochronologic, thermobarometric, and thermochronometric constraints are used to document long-term cyclic patterns of vertical deformation in the range. There have been 4 major uplift and exhumation events—each with a duration of ~3–10 m.y.—separated by 3 periods of subsidence—with durations from 15–22 m.y. Each uplift cycle corresponds to a major tectonic event and all are marked by angular unconformities that locally reach the crystalline basement. Rapid shoaling of the basin is common to all but the first uplift cycle, which records a ~10 m.y. period of rapid exhumation that brought mid-crustal rocks to the surface. Each subsidence cycle is marked by rapid submergence of the basin to mid-bathyal depths; unconformities within these cycles are locally present, but less extensive.

The emplacement of schist—demonstrably weaker than crystalline rocks and presumably several km-thick—beneath the range in the late Cretaceous may have weakened the upper crust and focused subsequent vertical deformation. A layered model of lithospheric strength is developed as a means to explain periodic high-amplitude uplift and subsidence cycles. This model demonstrates that for realistic physical parameters, the crustal strength of the of the Salinian block is substantially limited by even a modest thickness of schist, so long as the schist resides at depths above those corresponding to fully plastic quartz flow.

INTRODUCTION

The vertical distribution of strength in continental lithosphere fundamentally shapes how and where strain is accommodated (e.g. Jackson, 2002; Burov and Watts, 2006). Our general model is that brittle deformation occurs in the upper crust until conditions—often temperature—cause ductile deformation mechanisms such as dislocation creep to be favored with greater depth

(Byerlee, 1978; Brace and Kohlstedt, 1980; Kohlstedt et al., 1995). Such relationships indicate that the strength of the upper crust reaches a maximum at the mid-crustal depths where temperatures permit crystal-plastic deformation to dominate (e.g. Burov, 2011). In these models, rheologic stratification in the upper crust is almost always neglected because brittle behavior at the crustal scale depends little on lithology (Byerlee, 1978), and the nearly ubiquitous presence of quartz in continental rocks ensures that ductile behavior will largely be controlled by the rheology of quartz (Burov, 2011).

The presence of mica-bearing schist at the surface and at shallow depths throughout a large swath of central and southern California challenges the simple model of monolithologic upper and middle crustal rheology. Deformation experiments of biotite and muscovite schist indicate that it is many-times weaker than typical quartz-bearing continental rocks, and can deform plastically at depths of only 2–3 km (Shea and Kronenberg, 1992). There is a growing body of evidence that much of the Mojave Desert, the Transverse Ranges, and the Salinian block are underlain by such schist (Barth et al., 2003; Jacobson et al., 2007; Chapman et al., 2010). Collectively known as the Pelona–Orocopia–Rand schists, they are the manifestation of subduction erosion and tectonic underplating during Laramide shallow subduction (Saleeby, 2003; Ducea et al., 2009; Chapman et al., 2012). Thus, the rheologic conditions of many large crustal blocks throughout California may not be well represented by a simple, unlayered model of crustal strength. Furthermore, if these blocks are indeed much weaker than surrounding regions, they may serve to focus strain, and perhaps may even provide a first-order control on the location of major fault systems.

To evaluate how underplated schist may contribute to the localization of strain in the lithosphere, a layered rheologic model is developed to calculate yield strengths for a variety of scenarios, including the presence of underplated schist. One of the most significant predictions of the model is that mid-crustal strength can be completely destroyed by even a moderate thickness of schist if it lies within a critical depth window. If surrounded by stronger blocks, such a reduction in strength would tend to localize strain within the weaker block. The consequence of such strain localization would be that regions with underplated schist preserve evidence for greater amounts of strain than stronger regions with a similar tectonic history.

This prediction is tested in the Santa Lucia range of central California, where a nearly 8-km-thick late Cretaceous through late Miocene sedimentary basin was deposited on crystalline bedrock underlain by schist. During this time, the region experienced several major tectonic events, providing ample opportunity for the accumulation of strain. A subsidence analysis of the basin is developed and combined with constraints on bedrock crystallization, metamorphism, and exhumation to define the pattern of vertical deformation over the last ~80 m.y. These results are then compared against evidence of vertical deformation in the southern San Joaquin basin which lacks the same underplated schist but was exposed to a similar tectonic history. The data appear to support the prediction that strain is localized in regions with underplated schist, but several outstanding questions remain.

GEOLOGIC SETTING

The bedrock geology of the Santa Lucia range (Fig. 1-1) is characterized by high-grade metamorphic and deep-seated anhydrous igneous rocks (Compton, 1960; 1966a; Wiebe, 1966; Ross, 1976; Dibblee, 1974; 1979). The crystalline rocks are Late Cretaceous in age (Mattinson, 1978; Kistler and Champion, 2001; Barth et al., 2003; Colgan et al., 2012) and contain roof and screen pendants of marble and quartzite of the Paleozoic Sur Series (Trask, 1926; Wiebe, 1966; Ross, 1976). The Late Cretaceous schist of Sierra de Salinas crops out in the northeastern part of the range (Ross, 1976; Dibblee, 1974; 1979) and is the northernmost member of the Pelona-Orocopia-Rand schist—metasediments underplated during the Late Cretaceous (Barth et al., 2003; Grove et al., 2003; Kidder and Ducea, 2006; Chapman et al., 2010). Together, the crystalline rocks form an elongate belt of moderately to deeply exhumed Sierran basement—known as the Salinian block—that has been tectonically excised from its former location in the Mesozoic Sierra Nevada arc (Graham, 1978; Page, 1981; Dickenson, 1983). Restoration of slip along the San Andreas fault (e.g. Powell, 1993) partially restores the Salinian block to its original location, but further inboard displacement is required based on isotopic, thermobarometric, petrologic, and regional geologic constraints (e.g. Chapman et al., 2012). The structure responsible for this additional movement is most likely the Nacimiento fault, which separates plutonic and amphibolite–granulite-facies metamorphic rocks on the north from greenschist–blueschist-facies Franciscan mélange on the south (Ross, 1976; Dibblee, 1979; Hall, 1991; Page et al., 1998; Dickenson et al., 2005).

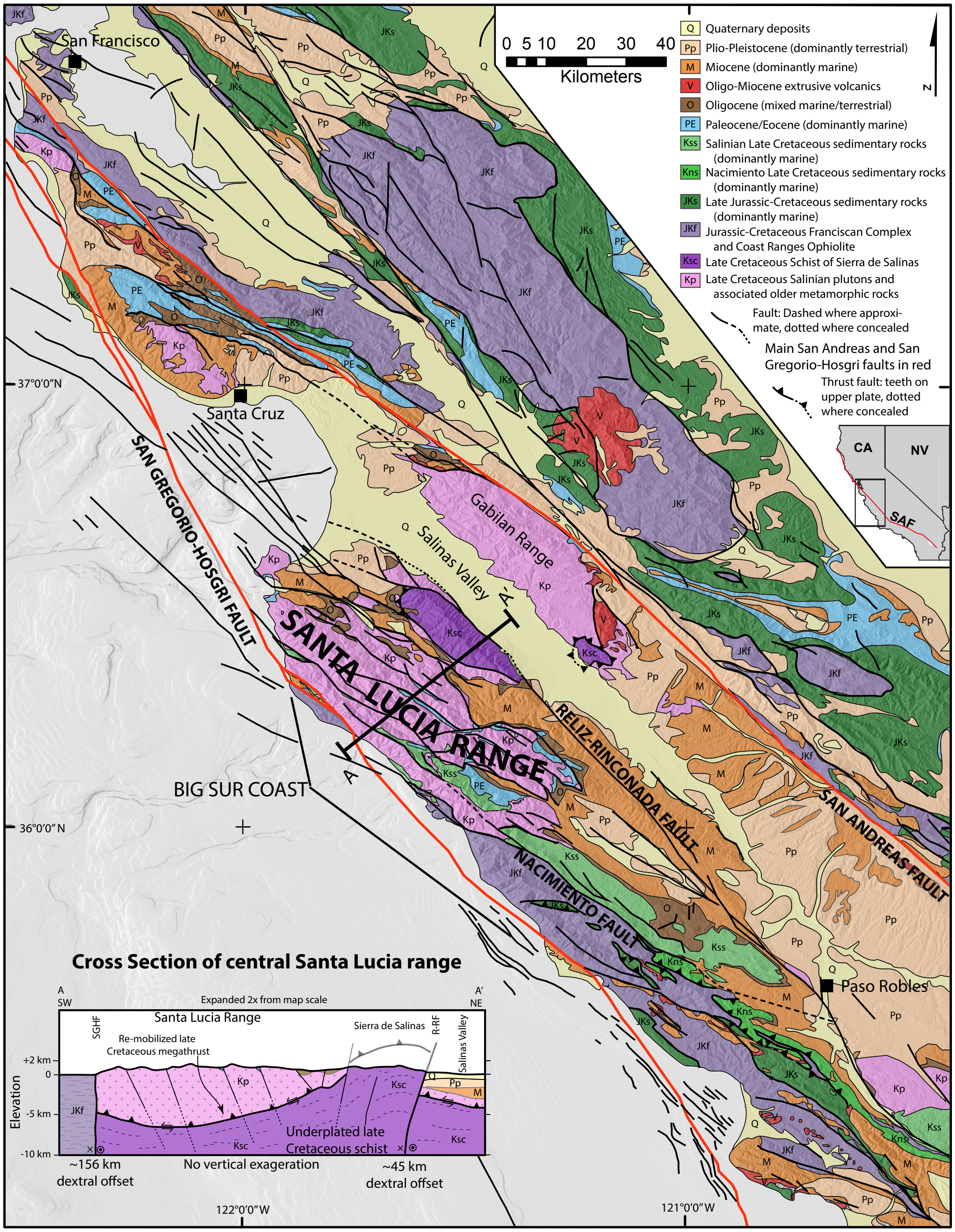

Figure 1-1. Generalized geologic map and cross section of the Santa Lucia range, central California. Geology and faults from Jennings and Bryant (2010) and Jennings et al. (2010). Simplified traces of the San Andreas and San Gregorio–Hosgri faults in red.

Substantial lithospheric reorganization occurred during the Late Cretaceous to Paleocene in the region that would later become the Mojave Desert, Transverse Ranges, and the Salinian block (Jacobson et al., 2007; Saleeby et al., 2007; Chapman et al., 2010). Rapid upper-crustal attenuation and exhumation in the Santa Lucia range brought >7.5 kbar and 850° C rocks to the surface over a 10 m.y. period from ~80–70 Ma, at rates of 2–3 mm/yr (Chapman et al., 2010). It was during this period that the schist of Sierra de Salinas was eroded from crystalline highlands, deposited on the down-going plate, subducted, and re-laminated at the base of the crust; the schist is now juxtaposed beneath the crystalline rocks that presumably provided the detritus for the schist protolith (Grove et al., 2003; Jacobson et al., 2011). It is hypothesized that these relationships are the result of subduction of a thick, buoyant, volcanic plateau during the transition to shallow Laramide-style subduction (Saleeby, 2003; Chapman et al., 2012).

The Late Cretaceous crustal restructuring quickly led to the accumulation of several kilometers of Late Cretaceous to Paleocene coarse-grained marine and non-marine basin fill (Fig. 1-2) that was deposited within normal-fault bound half grabens in the Santa Lucia and nearby La Panza ranges (Vedder and Brown, 1968; Ruetz, 1979; Graham, 1979; Dibblee, 1979; Grove, 1993). Marine deposition appears to have become more widespread by latest Paleocene through Eocene time, but major erosional and angular unconformities—and rapid changes in paleobathymetry—indicate several periods of subsidence and uplift during this time (Ruetz, 1979; Graham, 1976; 1979; Grove, 1993).

Marine basins rapidly shoaled at the end of the Eocene, a regional unconformity was developed, and the basins were completely re-submerged several m.y. later (Graham, 1976; Nilsen, 1981). This basin reorganization appears to precede the initial interaction of the Pacific and North America plates at ~30–28 Ma (e.g. Atwater and Stock, 1998; McQuarrie and Wernicke, 2005). The reason for this is not immediately clear, but is perhaps due to the proximity of the Pacific–Farallon spreading center and the subduction of young oceanic crust and (or) may be related to proto-San Andreas deformation (e.g. Graham, 1979).

Miocene paleogeography is complicated in the Santa Lucia range and Salinas Valley (Graham, 1976; 1978; 1979). In general, much of the range subsided and accumulated as much as 2.5 km of shallow to deep-marine deposits of the Monterey Formation (Graham,

Generalized stratigraphy of the Santa Lucia Range

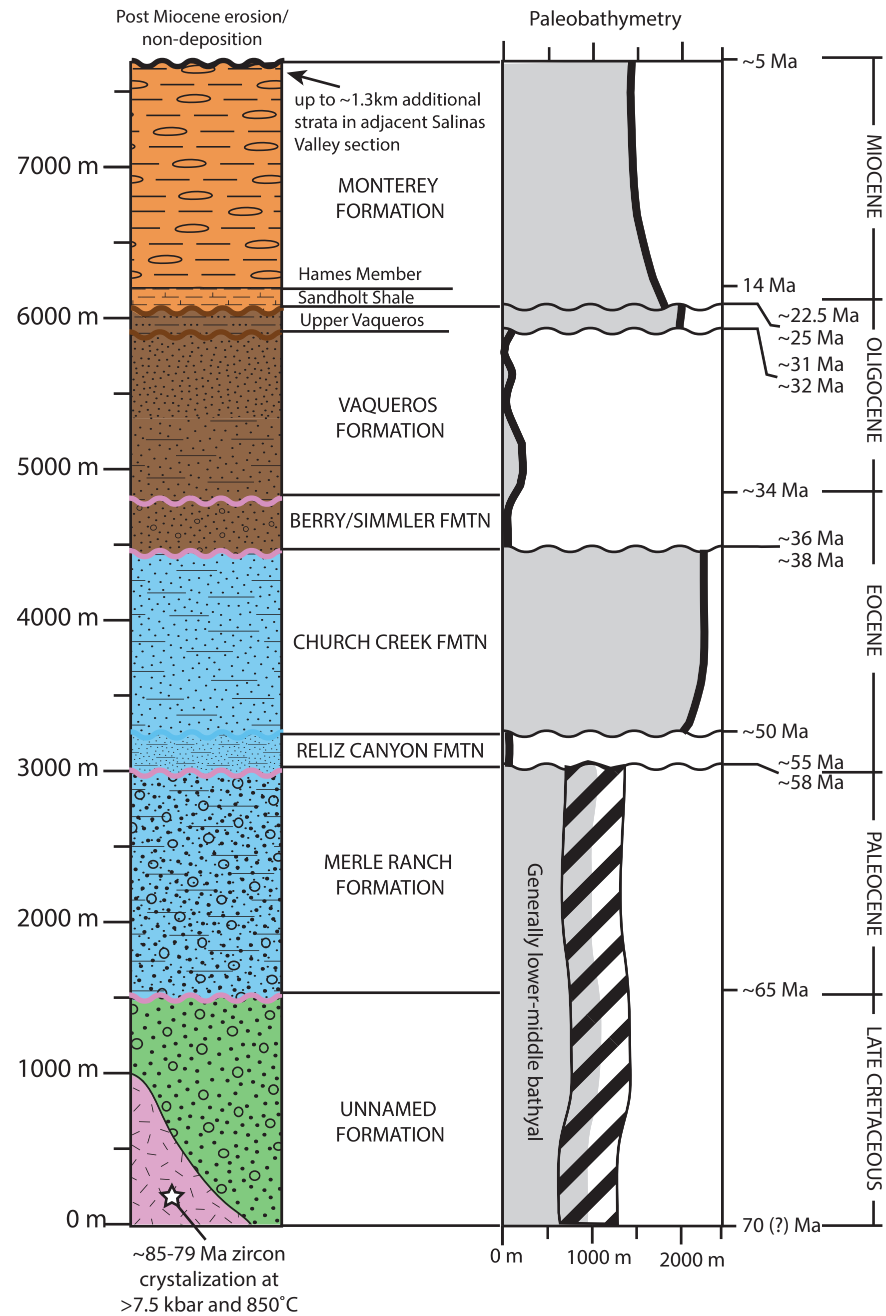

Figure 1-2. Generalized stratigraphy and paleobathymetry of the central Santa Lucia range near Indians Ranch. Color of unconformity indicates depth of erosion: pink, crystalline basement; blue, Paleocene–Eocene units; brown, Oligocene units. Data are from Graham (1976; 1978; 1979), Ruetz (1979), Dibblee (1974; 1979), Seiders et al. (1983), Grove (1993), and Anderson et al. (2006).

1978; Dibblee, 1976; 1979). Local emergent highs formed and subsided along the trace of the Reliz–Rinconada fault, indicating fault activity (Graham, 1978). Deposits of Monterey Formation flank the currently exposed crystalline core of the Santa Lucia range to the northwest, northeast, and southeast, and an incomplete faulted section is exposed in the central-northwest part of the range (Dibblee, 1974; Rosenberg and Wills, 2016). However, the thickness of Miocene deposits in the central and southwestern parts of the range—if any—remains uncertain. A regional-scale Pliocene regression is recorded by subaerial clastic progradation that commonly contains recycled Miocene basin fill clasts (e.g. Page et al., 1998).

BASIN SUBSIDENCE ANALYSIS

METHOD, SOURCES OF DATA, AND UNCERTAINTY

The thickness and age of layers in a sedimentary basin provide first-order constraints on the subsidence rate of the basin through time (Mial, 2000). A simple plot of sediment thickness through time can provide some insight into the basin-forming processes, however, two main processes reduce the usefulness of such an approach. The first is that the measured thickness of sedimentary units is an underestimate of their thickness during deposition because of subsequent burial, compaction, and lithification (e.g. Steckler and Watts, 1978; Sclater and Christie, 1980). The second is that the addition of sediment to a basin causes additional subsidence through isostatic compensation. Calculating and removing these two effects forms the basis for a backstripping analysis and provides a more-reasonable estimate of the subsidence history of the basin that can then be related to external processes (e.g. Steckler and Watts, 1978).

To calculate the history of subsidence in the Santa Lucia range, we use the MATLAB-based program BasinVis 1.0 (Lee et al., 2016), which assumes an Airy-type isostasy. Given the geologic history of the range and the modern-day presence of a closely spaced network of faults, neglecting the lateral strength of the crust is more reasonable than trying to establish a basis for its flexural strength. We use the sea-level curves of Haq et al. (1988), and the porosity-depth relationships of Sclater and Christie (1980). The stratigraphic data used in the subsidence analysis are shown in Figure 1-2 and Table 1-1, and are compiled from Graham (1976; 1978; 1979), Ruetz (1979), Dibblee (1974; 1979), Seiders et al. (1983), Grove (1993), and Anderson et al. (2006).

Table 1-1. Stratigraphic data used in the subsidence analysis.

Unit	Age, lower (Ma)	Age, upper (Ma)	Thickness, measured (km)	Water depth (km)	Sea level (km)	Porosity, initial (%)	Coef. of porosity-depth relat. (x10^{-5})	Density (g/cm^3)
Monterey Formation, Hames member	14	5	1.5	1.5	0.03	0.65	0.51	2.68
Monterey Formation, Sandholt member	22.5	14	0.15	1.8	0.12	0.63	0.51	2.68
Unconformity	25	22.5	– – –	1.9	0.12	– – –	– – –	– – –
Vaqueros Formation, upper	31	25	0.15	2	0.125	0.49	0.27	2.68
Unconformity	32	31	– – –	1	0.15	– – –	– – –	– – –
Vaqueros Formation, lower	34	32	1.1	0.2	0.18	0.49	0.27	2.68
Berry/Simmler formations	36	34	0.35	0.1	0.15	0.4	0.25	2.68
Unconformity	38	36	– – –	1	0.17	– – –	– – –	– – –
Church Creek Formation	50	38	1.2	2.2	0.19	0.56	0.39	2.68
Reliz Formation	55	50	0.25	0.15	0.22	0.56	0.39	2.68
Unconformity	58	55	– – –	0	0.21	– – –	– – –	– – –
Merle formation	65	58	1.5	1	0.2	0.4	0.25	2.68
Un-named Late Cretaceous formation	70	65	1.5	0.6	0.2	0.4	0.25	2.68

The stratigraphy of the central Santa Lucia range is complex, with imprecise age control, laterally varying unit thicknesses, and many regionally extensive unconformities (e.g. Ruetz, 1979; Graham, 1978; 1979; Dibblee, 1979). Three unconformities within the stratigraphy span 1–2.5 m.y. and for these we estimate that there was no sedimentation or erosion and use a linear interpolation of water depth. For the ~3-m.y.-long Paleocene–Eocene unconformity, we assume that there was no water in the basin—consistent with evidence of substantial uplift and erosion—but do not specifically account for any amount of subaerial erosion that may have occurred. Because of these simplifying assumptions, the calculated uplift rates for these periods are likely a minimum if there was relatively little submarine erosion of the basin stratigraphy. An additional complication arises from estimates of paleobathymetry in these strata (e.g. Graham, 1976; 1978; 1979), which have greater uncertainty than initially reported (S. Graham, Stanford University, oral commun., 2012). Because of this, we calculate a model using the published paleobathymetric estimates and additional models with 75% and 125% of these values to help determine the sensitivity of our model results to estimates of paleobathymetry.

RESULTS

The tectonic subsidence component of our analysis is shown in Figure 1-3 along with estimates of paleobathymetry. Two major periods of uplift and shoaling are identified by the analysis, at ~58–55 Ma, and between ~38–34 Ma; a third, ~5 Ma to present period is inferred by the exposure and erosion of late Miocene sediments beginning in the Pliocene (e.g. Christensen, 1965), and the late Miocene to ongoing uplift and exhumation of the range (Chapters 2 and 3). Uplift appears to have occurred more than twice as fast as subsidence, with the notable exception of very rapid subsidence from ~34–31 Ma. Each of the uplift events are correlated with a major change in tectonic regime, and is discussed further below.

Rates of subsidence and uplift should be viewed cautiously, however, considering the uncertainties in age (of the older units especially), the number and complexity of unconformities, and the uncertainties in paleobathymetry. For example, the uplift event at the end of the Paleocene (Fig. 1-3) is likely underestimated by our subsidence analysis because the several-m.y.-long unconformity indicates uplift, tilting, and erosion of up to 2 km of section in some locations (Graham, 1979; Ruetz, 1979). Additionally, the age of the upper-most Miocene Monterey Formation is uncertain in the Santa Lucia range; we used a relatively arbitrary value of 5 Ma because that is the age of the upper Monterey Formation to the north and northeast (e.g. Graham, 1978; Dibblee, 1979). A change in this value will alter the form of the subsidence curve since the late Miocene, but will not substantially change the overall pattern.

Figure 1-3. Tectonic subsidence curve for the central Santa Lucia range. Subsidence analysis parameters as indicated in the text. Rates are positive for subsidence, negative (and bold) for uplift, and are in mm/yr.

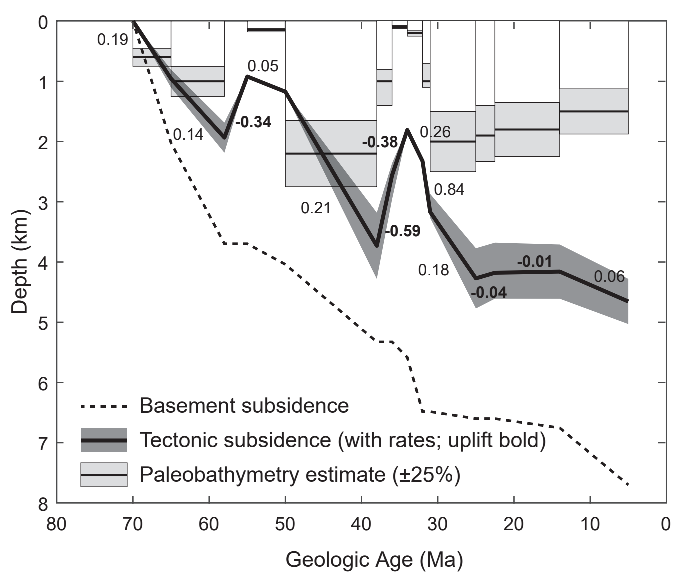

ESTIMATING CRUSTAL STRENGTH

METHOD AND SOURCES OF DATA

A simple 1-D model of crustal rheology with the ability to construct lithologic layering was developed to allow exploration of crustal strength for various upper- and mid-crustal scenarios. A two-slope Coulomb failure criteria was used to describe brittle behavior in the upper crust (e.g. Byerlee, 1978), whereby above confining pressures of 200 MPa the coefficient of friction (μ) is 0.6 and the cohesion is 50 MPa; at lower confining pressure, μ is 0.85 and there is no cohesion. A power-law equation for dislocation glide and creep was used to describe the plastic behavior of material in the mid to lower crust (e.g. Brace and Kohlstedt, 1980), except for mica schist, which is better described by an exponential equation (Table 1-2) (Shea and Kronenberg, 1992). The model calculates the differential stress at each depth using the hydrostatically adjusted confining pressure (φ=0.36) and the user-defined temperature gradient. The model allows the strain rate to vary, but for comparison between models and to published strength curves, a value of 10^{-14} s^{-1} was chosen. Material properties for a range of materials were taken from published laboratory experiments and are provided in Table 1-2.

Table 1-2. Rheologic properties of select geologic materials. A power-law equation is used to describe the bahvior of most materials except schist, which is better described by an exponential function. The sensitivity of schist relates to the temperature path and strain history of the rock. C, A, N and α are material parameters, σ_d is the differential stress, $\dot{\varepsilon}$ is the strain rate, Q is the activation energy, R is the Boltzman constant, and T is temperature.

Power-law equation: $\dot{\varepsilon} = A\sigma_d{}^N e^{(-Q/RT)}$

Material	A ($MPa^{-n}s^{-1}$)	N	Q ($kJ\ mol^{-1}$)	Source
Quartzite, wet	1.0×10^{-4}	2.4	160	Brace and Kohlstedt, 1980; Kohlstedt et a., 1995
Quartzite, wet	1.1×10^{-4}	4	223	Gleason and Tullis, 1995
Quartzite, dry	6.3×10^{-6}	2.4	156	Ranalli and Murphy, 1987
Granite, wet	2.0×10^{-4}	1.9	140	Mackwell et al., 1998
Diorite, wet	3.2×10^{-2}	2.4	212	Ranalli, 1995
Diabase, Maryland	8	4.7	485	Mackwell et al., 1998
Diabase, dry	2.2×10^{-4}	3.4	260	Kirby, 1983
Granulite, dry	1.4×10^{4}	4.2	445	Wilks and Carter, 1980
Granulite, Adirondack, undried	3.18×10^{-4}	3.1	243	Wilks and Carter, 1980
Dunite, wet	4.17×10^{2}	4.48	498	Chopra and Patterson, 1984

Exponential equation: $\dot{\varepsilon} = Ce^{(\alpha\sigma_d)} e^{(-Q/RT)}$

Material	C ($MPa^{-n}s^{-1}$)	α	Q ($kJ\ mol^{-1}$)	Source
Mica schist, strongly sensitive	1.4×10^{-10}	0.15	89	Shea and Kronenberg, 1992
Mica schist, weakly sensitive	4.3×10^{-52}	0.55	89	Shea and Kronenberg, 1992

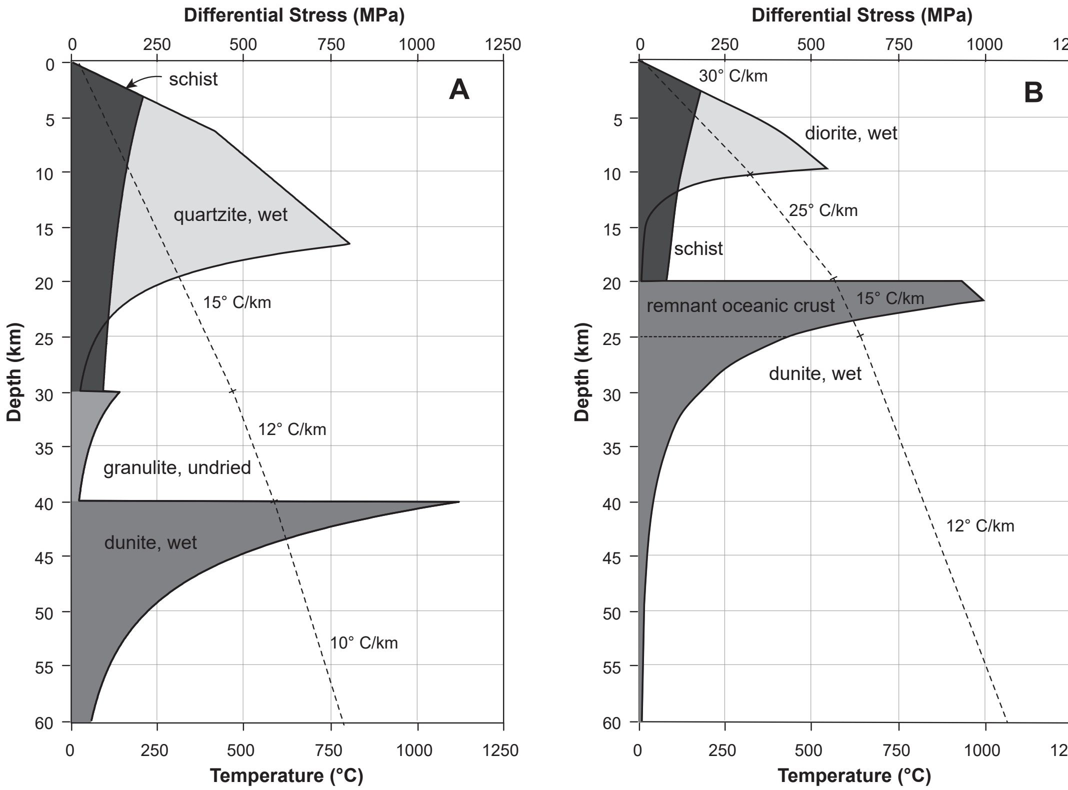

Figure 1-4. Yield strength model results comparing rheologically layered upper crust with more-typical unlayered model. A). 30-km-thick continental crust with a moderate geothermal gradient behaves very differently than mica schist. B) A possible crustal cross section of the modern-day Salinian block with up to 20-km-thick upper crust overlying a 5-km-thick remnant oceanic plate and moderate geothermal gradient. The strong mid crust is very sensitive to even small amounts of schist. Rheological parameters provided in Table 1-1.

RESULTS

The most basic observation from this model—and the overall conclusion of Shea and Kronenberg (1992)—is that schist is substantially weaker than quartz-bearing crystalline rocks. For a hypothetical crustal cross section with a strain rate of 10^{-14} s^{-1} and an upper-crustal geothermal gradient of 15° C/km, ductile behavior in schist begins at depths of ~3 km and schist is only ~1/4 as strong as quartz-rich rocks at their mid-crustal maximum (Fig. 1-4a). Depending on the depth where mica-schist-rich lithologies are found in the crust, the strength discrepancy could have wide-ranging effects on how strain is accommodated in the upper crust, for example, by serving as a ductile detachment zone at shallow depths (e.g. Zoback et al., 2002).

Such low geothermal gradients, however, are unlikely for the Santa Lucia range (e.g. Lachenbruch and Sass, 1980) which has experienced rapid exhumation in the late Cretaceous

(Chapman et al., 2010), was exposed to hot asthenosphere in the Oligo–Miocene (e.g. Groome and Thorkelson, 2009), and localized late Miocene exhumation. Additionally, a simple and thick upper crust is an unlikely scenario for the Salinian block, which has been displaced from its initial location within the Mesozoic arc (e.g. Dickenson, 1983; Hall, 1991; Thompson, 1999).

Thus, a second model of crustal strength was developed (Fig. 1-4b) using geologic and geophysical cross sections of the coast range (Page et al., 1998; Thompson, 1999), and higher estimates of geothermal gradient. The general parameters of this model are a 20-km-thick upper crust that overlies a 5 km-thick oceanic plate underlain by the upper mantle, with a geothermal gradient of 25–30° C/km in the upper 20 km. As expected from the much higher geothermal gradient, the second model indicates a shoaling of the brittle-ductile transition, a decrease in the maximum differential stress, and a narrowing of the strong mid crust. The presence of schist—even as thick as 10 km—near the top of the remnant oceanic plate where it would seem most likely to occur has apparently little effect on the overall shape of the yield envelope. However, at depths normally occupied by the strongest crystalline crust—between ~150° C to 300° C—the presence of schist can drastically reduce crustal strength.

DISCUSSION

INTEGRATED HISTORY OF VERTICAL DEFORMATION IN THE SANTA LUCIA RANGE

A compilation of geochronology, thermobarometry, and thermochronology from the Santa Lucia range (Chapman et al., 2010) provides the vertical deformation history just prior to marine deposition (Fig. 1-5). Two time-temperature paths are shown, one indicates the crystallization of young plutons in the Santa Lucia range at 7.5 kbar depths followed by rapid exhumation to the surface, a result supported by older apatite and zircon ages in the northeastern part of the range (Chapter 3). The other path indicates the youngest age component of detrital zircons in the schist of Sierra de Salinas, followed by rapid burial to ~10 kbar depths and equally rapid exhumation to near the surface. This pattern—coupled with inverted metamorphic gradients in the schist (e.g. Ducea et al., 2006)—are characteristic evidence of the late Cretaceous crustal restructuring event that occurred during Laramide shallow subduction (e.g. Saleeby, 2003) and can be found in many locations in central and southern California (Chapman et al., 2010).

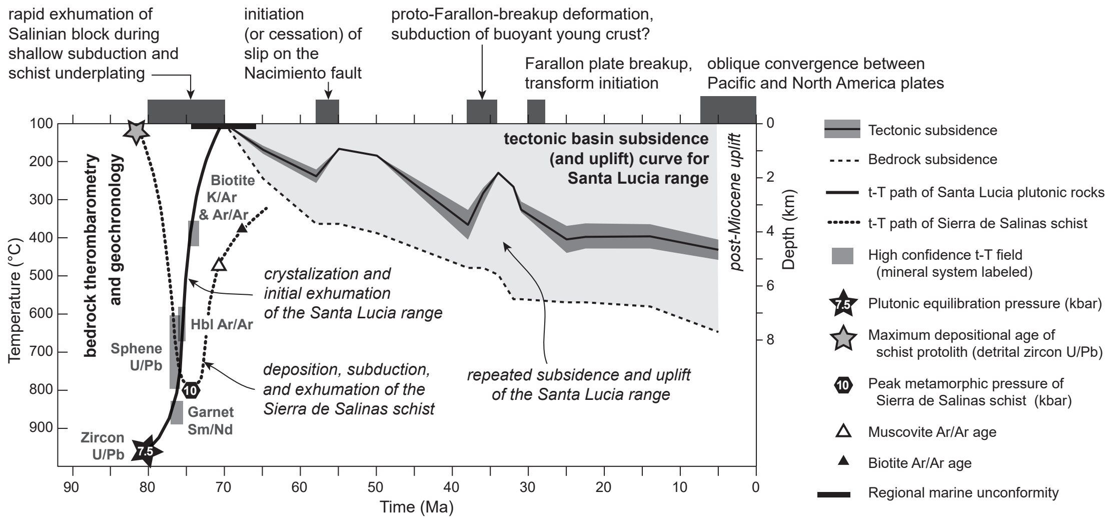

Figure 1-5. Integrated history of vertical deformation in the Santa Lucia range since the late Cretaceous. Constraints from geochronology, thermobarometry, and thermochronology—as summarized in Chapman et al. (2010)—provide t-T paths for the crystalline bedrock and underplated schist of the range. Post-late-Cretaceous history is from the subsidence analysis presented here. Note the change in vertical scale between t-T paths and th subsidence history.

When combined with the subsidence analysis, the two datasets show that there have been 4 major uplift and exhumation events since ~80 Ma: the initial exhumation of the bedrock, two events bracketed by periods of subsidence and deposition, and the most recent and ongoing event. Each of these events lasted between ~3 and 10 m.y. and are separated by periods of subsidence that lasted between 15 and 22 m.y. Thus, there appears to be a cyclic pattern of uplift and subsidence where each uplift is both shorter in length and faster in rate than intervening periods of subsidence. Despite the strong periodic signal in these data, it seems unlikely that the cyclic pattern is the manifestation of an underlying periodic physical process, but more likely reflects the stochastic, yet somewhat rhythmic major tectonic changes over the past 80 m.y.

RELATIONSHIP BETWEEN UPLIFT AND TECTONIC EVENTS

Each of the uplift events is closely associated with a major change in tectonic regime. Initial late Cretaceous exhumation was likely a combination of uplift and erosion during the subduction of a buoyant volcanic plateau, followed by tectonic denudation during gravitational collapse towards the trench after the passage of the buoyant plateau (Saleeby, 2003; Chapman et al., 2012). Coarse-grained near-shore and marine sediments were deposited on this exhumed bedrock in steep normal-fault-bound crustal blocks (e.g. Ruetz, 1979; Grove, 1993) and may reflect continuing gravitational collapse throughout the late Cretaceous and early Paleocene. The uplift event at the end of the Paleocene (Figs. 1-3 and 1-5) is perhaps related to slip along the Nacimiento fault (e.g. Dickenson et al., 2005), although whether it marks initiation or cessation of slip is uncertain. The major component of sinistral slip along the Nacimiento fault is constrained to pre-early Miocene based on an overlap sequence (Dickenson et al., 2005), but there is little definitive constraint beyond the late Cretaceous crystallization ages of Salinian plutons (Mattinson, 1978; Kistler and Champion, 2001; Barth et al., 2003) and their subsequent rapid exhumation (e.g. Chapman et al., 2010) on when the fault may have initiated.

The late Eocene to Oligocene event indicates a profound 7-m.y.-long restructuring of the basin (Figs. 1-3 and 1-5) which rapidly shoaled from >2-km-water depth, locally eroded to the crystalline basement, deposited coarse subaerial and nearshore sediment, and then rapidly re-submerged to >2-km-water depths (Dickenson, 1965; Graham, 1976; 1978; 1979; Dibblee, 1979). These events have been correlated with general 'proto-San Andreas' deformation (e.g. Graham, 1979), a hypothesis potentially supported by two additional lines of evidence. Palinspastic reconstructions (McQuarrie and Wernicke, 2005) indicate that at ~36 Ma, the Santa Lucia range—and the whole Salinian block in general—was located near where the Pacific plate would make initial contact with North America a few m.y. later, at 28–30 Ma (Atwater and Stock, 1998). The breakup of the Farallon plate into two microplates also appears to have occurred about ~28 Ma (Lonsdale, 1991; Atwater and Stock, 1998). The subduction of young and buoyant oceanic crust in the several m.y. prior to Farallon breakup and the establishment of two migrating triple junctions may provide a mechanism for uplift and disruption of basin deposystems along the most-westward parts of the continent. Together, these findings support the general idea that late Eocene to Oligocene basin restructuring in the Santa Lucia range is related to the transition from a convergent margin to transform plate boundary. Within this context, however, there is a notable lack of a strong signal in the subsidence analysis at ~23 Ma when the San Andreas fault initiated (Graham et al., 1989). This may suggest that by Miocene time the Santa Lucia range was structurally decoupled from crust to the northeast, perhaps along the Reliz-Rinconada fault.

The late Miocene to present phase of uplift is related to the increasing transpressional obliquity between the Pacific and Sierra Nevada-Great Valley plates (Page et al., 1998; Argus and Gordon, 2001; DeMets and Merkouriev, 2016). A substantial component of uplift and exhumation has been focused along the SW flank of the range adjacent to the SGHF (Chapters 2 and 3). Distributed late Miocene to present deformation (and uplift) within the range results from discrete slip along the closely spaced fault network (e.g. Compton, 1966b; Dibblee, 1974; 1979), and (or) as part of a broad and faulted contractional stepover between the SGHF and the RRF. Such a stepover has been suspected by many based on gradients in fault displacement, the presence of faulted late Miocene and older sedimentary rocks, and analysis of Plio–Pleistocene stratigraphy (Dickenson, 1965; Christiansen, 1965; Compton, 1966a; 1966b; Graham, 1978; Dibblee, 1979; Page et al., 1998; Dickenson et al., 2005; Langenheim et al., 2013). Although the timing and magnitude of late Miocene to present uplift are highly variable across the range (Chapters 2 and 3), the overall pattern is similar to previous disturbances and may not necessarily be more complex.

POSSIBLE ROLE OF UNDERPLATED SCHIST IN LOCALIZING STRAIN

Using the model developed here, even a modest 3–5-km-thick package of schist could limit mid-crustal strength if located at depths between ~5 and 10 km (Fig. 1-4b). Active subduction channels are typically between 1–7 km thick based on global fluxes of subducting material and seismic imaging (e.g. Stern, 2011), and underplated schist in central California is estimated to be of similar thickness (Ducea et al., 2009; Chapman et al., 2010). Within the Santa Lucia range—and elsewhere in central and southern California—underplated schist crops out at the surface and is inferred at shallow to moderate depths (Ross, 1976; Kidder and Ducea, 2006; Chapman et al., 2012; Niemi et al., 2013). These observations require that schist lies at these sensitive depths, or did at some time in the past, for locations adjacent to exposures of the Pelona–Orocopia–Rand schists.

Three simple predictions of shallow underplated schist are explored below. However, it can be difficult test these predictions at a range scale because differences in the geothermal gradient, initial thickness and depth of schist, and long-term temporal evolution of vertical deformation all have a strong effect on whether the schist drastically reduces strength, or does very little. Given the complicated geologic history of the regions in California which contain underplated schist, it is likely that these parameters vary both spatially and temporally.

In general, regions underlain by schist at depths corresponding to ~<300° C will deform more readily than other regions with a stronger mid crust (Fig. 1-4) because strain rate is often controlled by the weakest region (e.g. Zoback et al., 2002). Such a localization of strain predicts that regions with a weak mid crust will record a disproportionate fraction of accumulated geologic strain compared to adjacent crustal blocks with greater strength. An additional prediction is that fault density may be greater in regions where schist lies at shallow depths and the brittle portion of the crust is thinner (e.g. Mandl, 1988; Dauteuil and Mart, 1998).

A third prediction is that a positive feedback may develop between strain rate and schist depth once the schist begins to decrease crustal strength. For example, consider a scenario in which a fault-bound block contains 10 km of crystalline rock and a 5-km-thick package of schist above a remnant oceanic plate (Fig. 1-4b). The top of the schist is at ~10 km depth and affects the overall strength of the crust very little. The block is then subjected to a period of oblique convergence and erosional exhumation (or extension and tectonic exhumation). As time progresses, the schist is advected upward and reduces the strength of the crust. The reduction in strength is met with a higher strain rate (and increased exhumation) because the block is now easier to deform than its surroundings. Such a positive feedback is somewhat like the 'tectonic aneurysm' hypothesis (e.g. Zeitler et al., 2001), but is modulated by the strength of layers beneath the schist and does not require extremely high and focused erosion.

With these predictions in mind, it seems likely that the presence of underplated schist beneath the Santa Lucia range has likely played a role in focusing deformation. The schist of Sierra de Salinas is exposed in the northeast part of the range (e.g. Ross, 1976) and presumably dips to the SW beneath most of the range (Kidder and Ducea, 2006; Ducea et al., 2009). The range has experienced frequent and high-amplitude vertical fluctuations over an 80-m.y. period (Fig. 1-5), even compared to basins from the southern San Joaquin valley (Moxon and Graham, 1987; Bartow, 1991; Goodman and Malin, 1992) which did not develop above shallow underplated schist and have lower geothermal gradients. Since the late Miocene, exhumation has generally focused along the SW flank of the range, and appears to be greater in magnitude where crystalline rocks are permissibly underlain by schist at 5–10 km depth than in other lithologies (Chapters 2 and 3). Lastly, the density of mapped faults in the crystalline rocks of the Santa Lucia range appears to be much higher than in nearby areas (Jennings and Bryant, 2010; Graymer et al., 2014; Rosenberg and Wills, 2016).

Together, these observations fit our predictions well, but several observations remain puzzling. For example, paleogeographic reconstructions (Graham, 1978; Graham et al., 1989) and low-temperature thermochronometry (Naeser and Ross, 1976; Bürgmann et al., 1994; Spotila et al., 2007; Colgan et al., 2012) indicate that the La Panza range and Santa Cruz mountains have not experienced the same magnitude or frequency of vertical deformation as the Santa Lucia range (Ducea et al., 2003; Chapter 2; Chapter 3). This seems unusual because the these ranges are cored by crystalline rocks of the Salinian block and are presumably underlain by schist like the Santa Lucia range. Additionally, since underplated schist is currently exposed in the Sierra de Salinas and at the base of the Gabilan range (Fig. 1-1), these areas are presumably quite weak, yet much work indicates their relative stability compared to other parts of the range (Graham, 1976; 1978; Dibblee, 1976; Chapter 3). The inferred lateral ramp of the Laramide shallow subduction channel (fig. 13 in Chapman et al., 2012) might be able to explain the differences between the Santa Cruz mountains and Santa Lucia range, but does not explain the remaining observations. One possibility is that perhaps the weak mid crust along the southwest margin of the Santa Lucia range has acted as a crustal ‘crumple zone’, where fault-perpendicular components of strain were localized and did not penetrate to the more-interior ranges. This is not wholly satisfactory because it still predicts that regions underlain by a weak mid crust exhibit little vertical deformation adjacent to the main San Andreas fault.

CONCLUSION

The Santa Lucia range of central California exposes a nearly 8-km-thick composite section of basin fill on the Salinian block that spans ~60 m.y. between the late Cretaceous to late Miocene. Strata were deposited on the crystalline bedrock of the range, which records a ~10 m.y. period of rapid exhumation that brought mid-crustal rocks to the surface immediately prior to deposition of marine sediments. We perform a backstripping analysis to define the tectonic component of basin subsidence (or uplift). These results are combined with thermobarometric and geochronologic data to document long-term cyclic patterns of vertical deformation in the range.

There have been 4 major uplift and exhumation events—each with a duration of ~5–10 m.y.—separated by 3 periods of subsidence—with durations from 15–22 m.y. Each uplift cycle is marked by rapid shoaling of the basin and the development of regional angular unconformities that locally reach the crystalline basement. Each subsidence cycle is marked by rapid submergence of the basin to mid-bathyal depths; unconformities within these cycles are locally present, but less extensive. A period of relative calm in the mid- to late Miocene is suggested by our analysis, but nearby areas experienced significant tectonic disturbances as faults of the Rinconada-Reliz and San Andreas faults were forming.

Each of the uplift cycles appears to correspond to a major tectonic event. Initial exhumation of the Salinian block occurred during the drastic crustal restructuring which accompanied shallow-slab subduction and the replacement of strong lithosphere with weak underplated schist. The uplift cycle in the Paleocene is associated with outboard translation of the Salinian block during sinistral slip along the Nacimiento fault. The Oligocene-age cycle is tentatively associated with deformation preceding the breakup of the Farallon plate before establishment of a Pacific–North America transform boundary. The most-recent uplift cycle is likely related to oblique convergence between the Pacific and North America plates. This event is ongoing, has exposed the crystalline core of the range, and is actively eroding the older basin stratigraphy.

Based on this analysis it appears that the magnitude and rate of uplift and subsidence in the Santa Lucia range are greater than adjacent areas when restored for slip along the San Andreas fault. We suggest that the emplacement of several-km-thick weak schist beneath the range in the late Cretaceous profoundly weakened the Salinian block, permitting late Cretaceous excision of arc crust from southern California and subsequent high amplitude fluctuations in uplift and subsidence.

REFERENCES

Argus, D.F., Gordon, R.G., 2001, Present tectonic motion across the coast ranges and San Andreas fault system in central California. Geological Society of America Bulletin v. 113, p. 1580– 1592.

Anderson, K.S., Graham, S.A., Hubbard, S.M., 2006, Facies, architecture, and origin of a reservoir-scale sand-rich succession within submarine canyon fill: insights from Wagon Caves Rock (Paleocene), Santa Lucia Range, California, USA. Journal of Sedimentary Research, v. 76, p. 819-838.

Atwater, T., Stock, J., 1998, Pacific– North America plate tectonics of the Neogene southwestern United States: an update. International Geology Review v. 40, p. 375–402.

Bartow, J.A., 1991, The Cenozoic Evolution of the San Joaquin Valley, California. U.S. Geological Survey Professional Paper 1501, 40 pp.

Barth, A.P., Wooden, J.L., Grove, M., Jacobson, C.E., Pedrick, J.N., 2003, U-Pb zircon geochronology of rocks in the Salinas Valley region of California: A re-evaluation of the crustal structure and origin of the Salinian block. Geology, v. 31, p. 517-520.

Brace, W.F., Kohlstedt, D.L., 1980, Limits on lithospheric stress imposed by laboratory experiments. Journal of Geophysical Research, v. 85, p. 6248-6252.

Byerlee, J.D., 1978. Friction of rocks. Pure and Applied Geophysics, v.116, p. 615-626.

Burov, E.B., 2011, Rheology and strength of the lithosphere. Marine and Petroleum Geology, v. 28, p. 1402-1443. DOI: 10.1016/j.marpetgeo.2011.05.008

Burov, E., Watts, A.B., 2006, The long-term strength of continental lithosphere: jelly-sandwich or crème-brûlée? Geological Society of America Today v. 16, n. 1, p. 4-10.

Bürgmann, R., Arrowsmith, R., Dumitru, T., and McLaughlin, R., 1994, Rise and fall of the southern Santa Cruz Mountains, California, from fission tracks, geomorphology, and geodesy. Journal of Geophysical Research, v. 99, p. 20,181-20,202.

Chapman, A. D., Kidder, S., Saleeby, J.B., and Ducea, M.N., 2010, Role of extrusion of the Rand and Sierra de Salinas schists in late Cretaceous extension and rotation of the southern Sierra Nevada and vicinity. Tectonics, v. 29, TC5006.

Chapman, A.D. Saleeby, J.B., Wood, D.J., Piasecki, A., Kidder, S., Ducea, M.N., Farley, K.A., 2012, Late Cretaceous gravitational collapse of the southern Sierra Nevada batholith, California. Geosphere, v. 8, n. 2, p. 314-341. DOI:10.1130/GES00740.1

Christensen, M.N., 1965, Late Cenozoic deformation in the central Coast Ranges of California. Geological Society of America Bulletin, v. 76, p. 1105–1124.

Chopra, P.N., Paterson, M.S., 1984, The role of water in the deformation of dunite. Journal of Geophysical Research, v. 89, p. 7861-7876.

Colgan, J.P., McPhee, D.K., McDougall, K., and Hourigan, J.K., 2012, Superimposed extension and shortening in the southern Salinas Basin and La Panza Range, California: A guide to Neogene deformation in the Salinian block of the central California Coast Ranges. Lithosphere, v. 4, p. 411–429. DOI:10.1130/L208.1

Compton, R.R., 1960, Charnockitic rocks of the Santa Lucia Range, California. American Journal of Science, v. 258, p. 609-636.

Compton, R.R., 1966a, Granitic and metamorphic rocks of the Salinian block, California Coast Ranges, in Bailey, E.H., editor, Geology of northern California: California Division of Mines and Geology Bulletin 190, p. 277–287.

Compton, R.R., 1966b, Analysis of Pliocene–Pleistocene deformation and stresses in the northern Santa Lucia Range, California. Geological Society of America Bulletin, v. 77, p. 1361-1380.

Dauteuil, O., Mart, Y., 1998, Analogue modeling of faulting pattern, ductile deformation, and vertical motion in strike-slip fault zones. Tectonics, v. 17, n. 2, p. 303-310.

DeMets, C., and Merkouriev, S., 2016, High-resolution reconstructions of Pacific-North America plate motion: 20 Ma to present. Geophysical Journal International, v. 207, p. 741-773.

Dibblee, T.W., Jr., 1974, Geologic maps of the Monterey, Salinas, Gonzales, Point Sur, Jamesburg, Soledad and Junipero Serra 15′ quadrangles, Monterey County, California, U.S. Geological Survey Open File Report 74-1021.

Dibblee, T.W., Jr., 1976, The Rinconada and related faults in the southern Coast Ranges, California, and their tectonic significance, U.S. Geological Survey Professional Paper 981, 55 p.

Dibblee, T.W., 1979, Cenozoic tectonics of the northeast flank of the Santa Lucia Mountains from the Arroyo Seco to the Nacimiento River, California, in Graham, S.A., ed, Tertiary and Quaternary geology of the Salinas Valley and Santa Lucia range, Monterey County, California: Pacific Section, SEPM, Pacific Coast paleogeography Field Guide 4, p. 67-76.

Dickinson, W.R., 1965, Tertiary stratigraphy of the Church Creek area, Monterey County, California. California Division of Mines and Geology Special Report, v. 86, p. 25–44.

Dickinson, W.R., 1983, Cretaceous sinistral strike slip along Nacimiento fault in coastal California: The American Association of Petroleum Geologists Bulletin, v. 67, p. 624–645.

Dickinson, W.R., Ducea, M., Rosenberg, L.I., Greene, H.G., Graham, S.A., Clark, J.C., Weber, G.E., Kidder, S., Ernst, G.W., and Brabb, E.E., 2005, Net dextral slip, Neogene San Gregorio–Hosgri fault zone, coastal California; geologic evidence and tectonic implications. Geological Society of America Special Paper 391, 43 p.

Ducea, M., Kidder, S., Chelsey, J.T., Saleeby, J.B., 2009, Tectonic underplating of sediments beneath magmatic arcs: the California example. International Geology Review, v. 51, n. 1, p. 1-26.

Ducea, M., House, M.A., and Kidder, S., 2003, Late Cenozoic denudation and uplift rates in the Santa Lucia Mountains, California. Geology, v. 31, p. 139–142.

Evans, B., Kohlstedt, D.L., 1995, Rheology of rocks, in Ahrens, T.J., ed., Rock Physics and Phase Relations: A Handbook of Physical Constants. American Geophysical Union Reference Shelf 1, American Geophysical Union, p. 149-165.

Furlong, K.P., 1984, Lithospheric behavior with triple junction migration: An example based on the Mendocino triple junction. Physics of Earth and Planetary Interiors, v. 36, p. 213-233.

Gleason, G.C., Tullis, J., 1995, A flow law for dislocation creep of quartz aggregates determined with the molten salt cell. Tectonophysics, v. 247, p. 1-23.

Goodman, E.D., Malin, P.E., 1992; Evolution of the southern San Joaquin basin and mid-Tertiary “Transitional” tectonics, central California. Tectonics, v. 11, n. 3, p. 478-498.

Graham, S.A., 1976, Tertiary sedimentary tectonics of the central Salinian block of California. Stanford University Thesis.

Graham, S.A., 1978, Role of Salinian Block in evolution of the San Andreas fault system, California. AAPG Bulletin, v. 62, p. 2214-2231.

Graham, S.A., Stanley, R.G., Bent, J.V., Carter, J.B., 1989, Oligocene and Miocene paleogeography of central California and displacement along the San Andreas fault. Geological Society of America Bulletin, v. 101, p. 711–730.

Graymer, R.W., Langenheim, V.E., Roberts, M.A., and McDougall, K., 2014, Geologic and Geophysical Maps of the Eastern Three-Fourths of the Cambria 30′ × 60′ Quadrangle, Central California Coast Ranges: U.S. Geological Survey Scientific Investigations Map SIM-3287, scale 1:100,000.

Groome, W.G., and Thorkelson, D.J., 2009, The three-dimensional thermomechanical signature of ridge subduction and slab window migration. Tectonophysics, v. 464, n. 1-4, p. 70-83.

Grove, K., 1993, Latest Cretaceous basin formation within the Salinian Terrane of west-central California. Geological Society of America Bulletin, v. 105, n. 4, p. 307-310.

Grove, M., Jacobson, C.E., Barth, A.P., and Vucic, A., 2003, Temporal and spatial trends of Late Cretaceous-early Tertiary underplating Pelona and related schist beneath southern California and southwestern Arizona. Geological Society of America Special Paper 374, p. 381-406.

Hall, C. A., Jr., 1991, Geology of the Point Sur-Lopez Point region, Coast Ranges, California; a part of the southern California allochthon, Geological Society of America Special Paper 266, 40 pp.

Haq, B.U., Harenbol, J., Vail, P.R., 1988, Mesozoic and Cenozoic chronostratigraphy and cycles of sea-level change, in Sea Level Changes—an integrated approach. Society of Economic Paleontologists and Mineralogists Special Publication 42, p. 71-108.

Jackson, J., 2002, Strength of the continental lithosphere: Time to abandon the jelly sandwich? Geological Society of America Today, v. 12, n. 10, p. 4–10.

Jacobson, C.E. Grove, M., Vucic, A., Pedrick, J.N., Ebert, K.A., 2007, Exhumation of the Orocopia schist and associated rocks of southeastern California: relative roles of erosion, synsubduction tectonic denudation, and middle Cenozoic extension. Geological Society of America Special Paper 419, p. 1-37.

Jennings, C.W., Bryant, W.A., 2010, Fault activity map of California. California Geological Survey, Geologic Data Map No. 6, scale 1:750,000.

Kirby, S.H., 1983, Rheology of the lithosphere. Reviews in Geophysics, v. 21, p. 1458-1487.

Kidder, S., and Ducea, M.N., 2006, High temperatures and inverted metamorphism in the schist of Sierra de Salinas, California, Earth Planetary Science Letters, v. 241, p. 422-437.

Kistler, R.W., Champion, D.E., 2001, Rb-Sr whole-rock and mineral ages, K-Ar, 40Ar/39Ar, and U-Pb mineral ages, and strontium, lead, neodymium, and oxygen isotopic compositions for granitic rocks from the Salinian composite terrane, California. U.S. Geological Survey Open-File Report 01-453, 84 p.

Kohlstedt, D.L., Evans, B., Mackwell, S.J., 1995, Strength of the lithosphere: constraints imposed by laboratory experiments. Journal of Geophysical Research, v. 100, p. 17587-17602.

Lachenbruch, A.H., and Sass, J.H., 1980, Heat flow and energetics of the San Andreas Fault Zone. Journal of Geophysical Research, v. 85, n. B11, p. 6185-6222.

Langenheim, V.E., Jachens, R.C., Graymer, R.W., Colgan, J.P., Wentworth, C.M., and Stanley, R.G., 2013, Fault Geometry and cumulative offsets in the central Coast Ranges, California: Evidence for northward increasing slip along the San Gregorio-San Simeon-Hosgri fault. Lithosphere, v. 5, p. 29-48.

Lee, E.Y., Novotny, J., Wagreich, M., 2016, BasinVis 1.0: A MATLAB-based program for sedimentary basin subsidence analysis and visualization. Computers and Geosciences. V. 91, p. 119-127. DOI: 10.1016/j.cageo.2016.03.013

Mackwell, S.J., Zimmerman, M.E., Kohlstedt, D.L., 1998, High-temperature deformation of dry diabase with applications to tectonics on Venus. Journal of Geophysical Research, v. 103, p. 975-984.

Mandl, G., 1988, Mechanics of tectonic faulting: Models and basic concepts. Elsevier Science Publishing Co., New York, NY, 406 pp.

Mattinson, J.M., 1978, Age, origin, and thermal histories of some plutonic rocks from the Salinian Block of California. Contributions to Mineralogy and Petrology, v. 67, p. 233-245.

McQuarrie, N., Wernicke, B.P., 2005, An animated tectonic reconstruction of southwestern North America since 36 Ma. Geosphere, v. 1, n. 3, p. 147-172. DOI: 10.1130/GES00016.1

Mial, A.D., 2000, Principles of sedimentary basin analysis, 3rd ed.. Springer-Verlag, Berlin. 616 pp.

Moxon, I.W., Graham, S.A., 1987, History and controls of subsidence in the Late Cretaceous-Tertiary Great Valley forearc basin, California. Geology, v. 15, p. 626-629. DOI: 10.1130/0091-7613(1987)15<626:HACOSI>2.0.CO;2

Naeser, C.W., and Ross, D.C., 1976, Fission-track ages of sphene and apatite of granitic rocks of the Salinian Block, Coast Ranges, California. Journal of Research of the U.S. Geological Survey, v. 4, n. 4, p. 415-420.

Niemi, N.A., Buscher, J.T., Spotila, J.A., House, M.A., Kelley, S.A., 2013, Insights from low-temperature thermochronometry into transpressional deformation and crustal exhumation along the San Andreas fault in the western Transverse Ranges, California. Tectonics, v. 32, p. 1602-1622. DOI: 10.1002/2013TC003377

Nilsen, T.H., 1981, Early Cenozoic stratigraphy, tectonics and sedimentation of the central Diablo Range between Hollister and New Idria. Pacific Section SEPM Field Trip Guide Book.

Page, B.M., 1981, The southern Coast Ranges, in Ernst, W.G., ed., The geotectonic development of California: Rubey Volume I. Prentice-Hall, Englewood Cliffs, NJ, p. 329–417.

Page, B.M., Thompson, G.A., Coleman, R.G., 1998, Late Cenozoic tectonics of the central and southern Coast Ranges of California. Geological Society of America Bulletin, v. 110, p. 846–876.

Powell, R.E., 1993, Balanced palinspastic reconstruction of pre-late Cenozoic paleogeology, southern California: Geologic and kinematic constrains on evolution of the San Andreas fault system, in Powell, R.E., Weldon, R.J., and Matti, J.C., eds., The San Andreas fault system: Displacement, Palinspastic reconstruction, and geologic evolution, Geological Society of America Memoirs 178, p. 1-106.

Ranalli, G.,1995, Rheology of the Earth, second ed. Chapman and Hall, London, 413 pp.

Ranalli, G., Murphy, D. C., 1987, Rheological stratification of the lithosphere: Tectonophysics, v. 132, p. 281–295.

Rosenberg, L., Wills, 2016, Preliminary geologic map of the Point Sur 30' by 60' quadrangle, California, Version 1.0. California Geological Survey.

Ross, D.C., 1976, Reconnaissance geologic map of pre-Cenozoic basement rocks, northern Santa Lucia Range, Monterey County, California: U.S. Geological Survey Miscellaneous Field Studies Map MF-750, 7 p., 2 sheets, scale 1:125,000.

Ruetz, J.W., 1979, Paleocene submarine fan deposits of the Indians Ranch area, Monterey County, California, in Pacific Coast Paleogeography Field Guide #4: Tertiary and Quaternary Geology of the Salinas Valley and Santa Lucia Range, Monterey County, California, Pacific Section Society for Sedimentary Geology, p. 13-24.

Saleeby, J.B., 2003, Segmentation of the Laramide slab: Evidence from the southern Sierra Nevada region. Geological Society of America Bulletin, v. 115, n. 6, p. 655-668.

Saleeby, J.B., Farley, K.A., Kistler, R.W., Fleck, R.J., 2007, Thermal evolution and exhumation of deep-level batholithic exposures, southernmost Sierra Nevada, California. Geological Society of America Special Paper 419, p. 39-66.

Sclater, J.G., Christie, P.A.F., 1980, Continental stretching; an explanation of the post-mid-Cretaceous subsidence of the central North Sea basin. Journal of Geophysical Research, v.85, p. 3711–3739.

Seiders, V.M., Joyce, J.M., Leverett, K.A., and McLean, H., 1983, Geologic map of part of the Ventana Wilderness and the Black Butte, Bear Mountain, and Bear Canyon roadless areas, Monterey County, California. U.S. Geological Survey Miscellaneous Field Studies Map MF-1159-B, scale 1:50,000.

Sharman, G.R., Graham, S.A., Grove, M., Hourigan, J.K., 2013, A reappraisal of the early slip history of the San Andreas fault, central California, USA. Geology, v. 41, p. 727-730. DOI: 10.1130/G34214.1

Shea, W.T., Kronenberg, A.K., 1992, Rheology and deformation mechanisms of an isotropic mica schist. Journal of Geophysical Research, v. 97, n. B11, p. 15201-15237.

Spotila, J.A., Niemi, N., Brady, R., House, M., Buscher, J., Oskin, M., 2007, Long-term continental deformation associated with transpressive plate motion: the San Andreas fault. Geology, v. 35, p. 967-970.

Steckler, M.S., Watts, A.B., 1978, Subsidence of the Atlantic-type continental margin off New York. Earth and Planetary Science Letters, v. 41, p. 1-13.

Stern, C.R., 2011, Subduction erosion: rates, mechanism, and its role in arc magmatism and the evolution of the continental crust and mantle. Gondwana Research, v. 20, p. 284-308.

Suppe, J., 1970, Offset of late Mesozoic basement terrains by the San Andreas fault system: Geological Society of America Bulletin, v. 81, p. 3253–3258. DOI :10.1130/0016-7606(1970)81[3253:OOLMBT]2.0.CO;2

Thompson, G.A., 1999, California Coast Range Tectonics in Light of Geophysical Constraints: A Tribute to Ben Page. International Geology Review, v. 41, n. 5, p. 383-390. DOI: 10.1080/00206819909465148

Trask, P.D., 1926, Geology of Point Sur quadrangle, California. University of California Publications, Bulletin of the Department of Geological Sciences, v. 16, no. 6, p. 119–186, 1 sheet, scale 1:62,500.

Vedder, J.G., Brown, R.D., 1968, Structure and stratigraphic relations along the Nacimiento fault in the southern Santa Lucia range and San Rafael Mountains, California, in Dickenson, W.R., and Grantz, A., eds., Proceedings of a conference on Geologic Problems of the San Andreas Fault System. Stanford University Publications in the Geological Sciences 11, p. 242-259.

Watts, A.B., Burov, E., 2003, Lithospheric strength and its relationship to the elastic and seismogenic layer thickness. Earth and Planetary Science Letters, v. 213, p. 113-131.

Wiebe, R.A., 1966, Structure and petrology of Ventana Cones area, California. Stanford University Thesis, 95 p.

Wilks, K.R., Carter, N.L., 1990, Rheology of some continental lower crustal rocks. Tectonophysics, v. 182, p. 57-77.

Zeitler, P.K., Meltzer, A.S., Koons, P.O., Shroder, J.F., 2001, Erosion, Himalayan geodynamics, and the geomorphology of metamorphism. Geological Society of America Today, v. 11, n. 1, p. 4–9.

Zoback, M.D., Townend, J., Grollimund, B., 2002, Steady-state failure equilibrium and deformation of intraplate lithosphere. International Geology Review, v. 44, n. 5, p. 383-401. DOI: 10.2747/0020-6814.44.5.383

CHAPTER 2

THE SAN GREGORIO–HOSGRI FAULT LOCALIZES RAPID AND ASYMMETRIC VERTICAL DEFORMATION IN CENTRAL COASTAL CALIFORNIA

ABSTRACT

The Neogene through late Quaternary history of vertical strain is assessed along a 90-km-long length of the Santa Lucia range in central California to better understand how vertical strain is accommodated along the Pacific–North America plate boundary using new zircon and apatite (U-Th)/He cooling ages and the elevation of the lowest-emergent late Quaternary marine terrace. From the NE, apatite (n=15) and zircon (n=18) ages decrease towards the San Gregorio–Hosgri fault (SGHF), are as young as 1.9 Ma (apatite) and 7.1 Ma (zircon) adjacent to the fault, and are much older SW across the fault trace. These data indicate that long-term vertical strain has been highly focused in a narrow window NE of the SGHF since the late Miocene and suggests that much, if not all the high topography along the rugged Big Sur coast, is controlled by this fault. The elevation of the lowest-emergent marine terrace—likely correlated with MIS 5c—was surveyed between Monterey and Big Sur and substantially increases data density over previous studies. These new data indicate that, like bedrock exhumation, terrace uplift is focused in a 1.5–3-km-wide zone NE of the SGHF. The similarities in magnitude and pattern between the two data sets is compelling evidence that long-term rates of exhumation are similar to near-modern rates of uplift, and suggest that both are controlled by the SGHF. This is puzzling, however, considering the significantly lower late Quaternary to modern slip rates on the SGHF compared to the late Miocene and Pliocene rates during accrual of most exhumation.

INTRODUCTION

The Coast Ranges of central California are located within a broad zone of northwest-trending dextral shear and oblique convergence between the Pacific and Sierra Nevada–Great Valley plates (Page et al., 1998; Argus and Gordon, 2001). The Santa Lucia range is one such mountain range, has the steepest topographic gradient of any coastal mountains in the conterminous United States, reaches heights of >1,500 m, and draws millions of visitors to its Big Sur coast. The topographic relief of the range is anomalous along the central coast and

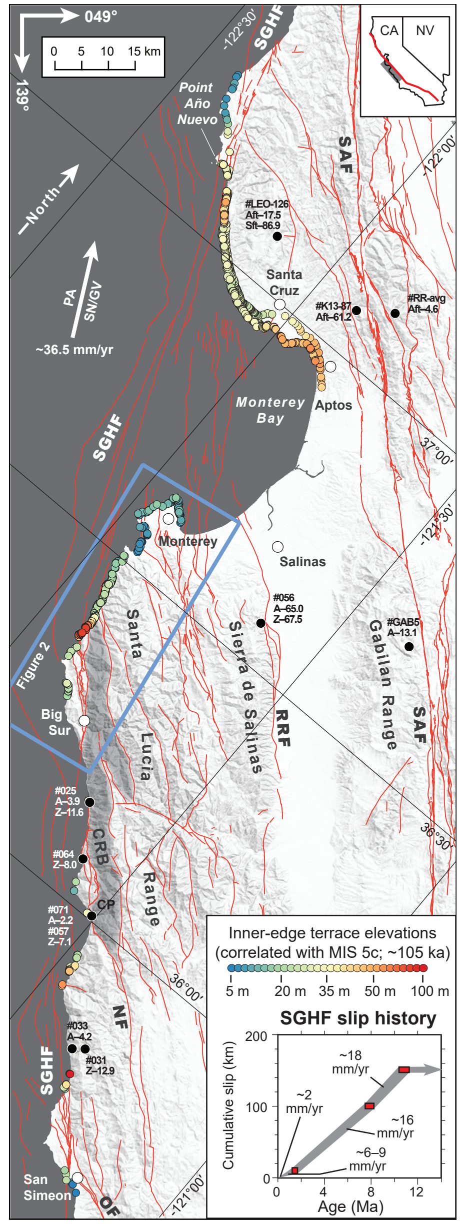

Figure 2-1. Focused zones of uplift and exhumation are found along the San Gregorio-Hosgri fault (SGHF) in central coastal California. Oblique mercator projection is rotated so that the long edge of the map is parallel to the N41°W trace of the main San Andreas fault (SAF). (U-Th)/He cooling ages (A–apatite; Z–zircon) are from this study (#025–064); #071 from Cone Peak (CP) transect of Ducea et al. (2003); #GAB5 from Spotila et al. (2007). Apatite fission track ages (Aft) #RR-avg are from Bürgmann et al. (1994); #LEO-126 and #K13-87 from Naeser and Ross (1976). Slip history constraints are from Weber (1990), Clark (1998), Dickenson et al. (2005), and d'Alessio et al. (2005). Terrace elevations are from this study (n=1,025), Alexander (1953), n=26; Bradley and Griggs (1976), n=151; Lajoie et al. (1979), n=15; and Hanson et al. (1994) n=6. Faults are from Jennings and Bryant (2010). General outcrop of Coast Ridge Belt (CRB) after Kidder et al. (2003). Relative plate vector and rate is from DeMets and Merkouriev (2016). NF-Nacimiento fault; OF-Oceanic fault; RRF-Reliz-Rinconada fault.

greater than any transpressional reach along the San Andreas fault outside of the 'Big Bend'. The range is bound on the southwest (Fig. 2-1) by the San Gregorio-Hosgri fault (SGHF)—a major strike-slip fault of the San Andreas system (e.g. Dickenson et al., 2005), and on the northeast by the Reliz–Rinconada fault (RRF; Dibblee, 1976), yet these faults only carry a small fraction of the late Quaternary central-California slip budget (Weber, 1990; Hanson et al., 2004; Rosenberg and Clark, 2009), and an even smaller fraction of the modern strain field (e.g. d'Alessio et al., 2008; DeMets et al., 2014).

Our general expectation is that regions of rock uplift along strike-slip plate boundaries are found where there are coaxial components of shortening perpendicular to the main fault boundary (Sanderson and Marchini, 1984; Tikoff and Fossen, 1993; Jones et al., 2004). This often occurs in regions of oblique convergence (transpression) or where faults define a contractional step-over, and the magnitude of uplift is proportional to the obliquity and magnitude of the relative plate vectors (Sylvester, 1988; Fossen and Tikoff, 1998). Within this context, the Santa Lucia range seems to defy model predictions—it is bound by faults with low modern slip rates, does not have a well-defined transpressional geometry, yet has higher topography, greater relief, and potentially faster rates of exhumation (e.g. Ducea et al., 2003) than nearby and well-documented transpressional regions of the main San Andreas fault (Bürgmann et al., 1994; Spotila et al., 2007; Hilley et al., 2013; Niemi et al., 2013).

Uplift of the Santa Lucia Range is generally considered to be part of the 'Coast Range Orogeny', a period of distributed transpressional uplift along much of the central California coast thought to result from increased convergence starting about 3.5 Ma (Christensen, 1965; Compton, 1966; Page et al., 1998). An update of relative plate motions indicates that oblique convergence began earlier, at ~6–8 Ma, and has been increasingly convergent since ~5.2 Ma (DeMets and Merkouriev, 2016). Thus, a late Miocene and Pliocene history of uplift might be expected, given that the SGHF initiated at ~11 Ma (Clark, 1998) and has accumulated ~156 ±4 km of dextral offset since then (Dickenson et al., 2005). Previous studies, however, have been unable to fully assess the uplift history because there are no sedimentary rocks of the correct age along the southwest or central part of the range (e.g. Rosenberg and Wills, 2016). A late Miocene to Pleistocene history of uplift is partly confirmed by an apatite (U-Th)/He transect (Ducea et al., 2003), and suggests a spatial association with the SGHF. Additional support for the localization of strain along the SGHF is provided by deformed late Quaternary marine terraces near Santa Cruz (e.g. Bradley and Griggs, 1976) and Monterey (McKittrick, 1988) that indicate higher rates of uplift on the northeast side of the fault.

Three testable hypotheses are suggested by these data, and provide an opportunity to assess the location and magnitude of the oblique component of strain along the Pacific–North America plate boundary: 1) slip on the SGHF drives modern topography, the uplift of late Quaternary marine terraces, and long-term bedrock exhumation along the rugged coastline of the Santa Lucia range; 2) exhumation began in the late Miocene, not the late Pliocene, and continues today, and; 3) rates of vertical strain have generally been decreasing through time as slip rates on the SGHF decrease. These hypotheses are tested with two new datasets along a coastal transect from Monterey, CA southward across the SGHF near Big Sur: 1) long-term rates of bedrock exhumation from low-temperature thermochronometry in the abundantly exposed crystalline bedrock, and; 2) the late Quaternary pattern of uplift recorded by re-surveyed deformed marine terraces.

METHODS

(U-TH)/HE THERMOCHRONOMETRY

The zircon and apatite (U-Th)/He thermochronometers utilize the temperature-dependent retention of ^{4}He produced during radioactive decay of trace amounts of matrix-bound ^{238}U, ^{235}U, and ^{232}Th (Zeitler et al., 1987; Reiners et al., 2004). These two systems have nominal closure temperatures of ~180–200° C (zircon) and 65–75° C (apatite) and thus record the time-averaged vertical advection of rock from depths of ~6 and 2 km (Farley, 2000; Reiners et al., 2004). Bedrock samples were collected along an oblique crustal transect from Point Lobos southward across the SGHF (Fig. 2-2), and along the length of the Big Sur coast (Fig. 2-1); all analyses were performed at the UCSC Thermochronology and Plasma Analytical facility. New cooling ages for zircon (n=18) and apatite (n=15) are the weighted mean of 4–6 single-grain aliquots; a detailed description of methods can be found in Appendix A, a summary of ages is provided in Table 3-2, and analytical data are in Appendix B.

Exhumation rate and total exhumation since 10 Ma are calculated from cooling ages with some simplifying assumptions about the thermal state of the crust, an assumption of monotonic cooling since the Miocene, and estimated closure temperatures and depths for each sample; a detailed description of this method is available in Appendix A. Closure temperature is estimated using the sphere-equivalent radius of each aliquot (e.g. Meesters and Dunai, 2002), the relevant diffusion parameters for zircon (Reiners et al., 2004) or apatite (Farley, 2000), and iteratively solving the closure-temperature equation of Dodson (1973); sample-level values are the weighted mean of all aliquots. Isotherm depths were calculated in two ways: based on the wavelength and amplitude of modern topography and the exhumation rate (e.g Manktelow and Grasemann, 1997), and using a simple geothermal gradient (30° C/km) with the assumption

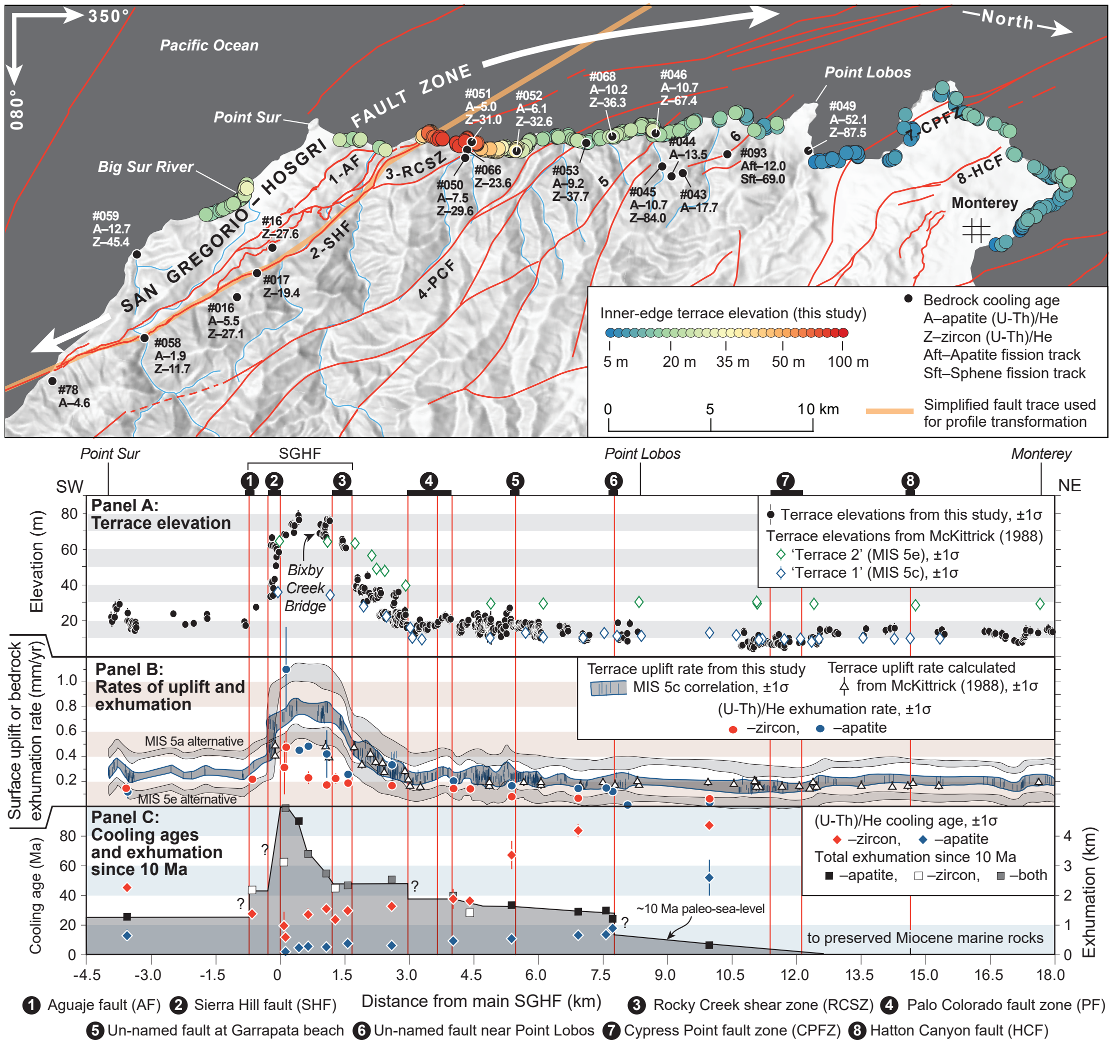

Figure 2-2. Uplift and exhumation are focused in a narrow zone NE of the SGHF. Map: (U-Th)/He ages are from this study, except #078, which is from Ducea et al. (2003); fission track ages (Aft, Sft) are from Naeser and Ross (1976). Terrace elevations on the map are from this study only. Faults are from Jennings and Bryant (2010); fault nomenclature is from Dickenson et al. (2005). Panel A: Terrace elevations are from within the extent of the map (this study) and show a ~70 m relative change in elevation. Panel B: Terrace uplift rates use a MIS 5c correlation and the adjusted sea-level curves and summary of ages from Simms et al. (2016); alternative correlations also shown. Although terrace uplift appears faster, the overall pattern of higher vertical strain just NE of the SGHF is consistent across both data sets. Panel C: Cooling ages and estimate of total bedrock exhumation since 10 Ma using individual and paired-mineral exhumation rates.

that topography does not deflect the isotherm; the final sample-level value was the average of these two methods because there are no independent constraints on which is more likely. Interval exhumation rates were calculated for paired apatite and zircon samples.

MARINE TERRACE ELEVATIONS

Late Quaternary marine terraces are found along much of the central California coast (e.g. Simms et al., 2016), and their lateral continuity and initially uniform elevation provide an excellent passive strain marker for vertical deformation. Along the southwest margin of the Santa Lucia range, the MIS 5c terrace is the lowest-emergent and most-prominent surface, and can be traced nearly continuously from Monterey southward to Big Sur (McKittrick, 1988; Clark and Rosenberg, 1997; Rosenberg and Wills, 2016). However, colluvial cover precludes the use of geologic maps to determine accurate bedrock terrace elevations, and previous survey results (McKittrick, 1988) are presented on sketch maps unsuitable for the level of detail required for this effort.

Thus, to compare exhumation rates with estimates of late Quaternary uplift, the elevation of the contact between bedrock and sedimentary cover for the lowest and most-prominent marine terrace was surveyed along 180 km of coast, from Point Año Nuevo to the southern end of the Santa Lucia range near San Simeon (Fig. 2-1). The survey effort used a laser rangefinder, survey grade GPS receiver, and rugged tablet computer, which has the advantage over previous efforts (e.g. Alexander, 1953; Bradley and Griggs, 1976; McKittrick, 1988) of surveying the marine terrace where it is abundantly exposed along coastal bluffs. Typical vertical measurement uncertainty is ~0.7 m and measurement density is significantly higher (577 new vs. 32 existing measurements in Fig. 2-2 alone). Because the measurements were made along coastal bluffs, elevations are corrected for the distance to the back edge of the terrace as defined by previous workers and supplemented with lidar from the 2009–2011 California Coastal Conservancy Lidar Project. All efforts were made to survey only the lowest, most-prominent marine terrace and with few exceptions visual continuity of the terrace surface was maintained in the field. In those areas where continuity was difficult to establish, coastal lidar and oblique aerial photographs from the California Coastline Project were used. Appendix A contains a detailed description and validation of the method; Appendix C contains elevation data.

Terrace ages in central California—and near Santa Cruz in particular—are the subject of much disagreement (e.g. Bradley and Griggs, 1976; Weber, 1990; Perg et al., 2001). Using morphology, detailed soil profile analysis, and a calculation of steady uplift rates, McKittrick (1988) correlated the lowest-emergent terrace near Monterey (‘Terrace 1’) with the ‘Highway 1’ terrace level near Santa Cruz (e.g. Bradley and Griggs, 1976) that appears most robustly correlated with MIS 5c (e.g. Weber, 1990). Future work may alter the age assignment of this terrace and shift uplift rates higher (for MIS 5a) or lower (for MIS 5e), but does not alter the physical pattern of uplift. The sea level curves and compilation of ages in Simms et al. (2016), which account for glacial isostatic adjustments, are used in the calculation of uplift rates.

RESULTS

UP TO 5 KM OF FOCUSED EXHUMATION NE OF THE SGHF SINCE 10 MA

Cooling ages for both apatite and zircon decrease consistently SW towards the SGHF and increase rapidly across its trace (Fig. 2-2) both in map view and when projected onto a SGHF-perpendicular profile. Estimates of exhumation rate indicate faster bedrock exhumation in a narrow ~1.5-km-wide zone NE of the SGHF, similar in style to the pattern of terrace uplift. Our profile transformation makes it appear that this highly exhumed region lies soley between the main SGHF and the Rocky Creek shear zone (RCSZ), but many <6 Ma cooling ages are found adjacent to the main fault SE of the RCSZ. Total exhumation since 10 Ma is at a maximum adjacent to the SGHF, and decreases rapidly to the NE or SW. Exhumation is minimal >10 km NE of the SGHF where Miocene-age marine rocks are preserved near Monterey (Clark and Rosenberg, 1997).

TERRACE UPLIFT IS FOCUSED IN A NARROW ZONE NE OF THE SGHF

The new terrace elevation data confirm and enhance the general pattern of increasing uplift with proximity to the SGHF. The improved spatial resolution indicates that terraces from near Monterey to ~6 km NE of the SGHF are uniformly low, rise gently between ~6 and 3 km, and rise rapidly between 0 and 3 km. The maximum amplitude of this elevation change is ~ 70 m. Terrace elevation rapidly decreases to the SW within a narrow crustal sliver between strands of the Sierra Hill fault; south of the Aguaje fault terraces are again relatively low and flat-lying.

Our terrace elevations differ slightly from those of McKittrick (1988) in the region of highest terrace elevation (between the RCSZ and the Sierra Hill fault). Four lines of reasoning support our interpretation: 1) there was no evidence for lower-elevation terraces between these two faults; 2) if a lower-elevation terrace was preserved (as it is to the north and south), its absence here would require focused and differential coastal erosion in this location only, for which there is no obvious mechanism; 3) the rapid changes in elevation are all co-located with major faults (e.g. Rosenberg and Wills, 2016), many of which were not yet mapped during the previous study, yet may have influenced possible correlations; 4) a faulted marine terrace is noted at ~110 m elevation in this area by Dickenson et al. (2005) and likely represents the next-older terrace level. Thus, the simplest explanation is that the two ~65-m-elevation data points of McKittrick (1988) on Figure 2-2 are incorrectly correlated with ‘Terrace 2’.

DISCUSSION

THE SAN GREGORIO-HOSGRI FAULT EXERTS A FUNDAMENTAL CONTROL ON VERTICAL DEFORMATION

Rates and amplitudes of terrace uplift and bedrock exhumation increase SW towards the SGHF (Fig. 2-2), drop rapidly across its trace, and Plio–Pleistocene apatite cooling ages can be found adjacent to the SGHF for ~90 km (Fig. 2-1). These data confirm our hypothesis that uplift along the Pacific coast of the range is responding to slip along this major fault. The timing of uplift is more difficult to constrain, but the presence of late Miocene zircon cooling ages (as young as 7.1 Ma; Fig. 2-1), and a break-in-slope on a nearby age-elevation transect at ~6 Ma (Ducea et al., 2003) strongly support high rates of exhumation since the late Miocene. Nearly half of the total exhumation is focused between the main SGHF and the Palo Colorado fault, and most is within ~1.5 km of the SGHF. Such focused exhumation has been documented along thin crustal slivers along the main SAF, such as at Yucaipa Ridge (Spotila et al., 1998).

FOCUSED EXHUMATION EXPLAINS THE DEEPLY EXHUMED COASTLINE, BUT NOT UPLIFT OF THE WHOLE RANGE

The pattern of exhumation may partly explain the presence and orientation of deeply exhumed mid-crustal rocks of the Coast Ridge belt. The Coast Ridge belt crops out adjacent to the SGHF between Big Sur and the Nacimiento fault (Fig. 2-1), and is a mid-crustal (~25 km deep) exposure of the Sierran arc that that has been tilted ~30° NE (Kidder et al., 2003); most exhumation of these rocks occurred in the late Cretaceous during orogenic collapse above recently underplated schist (Kidder and Ducea, 2006; Chapman et al., 2010). The addition of as much as 5 km of exhumation since the late Miocene—and a steep NE gradient—provide a plausible mechanism to explain their NE dip and SGHF-parallel outcrop pattern.

Exhumation in a narrow band NE of the SGHF explains young coastal cooling ages and local high topography, but is insufficient to explain the >30 km width of the central Santa Lucia range or the Plio-Pleistocene uplift documented along the N, NE, and SW sides of the range (e.g. Christiansen, 1965). Two additional sources of uplift may explain this discrepancy. First, many steeply to moderately dipping faults obliquely cross the central portion of the range and have post-Pliocene shortening estimates of 10–12% (Compton, 1966). Second, the Reliz-Rinconada fault forms the steep NE margin of the range and has a Miocene to Quaternary history of transpressional deformation (Dibblee, 1976; Titus et al., 2007). Post-Pliocene shortening across these structures—in addition to a focused component of uplift along the SGHF—is perhaps sufficient to create the modern topography and relief of the entire range.

STRUCTURAL COMPLEXITIES ALONG THE SGHF AND THEIR EFFECT ON UPLIFT RATES

The reach between the Sierra Hill fault and RCSZ (Fig. 2-2) is anomalous in that rates of terrace uplift are 50% greater than exhumation rates at a similar distance from the SGHF. We suspect that this discrepancy is related to a local, and possibly evolving, structural complexity along the SGHF in this location. The Sierra Hill fault forms the structural boundary between Salinian bedrock on the NE and Franciscan mélange on the SW and is the main expression of the SGHF (Dickenson et al., 2005). The RCSZ is an intra-Salinian structure that offsets the course of Bixby Creek ~1.3 km in a right-lateral sense (Dickenson et al., 2005) and is composed of a broad zone of closely spaced small faults (e.g. Rosenberg and Wills, 2016); both faults appear to offset the surveyed marine terrace in this study. Offshore, the RCSZ trends into a scarp that cuts Holocene deposits (Greene et al., 1973). Onshore mapping indicates that the RCSZ provides a straighter continuation of the main Sierra Hill fault (Fig. 2-2), and shows that the most-NW portion of the Sierra Hill fault is transpressional. Together, these observations suggest an evolving faulted transpressional stepover between the RCSZ and the main Sierra Hill fault that could plausibly explain higher terrace uplift rates in this fault-bound domain.

VERTICAL STRAIN ALONG THE CENTRAL CALIFORNIA PLATE MARGIN

It is puzzling that rates of terrace uplift adjacent to the SGHF near Big Sur (up to 0.8 mm/yr) are greater than those adjacent to the SAF near Santa Cruz (up to ~0.6 mm/yr; Anderson and Menking, 1994) because maximum late Quaternary slip rates are only 6–9 mm/yr on the SGHF (Weber, 1990). It is especially puzzling considering that the modern strain field indicates slip rates of only ~2 mm/yr along much of the SGHF (d'Alessio et al., 2005; DeMets et al., 2014) and that modern SAF-perpendicular convergence appears to be accounted for without significant convergence across the SGHF (Titus et al., 2011; DeMets et al., 2014). Furthermore, bedrock exhumation accrued along the SGHF during a time when slip rates were substantially higher (~16 mm/yr; Fig. 2-1), yet exhumation rates are comparable, or less than, late Quaternary uplift rates.

These observations raise fundamental questions about our knowledge of how vertical strain is being accommodated along this region of the plate boundary, and highlight the need for additional inquiry. Three hypotheses can potentially explain the rate discrepancy, and each has testable predictions for future work. 1) The terrace may be older than MIS 5c. A MIS 5e correlation might alleviate the rate discrepancy in the Santa Lucia range, but would likely alter terrace interpretations along the coast. 2) The range may be experiencing erosion-induced isostatic rebound that augments a smaller component of late Quaternary transpression. If erosion and exhumation were well matched during the Pliocene, a rapid reduction in exhumation with continued erosion could cause up to ~80% of the Pliocene rate and persist for several m.y. (e.g. Spotila, 2005). Such a mechanism would suggest that erosion-induced isostasy is the primary driver of vertical components of fault slip, and would force a significant reassessment of seismic probabilities in the region. 3) Relatively continuous clockwise rotation of plate vectors since the late Miocene (DeMets and Merkouriev, 2016) may have kept pace with the reduction in slip rate so that the resolved convergence has remained relatively constant through time. Although not supported by the modern strain field—which indicates that the Santa Lucia range behaves as a relatively rigid block (Titus et al., 2011; DeMets et al., 2014)—such a hypothesis is supported by reconstructed flow lines between the Pacific and Sierra Nevada/Great Valley plates, which indicate that the strike of the SGHF near Big Sur may not have become transpressional until ~0.78 Ma (DeMets and Merkouriev, 2016).

CONCLUSION

We use apatite and zircon (U-Th)/He thermochronometry in tandem with the elevation of the lowest-emergent marine terrace along the central California coast to tie high rates of bedrock exhumation and terrace uplift to slip along a >90-km length of the SGHF. Both data sets show that rates are low SW of the fault, become highly focused in a <3 km-wide zone NE of the fault, and decay slowly to reach minima at >10 km from the fault. The magnitude and gradient of exhumation help to explain the distribution and geometry of the deeply exhumed Coast Ridge belt plutonic and metamorphic rocks, but do not explain uplift of the entire range. Rates of terrace uplift are higher than those farther north or south of the Santa Lucia range, higher than exhumation rates, and are perplexing in light of low modern slip rates on the SGHF.

ACKNOWLEDGMENTS

Noah Finnegan of the University of California-Santa Cruz (UCSC) provided surveying equipment; Rob Franks of the UCSC Plasma Analytical Laboratory and Terry Blackburn of the W.M. Keck Isotope Laboratory provided analytical support for (U-Th)/He analyses; Sam Anderson provided field support and mineral separations; the staff of the UC Big Creek Reserve provided logistical support. This work was partially supported by grants to A.S. from the Northern California Geological Society, the Casey Moore Foundation, and a GSA Graduate Student Grant.

REFERENCES

Alexander, C.S., 1953, The marine and stream terraces of the Capitola-Watsonville area. University of California Publications in Geography, v. 10, p. 1–44.

Anderson, R.S., and Menking, K.M., 1994, The Quaternary marine terraces of Santa Cruz, California: Evidence for coseismic uplift on two faults. Geological Society of America Bulletin, v. 106, n. 5, p. 649-664.

Argus, D.F., Gordon, R.G., 2001, Present tectonic motion across the coast ranges and San Andreas fault system in central California. Geological Society of America Bulletin 113, 1580– 1592.

Bradley, W.C., and Griggs, G.B., 1976, Form, genesis, and deformation of central California wave-cut platforms. Geological Society of America Bulletin, v. 87, p. 433–449.

Bürgmann, R., Arrowsmith, R., Dumitru, T., and McLaughlin, R., 1994, Rise and fall of the southern Santa Cruz Mountains, California, from fission tracks, geomorphology, and geodesy. Journal of Geophysical Research, v. 99, p. 20,181-20,202.

Clark, J.C., 1998, Neotectonics of the San Gregorio fault zone: Age dating controls on offset history and slip rates. American Association of Petroleum Geologists Bulletin, v. 82, p. 884–885.

Clark, J.C., Dupre, W.R., Rosenberg, L.I., 1997, Geologic map of the Monterey and Seaside 7.5-minute quadrangles, Monterey County, California: a digital database. U.S. Geological Survey Open-File Report 97-30, scale 1:24,000, 1 plate.

Chapman, A. D., Kidder, S., Saleeby, J.B., and Ducea, M.N., 2010, Role of extrusion of the Rand and Sierra de Salinas schists in late Cretaceous extension and rotation of the southern Sierra Nevada and vicinity. Tectonics, v. 29, TC5006.

Christensen, M.N., 1965, Late Cenozoic deformation in the central Coast Ranges of California. Geological Society of America Bulletin, v. 76, p. 1105–1124.

Compton, R.R., 1966, Analysis of Pliocene–Pleistocene deformation and stresses in the northern Santa Lucia Range, California. Geological Society of America Bulletin, v. 77, p. 1361-1380.

d'Alessio, M.A., Johanson, I.A., Bürgmann, R., Schmidt, D.A., and Murray, M.H., 2005, Slicing up the San Francisco Bay area; block kinematics and fault slip rates from GPS-derived surface velocities. Journal of Geophysical Research, v. 110, B06403, doi: 10.1029/2004JB003496.

DeMets, C., Marquez-Azua, B., and Cabral-Cano, E., 2014, A new GPS velocity field for the Pacific Plate-Part 2: implications for fault slip rates in western California. Geophysical Journal International, v. 199, p. 1900-1909.

DeMets, C., and Merkouriev, S., 2016, High-resolution reconstructions of Pacific-North America plate motion: 20 Ma to present. Geophysical Journal International, v. 207, p. 741-773.

Dibblee, T.W., Jr., 1976, The Rinconada and related faults in the southern Coast Ranges, California, and their tectonic significance, U. S. Geological Survey Professional Paper 981, 55 p.

Dickinson, W.R., Ducea, M., Rosenberg, L.I., Greene, H.G., Graham, S.A., Clark, J.C., Weber, G.E., Kidder, S., Ernst, G.W., and Brabb, E.E., 2005, Net dextral slip, Neogene San Gregorio–Hosgri fault zone, coastal California; geologic evidence and tectonic implications. Geological Society of America Special Paper 391, 43 p.

Dodson, M.H., 1973, Closure temperature in cooling geochronological and petrological systems. Contributions to Mineral Petrology, v. 40, p. 259-274.

Ducea, M., House, M.A., and Kidder, S., 2003, Late Cenozoic denudation and uplift rates in the Santa Lucia Mountains, California. Geology, v. 31, p. 139–142.

Farley, K.A. 2000, Helium diffusion from apatite: General behavior as illustrated by Durango Fluorapatite. Journal of Geophysical Research, v. 105, p. 2903-2914.

Greene, H.G., Lee, W.H.K., McCulloch, D.S., and Brabb, E.E., 1973, Fault map of the Monterey Bay region, California. USGS Miscellaneous Field Studies Map MF-518, 4 sheets, 1:200,000 scale.

Hanson, K.L., Wesline, J.R., Lettis, W.R., Kelson, K.I., and Mezger, L., 1994, Correlation, ages, and uplift rates of Quaternary marine terraces: south-central coastal California, in Alterman, I.B., McMullen, R.B., Cluff, L.S., and Slemmons, D.B., eds., Seismotectonics of the Central California Coast Ranges, Geological Society of America Special Paper 292, p. 45-71.

Hanson, K. L., Lettis, W.R., McLaren, M.K., Savage, W.U., Hall, N.T., 2004, Style and rate of quaternary deformation of the Hosgri fault zone, offshore south-central California, in Keller, M.A., ed., Evolution of Sedimentary Basins/Offshore Oil and Gas Investigations—Santa Maria Province. U.S. Geological Survey Bulletin 1995–BB.

Hilley, G.E., Dumitru, T., Gudmundsdottir, M.H., Bürgmann, R., 2008, Exhumation history of the Sierra Azul block of the Santa Cruz mountains revealed using low temperature thermochronology. EOS Transactions, American Geophysical Union 89.53, Abstract T43E-02.

Jennings, C.W., Bryant, W.A., 2010, Fault activity map of California. California Geological Survey, Geologic Data Map No. 6, scale 1:750,000.

Kidder, S., Ducea, M.N., Gehrels, G., Patchett, P.J., and Vervoort, J., 2003, Tectonic and magmatic development of the Salinian Coast Ridge belt, California. Tectonics, v. 22, n.5, 1058.

Kidder, S., and Ducea, M.N., 2006, High temperatures and inverted metamorphism in the schist of Sierra de Salinas, California, Earth Planetary Science Letters, v. 241, p. 422-437.

Lajoie, K.R., Weber, G.E., Mathieson, S.A., and Wallace, J., 1979, Quaternary tectonics of coastal Santa Cruz and San Mateo counties, California, as indicated by deformed marine terraces and alluvial deposits, in Weber, G.E., Lajoie, K.R., and Griggs, G. B., eds., Coastal tectonics and coastal geologic hazards in Santa Cruz and San Mateo counties, California. Geological Society of America Field Trip Guidebook, p. 61-80.

Mancktelow, N.S., Grasemann, B., 1997, Time-dependent effects of heat advection and topography on cooling histories during erosion. Tectonophysics, v. 270, p. 167–195.

McKittrick, M.A., 1988, Elevated marine terraces near Monterey, California. University of Arizona Thesis, 46 p.

Naeser, C.W., and Ross, D.C., 1976, Fission-track ages of sphene and apatite of granitic rocks of the Salinian Block, Coast Ranges, California. Journal of Research of the US Geological Survey, v. 4, n. 4, p. 415-420.

Page, B.M., Thompson, G.A., and Coleman, R.G., 1998, Late Cenozoic tectonics of the central and southern Coast Ranges of California. Geological Society of America Bulletin, v. 110, p. 846–876.

Perg, LA., Anderson, R., Finkel, R.C., 2001, Use of new 10Be and 26Al inventory method to date marine terraces, Santa Cruz, CA, USA. Geology, v. 29, p. 879-882.

Reiners, P.W., Spell, T.L., Nicolescu, S., Zanetti, K.A., 2004, Zircon (U-Th)/He thermochronometry: He diffusion and comparisons with 40Ar/39Ar dating. Geochimica Cosmochimica Acta, v. 68, p. 1857-1887.

Rosenberg, L., Clark, J.C., 2009, Map of the Rinconada and Reliz fault zones, Salinas River valley, California. U.S. Geological Survey Scientific Investigations Map SIM-3059.

Rosenberg, L., Wills, 2016, Preliminary geologic map of the Point Sur 30' by 60' quadrangle, California, Version 1.0. California Geological Survey.

Simms, A.R., Rouby, H., and Lambeck, K., 2016, marine terraces and rates of vertical tectonic motion: The important of glacio-isostatic adjustment along the Pacific coast of central North America. Geological Society of America Bulletin, v. 128, n. 1-2, p. 81-93.

Spotila, J.A., 2005, Applications of low-temperature thermochronometry to quantification of recent exhumation in mountain belts, in Reiners, P.W., and Ehlers, T.A., eds., Low-temperature thermochronology: techniques, interpretations, and applications: Reviews in Mineralogy and Geochemistry Volume 58, p. 449-466.

Spotila, J.A., Farley, K.A., Sieh, K., 1998, Uplift and erosion of the San Bernardino Mountains associated with transpression along the San Andreas fault, California, as constrained by radiogenic helium thermochronometry. Tectonics, v. 17, n. 3, p. 360-378.

Spotila, J.A., House, M.A., Niemi, N.A., Brady, R.C., Oskin, M., Buscher, J.T., 2007, Patterns of bedrock uplift along the San Andreas fault and implications for mechanisms of transpression, in Till, A.B., Roeske, S.M., Sample, J.C., Foster, D.A., eds., Exhumation Associated with Continental Strike slip Fault Systems. Geological Society of America Special Paper 434, p. 15-34.

Titus, S.J., Housen, B., and Tikoff, B., 2007, A kinematic model for the Rinconada fault system in central California based on structural analysis of en echelon folds and paleomagnetism. Journal of Structural Geology, v. 29, p. 961-982.

Titus, S.J., Dyson, M., DeMets, C., Tikoff, B., Rolandone, F., 2011, Geologic versus geodetic deformation adjacent to the San Andreas fault, central California. Geological Society of America Bulletin, v. 123, n. 5-6, p. 794-820.

Weber, G.E., 1990, Late Pleistocene slip rates on the San Gregorio fault zone at Point Ano Nuevo, San Mateo County, California, in Garrison, R.E., Greene, H.G., Hicks, K.R., Weber, G.E., and Wright, T.L., eds., Geology and tectonics of the Central California coast region, San Francisco to Monterey: Pacific Section, American Association of Petroleum Geologists Book GB67, p. 193-203.

CHAPTER 3

FAULT-CONTROLLED PATTERNS OF RAPID UPLIFT AND EXHUMATION ALONG THE LEADING EDGE OF THE CENTRAL CALIFORNIA COAST RANGE

ABSTRACT

The Santa Lucia range of central California is exhuming as fast or faster than many transpressional reaches along the main San Andreas fault system and has greater topographic relief than any coastal mountains in the continental United States. We define the spatial pattern of uplift and long-term exhumation of the range and elucidate the major structures responsible for this deformation using new low-temperature thermochronometry, geomorphic metrics of erosion, the elevation of deformed late Quaternary marine terraces, and geologic constraints. The collection of 44 apatite and 39 zircon (U-Th)/He cooling ages substantially increases existing coverage in the range (8 apatite ages) and is one of the most cohesive low-temperature thermochronometric datasets along the San Andreas fault system.

Apatite and zircon (U-Th)/He cooling ages indicate rapid late Miocene cooling along the entire 90 km-long southwest flank of the range following a period of low exhumation since at least the Oligocene. A ~6 Ma onset of rapid exhumation is most consistent with available constraints, but a range of ~5–10 Ma is permissible. The spatial distribution of ages indicates an overall decrease in age from NE to SW; the youngest ages lie adjacent to the San Gregorio–Hosgri fault (SGHF) on its northeast side and ages are substantially older across its trace. Late Miocene to modern exhumation rates vary substantially as a function of proximity to the SGHF: within a few km of the fault, rates from apatite are typically 0.35–0.8 mm/yr, and locally as high as 1.1 mm/yr while rates from zircon are 0.2–0.7 mm/yr; rates from both apatite and zircon are generally below 0.2 mm/yr at distances greater than 7 km to the NE of the fault, or SW across its trace.

Deformed marine terraces along the Big Sur coast also indicate a strong fault control on uplift; terrace elevations are 3–5 times higher directly NE of the SGHF and decay to baseline values over a ~5 km-wide zone; elevations drop rapidly across the fault to the SW. This pattern of NE-side uplift is a consistent feature of the SGHF from its junction with the Oceanic fault

to its junction with the San Andreas fault ~250 km to the northwest, although the magnitude of uplift is greatest along the Santa Lucia range. Southeast of the Oceanic fault, the pattern reverses and terrace elevations drop to the NE of the SGHF. Coupled with available data, this strongly suggests that the vertical component of strain is transferred from the SGHF to inland structures across the Oceanic fault.

At a range-wide scale, rates of bedrock exhumation are well correlated with topographic relief in a 2.5-km window, normalized channel steepness, and hillslope gradient and suggest that the range is perhaps near long-term equilibrium between uplift and erosion. These correlations allow us to construct a continuous map of exhumation rate that we use to supplement our individual observations and define range-scale patterns of vertical deformation. These data confirm the presence of a rapidly exhuming band directly NE of the SGHF and Oceanic faults and indicate that high rates of exhumation are localized in a narrow zone between the Oceanic and Nacimiento faults in the south but decay slowly to the NE in the north, perhaps because of distributed transpressional uplift between the SGHF and Rinconada–Reliz fault. A geomorphic analysis using range-wide normalized channel steepness and river-profile plots of χ indicates higher rates of uplift in the fault-bound domains of high bedrock exhumation, even when controlled for changes in lithology.

Together, our data indicate that the San Gregorio–Hosgri fault system has focused uplift and exhumation along its northeast side since the late Miocene, has continued to do so in the late Quaternary, and is the primary driver of high topography and relief in the Santa Lucia range. These results call into question the long-held assumption that transpressional strain along the Pacific–North America plate boundary is focused along the San Andreas fault. The intense localization of strain in a narrow region of crystalline rocks adjacent to the SGHF is also puzzling. Perhaps the anomalous localization of uplift and exhumation at all scales in the range is related to the profound lithospheric reorganization that accompanied the Late Cretaceous underplating of the schist of Sierra de Salinas.

ACKNOWLEDGMENTS

Rob Franks of the University of California-Santa Cruz (UCSC) Plasma Analytical Laboratory and Terry Blackburn of the W.M. Keck Isotope Lab provided assistance and support for mineral dissolution and analysis. Noah Finnegan graciously provided the surveying equipment. UCSC undergraduates Andre Mere, Devon Orme, Jonathon Ooms, and Chris Gallagher all analyzed samples; Sam Anderson provided field support and mineral separations. The staff of the U.C. Big Creek Reserve provided logistical support for field work. This work was partially supported by grants from the Northern California Geological Society, the Casey Moore Foundation, and the Geological Society of America.

INTRODUCTION

The Coast Ranges of central California are located within a broad zone of northwest-trending dextral shear and oblique convergence between the Pacific and Sierra Nevada–Great Valley plates (Page et al., 1998; Argus and Gordon, 2001). The Santa Lucia range, one such mountain range, lies SW of the San Andreas fault, reaches heights of >1,500 m, and draws millions of visitors to its Big Sur coast. The topographic relief of the range is anomalous along the central coast (Fig. 3-1), and is greater than any transpressional reach along the San Andreas fault outside of the 'Big Bend', including the nearby and rapidly exhuming Sierra Azul block (Bürgmann et al., 1994; Hilley et al., 2013) and the King Range (Dumitru, 1991). The range is bound on the southwest by the San Gregorio-Hosgri fault (SGHF)—a major strike-slip fault of the San Andreas system (e.g. Dickenson et al., 2005), and on the northeast by the Reliz–Rinconada fault (RRF; Dibblee, 1976), yet these faults only carry a small fraction of the late Quaternary central-California slip budget (Weber, 1990; Hanson et al., 2004), and an even smaller fraction of the modern strain field (e.g. d'Alessio et al., 2008; DeMets et al., 2014).

Regions of rock uplift along strike-slip plate boundaries are predicted where there are coaxial components of shortening perpendicular to the main fault boundary (Sanderson and Marchini, 1984; Tikoff and Fossen, 1993; Jones et al., 2004). This often occurs in regions of oblique convergence (transpression) or where faults define a contractional step-over (Sylvester, 1988; Fossen and Tikoff, 1998). The magnitude of such rock uplift is thought to be proportional to the obliquity and magnitude of the relative plate vectors (Fossen and Tikoff, 1998). Along the main Pacific–North America plate boundary, this type of model successfully predicts the regions of modern high topography (e.g. Montgomery, 1993; Argus and Gordon, 2001), the accrual of long-term geologic strain adjacent to the San Andreas fault (e.g. Sylvester, 1988; Titus et al., 2011), and to a first order, the distribution of bedrock exhumation (Spotila et al., 2001; 2007).

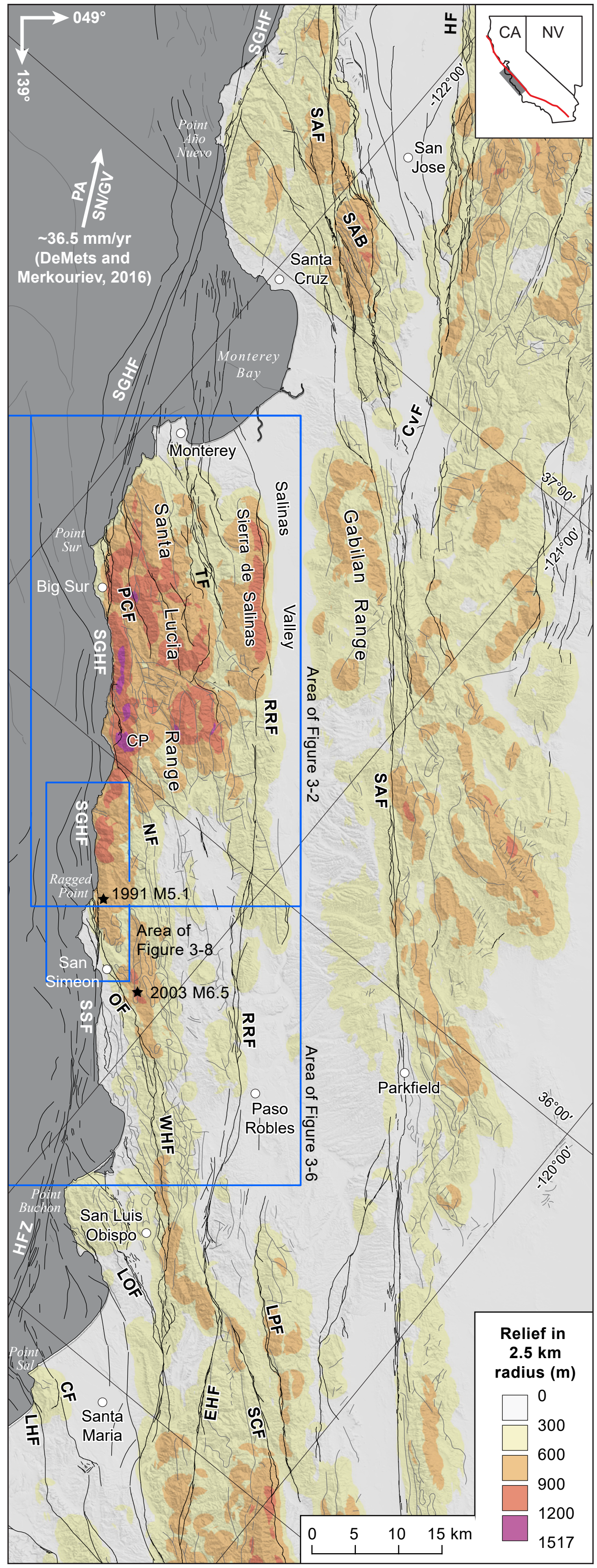

Figure 3-1. The Santa Lucia range is located in central California and has higher relief than anywhere along the San Andreas fault (SAF) north of the 'Big Bend'. The range is bound by the San Gregorio-Hosgri fault (SGHF) along its southwestern coastal side and by the Rinconada-Reliz fault (RRF) on the northeast inland side; the southern boundary of the range is uncertain. Near San Simeon, the Oceanic fault (OF) and West Huasana fault (WHF) step northwestward and merge with the SGHF and have been hypothesized to transfer strain to the SGHF (McLaren et al., 2008). The Oceanic fault was the primary structure responsible for the 2003 San Simeon and 1991 Ragged Point oblique reverse earthquakes (McLaren et al., 2008; Hardebeck, 2010). CF, Casmalia fault zone; CvF, Calaveras fault; EHF, East Huasana fault; HF, Hayward fault; HFZ, Hosgri fault zone; LPF, La Panza fault; LHF, Lions Head fault; LOF, Los Osos fault zone; SAB, Sierra Azul block; SCF, South Cuyama fault SSF, San Simeon fault zone. Relief from 10 m National Elevation data; faults from Jennings and Bryant (2010).

Within this context, it seems anomalous that the Santa Lucia range—bound by low-slip-rate faults without any clear stepover or well-documented transpressional reach—appears to have higher topography, greater relief, and potentially faster rates of exhumation (e.g. Ducea et al., 2003) than nearby and well-documented transpressional regions of the main San Andreas fault (Bürgmann et al., 1994; Spotila et al., 2007; Hilley et al., 2013). Uplift of the Santa Lucia Range is generally considered to be part of the post-Pliocene 'Coast Range Orogeny', a period of distributed transpressional uplift along much of the central coast of California thought to result from increased convergence across the Pacific–North America plate boundary at ~3.5 Ma (Christensen, 1965; Compton, 1966b; Graham, 1976; Dibblee, 1979; Page et al., 1998). Several lines of evidence suggest that uplift of the Santa Lucia range may have a more complex and longer history.

The SGHF—which bounds the southwest margin of the range—initiated at ~11 Ma (Clark, 1998) and has accumulated ~156 ±4 km of dextral offset since then (Dickenson et al., 2005). The RRF—which bounds the northeast margin of the range—has offset a suite of mid to late Miocene facies tracts 44 ±4 km and Pliocene markers by at least 18 km (Graham, 1978; Dibblee, 1979). An update of relative plate motions indicates a smoother and older transition from oblique divergence to oblique convergence (e.g. Cox and Engebretson, 1985; DeMets and Merkouriev, 2016). At the latitude of central California, there was oblique divergence in the Oligocene through late Miocene, a period of alternating oblique convergence and divergence from ~8 to 6 Ma, and increasing amounts of oblique convergence after ~5.2 Ma (Atwater and Stock, 1998; Argus and Gordon, 2001; DeMets and Merkouriev, 2016).

The Santa Lucia range thus appears to have been bound by active faults on both sides since at least ~11 Ma and has likely experienced oblique convergence since ~8 Ma. The observation of rapid late Miocene–Pleistocene exhumation adjacent to the SGHF from an apatite (U-Th)/He transect (Ducea et al., 2003) in the southwestern part of the range appears to confirm the presence of an older history of uplift, and suggests that it may be spatially associated with the SGHF. Additional support for the localization of strain along the SGHF is provided by deformed late Quaternary marine terraces north of Santa Cruz and near Monterey that indicate higher rates of uplift on the northeast side of the fault (Bradley and Griggs, 1976; Lajoie et al., 1979; McKittrick, 1988; Anderson and Menking, 1994).

Uplift along the SGHF could explain the rugged Big Sur coast of the Santa Lucia range, but may not be adequate to explain the uplifted crystalline core of the range or the differences in morphology between the northern and southern portions of the range (Figs. 3-1 and 3-2). Uplift and erosion of the range interior could be accounted for by discrete slip along the closely spaced fault network (e.g. Compton, 1966b; Dibblee, 1974; 1979), and (or) as part of a broad and faulted contractional stepover between the SGHF and the RRF. Such a stepover has been suspected by many based on gradients in fault displacement, the presence of faulted late Miocene and older sedimentary rocks, and analysis of Plio–Pleistocene stratigraphy (Christiansen, 1965; Compton, 1966a; 1966b; Graham, 1978; Dibblee, 1979; Page et al., 1998; Dickenson et al., 2005; Langenheim et al., 2013). Farther to the southeast, the oblique-reverse Oceanic fault directly connects the southern SGHF and more-inland West Huasana faults (Hall, 1974; 1976; 1991; Hall and Prior, 1975) and likely transfers strain between the two (e.g. Hardebeck, 2010). The 2003 M6.5 San Simeon earthquake occurred on the Oceanic fault (Fig. 3-1) and was accompanied by NE-side up vertical movement (McLaren et al., 2008). The transfer of strain from the SGHF to more inland faults is also supported—but not required—by the discrepancy in late Quaternary slip rates north of (Weber, 1990; Weber et al., 1995; Simpson et al., 1997) and south of (Hanson and Lettis, 1994; Hanson et al., 2004; Johnson et al., 2014) the Santa Lucia range.

Together, these data provide three testable hypotheses: 1) that uplift accompanies slip on the SGHF and is the primary driver for both modern topography and long-term bedrock exhumation along the rugged coastline of the Santa Lucia range; 2) exhumation of the range began in the late Miocene, not the late Pliocene, and continues today; 3) that oblique faults through the range help to focus uplift and exhumation while transferring strain between the SGHF and more-inland fault systems. We test these hypotheses with three new datasets: 1) 44 apatite and 39 zircon (U-Th)/He cooling ages (in addition to 8 existing apatite ages) to document the million-year timescales of bedrock exhumation throughout the range; 2) the assessment of five key geomorphic metrics of erosion—topographic relief in a 2.5-km window, local hillslope gradient, normalized channel steepness (ksn), χ, and mean annual precipitation—to determine the landscape response to the vertical deformation field and identify potentially active faults, and; 3) the elevation of deformed late Quaternary marine terraces along the SGHF to document

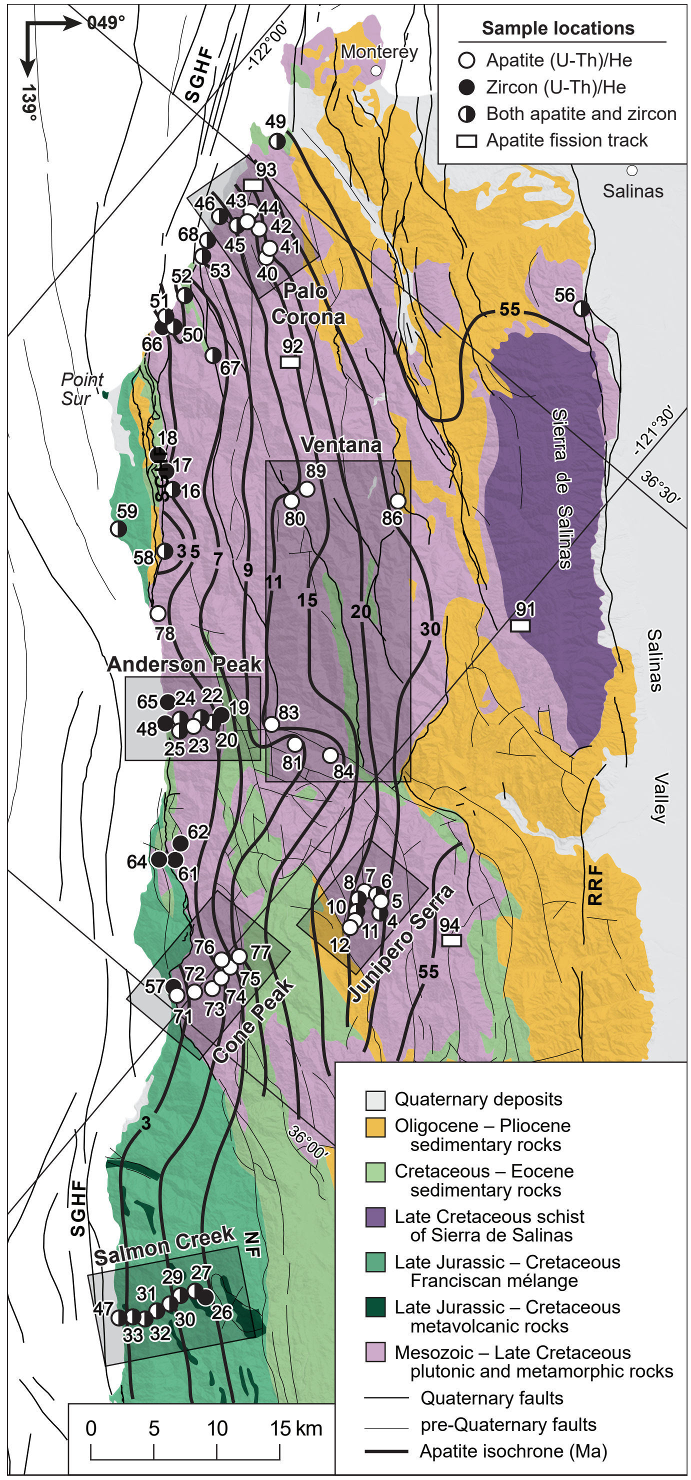

Figure 3-2. New and existing low-temperature thermochronometry indicate more recent exhumation along the SGHF. Approximate contours of equal age (isochrones) indicate a generally NE-dipping crustal panel with strike lines that parallel the SGHF. Major transects are shaded in gray. Apatite data from the Cone Peak transect are from Ducea et al. (2003); all fission track data are from Naeser and Ross (1976); the remaining samples are from this study. Sample location numbers correspond to data reported in Table 3-2. Simplified geology and faults are from Jennings et al. (2010) and Jennings and Bryant (2010).

patterns in late Quaternary rock uplift. We also compare our results against an existing ^{10}Be cosmogenic denudation rate dataset (Young et al., 2015) and develop a working hypothesis for the relationship between millennial-scale denudation and long-term exhumation.

GEOLOGIC SETTING

The bedrock geology of the Santa Lucia range (Fig. 3-2) is characterized by high-grade metamorphic and deep-seated anhydrous igneous rocks (Compton, 1960; 1966a; Wiebe, 1966; Ross, 1976; Dibblee, 1974; 1979; Kidder et al., 2003). The crystalline rocks are Late Cretaceous in age (Mattinson, 1978; Kistler and Champion, 2001; Barth et al., 2003; Colgan et al., 2012) and contain roof and screen pendants of marble and quartzite of the Paleozoic Sur Series (Trask, 1926; Wiebe, 1966; Ross, 1976). The Late Cretaceous schist of Sierra de Salinas crops out in the northeastern part of the range (Dibblee, 1974; 1979) and is the northernmost member of the Pelona-Orocopia-Rand schist—metasediments underplated during the Late Cretaceous (Grove et al., 2003; Kidder and Ducea, 2006; Chapman et al., 2010). Together, the crystalline rocks form an elongate belt of deeply exhumed Sierran basement—known as the Salinian block—that has been tectonically excised from its former location in the Mesozoic Sierra Nevada arc (Graham, 1978; Dickenson, 1983). Restoration of slip along the San Andreas fault (e.g. Powell, 1993) partially restores the Salinian block to its original location, but further inboard displacement is required based on isotopic, thermobarometric, petrologic, and regional geologic constraints (e.g. Chapman et al., 2012). The structure responsible for this additional movement is most likely the Nacimiento fault, which separates plutonic and amphibolite–granulite-facies metamorphic rocks on the north from greenschist–blueschist-facies Franciscan mélange on the south (Ross, 1976; Dibblee, 1979; Hall, 1991; Page et al., 1998; Dickenson et al., 2005).

Substantial lithospheric reorganization occurred during the Late Cretaceous to Paleocene in the region that would later become the Mojave Desert, Transverse Ranges, and the Salinian block (Jacobson et al., 2007; Saleeby et al., 2007; Chapman et al., 2010). Rapid upper-crustal attenuation and exhumation in the Santa Lucia range brought >7.5 kbar and 850° C rocks to the surface over a 10 m.y. period from ~80–70 Ma, at rates of 2–3 mm/yr (Chapman et al., 2010). It was during this time of rapid exhumation and erosion that the schist of Sierra de Salinas was eroded from crystalline highlands, deposited in the subduction channel, and re-laminated at the base of the crust where it is now juxtaposed against the crystalline rocks that presumably provided the detritus for the schist protolith (Grove et al., 2003; Jacobson et al., 2011). It is hypothesized that these relationships are the result of subduction of a thick, buoyant, volcanic plateau (Saleeby, 2003; Chapman et al., 2012).

The Late Cretaceous crustal restructuring quickly led to the accumulation of several kilometers of Late Cretaceous to Paleocene coarse-grained marine and non-marine basin fill that was deposited within normal-fault bound half grabens in the Santa Lucia and nearby La Panza ranges (Vedder and Brown, 1968; Ruetz, 1979; Graham, 1979; Dibblee, 1979; Grove, 1993). Marine deposition appears to have become more widespread by latest Paleocene through Eocene time, but several major erosional and angular unconformities—and rapid changes in paleobathymetry—indicate several periods of subsidence and uplift during this time (Ruetz, 1979; Graham, 1976; 1979; Grove, 1993).

Marine basins rapidly shoaled at the end of the Eocene, a regional unconformity was developed, and the basins were completely re-submerged several m.y. later million years (Graham, 1976; Nilsen, 1981). Such rapid changes may have been related to initial interaction of the Pacific and North America plates (e.g. Atwater and Stock, 1998), in a process like the well-documented wave of dynamic topography that follows the northwestward migration of the Mendocino Triple Junction (Furlong, 1984; Merrits and Bull, 1989; Groome and Thorkelson, 2009).

Miocene paleogeography is complicated in the Santa Lucia range and Salinas Valley (e.g. Graham, 1976; 1979; Graham et al., 1989). In general, much of the range subsided and accumulated as much as 2.5 km of shallow to deep-marine deposits of the Monterey Formation (Graham, 1978; Dibblee, 1976; 1979). Local emergent highs formed and subsided along the trace of the Reliz–Rinconada fault, indicating fault activity (Graham, 1978). Deposits of Monterey Formation flank the currently exposed crystalline core of the Santa Lucia range to the northwest, northeast, and southeast, and an incomplete faulted section is exposed in the central-northwest part of the range (Dibblee, 1974; Rosenberg and Wills, 2016). However, the thickness of Miocene deposits in the central and southwestern parts of the range—if any—remains uncertain. A regional-scale Pliocene regression is recorded by subaerial clastic progradation that commonly contains recycled Miocene basin fill clasts (e.g. Page et al., 1998).

METHODS

LOW-TEMPERATURE THERMOCHRONOMETRY

ACQUISITION OF NEW (U-TH)/HE AGES

OVERVIEW

We use the apatite and zircon (U-Th)/He thermochronometers to document the million-year timescales of vertical deformation in the Santa Lucia range of central coastal California. The basis of (U-Th)/He dating is the quantitative retention of alpha particles (^{4}He) produced during decay of matrix-bound radiogenic U and Th (Dodson, 1973; Zeitler et al., 1987). The retention of ^{4}He is controlled by temperature-dependent diffusivity such that there is a temperature window—or 'partial-retention zone' (PRZ)—that spans behavior between complete retention and complete diffusion. A common simplification is to assume that relatively little geologic time is spent in the PRZ and that a single temperature—the 'closure temperature'—approximates the moment that ^{4}He begins to be retained (Dodson, 1973). Other parameters, such as mineral species, grain morphology and size, and accumulated radiation damage all affect the diffusion behavior, and thus the closure temperature, of a sample (Farley, 2000; Reiners et al., 2004; Farley et al., 2011; Guenthner et al., 2013), For typical grain sizes and cooling rates of ~10° C/m.y., closure temperatures of apatite are ~70° C and zircon ~175° C, and record exhumation from 1.5–6 km paleodepths with typical geothermal gradients (Farley, 2000; Reiners et al., 2004).

SAMPLING STRATEGY AND LOCATIONS

We sampled along the Big Sur coast, from the interior part of the range, and along the NE edge of the range with a combination of near-horizontal and 'vertical' transects to constrain range-wide patterns of exhumation (Fig. 3-2). Equal-elevation transects can provide constraints on the relative spatial pattern of exhumation and (or) the long-term production of relief (House et al., 1998). Transects in steep topography ('vertical' transects) can provide constraints on the rate and timing of exhumation, especially if a preserved PRZ is encountered at high elevations (Ehlers, 2005; Gallagher et al., 2005). We maximized our constraining power by linking steep transects in the regions of highest relief (Fig. 3-1) with a low-elevation coastal transect and supplemented these data with dispersed samples throughout the range (e.g. Valla et al., 2011). Transects were selected based on high relief, accessibility, and bedrock type, with an emphasis on Late Cretaceous crystalline rocks. This emphasis reflects the known ability of these rocks to provide apatite and zircon for analysis (Mattinson, 1978; Barth et al., 2003; Ducea et al., 2003; Kidder et al., 2003). Samples were also successfully collected from metasandstone of the Mesozoic Franciscan mélange near Point Sur and Salmon Creek.

Thermal anomalies from wildfire and fluid flow can substantially bias (U-Th)/He ages, and especially so for apatite (Ehlers, 2005; Reiners et al., 2007). The Santa Lucia range has many hot springs, a testament to its relatively high geothermal gradient and abundant fractures, and has experienced many large and damaging wildfires in recent history. Thus, to prevent bias in our ages: 1) we did not sample near any active hot springs, 2) we did not sample where there was any evidence of past hydrothermal activity, and 3) every sample was extracted from an area that would have been shielded during a wildfire. Despite these efforts, many aliquots from the Junipero Serra transect—which burned in 2008—appear to have been partially reset, as discussed below. To our knowledge, this is the only location where this occurred.

ANALYTICAL SUMMARY

Analytical procedures for (U-Th)/He dating are detailed in Appendix A. In summary, apatite and zircon are extracted from the rock sample using standard crushing and separation techniques. Large, clear, and euhedral grains are picked, measured, and packed into Nb foil packets. The packets and grains are heated to ~1100–1300° C with a diode laser for several minutes in an ultra-high vacuum helium extraction cell. Evolved ^{4}He gas is spiked with a calibrated ^{3}He tracer, cooled to 16°K in a cryogenic trap, purified, and analyzed by a noble gas mass spectrometer. The mineral grains are then dissolved in acid with a radiogenic spike and analyzed on an inductively-coupled plasma mass spectrometer to determine U and Th contents of each grain. Apparent ages are calculated using the production-diffusion equation of Meesters and Dunai (2002) and corrected for the fraction of ^{4}He ejected from the outer ~20 μm of the grain (Farley, 2002; Hourigan et al., 2005). Analytical data for each aliquot are available in Appendix B.

ESTIMATES OF EXHUMATION RATE

We use three separate methods to estimate exhumation rates in the Santa Lucia range, each of which requires different assumptions about the thermal state of the crust. In this section, we outline the basic assumptions for each method, discuss the estimation of closure temperature, and address the thermal state of the crust in the Santa Lucia range.

ESTIMATING THE CLOSURE TEMPERATURE

We estimate the bulk closure temperature for each sample using the individual aliquot grain measurements and iteratively solving the closure-temperature equation. We simplify our calculation by using the radius of a sphere with an identical surface area to volume ratio as the original grain (e.g. Meesters and Dunai, 2002). A sphere-equivalent radius is calculated for each aliquot using the equations provided in Farley (2002) and Hourigan et al., (2005) for apatite and zircon, respectively. We use the closure equation from Dodson (1973) and the aliquot age to iteratively determine a closure temperature that results in a <0.25° C difference between the predicted and observed cooling rate. Sphere-equivalent radii and aliquot closure temperatures are provided in the analytical data (Appendix B). Sample-level closure temperature is estimated as the mean of the aliquot values weighted by the inverse-square-error of the aliquot age. In this manner, the sample-level closure temperature is weighted the same way as the sample-level age. Alternative methods—such as aggregating the aliquot surface area and volume to calculate a sample-level sphere-equivalent radius (e.g. Gautheron and Tassan-Got, 2010)—are unsatisfying because the resulting closure temperature is weighted by geometry, but the sample-level age is not.

ESTIMATING THE GEOTHERMAL GRADIENT

It is likely that the geothermal gradient varies spatially throughout the Santa Lucia range as a function of both long- and medium-wavelength topography (e.g. Stüwe et al., 1994) and as a function of spatially varying exhumation rate (e.g. Manktelow and Grasemann, 1997). However, there are only sparse measurements of heat flow (65 mWm^{-2} near Monterey; 75 mWm^{-2} near San Simeon; 96 mWm^{-2} in the central part of the range; Lachenbruch and Sass, 1980) and none are close to sample locations. Because of this, a single value for the bulk geothermal gradient (30° C/km) is chosen, like in other thermochronologic studies along the nearby San Andreas fault (e.g. Bürgmann et al., 1994). Two of the three approaches for estimating exhumation rate outlined below do not explicitly require a geothermal gradient. The third approach accounts for advection of isotherms during exhumation and the effect of topography. The geothermal gradient is used in this case to define the temperature at the base of the 1D thermal model;

local geothermal gradients are evaluated for each sample and depart from the bulk value. This method does not address the long-wavelength (>20 km) variation of temperature that may exist along the length or across the width of the range.

A surface temperature value of 15° C (at sea level) is used in our calculations because it is the 30-yr average for this region (http://www.prism.oregonstate.edu/, accessed 09/01/2016), and we use an atmospheric lapse rate of -4.5° C/km to calculate surface temperature at elevation. We further assume that our samples have experienced monotonic cooling since they passed through their closure temperature. This assumption is likely true for Miocene and younger samples, but analysis of nearby sedimentary basins indicates several periods of pre-Miocene uplift and subsidence (e.g. Graham, 1978; Chapter 1).

RELATIONSHIP BETWEEN TOPOGRAPHY, SUB-SURFACE TEMPERATURE, AND EXHUMATION

The thermal structure in the upper several km of crust is affected by the amplitude and wavelength of surface topography and the vertical advection of heat during erosion and exhumation (Stüwe et al., 1994; Mancktelow and Grasemann, 1997). To explore how these parameters affect the shape of isotherms, we determined the ratio of isotherm amplitude to topographic amplitude (α) for each of our vertical transects using the approximating equations for temperature and depth from Mancktelow and Grasemann (1997). The results of these calculations (Table 3-1) show that the amplitude of the 70° C isotherm—corresponding to the approximate closure depth of apatite—is between ~10–50% of the surface topography. Because of the dampening effect of depth, the 180° C isotherm—corresponding to the approximate closure temperature of zircon—is deflected <10% for rates up to ~1 mm/yr and thus can be simplified as a low-relief, nearly horizontal surface.

Table 3-1. Effects on the shape of the 70°C isotherm for varying parameters of topography and exhumation rate. Calculated using equations from Manktelow and Grasemann (1997) with amplitude and wavelength from modern topography; L=45 km; mean geotherm=30°C/km; $k=10^{-6}$.

Transect	Topographic wavelength (km)	Topographic amplitude (km)	Base elevation (km)	Deflection of 70°C isotherm relative to topography (α) for exhumation rates of 0.1/0.2/0.5/1.0 mm/yr[a]
Palo Corona	11.0	0.45	0.0	0.22/0.27/0.35/0.48
Anderson Peak	7.6	0.65	0.0	0.08/0.12/0.21/0.37
Cone Peak	11.0	0.75	0.0	0.21/0.25/0.36/0.52
Salmon Creek	13.0	0.50	0.0	0.27/0.32/0.42/0.54

These results indicate that estimates of exhumation rate from apatite cooling ages need to consider the shape of isotherms; two simple cases make the point. If there has been little change in topographic relief between now and when a sample passed through its closure isotherm, using the shape of the present isotherm to calculate exhumation rates should provide a reasonable estimate of the true rate. If, however, the present topography was created entirely during the period of exhumation, the shape of the closure isotherm would have originally been flat and using the present isotherm would underestimate the true exhumation rate. The effect of rapid and recent changes in the location of high topography—perhaps resulting from drainage capture—may also locally affect these relationships.

SINGLE-SAMPLE ESTIMATES

We calculate exhumation rate for each sample using the sample-specific depth to the closure temperature and the cooling age. The closure depth is calculated in two separate ways that represent the two end-member scenarios for the shape of the closure isotherm: 1) with a horizontal isotherm and a geothermal gradient of 30° C/km—corresponding to a scenario of total relief production during exhumation, and; 2) by accounting for the effect of topography and advection of isotherms during exhumation using the equations of Mancktelow and Grasemann (1997) and parameters from Table 3-2—corresponding to a scenario of no relief production. The latter calculation is accomplished by using sample-specific topographic parameters estimated from a DEM, and by iteratively solving for depth and exhumation rate until the convergence is <1° C for closure temperature and <0.01 mm/yr for exhumation rate.

It is important to note that neither of these approaches is likely to capture the actual evolution of relief during exhumation. Because of this, an 'average' exhumation rate is calculated from the two approaches that conceptually corresponds to about half of the relief being produced during exhumation. Uncertainties on this value include the propagated uncertainty in cooling age for each of the two estimates, but do not consider uncertainties in model parameters; in most cases, the age uncertainties are much larger than the difference between the two model results (Fig. 3-3b). Figure 3-3a shows how the two isotherm models differ in their distribution of exhumation rates for a series of possible bulk geothermal gradients. In all cases, the 'flat-isotherm' model has higher rates and the 'deflected-isotherm' model is less sensitive to changes in

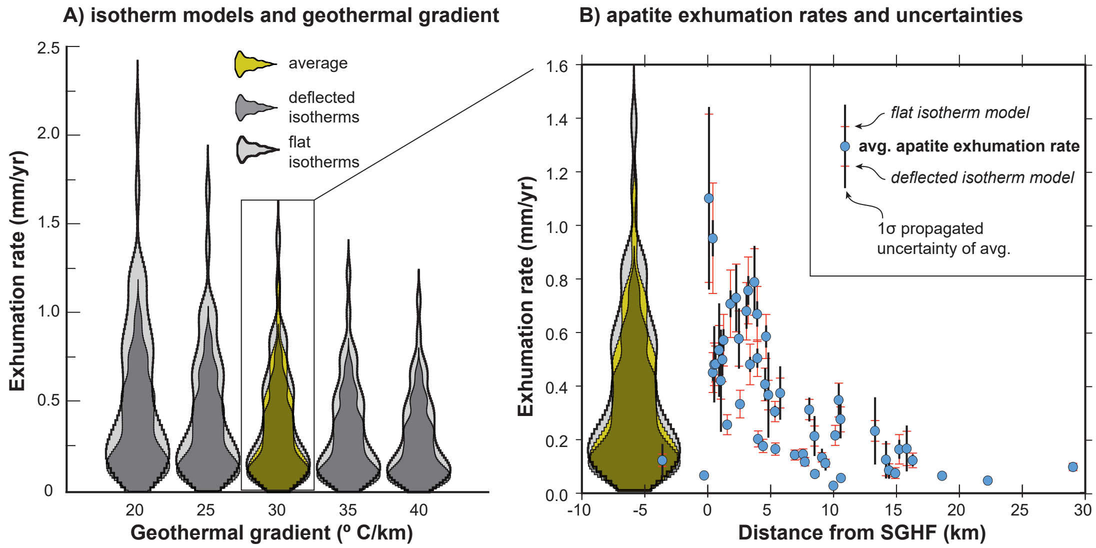

Figure 3-3. Variation of apatite exhumation rate as a function of isotherm model and average geothermal gradient. **Plot A**—Violin plots show the gaussian kernel density estimate of exhumation rate for potential average geothermal gradients and the two end-member scenarios of either completely flat isotherms or isotherms that are deflected based on exhumation rate and modern topography (e.g. Manktelow and Grasemann, 1997). **Plot B**—For a given geothermal gradient, the range of exhumation rates estimated by the two end-member scenarios is typically less than or comparable to the propagated 1σ uncertainty, which is based entirely on the relative uncertainty of the cooling age.

the bulk geothermal gradient. All estimates of exhumation rate, and the topographic parameters for each sample, can be found in Table 3-2.

AGE-ELEVATION RELATIONSHIPS

The age-elevation relationship (AER) for steep transects can provide estimates of the long-term exhumation rate in addition to estimates of the timing of major changes in exhumation (Braun et al., 2006). This method does not require assuming a value for the geothermal gradient if the closure isotherm is near horizontal. The slope of a line between two samples with a large change in elevation provides an estimate of the exhumation rate over the time interval of the samples (Ehlers, 2005). This scenario is likely the case for our zircon ages. However, when the closure temperature varies substantially in depth—as is the case for the 70° C isotherm—the slope of the AER will overestimate the actual exhumation rate by a factor of $(1-\alpha)^{-1}$ (Braun, 2002a), where α is the ratio of isotherm amplitude to topographic amplitude. For an apparent exhumation rate of 0.4 mm/yr in a region with α=0.5, the AER overestimates the actual exhumation rate by a factor of 2. Large changes in relief during exhumation can also alter the relationship between surface topography and the shape of the closure isotherm. If the parameter β is the relative change in relief, then the apparent exhumation rate from an AER may be modified by a factor of $\beta(\beta-\alpha)^{-1}$, potentially resulting in vertical or negative slopes when $\beta<\alpha$ (Braun, 2002a).

Changes in exhumation rate with time may also alter the relationship between surface topography and isotherms. For example, consider a system in equilibrium with an exhumation rate of 0.5 mm/yr and surface topography similar to the Anderson Peak transect (Table 3-1). The 70° C isotherm will have an amplitude 20% of the surface topography with these conditions. A sudden increase in the exhumation rate to 1.0 mm/yr will be accompanied by re-equilibration of the thermal structure in less than a few hundred ka (Mancktelow and Grasemann, 1997). The amplitude of the new isotherm will be nearly double its earlier value, and compared to surface topography, will have an identical signature to a reduction in surface relief. Thus, nearly vertical or reversely dipping age-elevation relationships can be produced by reductions in surface relief *or* increases in exhumation rate with near-constant surface relief.

We can increase the resolving power of age-elevation relationships by taking advantage of the difference in closure temperature between apatite and zircon. We plot zircon cooling ages as a function of 'pseudo-elevation' which shifts each zircon age higher than the corresponding apatite from the same sample by $(T_cz-T_ca)/(dT/dz)$, where T_cz and T_ca are the estimated closure temperature for zircon and apatite, respectively (e.g. Reiners, 2005). Where no corresponding apatite sample exists, we use the average closure temperature of the nearest 6 apatite samples. Although the geothermal gradient (dT/dz) is explicit in this formulation (a value of 30° C/km is used), the technique provides additional constraints on the possible timing of exhumation that is largely independent of assumed values.

An additional constraint that can help with interpreting age-elevation relationships is identification of the base of the partial-retention zone (e.g. Reiners, 2005). Samples from within the partial-retention zone (PRZ) often have a spread of ages that reflect differences in diffusion behavior. At a sample level, these differences manifest as large aliquot age dispersion and high propagated uncertainty; at a transect level, the PRZ is characterized by high variation in age with low variation in elevation. A linear regression of samples from below the PRZ can be used to determine the exhumation rate over that time interval, and the age of the break-in-slope between the regression and samples in the PRZ is often interpreted as the onset of exhumation (e.g. Ehlers, 2005).

DIRECT INVERSION THROUGH SPECTRAL ANALYSIS

Overview

To further characterize the relationship between elevation and age, we employ a spectral analysis method developed by Braun (2002b). The conceptual model is that at short wavelengths along a transect of cooling ages through a mountain range, any gradient in age reflects the local exhumation rate because the isotherm is essentially flat with respect to the wavelength of topography (e.g. Turcotte and Schubert, 2002). At very long wavelengths along a transect—such as those approaching the length of the range itself—the isotherms will completely mimic the topography and any gradient in age must be due to changes in surface relief.

Method

The goal of the spectral analysis is to separate the short-wavelength from the long-wavelength signals. This is accomplished through analyzing the ‘frequency response’ or ‘admittance’ function of the system, using elevation (z) as the stimulus signal and cooling age (a) as the response signal (Braun, 2002b). The frequency response function provides the gain at each sampled frequency and is computed with:

$$G(\lambda) = \frac{S_{za}(f)}{S_{zz}(f)}$$

Where $S_{za}(f)$ is the cross-power spectrum of elevation and age and $S_{zz}(f)$ is the auto-power spectrum of elevation. This provides a plot of inverse exhumation rate (m.y./km) as a function of wavelength. Gain values at short wavelength G_S (typically less than 8–10 km) estimate the local exhumation rate; gain values at asymptotically long wavelength G_L indicate relief production when positive and relief decay when negative; the relative change in relief since the mean age of the system is given by $(1- G_L/G_S)^{-1}$ (Braun, 2002b). No assumption of an average geothermal gradient is necessary because the method specifically deconvolves the response of age from the effect of elevation.

We compute the frequency response function for both apatite and zircon ages using a nearly 90-km-long by 12-km-wide swath of ages along the southwestern margin of the range; we do not include ages from SW of the SGHF. Because our data is not sampled in a regular grid, we use a Lomb-Scagle periodogram and Welch's overlapped-segment averaging estimator to compute the cross-power and auto-power spectra, as implemented in the program *REDFIT-X* (Ólafsdóttir et al., 2016). To test the robustness of our spectral analysis and evaluate analysis parameters, a LabView program was developed to interface with *REDFIT-X* that allowed us to randomly subsample our data and compile the results. We searched the *REDFIT-X* parameter space to determine the effect of amount of oversampling, number of overlapping segments, and number of withheld data points on the results. We concluded that an oversampling value (OFAC) of 5.0, four overlapping segments, and 4–5 withheld data points yielded the most stable results and these are the values we used in our final analysis.

Values of short-wavelength gain are calculated as the average of all data points with wavelengths <8 km (apatite) or <10 km (zircon). Although there are difficulties with sampling a periodic signal in this manner, it is a uniform criterion that can be applied to all model runs equally. We use a higher cut-off value for zircons because their exhumation from greater depth dampens their isotherm amplitude (Braun, 2002b).

METRICS OF EROSION AND DRAINAGE EVOLUTION

The study of tectonic geomorphology over the last century has largely confirmed the idea that the topography of landscapes can encode information about the spatial and temporal distribution of rock uplift (e.g. Wobus et al., 2006; Kirby and Whipple, 2001; 2012). In many non-glacial orogens, this information can often be successfully decoded from parametrizing and measuring characteristics of the fluvial network (Wobus et al., 2006). Such a focus on the role of fluvial incision, however, does not adequately address the erosion of steep uplands by debris flows and landslides (Stock and Dietrich, 2003), nor does it address the role of diffusive hillslope processes (e.g. Roering et al., 1999). To cover a range of possible mechanisms of erosion, we use five geomorphic metrics—normalized channel steepness, χ, local hillslope gradient, relief, and mean annual precipitation—to infer rates and patterns of erosion (Ahnert, 1970; Wobus et al., 2006; Kirby and Whipple, 2001; 2012; DiBiase et al., 2010; Perron and Royden, 2013) for all catchments draining the Santa Lucia range. We chose to isolate tributary catchments of the

Salinas River and analyze only those in the Santa Lucia range because much of the Salinas catchment lies outside of our study area. The basis for each metric is discussed below.

CHANNEL STEEPNESS

We focus on the stream-power model of river incision (Howard, 1994; Whipple and Tucker, 1999, Whipple, 2004) which, for a river channel in steady state equilibrium between incision and uplift, can be written as:

$$S(x) = k_s A(x)^{-m/n}$$

and:

$$k_s = \left(U/K\right)^{1/n}$$

The change in elevation with respect to upstream distance (channel slope; $S(x)$) is a function of the ratio of uplift to erodibility—also known as the steepness index—(U/K), the upstream drainage area $A(x)$, and constants m and n. This construct is similar to the relationship first noted by Hack (1957) and Flint (1974) where local channel slope is a power-law function of upstream drainage area with a 'concavity index' and a steepness index; in the steady state formulation above, the ratio m/n is the 'concavity index'. The power-law relationship between slope and drainage area can be used to infer the parameters m/n and ks (e.g. Snyder et al., 2000; 2003), or alternatively, to infer the presence of transient signals in the system (Whipple and Tucker, 1999; 2002).

Departures from spatially uniform ks can be useful and indicate at least one of three possibilities: 1) spatial gradients in the ratio of uplift to erodibility—such as an uplifting fault block or substantial changes in rock type, 2) changes to base level that are moving through the system—such as a migrating knickpoint or a temporal change in uplift rate across a bounding fault, or 3) behavior that is not well described by the model—such as a poor choice of m/n (e.g. Wobus et al., 2006; Kirby and Whipple, 2012; Perron and Royden, 2013; Mudd et al., 2014). In practice, it is often difficult to deconvolve the dual signals of uplift and rock erodibility encoded in *ks* if both vary substantially over a study area (as is the case for the Santa Lucia range). This can be accounted for by only analyzing *ks* in regions of relatively similar bedrock lithology.

Furthermore, we restrict our analysis to regions downstream of a threshold drainage area of 1 km^2 to avoid sampling parts of the catchment where the stream-power model is inappropriate and erosion is more likely dominated by debris flows and landslides (e.g. Stock and Dietrich, 2003).

The determination of ks for a fluvial network requires measurement of drainage area and local channel slope which can be accomplished by a linear regression of channel slope and contributing drainage area on a log-log plot (Wobus et al., 2006). This approach, however, suffers from difficulties arising from the differentiation of inherently noisy elevation data and it can be difficult to accurately determine the relevant parameters. An alternative approach, first described by Royden et al. (2000) and Sorby and England (2004) and expanded in Perron and Royden (2013), is to integrate the stream-power equation instead of differentiating to obtain:

$$z(x) = z(x_b) + A_0^{-m/n} k_s \chi$$

and

$$\chi = \int_{x_b}^{x} \left(\frac{A_0}{A(x')} \right)^{m/n} dx$$

In this formulation, the elevation in the river channel at an upstream point $z(x)$ is a function of the steepness index ks and the integrated upstream drainage area χ; a constant $z(x_b)$ represents the elevation of the base of the fluvial network, and A_0 is a reference drainage area (Perron and Royden, 2013). This transforms the x-coordinate of the river system into χ and linearizes the relationship between elevation and upstream drainage area. Because χ is an integral quantity, determining ks does not suffer from the aliasing and noise issues of log-log slope-area plots. The slope of the stream in the transformed coordinate system—Mχ—is the quantity $A_0^{-m/n}ks$.

Mχ AND KSN AS A POTENTIAL MEASURE OF UPLIFT AND EROSION

In a simple fluvial network, a single value of m/n collapses and co-linearizes the main stem and tributaries onto a single line with the slope Mχ (Perron and Royden, 2013). Although calculated differently, the quantity Mχ, when multiplied by the constant $A_0^{-m/n}$ is identical to normalized channel steepness, ksn. We calculate ksn throughout the study area to test our predications of which faults control vertical deformation in the Santa Lucia range. In theory, an increase in uplift rate across a fault without a change in lithology should result in a proportional increase in ksn, and ksn should generally be larger in areas of higher uplift. Thus, the map-view distribution of ksn can become a screening tool for faults with relative vertical motion where lithologies are similar on either side.

χ AS A POTENTIAL MEASURE OF DRAINAGE DISEQUILIBRIUM

The topology of drainage networks is often considered to represent the long-term (>10^5 yr) erosive response to the boundary conditions of rock uplift, erodibility, and climate (e.g. Montgomery and Dietrich, 1988). The ability of the χ transformation to reveal patterns in river channel slope, normalized for upstream drainage area, makes it an excellent tool to examine drainage basin dynamics (Willet et al., 2014). Two streams that meet at a common divide and end at a common base level must have the same drop in elevation. However, how the change in elevation is distributed over their length can vary substantially and it is this distribution of slope, normalized for drainage area, that the χ transformation reveals.

Mismatches in χ across a drainage divide indicate that the stream with lower χ is steeper and more aggressively eroding than the stream with higher χ. For regions with similar uplift and erodibility, this disequilibrium leads to the migration of the drainage divide towards the higher χ stream (Willet et al., 2014). Alternatively, a mismatch in chi across a drainage divide could also indicate equilibrium if there is a significant asymmetry in the distribution of uplift or erodibility (e.g. Shikakura et al., 2012). Thus, map-view patterns of χ can be judiciously used to infer drainage divide stability or the presence of equilibrium landscapes with asymmetric forcing.

CALCULATION OF χ AND M_χ

We employ a method to calculate χ and ksn similar to that described by Mudd et al. (2014), but modified to run in MATLAB and with much less computational overhead. χ is calculated using the TopoToolbox MATLAB script (Schwanghart and Scherler, 2014) using the equations of Perron and Royden (2013) and the USGS 10m National Elevation Dataset resampled to 30m resolution. Our script is modified to iterate through all stream networks in the DEM. After an initial run using the best-fitting m/n algorithm, we determined that the m/n value that best transforms all the data is ~0.5 and use this value for all streams to allow inter-network comparison of chi and ksn. We use sea level as the base elevation for all drainages except for tributaries of the Salinas River where the local elevation of the confluence is used.

Once χ is calculated, we implement an algorithm that separates each stream segment and iteratively determines an optimum set of best-fit linear regressions. This is done using an implementation of the Shape Language Modeling toolbox (SLM), written by John D'Errico and modified for our purposes. The SLM toolbox uses an optimization routine to determine the location of a set number of 'knots' and the slope of intervening linear segments that minimizes the misfit using the least-squares method. The knot locations are free to vary anywhere between the two end points and we require the slope of the line to be non-decreasing, since any 'upstream flow' is a result of noise in the elevation data and not a physically meaningful result.

The number of fit segments is determined iteratively. A starting number of knots is provided based on the length of the stream segment and a goodness of fit is assessed using the adjusted R^2 statistic. If the goodness of fit is too low, a knot is added and the SLM model runs again; if the goodness of fit is too high, a knot is removed. In this manner, poor fits are given additional degrees of freedom and overfit data are penalized. Based on the results of hundreds of model runs, the acceptable range of adjusted R^2 was set between 0.997 and 0.999, the minimum number of knots is 3 (counting end points), and the maximum number of knots is 18. Although the adjusted R^2 values are inflated because of serial correlation, their relative magnitudes are still meaningful.

Our approach to determining best-fit segments of ksn is a less-robust implementation than that described by Mudd et al. (2014) and trades computational efficiency for decreased parameterization. First, our fit segments of $M\chi$ must always be linked, even where parallel $M\chi$ segments are separated by a vertical drop, such as at a waterfall. In our implementation, a waterfall would manifest as three segments, two with identical $M\chi$ separated by a short segment with much higher $M\chi$; in the Mudd et al. (2014) implementation, this would result in only two segments with differences in their y-intercept values. Second, we use a much more limited number of possible $M\chi$ segments. Our implementation is set to only allow a maximum of 16 independent segments, whereas hundreds are allowed in the Mudd et al. (2014) version. Despite using our relatively sparse set of knot parameters, even the longest stream segments appear adequately fit at the scale of our study. Third, the relatively simple least-squares search through m/n space as described by Perron and Royden (2013) and implemented in the TopoToolbox script is not nearly as thorough and rigorous as the approach developed by Mudd et al. (2014). This is a justified difference, in part, because the large scale of our analysis requires that we pick a m/n value to use for all networks.

OTHER TOPOGRAPHIC METRICS OF EROSION

HILLSLOPE ANGLE

Hillslopes deliver sediment to fluvial networks through a variety of processes, from non-linear diffusion of soil and colluvium (e.g. Roering et al., 1999), to debris flows and landslides (e.g. Stock and Dietrich, 2003). In many tectonically active and eroding landscapes, hillslopes rapidly attain a threshold value and respond to further channel incision at their base through increased frequency of debris flows and landslides (Burbank et al., 1996; Montgomery, 2001; Larsen and Montgomery, 2012). This leads to the observation that erosion rates correlate well with hillslope angle until their threshold value is reached, but vary widely above this value (Burbank et al., 1996; Montgomery and Brandon, 2002; Binnie et al., 2007; Ouimet et al., 2009). Catchment-mean hillslope angle has been successfully used in many studies to document this transition from transport-limited erosion below the threshold to detachment-limited erosion above (e.g. Binnie et al., 2007; DiBiase et al., 2010). In the nearby San Bernardino and San Gabriel mountains, this transition occurs over a range of hillslope angles from ~20–30° (Binnie et al., 2007; DiBiase et al., 2010). We calculate slope from the 10m USGS National Elevation Dataset and determine mean values for all catchments in the study area.

RELIEF

Relief of mountain ranges has long been considered a key metric that relates topography and erosion (Ahnert, 1970; Schmidt and Montgomery, 1995). The scale at which relief should be calculated is more uncertain; at short lengths relief becomes a metric of local surface slope; at long lengths it mimics maximum topography. We calculate relief in a 2.5-km-radius window because it is linearly proportional to normalized channel steepness (and positively correlated with rates of long-term erosion) in the San Gabriel and San Bernardino mountains (Binnie et al., 2007; DiBiase et al., 2010). Relief calculated in 5-km and 1-km-radii are not as well correlated with channel steepness (DiBiase et al., 2010). The Santa Lucia range is similar in lithology to the San Gabriel and San Bernardino ranges, has similar young cooling ages, and thus may display similar relationships between relief and erosion. Relief is calculated from the 30m USGS National Elevation Dataset and average values are calculated for all catchments in the study area.

DEFORMED MARINE TERRACES

To compare time-averaged exhumation rates and metrics of erosion with more recent rates of surface uplift along the Big Sur coast, we surveyed the bedrock-surface elevation of the lowest-emergent marine terrace near Ragged Point (this study), between Big Sur and Monterey (Chapter 2) and from Aptos northward to Point Año Nuevo (Chapter 1). The lowest terrace level was chosen specifically because reconnaissance work in Big Sur revealed that only a single marine terrace is preserved in most locations, that the lowest-emergent terrace throughout the region is morphologically distinct from older terraces owing to its generally excellent preservation and both prominent and wide wave-cut platform, and the terrace remnants in Big Sur can be nearly continuously mapped into the first widespread emergent terrace near Monterey (McKittrick, 1988; Clark et al., 1997; Rosenberg and Wills, 2016) and San Simeon (Hanson et al., 1994).

The survey was completed using a laser rangefinder, survey grade GPS receiver, and rugged tablet computer; typical vertical measurement uncertainties with this method are ~0.7 m (a detailed description of uncertainty estimation is provided in Appendix A). Our method has the advantage over previous efforts (Alexander, 1953; Bradley and Griggs, 1976; McKittrick, 1988) of surveying the marine terrace where it is abundantly exposed along coastal bluffs. Because these measurements were made along coastal bluffs, elevations are corrected for the distance to the back edge, as defined by a prominent break-in-slope in airborne lidar from the 2009–2011 California Coastal Conservancy Lidar Project (http://coast.noaa.gov/dataviewer/) or where detailed geologic mapping exists (Clark et al., 1997; Graymer et al., 2014; Rosenberg and Wills, 2016). All efforts were made to survey only the lowest, most-prominent marine terrace. Elevation data and a detailed description of the methods used are available in Appendices A and C.

The lateral continuity and initially uniform elevation of the lowest-emergent marine terrace along the central California coast make it an excellent strain marker, regardless of its age (e.g., Anderson, 1990; Valensise and Ward, 1991). Terrace ages in central California—and near Santa Cruz in particular—are the subject of disagreement (e.g. Perg et al., 2001; Weber, 1990), but the closest ages to Ragged Point (Hanson et al., 1994) seem less contentious. Near San Simeon the 'San Simeon terrace' is the lowest well-developed terrace and is correlated with the MIS 5c sea level high stand (Hanson et al., 1994). We tentatively correlate the uplifted marine terraces found along the Big Sur coast to the north of and near Ragged Point with the MIS 5c terrace near San Simeon based on the lack of any lower-elevation terraces, and on their similar morphologic character. This correlation is further supported by a late Quaternary uplift rate of >=0.75 mm/yr near Ragged Point provided—but not discussed—by Hanson et al. (1994). This rate predicts a terrace elevation near Ragged Point >78 m, in reasonable agreement with our surveyed terrace heights.

RESULTS

LOW-TEMPERATURE THERMOCHRONOMETRY

Table 3-2 presents the results of new apatite and zircon (U-Th)/He ages collected in 4 steep transects—three along the Big Sur coast, and one in the highest-relief part of the interior of the range in addition to 11 new ages scattered throughout the range. The results of a coastal transect between Monterey and Big Sur (Chapter 2), the original data for the apatite Cone Peak transect (Ducea et al., 2003), and several apatite fission track results from Naeser and Ross (1976) are also provided.

STEEP TRANSECTS

PALO CORONA

Overview

The Palo Corona transect is the farthest north of our vertical transects (Fig. 3-2), covers an area from Soberanes Creek at sea level to Palo Corona at ~830 m elevation, and is the only transect that is sub-parallel to the SGHF instead of perpendicular. Bedrock consists predominantly of the hornblende-biotite quartz diorite of Soberanes Point (Wiebe, 1966; Ross, 1976, Clark and Rosenberg, 1999; Rosenberg and Wills, 2016) and the granodiorite of Cachagua (Dibblee, 1974; Ross, 1976). Apatite ages increase steadily from 10.7 Ma at sea level to 17–27

Table 3-2. Summary of low-temperature thermochronometric ages, exhumation rates, and parameters. Topography values indicate wavelength (λ), amplitude (Δ), and base elevation (z_0) and are estimated from a 30 m DEM. Sources of data: 1, A. Steely, 2016; 2, A. Mere, 2016; 3, D. Orme, 2009; 4, J. Ooms, 2012; 5, Ducea et al. (2003); 6, Naeser and Ross, 1976.

Map ID/ Sample #	Latitude/ Longitude	Distance to SGHF (km)	Elevation (m)	Relief in 2.5 km radius (m)	Analysis type/ No. of aliquots	Cooling age ±1σ	Est. bulk T_c (°C)	Topography λ,/ Δ,/ z_0/ (km)	Depth to T_c (km)	Local geothermal gradient (°C/km)	Exhumation rates deflected/flat (mm/yr)	Average exhumation rate ±1σ (mm/yr)	Source
						Zircon (U-Th)/He							
4	36.1461	16.25	1780	967	ZHe	78.07	171.4	5.2/ 0.48/	5.25	27.8	0.08	0.09	1
AS004	-121.4208				3	±3.85		0.85			0.10	±0.006	
6	36.1467	15.78	1556	1042	ZHe	86.39	167.4	5.2/ 0.48/	5.12	28.9	0.07	0.07	1
AS006	-121.4285				4	±8.61		0.85			0.08	±0.011	
8	36.1430	15.19	1360	1110	ZHe	90.61	169.2	5.2/ 0.48/	5.16	29.9	0.06	0.07	1
AS008	-121.4332				4	±12.72		0.85			0.08	±0.014	
10	36.1366	14.87	1073	1146	ZHe	108.50	166.7	5.2/ 0.48/	5.07	31.6	0.05	0.05	1
AS010	-121.4309				4	±5.86		0.85			0.06	±0.004	
16	36.2844	0.66	719	1064	ZHe	27.05	180.8	5.6/ 0.55/	5.04	31.5	0.21	0.23	1
AS016	-121.8010				4	±4.25		0.0			0.25	±0.051	
17	36.2914	0.10	606	1038	ZHe	19.45	182.6	8.0/ 0.55/	4.87	33.3	0.28	0.31	1
AS017	-121.8156				3	±9.45		0.0			0.34	±0.215	
18	36.2963	-0.65	463	881	ZHe	27.58	182.8	10.0/	5.07	33.2	0.20	0.22	1
AS018	-121.8305				7	±2.61		0.55/ 0.0			0.24	±0.029	
19	36.1803	4.13	1189	1017	ZHe	25.15	180.4	7.6/ 0.65/	5.05	29.0	0.25	0.27	1
AS019	-121.6422				3	±4.60		0.0			0.29	±0.069	
20	36.1770	3.73	1051	1115	ZHe	20.02	180.9	7.6/ 0.65/	4.89	30.4	0.30	0.33	1
AS020	-121.6443				3	±0.47		0.0			0.35	±0.011	
22	36.1721	3.11	835	1202	ZHe	20.52	187.6	7.6/ 0.65/	5.06	31.7	0.29	0.32	1
AS022	-121.6481				4	±3.42		0.0			0.35	±0.075	
24	36.1598	1.29	370	1122	ZHe	11.66	187.0	7.6/ 0.65/	4.55	37.9	0.42	0.49	1
AS024	-121.6615				4	±0.39		0.0			0.57	±0.023	
25	36.1584	0.94	245	995	ZHe	12.22	187.1	7.6/ 0.65/	4.59	38.6	0.40	0.46	1
AS025	-121.6653				5	±1.18		0.0			0.53	±0.063	
26	35.8547	6.04	980	641	ZHe	19.13	181.4	13.0/	4.84	31.1	0.30	0.34	1
AS026	-121.3235				4	±5.03		0.50/ 0.0			0.37	±0.125	
27	35.8564	5.77	897	658	ZHe	35.73	180.8	13.0/	5.15	30.0	0.17	0.18	1
AS027	-121.3302				4	±6.92		0.50/ 0.0			0.19	±0.050	
29	35.8473	4.58	635	804	ZHe	12.85	181.7	13.0/	4.52	35.1	0.40	0.46	1
AS029	-121.3376				4	±1.45		0.50/ 0.0			0.52	±0.074	
30	35.8354	3.39	442	946	ZHe	67.33	175.3	13.0/	5.16	31.4	0.08	0.09	1
AS030	-121.3407				4	±17.21		0.50/ 0.0			0.09	±0.032	
31	35.8279	2.51	402	1052	ZHe	28.94	182.9	13.0/	5.10	33.4	0.19	0.21	1
AS031	-121.3448				4	±5.31		0.50/ 0.0			0.22	±0.054	
32	35.8167	1.19	320	906	ZHe	23.30	184.4	13.0/	5.03	34.6	0.23	0.25	1
AS032	-121.3511				4	±3.09		0.50/ 0.0			0.28	±0.047	
33	35.8136	0.55	150	891	ZHe	23.95	182.0	13.0/	4.97	35.7	0.21	0.24	1
AS033	-121.3575				7	±7.11		0.50/ 0.0			0.26	±0.099	
45	36.4603	6.93	120	676	ZHe	83.98	173.1	10.0/	5.08	33.2	0.06	0.07	1
AS045	-121.9084				4	±4.47		0.45/ 0.0			0.07	±0.005	
46	36.4551	5.38	4	564	ZHe	67.39	170.3	10.0/	4.96	34.4	0.07	0.08	1
AS046	-121.9256				4	±9.58		0.45/ 0.0			0.08	±0.016	
47	35.8086	-0.24	5	817	ZHe	67.13	172.4	13.0/	5.05	34.3	0.07	0.08	1
AS047	-121.3639				3	±2.15		0.50/ 0.0			0.09	±0.004	
48	36.1564	0.37	20	824	ZHe	16.35	184.5	7.6/ 0.65/	4.75	38.6	0.29	0.33	1
AS048	-121.6720				5	±2.90		0.0			0.38	±0.084	
49	36.5227	9.98	3	390	ZHe	87.55	173.5	6.0/ 0.30/	5.08	34.1	0.06	0.06	1
AS049	-121.9298				3	±2.41		0.0			0.07	±0.002	
50	36.3739	1.57	98	488	ZHe	29.65	179.7	12.0/	5.00	35.4	0.17	0.19	2
AS050	-121.8955				3	±3.90		0.45/ 0.0			0.21	±0.035	
51	36.3756	1.08	61	477	ZHe	31.00	173.7	12.0/	4.84	35.6	0.16	0.17	2
AS051	-121.9047				5	±2.14		0.45/ 0.0			0.19	±0.017	
52	36.3958	2.60	4	489	ZHe	32.65	178.7	12.0/	5.00	35.8	0.15	0.17	2
AS052	-121.9038				5	±3.59		0.45/ 0.0			0.18	±0.026	

Map ID/ Sample #	**Latitude/ Longitude**	**Distance to SGHF (km)**	**Elevation (m)**	**Relief in 2.5 km radius (m)**	**Analysis type/ No. of aliquots**	**Cooling age ±1σ**	**Est. bulk T_c (°C)**	**Topography λ,/ Δ,/ z_0/ (km)**	**Depth to T_c (km)**	**Local geothermal gradient (°C/km)**	**Exhumation rates deflected/flat (mm/yr)**	**Average exhumation rate ±1σ (mm/yr)**	**Source**
53	36.4255	4.02	2	605	ZHe	37.68	176.3	10.0/	4.98	35.5	0.13	0.14	2
AS053	-121.9142				4	±6.77		0.45/ 0.0			0.16	±0.037	
56	36.5722	34.09	223	660	ZHe	67.48	173.3	7.5/ 0.40/	5.06	33.9	0.08	0.08	2
AS056	-121.6279				5	±3.35		0.15			0.09	±0.006	
58	36.0129	0.15	45	916	ZHe	7.09	189.4	11.0/	4.19	44.9	0.59	0.75	2
AS057	-121.5171				5	±0.67		0.78/ 0.0			0.90	±0.100	
58	36.2470	0.13	80	1022	ZHe	11.70	191.4	8.0/ 0.55/	4.64	41.0	0.40	0.48	2
AS058	-121.7710				5	±2.26		0.06			0.55	±0.130	
59	36.2378	-3.55	3	370	ZHe	45.37	177.3	5.0/ 0.20/	5.06	35.2	0.11	0.12	2
AS059	-121.8150				1	±0.98		0.0			0.13	±0.004	
61	36.0833	1.62	150	963	ZHe	15.77	185.1	14.0/	4.79	37.4	0.31	0.36	3
09DO01	-121.5880				3	±3.18		0.70/ 0.0			0.40	±0.102	
62	36.0947	1.98	488	1047	ZHe	14.87	178.8	14.0/	4.60	35.0	0.34	0.39	3
09DO02	-121.5938				2	±7.16		0.70/ 0.0			0.43	±0.265	
64	36.0760	0.33	15	688	ZHe	7.98	195.5	14.0/	4.44	44.1	0.56	0.69	3
09DO04	-121.5991				2	±1.03		0.70/ 0.0			0.82	±0.126	
65	36.1659	0.84	116	951	ZHe	11.54	181.6	7.6/ 0.65/	4.41	40.0	0.39	0.46	3
09DO05	-121.6767				4	±1.50		0.0			0.53	±0.085	
66	36.3742	1.29	90	477	ZHe	23.63	172.9	12.0/	4.70	36.2	0.20	0.22	3
09DO06	-121.9001				4	±3.15		0.45/ 0.0			0.25	±0.042	
67	36.3763	4.83	387	780	ZHe	56.82	166.3	12.0/	4.83	32.0	0.09	0.10	3
09DO07	-121.8503				3	±5.16		0.45/ 0.0			0.10	±0.013	
68	36.4364	4.41	10	556	ZHe	36.34	167.2	10.0/	4.70	35.6	0.13	0.14	3
09DO08	-121.9201				5	±1.69		0.45/ 0.0			0.15	±0.009	
						Apatite (U-Th)/He							
4	36.1461	16.25	1780	967	AHe	25.28	62.2	5.2/ 0.48/	1.70	25.1	0.10	0.13	1
AS004	-121.4208				7	±3.19		0.85			0.15	±0.022	
5	36.1491	16.18	1680	972	AHe	6.58	68.5	5.2/ 0.45/	1.67	27.3	0.38	0.49	1
AS005	-121.4252				5	±1.01		0.85			0.60	±0.107	
6	36.1467	15.78	1556	1042	AHe	15.19	59.8	5.2/ 0.48/	1.62	37.2	0.11	0.17	1
AS006	-121.4285				7	±5.41		0.85			0.23	±0.085	
7	36.1444	15.44	1460	1080	AHe	8.87	62.9	5.2/ 0.45/	1.59	28.4	0.25	0.32	1
AS007	-121.4311				6	±1.08		0.85			0.40	±0.056	
8	36.1430	15.19	1360	1110	AHe	15.34	61.0	5.2/ 0.48/	1.65	35.6	0.11	0.17	1
AS008	-121.4332				8	±2.30		0.85			0.22	±0.035	
10	36.1366	14.87	1073	1146	AHe	30.24	56.9	5.2/ 0.48/	1.55	32.5	0.06	0.08	1
AS010	-121.4309				7	±0.75		0.85			0.10	±0.003	
11	36.1298	14.38	923	1216	AHe	25.56	58.6	5.2/ 0.48/	1.59	35.7	0.06	0.09	1
AS011	-121.4312				5	±6.43		0.85			0.11	±0.031	
12	36.1269	14.14	868	1237	AHe	14.78	56.8	5.2/ 0.48/	1.53	56.3	0.07	0.13	1
AS012	-121.4316				4	±5.72		0.85			0.19	±0.070	
16	36.2844	0.66	719	1064	AHe	5.50	69.3	5.6/ 0.55/	1.56	30.2	0.42	0.48	1
AS016	-121.8010				4	±0.30		0.0			0.55	±0.038	
20	36.1770	3.73	1051	1115	AHe	3.71	70.1	7.6/ 0.65/	1.44	28.4	0.67	0.79	1
AS020	-121.6443				5	±0.45		0.0			0.91	±0.134	
22	36.1721	3.11	835	1202	AHe	4.04	70.2	7.6/ 0.65/	1.50	30.3	0.57	0.68	1
AS022	-121.6481				6	±0.27		0.0			0.79	±0.065	
23	36.1647	2.29	685	1251	AHe	3.66	73.3	7.6/ 0.65/	1.54	33.2	0.60	0.73	1
AS023	-121.6517				3	±0.44		0.0			0.86	±0.124	
24	36.1598	1.29	370	1122	AHe	4.09	70.9	7.6/ 0.65/	1.56	36.4	0.48	0.57	1
AS024	-121.6615				5	±0.21		0.0			0.67	±0.041	
25	36.1584	0.94	245	995	AHe	3.87	65.5	7.6/ 0.65/	1.46	38.1	0.44	0.54	1
AS025	-121.6653				3	±0.89		0.0			0.63	±0.174	
27	35.8564	5.77	897	658	AHe	6.78	60.9	13.0/	1.26	28.0	0.32	0.38	1
AS027	-121.3302				4	±1.27		0.50/ 0.0			0.43	±0.100	
29	35.8473	4.58	635	804	AHe	5.61	59.8	13.0/	1.30	30.7	0.35	0.41	1
AS029	-121.3376				1	±0.59		0.50/ 0.0			0.47	±0.061	
30	35.8354	3.39	442	946	AHe	5.02	70.8	13.0/	1.59	34.7	0.41	0.48	1
AS030	-121.3407				3	±0.21		0.50/ 0.0			0.56	±0.028	

Map ID/ Sample #	Latitude/ Longitude	Distance to SGHF (km)	Elevation (m)	Relief in 2.5 km radius (m)	Analysis type/ No. of aliquots	Cooling age ±1σ	Est. bulk T_c (°C)	Topography λ,/ Δ,/ z_0/ (km)	Depth to T_c (km)	Local geothermal gradient (°C/km)	Exhumation rates deflected/flat (mm/yr)	Average exhumation rate ±1σ (mm/yr)	Source
31 AS031	35.8279 -121.3448	2.51	402	1052	AHe 2	3.87 ±0.53	67.0	13.0/ 0.50/ 0.0	1.46	36.4	0.48 0.68	0.58 ±0.112	1
32 AS032	35.8167 -121.3511	1.19	320	906	AHe 3	4.53 ±0.38	69.3	13.0/ 0.50/ 0.0	1.56	36.6	0.42 0.58	0.50 ±0.059	1
33 AS033	35.8136 -121.3575	0.55	150	891	AHe 4	4.18 ±0.87	65.9	13.0/ 0.50/ 0.0	1.52	39.1	0.40 0.56	0.48 ±0.142	1
40 AS040	36.4543 -121.8706	9.07	832	683	AHe 6	18.16 ±2.99	59.0	10.0/ 0.45/ 0.0	1.36	27.2	0.12 0.15	0.14 ±0.032	1
41 AS041	36.4610 -121.8735	9.36	722	706	AHe 6	20.14 ±3.42	56.7	10.0/ 0.45/ 0.0	1.32	28.0	0.10 0.13	0.12 ±0.028	1
42 AS042	36.4666 -121.8917	8.52	561	821	AHe 5	27.16 ±3.09	52.7	10.0/ 0.45/ 0.0	1.24	29.6	0.07 0.09	0.08 ±0.012	1
43 AS043	36.4697 -121.9067	7.73	516	680	AHe 4	17.74 ±0.83	56.9	10.0/ 0.45/ 0.0	1.37	30.5	0.10 0.14	0.12 ±0.008	1
44 AS044	36.4650 -121.9040	7.58	332	718	AHe 5	13.49 ±0.39	58.1	10.0/ 0.45/ 0.0	1.44	33.1	0.13 0.17	0.15 ±0.006	1
45 AS045	36.4603 -121.9084	6.93	120	676	AHe 5	13.07 ±1.04	60.7	10.0/ 0.45/ 0.0	1.55	36.7	0.13 0.16	0.15 ±0.016	1
46 AS046	36.4551 -121.9256	5.38	4	564	AHe 3	10.72 ±0.27	61.0	10.0/ 0.45/ 0.0	1.56	39.5	0.14 0.19	0.17 ±0.006	1
47 AS047	35.8086 -121.3639	-0.24	5	817	AHe 3	24.64 ±0.63	55.9	13.0/ 0.50/ 0.0	1.55	36.3	0.06 0.08	0.07 ±0.003	1
49 AS049	36.5227 -121.9298	9.98	3	390	AHe 5	52.10 ±12.20	55.9	6.0/ 0.30/ 0.0	1.41	39.0	0.03 0.04	0.03 ±0.010	1
50 AS050	36.3739 -121.8955	1.57	98	488	AHe 4	7.45 ±0.25	63.1	12.0/ 0.45/ 0.0	1.57	38.3	0.22 0.30	0.26 ±0.012	2
51 AS051	36.3756 -121.9047	1.08	61	477	AHe 4	5.05 ±1.61	72.5	12.0/ 0.45/ 0.0	1.71	40.6	0.35 0.49	0.42 ±0.190	2
52 AS052	36.3958 -121.9038	2.60	4	489	AHe 5	6.06 ±0.17	70.0	12.0/ 0.45/ 0.0	1.70	40.8	0.28 0.39	0.33 ±0.014	2
53 AS053	36.4255 -121.9142	4.02	2	605	AHe 5	9.23 ±0.43	65.0	10.0/ 0.45/ 0.0	1.64	40.2	0.18 0.23	0.21 ±0.014	2
56 AS056	36.5722 -121.6279	34.09	223	660	AHe 5	65.00 ±5.84	51.3	7.5/ 0.40/ 0.15	1.34	36.0	0.02 0.03	0.03 ±0.003	2
58 AS058	36.2470 -121.7710	0.13	80	1022	AHe 4	1.85 ±0.40	75.8	8.0/ 0.55/ 0.06	1.42	52.2	0.79 1.41	1.10 ±0.340	2
59 AS059	36.2378 -121.8150	-3.55	3	370	AHe 2	12.73 ±4.33	56.8	5.0/ 0.20/ 0.0	1.33	43.3	0.10 0.15	0.13 ±0.061	2
67 09DO07	36.3763 -121.8503	4.83	387	780	AHe 5	6.07 ±1.85	65.4	12.0/ 0.45/ 0.0	1.50	34.4	0.31 0.42	0.37 ±0.159	3
68 09DO08	36.4364 -121.9201	4.41	10	556	AHe 3	10.25 ±0.02	62.3	10.0/ 0.45/ 0.0	1.59	39.4	0.15 0.20	0.18 ±0.001	3
71 DCONE1	36.0099 -121.5099	0.44	152	1013	AHe 1	2.27 ±0.11	74.3	11.0/ 0.78/ 0.0	1.56	43.8	0.75 1.16	0.95 ±0.067	5
72 DCONE2	36.0199 -121.5000	1.84	330	1148	AHe 2	3.51 ±0.18	77.8	11.0/ 0.78/ 0.0	1.73	38.1	0.58 0.83	0.71 ±0.050	5
73 DCONE3	36.0300 -121.4900	3.24	700	1398	AHe 2	3.43 ±0.17	69.8	11.0/ 0.78/ 0.0	1.49	32.1	0.63 0.88	0.76 ±0.054	5
74 DCONE4	36.0400 -121.4899	3.95	780	1270	AHe 1	4.02 ±0.20	69.8	11.0/ 0.78/ 0.0	1.52	30.6	0.57 0.77	0.67 ±0.047	5
75 DCONE5	36.0499 -121.4899	4.65	1320	1091	AHe 2	5.31 ±0.27	66.8	11.0/ 0.78/ 0.0	1.38	24.9	0.50 0.67	0.59 ±0.041	5
76 DCONE6	36.0499 -121.4999	3.96	1490	1104	AHe 1	6.13 ±0.31	60.8	11.0/ 0.78/ 0.0	1.18	22.7	0.44 0.57	0.51 ±0.036	5
77 DCONE7	36.0599 -121.4900	5.36	1510	825	AHe 1	9.92 ±0.50	57.3	11.0/ 0.78/ 0.0	1.15	21.4	0.27 0.34	0.31 ±0.022	5
78 DSUR1	36.2100 -121.7399	0.44	180	938	AHe 2	4.57 ±0.23	66.8	7.6/ 0.65/ 0.0	1.53	38.7	0.38 0.53	0.45 ±0.032	5
80 VW10	36.3330 -121.7141	10.12	1095	909	AHe 5	12.30 ±0.50	61.5	11.0/ 0.55/ 0.35	1.50	27.6	0.18 0.26	0.22 ±0.013	4

Map ID/ Sample #	Latitude/ Longitude	Distance to SGHF (km)	Elevation (m)	Relief in 2.5 km radius (m)	Analysis type/ No. of aliquots	Cooling age ±1σ	Est. bulk T_c (°C)	Topography λ_x/ Δ_x/ z_0/ (km)	Depth to T_c (km)	Local geothermal gradient (°C/km)	Exhumation rates deflected/flat (mm/yr)	Average exhumation rate ±1σ (mm/yr)	Source
81	36.2018	10.40	847	909	AHe	7.30	65.0	20.0/	1.53	31.0	0.29	0.35	4
VW1	-121.5729				1	±0.90		0.50/ 0.30			0.41	±0.061	
83	36.2019	8.48	848	798	AHe	11.50	61.9	20.0/	1.52	30.2	0.18	0.22	4
VW3	-121.6001				2	±2.80		0.50/ 0.30			0.25	±0.074	
84	36.2120	13.27	432	868	AHe	9.30	63.3	20.0/	1.72	34.7	0.20	0.23	4
VW4	-121.5427				5	±3.50		0.50/ 0.30			0.27	±0.125	
86	36.3823	18.58	475	617	AHe	30.10	55.5	17.0/ 0.58/	1.60	31.6	0.06	0.07	4
VW6	-121.6421				5	±4.60		0.30			0.08	±0.015	
89	36.3426	10.54	1148	909	AHe	10.00	62.9	11.0/ 0.55/	1.50	27.2	0.23	0.28	4
VW9	-121.7173				5	±1.80		0.35			0.32	±0.071	
						Apatite fission track							
91	36.3705	28.94	1031	700	AFT	39.50	104.6	13.0/	2.94	30.3	0.09	0.10	6
DR1748BA	-121.4882				–	±4.00		0.28/ 0.50			0.11	±0.014	
92	36.4083	10.58	681	876	AFT	60.00	100.7	15.0/ 0.47/	2.93	31.7	0.05	0.06	6
DR1937A	-121.7944				–	±6.00		0.42			0.07	±0.009	
93	36.4878	8.07	413	584	AFT	12.00	114.4	6.0/ 0.30/	2.89	34.4	0.28	0.31	6
DR1981A	-121.9208				–	±1.20		0.0			0.35	±0.044	
94	36.1665	22.20	775	1209	AFT	74.00	98.8	15.0/ 0.65/	2.88	29.4	0.05	0.05	6
152064BA	-121.3557				–	±7.00		0.28			0.05	±0.007	

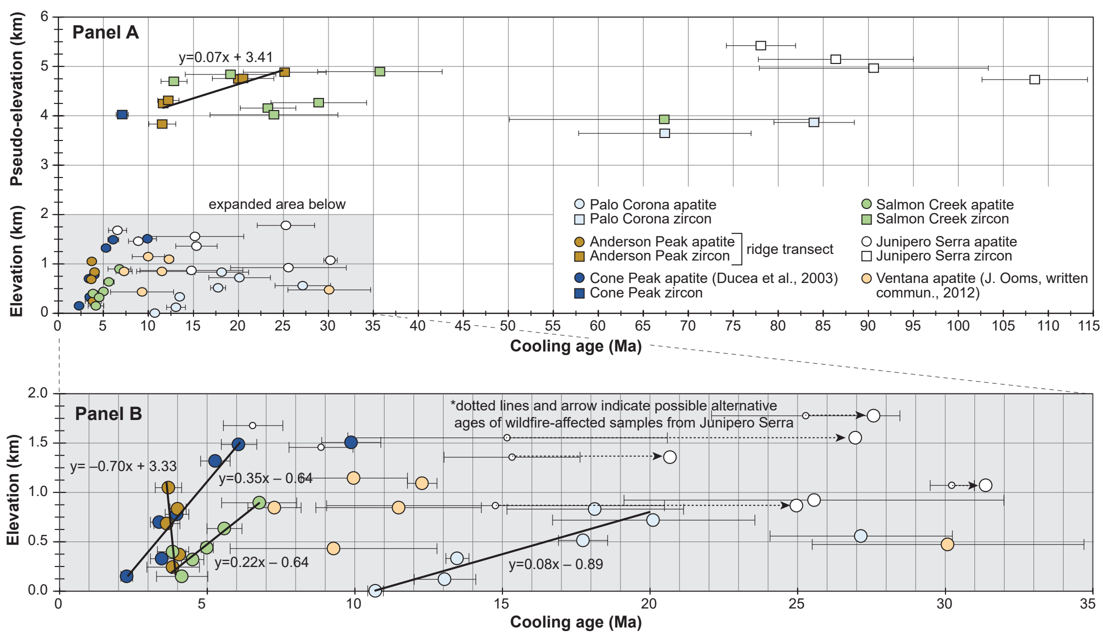

Figure 3-4. Age-elevation relationships for apatite and zircon (U-Th)/He suggest exhumation began in the late Miocene between ~6 and 12 Ma. **Panel A** shows ages for both minerals. Elevations for zircon samples are shifted upwards to account for their higher closure temperature. In general, pre-15 Ma zircon ages are highly variable, show little trend with topography, and likely represent sampling from either above or within the partial retention zone. The youngest zircon samples are found at the lowest elevation and may reflect more rapid late-Miocene cooling. **Panel B** shows the apatite samples in more detail, with linear regressions for vertical transects discussed in the text; regression parameters can be found in Table 3-1. The alternative ages for some samples from the Junipero Serra transect are discussed in the text

Ma along the higher ridgeline. We analyzed only the lowest two samples for zircon, and these yielded late Cretaceous cooling ages.

Rates of exhumation

The presence of widely varying age—and high within-sample age dispersion—above ~500 m on an age-elevation plot suggest the presence of an exhumed partial retention zone (Fig. 3-4). Low within-sample dispersion and monotonic changes in age with elevation below 500 m suggest that the lower part of the transect has been exhumed from beneath the PRZ. The break-in-slope between the fossilized PRZ and more-rapidly cooled samples is sometime in the mid to late Miocene, between ~15–20 Ma. Age-elevation relationships (AER) indicate ~0.08 mm/yr of apparent exhumation during the mid to late Miocene (Table 3-3). Exhumation rates of ~0.14 mm/yr since 10.7 Ma are needed to exhume the youngest samples and are nearly double the older rates. Exhumation rates calculated for individual samples are 0.08–0.17 mm/yr.

ANDERSON PEAK

Overview

The Anderson Peak transect begins near sea level at Julia Pfeiffer-Burns State Park and ascends to nearly 1,200 m elevation at the top of Anderson Peak. The lowest-most sample (ID-48) is from a rounded granitic boulder in the unnamed Cretaceous conglomerate of Hall (1991), located SW of the Sur fault, a likely strand of the SGHF (Dickenson et al., 2005). The remainder of samples are from garnetiferous charnockitic tonalite and quartzofeldspathic gneiss of the Coast Ridge belt (Compton, 1960; Ross, 1976); the tonalite has an emplacement ages of ~98–99 Ma (Mattinson, 1978). Apatite cooling ages are 3.7–4.1 Ma between 250–1050 m elevation; zircon ages are 11.5–12.2 Ma below 250 m elevation and increase steadily to ~25 Ma at the highest elevation (Fig. 3-4; Table 3-2). The lowest-most sample (ID-48) did not yield apatite, and its zircon cooling age (~16.4 Ma; Table 3-2) is much older than nearby and higher samples from the NE side of the Sur fault.

Rates of exhumation

The apatite AER for this transect is vertical to reversely dipping (Fig. 3-4) and suggests either: 1) changes in surface relief since the mean age of the system that are similar in magnitude to the deflection of isotherms (e.g. Braun, 2002a), or 2) very rapid late Miocene to Pliocene

Table 3-3. Estimates of exhumation rate for steep transects along the coast of the Santa Lucia range using age-elevation relationships (AER), individual sample exhumation rates, and paired-sample estimates.

			AER estimates			Post-apatite estimates			Paired-sample estimates		
Transect	**Age range (Ma)**	**Exh. rates from ind. samples (mm/yr)**	**AER exh. rate (mm/yr)**	**AER intercept (km)**	**R^2**	**Age of lowest sample ±1σ (Ma)**	**Ind. sample exh. estimate (mm/yr)[e]**	**AER exh. estimate (mm/yr)[d]**	**Age range (Ma)**	**Exhumation rate (mm/yr)[f]**	**Sample**
					Apatite (U-Th)/He						
Palo Corona[a]	10.7–20.1	0.08–0.17	0.08	-0.89	0.875	10.7 ±0.3	0.16–0.18	0.14	10.7–67.4	0.05–0.07	AS046
Anderson Peak	3.7–4.1	0.54–0.79	-0.70	3.33	0.1622	3.9 ±0.9	0.39–0.71	–––	4.1–11.7	0.43–0.48	AS024
Cone Peak[b]	2.3–6.1	0.51–0.95	0.35	-0.64	0.932	2.3 ±0.1	0.88–1.02	0.89	2.3–7.1	0.58–0.72	AS057, DCONE1
Salmon Creek	3.9–6.8	0.38–0.58	0.22	-0.64	0.831	4.2 ±0.9	0.34–0.52	0.47	5.6–12.8	0.43–0.58	AS029
					Zircon (U-Th)/He						
Palo Corona	67.4–84.0	0.07–0.08	–––	–––	–––	–––	–––	–––			
Anderson Peak	11.5–25.1	0.27–0.49	0.07	-3.41	0.927	11.8 ±1.2[c]	0.42–0.52[c]	0.44–0.54			
Cone Peak	7.1	0.75	–––	–––	–––	–––	–––	–––			
Salmon Creek	12.8–67.3	0.09–0.46	–––	–––	–––	–––	–––	–––			

[a] AER does not include sample AS042

[b] AER does not include sample D_CONE_7

[c] Calculated using average of youngest three ages, ID-24, 25, 65

[d]Estimated using the zero-intercept method, average closure temperature for all samples in the transect, and assuming a geotherm of 30°C/km

[e] Estimated using the closure temperature of the youngest sample, a geotherm of 30°C/km, and the 1σ uncertainty in age

[f] Estimated using paired apatite and zircon ages from the indicated sample

exhumation (e.g. Spotila et al., 1998). Using plausible values of α (Table 3-1), modern relief would have to be a small fraction (0.2–0.4) of its early Pliocene value if the over-steepened AER were caused by changes solely in surface relief. A more-likely scenario is a rapid change in exhumation rate accompanied by modest changes in surface relief. Such punctuated exhumation has been invoked to explain vertical AERs in narrow fault blocks along the San Andreas fault (Spotila et al., 1998). Apparent exhumation rates calculated from individual apatite samples are 0.54–0.79 mm/yr.

The AER for zircon records a more-simple cooling history (Fig. 3-4), with 0.07 mm/yr of exhumation during the mid to late Miocene (Table 3-3). This rate is nearly identical to that obtained over a similar time period from apatite of the Palo Corona transect. Regardless of the complexities in the Pliocene exhumation history, average exhumation rates ~0.47–0.56 mm/yr are required since the late Miocene to bring the zircon samples to the surface (Table 3-3).

SALMON CREEK

Overview

The Salmon Creek transect begins at sea level and reaches heights of 980 m near Lions Peak (Fig. 3-2). The lowest sample, taken at a beach cove, is from a brown, indurated, coarse-grained arkosic sandstone with stringers and beds of finer-grained mudstone and muddy sandstone. The arkose was penetratively brecciated and fractured to the northeast, and greenstone and serpentinite were found upstream of the damaged rock. The most-northeastward strand of the SGHF at Ragged Point, 4 km to the SE, projects into this area (Graymer et al., 2014) and based on our mapping during sample collection, likely separates the metavolcanic block on the NE from the sampled arkose on the SW. A strand of the SGHF was mapped in this location at a regional scale by Dibblee (1976). The remainder of the transect samples are from sandstone blocks and slabs within argillitic matrix of the Franciscan mélange (Dibblee and Minch, 2007; Graymer et al., 2014).

Apatite ages range from 3.9–24.6 Ma and zircon ages range from 12.9–87.5 Ma. For both apatite and zircon, the oldest ages within the transect are found at the lowest elevation across the projected trace of a strand of the SGHF. This relationship—of substantially older cooling ages directly SW across strands of the SGHF—is also observed at the base of the Anderson Peak transect and in an equal-elevation transect between Monterey and Big Sur (Chapter 2). The youngest apatite sample NE of the fault strand (ID-33) has a weighted mean age of 3.9 ±0.9 Ma (n=5) but contains two aliquots <2.5 Ma (Appendix B). Zircon ages from the same sample show a nearly bimodal distribution of individual ages, with a population at ~13 Ma (n=4 and as young as 10.3 Ma) and an early Miocene to Eocene population (n=3) (Appendix B). These observations, coupled with a uniformly young zircon sample at higher elevation (ID-29), the generally large within-sample dispersion of zircon ages, and lack of consistent zircon age-elevation relationships all suggest that base of the zircon PRZ may now just beginning to become exhumed.

Rates of exhumation

The apatite AER indicates an apparent exhumation rate of ~0.22mm/yr during the latest Miocene and Pliocene (Fig. 3-4; Table 3-3). The wavelength and amplitude of topography in this area (Table 3-1) suggest that that this rate may be an overestimate if topographic amplitude has not changed since the Pliocene. Apparent exhumation since ~4.2 Ma is estimated at 0.34–0.52 mm/yr; average rates calculated for individual apatite ages are 0.38–0.58 mm/yr. Average apparent exhumation since 13 Ma from zircon ages (using either the young population of sample ID-33 or the entire sample of ID-29) is ~0.4 mm/yr.

JUNIPERO SERRA

Overview

The Junipero Serra transect begins near Indians Ranch in the central part of the Santa Lucia range (Fig. 3-2); the lowest sample is from ~868 m elevation and the transect ascends to the top of Junipero Serra Peak at 1780 m elevation (the highest peak in the range). Rocks in the transect are the porphyritic granodiorite and quartz diorite of the Bear Mountain and Junipero Serra Peak plutons, and quartzofeldspathic gneiss (Ross, 1976); garnets, in euhedral grains up to several mm and in rare clots up to 1 cm were observed in the gneiss and in aplite dikes throughout the transect. A fault across the transect near sample ID 10 is depicted on some maps (e.g. Dibblee, 1974; 1979) but is placed south of our transect on the most recent compilation (Rosenberg and Wills, 2016).

Apatite ages range from 6.6 Ma to 30.2 Ma, lack a clear age-elevation relationship, and have large within-sample age dispersion (Fig. 3-4; Table 3-2). The presence of much younger samples at higher elevation than older samples is difficult to interpret and most samples appear to contain two distinct populations—an older, typically mid Miocene to Oligocene population—and a younger <12 Ma population. We suspect that the young population of ages is not geologically meaningful, but is the result of resetting during wildfire. The Junipero Serra area experienced a large wildfire in 2008 and although we tried to collect samples from areas that would have been shielded from the fire, it is possible that the heating from that event has reset some of the apatite grains; the youngest ages are from an area that experienced the greatest fire intensity. There is no correlation between young ages and grain geometry that could be used to screen for reset ages. A simple screening for 'too young' ages is unsatisfactory because it is impossible to know if the remaining analyses are also too young because of resetting. With these difficulties in mind, we provide a tentative estimate of some samples from this transect by simply removing ages that fall far outside of the oldest ages and consider the resulting age to be a lower estimate of the actual sample cooling age (Fig. 3-4; Appendix B).

Rates of exhumation

We do not consider exhumation estimates from the apatite ages to be robust enough to indicate anything more than late Oligocene through mid-Miocene cooling. Zircon ages are not affected by wildfire in the same way as apatite because of their different diffusion kinetics (Reiners et al., 2004). Ages vary from ~78 to 108 Ma, and are the oldest within the Santa Lucia range. The oldest zircon (U-Th)/He ages are similar to—and nearly overlap—the 117 ±12 Ma Rb-Sr age for the Bear Mountain and Junipero Serra Peak plutons (Everenden and Kistler, 1970). The old cooling ages are difficult to explain considering substantial evidence for rapid cooling of most plutonic and metamorphic rocks in the range during the late Cretaceous (Naeser and Ross, 1976; Mattinson, 1978; Kidder and Ducea, 2006). Equally puzzling is the inverted age-elevation relationship that indicates younger cooling at higher elevations. There are no age-eU correlations (e.g. Guenthner et al., 2013) that could be used to explain this relationship (Table 3-2; Appendix B).

COASTAL SAMPLES

A single sample (ID-57) of quartzofeldspathic gneiss from the Coast Ridge belt (Ross, 1976) was collected just NE of the major bounding fault with Franciscan rocks at the base of the Cone Peak transect of Ducea et al. (2003). Although insufficient apatite was recovered to replicate the young ages reported by Ducea et al. (2003), the sample yielded a 7.1 ±0.7 Ma zircon cooling age. This age is identical to a 7.1 ±0.5 Ma (n=14) zircon (U-Th)/He age from metasandstone in this area reported by Lori (2016), although the exact location of her sample was not provided. These zircon ages are the youngest in the entire range and indicate apparent exhumation rates of ~0.75 mm/yr since the late Miocene. The youngest apatite age from the

Ducea et al. (2003) transect is 2.2 Ma and suggests similar exhumation rates of 0.88–1.02 mm/yr (Tables 3-2 and 3-4).

Three samples from charnockitic plutonic rocks between fault strands of the SGHF near Big Creek (ID-61, 62, and 64) yielded zircon cooling ages of 8.0–15.8 Ma. The youngest sample (8.0 ±1.0) is from a narrow fault-bound sliver of Salinian plutonic and metamorphic rock within Franciscan mélange (Hall, 1991; Rosenberg and Wills, 2016) and suggests an average exhumation rate of 0.56–0.82 mm/yr, similar to rates a few km to the south at the base of the Cone Peak transect. The remaining two show little variation in age with elevation (150–488 m) and are within discrete fault blocks NE of the main fault separating Franciscan mélange from Salinian rocks (Rosenberg and Wills, 2016). These two samples have apparent exhumation rates of ~0.38 mm/yr (Table 3-2).

RANGE-INTERIOR SAMPLES

One sample (ID-56) was collected on the northeast side of the Santa Lucia range, in a quarry near Salinas, from the ~81 Ma (Kistler and Champion, 2001) garnetiferous quartz monzonite of Pine Creek (Ross, 1976). The sampled location lies several km structurally above the schist of the Sierra de Salinas and is overlain along a nonconformity several km to the north by Miocene and Plio-Pleistocene units (Clark et al., 2001). The apatite cooling age (65.0 ±5.8 Ma) is the oldest in the range and close to the zircon cooling age (67.5 ±3.4 Ma). These ages indicate very rapid cooling in the late Cretaceous (~1.5 mm/yr between 65 and 67 Ma), possibly associated with unroofing of the underlying schist of Sierra de Salinas (Chapman et al., 2010).

Several samples from the interior part of the range were collected and analyzed by J. Ooms and C. Gallagher (UCSC, written commun., 2012) within quartz diorite, granodiorite, and quartzofeldspathic gneiss (Ross, 1976). Apatite cooling ages from these samples indicate late Miocene cooling at high elevation near Uncle Sam Mountain (ID-80 and 89), late Miocene cooling in the high-elevation headwaters of Arroyo Seco near Black Cone Peak (ID-81–84), and Oligocene cooling near Cachagua (ID-86) (Table 3-2).

SPECTRAL ANALYSIS

Results from spectral analysis of apatite and zircon in a 12-km-wide by 90-km-long swath are shown in Figure 3-5. The frequency response function at short wavelength of all apatite

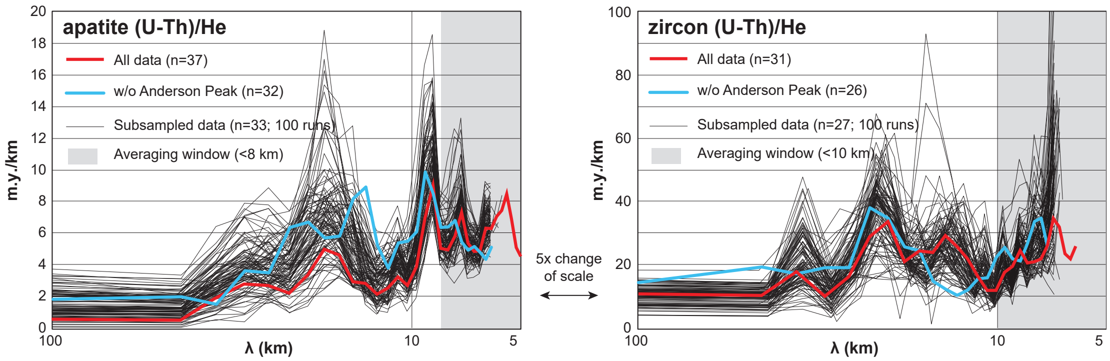

Group	Mean age (Ma)	Asymptotic gain (m.y./km)	Mean gain <8 km	Relative relief change (β)	Mean exhumation rate (km/m.y.)	Mean age (Ma)	Asymptotic gain (m.y./km)	Mean gain <10 km	Relative relief change (β)	Mean exhumation rate (km/m.y.)
All data	9.05	1.13	4.61	1.3	0.22	30.01	14.39	21.11	3.1	0.05
w/o Anderson Peak	9.86	0.54	5.45	1.1	0.18	32.34	15.80	21.45	3.8	0.05

Figure 3-5. Results from spectral analysis of age-elevation relationships from apatite and zircon (U-Th)/He thermochronometry along a ~12 km-wide swath adjacent to the SGHF. Gain values at short wavelength indicate the inverse of the mean exhumation rate (Braun, 2002b). The value β is a measure of the relief generation since the average age of the system and uses the ratio between the asymptotic gain at long wavelength (G_l) and the short-wavelength gain (G_s) in the form $\beta=(1-G_l/G_s)-1$. Apatite data suggest that, when analyzed together, relief has increased since ~9 Ma and average exhumation is ~0.2 mm/yr. Zircon data indicate a higher proportion increase in relief since ~30 Ma, but with lower long-term rates.

data suggests an exhumation rate of ~0.22 mm/yr and an ~30% increase in relief since ~9 Ma; excluding the somewhat-anomalous Anderson Peak data changes this result slightly, but is still within the envelope of subsampled model runs. Analysis of zircon data suggest an average exhumation rate of ~0.05 mm/yr and >300% increase in relief since ~30 Ma. To a first order, the amount of exhumation indicated by the zircon analysis (~1.5 km) can be completely explained by the exhumation indicated by the apatite analysis (~1.9 km). Given that relief in the analyzed swath is presently ~1,200 m, it suggests relief of ~900 m in the late Miocene and ~350 m in the Oligocene.

METRICS OF EROSION AND DRAINAGE EVOLUTION

We present the results of five catchment-averaged geomorphic metrics (Fig. 3-6) to understand the general response of the Santa Lucia range to the processes of uplift and erosion. We then examine the map-pattern and profile results of our χ and ksn analysis to understand the spatial variation in these values. Data for each drainage basin are provided in Table 3-4 and the location of basins can be found on Figure 3-14. Data from the San Gabriel Mountains are provided for comparison and are from DiBiase et al. (2010).

Table 3-4. Catchment-mean values of geomorphic metrics, exhumation rate, and denudation rate for catchments >5 km^2 in the Santa Lucia range. ^{10}Be cosmogenic denudation rates from H. Young (Stanford University, written commun., 2016). Basins with a 'b' and those with area <5 km^2 denote sub-basins used in the estimate of denudation rate and are included for comparison.

Map ID	Lat. Long. WGS84	Dist. to coast (km)	Drainage area (km^2)	Mean annual precipitation ±1σ (mm/yr)	Mean value of relief in 2.5-km radius ±1SD (m)	Mean hillslope angle ±1SD (°)	Mean ksn ±1σ (m^1)	Mean ksn (m$^{0.9}$)	Mean exhumation rate ±1σ (mm/yr)	^{10}Be cosmogenic denudation rate ±1σ (mm/yr)
1	36.6717 -121.7898	33.3	16.6	373 ±2	90 ±29	3.1 ±2.8	16 ±4	12	-0.12 ±0.009	– – –
2	36.6220 -121.7863	30.0	17.3	373 ±11	160 ±30	5.5 ±3.5	35 ±12	25	-0.10 ±0.009	– – –
3	36.6232 -121.8146	28.1	8.7	383 ±6	162 ±15	4.1 ±2.6	48 ±10	33	-0.10 ±0.005	– – –
4	36.5833 -121.8078	25.7	50.0	415 ±22	250 ±76	9.1 ±7.6	41 ±5	29	-0.07 ±0.023	– – –
5	36.5873 -121.8793	21.1	14.0	446 ±53	253 ±61	7.9 ±6.9	25 ±5	18	-0.05 ±0.020	– – –
6	36.5793 -121.8864	20.1	10.1	469 ±52	291 ±45	11.5 ±8.3	27 ±4	20	-0.03 ±0.016	– – –
7	36.4272 -121.6820	23.1	659.7	692 ±216	632 ±177	22.4 ±10.6	144 ±4	88	0.07 ±0.068	0.09 ±0.01
8	36.4861 -121.8696	14.5	36.9	662 ±122	598 ±81	23.1 ±9.4	117 ±9	73	0.11 ±0.032	– – –
9	36.4779 -121.9033	11.6	8.6	749 ±77	633 ±69	27.2 ±9.6	144 ±14	87	0.17 ±0.024	0.07 ±0.01
10	36.4351 -121.8834	9.9	7.2	971 ±211	778 ±97	28.7 ±8.5	199 ±34	117	0.27 ±0.056	– – –
11	36.4139 -121.8588	10.1	27.5	1142 ±263	794 ±91	27.7 ±8.8	221 ±12	129	0.27 ±0.060	0.20 ±0.01
12	36.3855 -121.8464	8.9	13.8	1150 ±272	803 ±145	26.1 ±8.6	201 ±18	118	0.32 ±0.061	– – –
13	36.3657 -121.8429	7.7	29.4	1037 ±276	824 ±129	26.0 ±8.8	200 ±22	118	0.40 ±0.101	0.09 ±0.02
14	36.3270 -121.7895	8.6	104.1	1069 ±184	913 ±144	29.9 ±9.2	179 ±9	107	0.38 ±0.170	0.27 ±0.02
15	36.2490 -121.7061	8.7	153.2	1091 ±127	922 ±151	30.0 ±10.0	187 ±10	111	0.33 ±0.162	0.70 ±0.11
16	36.1931 -121.6823	6.3	9.7	1121 ±76	1116 ±88	30.5 ±8.1	312 ±25	176	0.56 ±0.068	0.35 ±0.02
17	36.1387 -121.6141	7.1	11.0	1093 ±86	1088 ±120	29.5 ±8.7	368 ±44	204	0.50 ±0.087	0.23 ±0.02
18	36.0913 -121.5556	7.7	57.8	1138 ±132	1002 ±153	29.4 ±8.7	308 ±25	174	0.46 ±0.117	0.21 ±0.01
19	36.0328 -121.5064	6.9	22.1	1090 ±93	1234 ±141	32.3 ±8.8	321 ±28	180	0.61 ±0.108	0.28 ±0.02
20	35.9919 -121.4582	7.3	16.6	1023 ±74	955 ±93	28.5 ±9.6	282 ±26	161	0.43 ±0.085	0.28 ±0.02
21	35.9490 -121.4467	5.0	16.0	976 ±106	948 ±72	28.0 ±8.8	242 ±15	140	0.45 ±0.069	– – –
22	35.9097 -121.4089	4.8	42.3	977 ±91	796 ±91	26.4 ±9.0	238 ±16	138	0.34 ±0.109	– – –
23	35.8743 -121.3925	3.4	10.9	1040 ±104	926 ±102	26.3 ±9.1	331 ±95	185	0.44 ±0.097	– – –
24	35.8586 -121.3736	3.6	11.3	1100 ±75	897 ±146	26.0 ±9.0	328 ±41	184	0.44 ±0.103	– – –

Map ID	Lat. Long. WGS84	Dist. to coast (km)	Drainage area (km^2)	Mean annual precipitation ±1σ (mm/yr)	Mean value of relief in 2.5-km radius ±1SD (m)	Mean hillslope angle ±1SD (°)	Mean ksn ±1σ (m^1)	Mean ksn ($m^{0.9}$)	Mean exhumation rate ±1σ (mm/yr)	^{10}Be cosmogenic denudation rate ±1σ (mm/yr)
25	35.8362 -121.3375	4.5	22.0	1069 ±96	829 ±135	26.2 ±8.9	288 ±41	164	0.42 ±0.128	– – –
26	35.7951 -121.2663	6.5	92.9	846 ±77	665 ±98	23.5 ±8.6	149 ±12	90	0.29 ±0.136	– – –
27	35.7240 -121.1946	6.3	112.7	821 ±104	647 ±125	20.3 ±8.5	123 ±10	76	0.29 ±0.152	– – –
28	35.6787 -121.2185	1.5	18.7	612 ±35	344 ±121	11.7 ±7.9	41 ±8	28	0.13 ±0.278	– – –
29	35.6697 -121.1793	3.5	9.1	675 ±85	458 ±100	14.0 ±8.3	78 ±23	51	0.27 ±0.268	– – –
30	35.6633 -121.1444	5.5	18.7	752 ±103	569 ±140	19.0 ±7.7	87 ±17	56	0.29 ±0.249	– – –
31	35.6552 -121.1006	8.0	35.0	846 ±147	674 ±195	19.6 ±8.3	155 ±21	94	0.34 ±0.222	0.35 ±0.03
32	35.6202 -121.0456	9.3	83.5	754 ±149	569 ±193	18.0 ±8.3	114 ±12	71	0.25 ±0.255	– – –
33	35.5587 -121.0057	7.7	123.8	603 ±135	389 ±188	15.9 ±9.0	54 ±6	36	0.07 ±0.247	– – –
34	35.5076 -120.9599	7.2	52.2	546 ±112	341 ±124	16.5 ±8.3	42 ±5	29	-0.01 ±0.170	– – –
35	35.4901 -120.9166	9.0	33.9	505 ±54	320 ±71	16.8 ±7.4	37 ±3	26	-0.06 ±0.021	– – –
36	35.4877 -120.8523	13.3	53.6	616 ±98	427 ±85	19.9 ±9.0	74 ±9	48	0.20 ±0.247	– – –
37	35.4491 -120.8581	10.2	8.6	482 ±48	344 ±105	16.0 ±6.9	40 ±4	28	-0.05 ±0.031	– – –
38	35.4533 -120.8104	13.8	39.6	612 ±118	422 ±96	19.0 ±8.9	77 ±13	50	0.16 ±0.218	– – –
39	35.4222 -120.7847	13.4	65.3	614 ±132	413 ±136	17.4 ±9.8	68 ±11	45	0.14 ±0.235	– – –
40	35.3603 -120.7454	11.7	115.5	601 ±148	454 ±147	14.1 ±9.2	63 ±4	42	0.05 ±0.197	– – –
41	36.6142 -121.7379	32.7	24.3	389 ±11	212 ±26	11.6 ±6.7	42 ±5	29	-0.08 ±0.008	– – –
42	36.5530 -121.6928	31.4	109.8	504 ±87	457 ±150	17.5 ±9.3	85 ±10	54	-0.01 ±0.044	– – –
43	36.5580 -121.6218	36.6	15.9	564 ±96	797 ±135	23.1 ±10.4	143 ±17	87	0.09 ±0.040	– – –
44	36.5505 -121.5920	38.1	8.1	527 ±115	801 ±191	21.3 ±10.3	133 ±16	82	0.09 ±0.056	– – –
45	36.5114 -121.5554	37.8	13.2	539 ±50	888 ±89	30.4 ±9.8	155 ±19	93	0.11 ±0.026	– – –
46	36.4943 -121.5284	38.4	7.7	488 ±79	836 ±181	24.0 ±14.2	106 ±13	66	0.10 ±0.053	– – –
47	36.4584 -121.4866	38.7	11.1	461 ±138	704 ±313	18.4 ±14.6	111 ±13	69	0.06 ±0.092	– – –
48	36.4267 -121.4754	37.2	9.1	561 ±123	955 ±235	27.4 ±12.7	199 ±24	117	0.13 ±0.069	– – –
49	36.3945 -121.4326	37.8	10.9	568 ±133	906 ±172	23.8 ±11.8	197 ±24	116	0.12 ±0.050	– – –
50	36.3733 -121.3762	40.2	29.8	427 ±149	651 ±324	15.2 ±12.4	94 ±11	59	0.04 ±0.096	– – –
52	36.2222 -121.2442	38.5	28.4	467 ±73	431 ±80	18.7 ±11.3	79 ±9	51	-0.02 ±0.024	– – –

Map ID	Lat. Long. WGS84	Dist. to coast (km)	Drainage area (km^2)	Mean annual precipitation ±1σ (mm/yr)	Mean value of relief in 2.5-km radius ±1SD (m)	Mean hillslope angle ±1SD (°)	Mean ksn ±1σ (m^1)	Mean ksn ($m^{0.9}$)	Mean exhumation rate ±1σ (mm/yr)	^{10}Be cosmogenic denudation rate ±1σ (mm/yr)
53	36.1912 -121.2275	37.4	34.6	499 ±73	477 ±38	22.4 ±9.8	90 ±11	57	-0.01 ±0.012	– – –
54	36.1563 -121.1999	36.8	48.6	464 ±105	469 ±112	20.5 ±10.4	85 ±10	54	-0.01 ±0.034	– – –
55	36.1174 -121.1625	36.6	80.7	457 ±99	413 ±131	18.8 ±10.6	66 ±8	43	-0.03 ±0.039	– – –
56	36.1161 -121.1055	40.5	23.3	366 ±47	296 ±127	12.0 ±11.6	37 ±4	26	-0.06 ±0.038	– – –
57	36.0847 -121.0734	40.4	39.5	379 ±81	314 ±147	14.3 ±11.5	44 ±5	30	-0.06 ±0.043	– – –
58	36.0485 -121.0610	38.7	24.4	428 ±88	419 ±143	19.1 ±12.2	75 ±9	49	-0.03 ±0.042	– – –
59	36.0494 -121.0187	41.7	28.2	353 ±62	309 ±123	12.5 ±10.6	46 ±6	32	-0.06 ±0.036	– – –
60	36.0387 -120.9941	42.6	14.0	356 ±61	304 ±123	14.5 ±10.9	49 ±6	33	-0.06 ±0.036	– – –
61	36.0166 -120.9883	41.5	21.0	389 ±81	364 ±82	18.1 ±11.1	65 ±8	43	-0.04 ±0.024	– – –
62	35.9953 -120.9722	41.1	19.8	417 ±80	424 ±73	20.3 ±11.0	79 ±10	51	-0.03 ±0.022	– – –
63	35.9763 -120.9406	41.9	8.0	395 ±58	420 ±50	22.4 ±9.6	93 ±11	59	-0.03 ±0.015	– – –
64	35.9623 -120.9272	41.8	11.6	404 ±51	424 ±35	21.9 ±9.3	81 ±10	52	-0.02 ±0.010	– – –
65	35.9044 -120.8724	41.5	7.3	320 ±26	329 ±61	15.8 ±8.3	54 ±6	36	-0.05 ±0.018	– – –
66	35.8929 -120.9130	37.9	116.8	378 ±75	325 ±93	14.0 ±10.3	49 ±6	33	-0.05 ±0.027	– – –
69	35.4834 -120.5794	32.0	1589.1	568 ±121	278 ±140	13.2 ±9.7	45 ±5	31	0.00 ±0.112	– – –
100	36.2380 -121.8130	– – –	< 5.0	– – –	– – –	24.3 ±8.2	– – –	– – –	0.00 ±0.045	0.09 ±0.01
101	36.1610 -121.6670	– – –	< 5.0	– – –	– – –	31.0 ±7.8	– – –	– – –	0.58 ±0.067	0.13 ±0.01
102	36.0450 -121.5840	– – –	< 5.0	– – –	– – –	25.2 ±8.6	– – –	– – –	0.47 ±0.279	0.19 ±0.01
103	35.9890 -121.4950	– – –	< 5.0	– – –	– – –	31.0 ±8.1	– – –	– – –	0.57 ±0.046	0.28 ±0.02
51a	36.2413 -121.4366	26.6	777.7	719 ±221	735 ±229	23.8 ±12.0	153 ±18	92	0.10 ±0.089	0.00 ±0.00
51b	– – –	– – –	– – –	– – –	– – –	26.2 ±10.6	– – –	– – –	0.12 ±0.072	0.23 ±0.02
67a	35.9696 -121.1549	26.6	894.1	545 ±193	385 ±225	15.6 ±11.3	58 ±7	39	-0.02 ±0.090	0.00 ±0.00
67b	– – –	– – –	– – –	– – –	– – –	17.2 ±11.8	– – –	– – –	0.01 ±0.101	0.23 ±0.02
68a	35.8007 -121.0830	19.5	962.9	568 ±195	397 ±165	17.4 ±10.2	61 ±7	40	0.04 ±0.100	0.00 ±0.00
68b	– – –	– – –	– – –	– – –	– – –	25.1 ±10.4	– – –	– – –	0.14 ±0.077	0.20 ±0.02

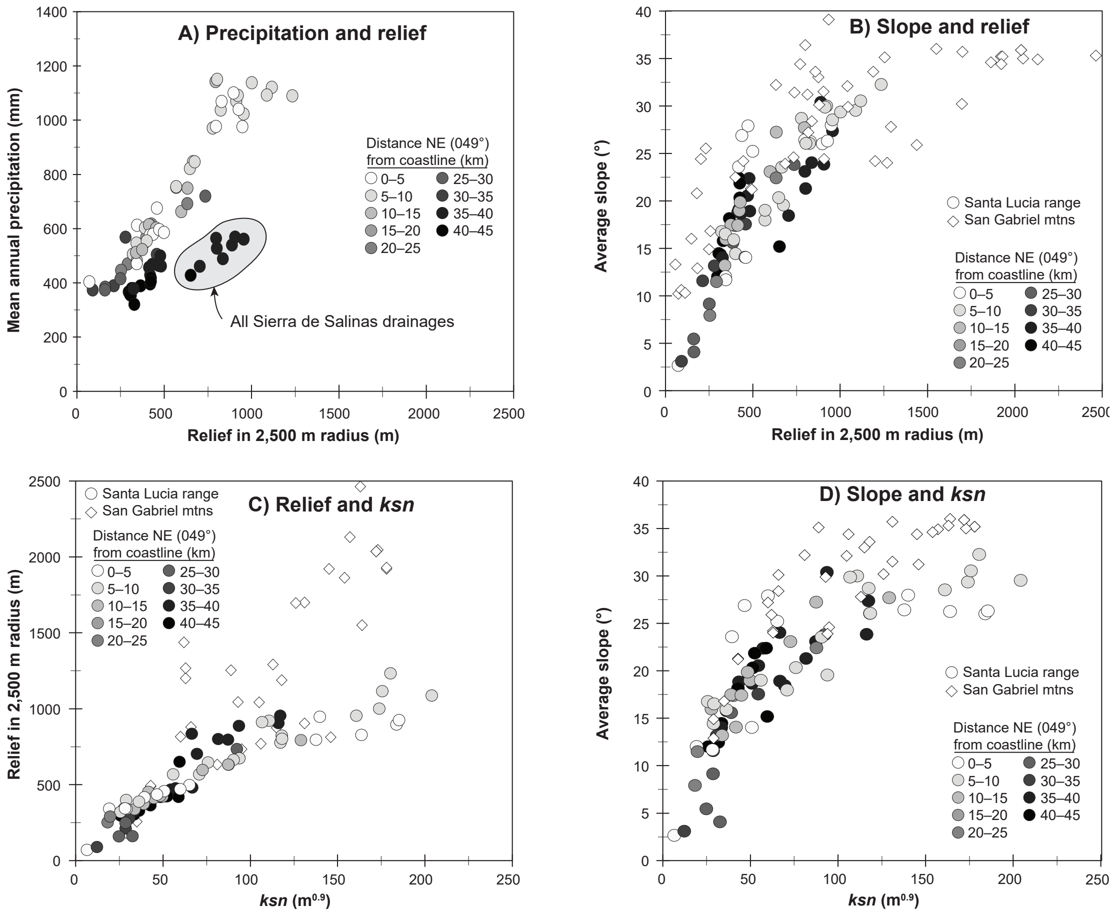

Figure 3-6. Catchment-mean metrics of erosion as a function of distance NE from coastline. Data are available in Table 3-4. **Plot A—**Precipitation, relief, and distance from the coast are all strongly correlated. Precipitation reaches maximum values in the greatest-relief catchments, although the high-relief catchments in the Sierra de Salinas are noTable outliers to this trend. **Plot B—**Relief and slope are well correlated, with a change in behavior suggested at slopes near ~25°. **Plot C—**Relief increases linearly with channel steepness with a possible break-in-slope at ~100 ksn. Values of relief are more dispersed and generally higher in the San Gabriel mountains than in the Santa Lucia range for similar ksn. **Plot D—**Mean slope increases consistently to ksn of ~100 before becoming invariant at values of 25–30°. This invariance is similar in style, but lower in value, to the San Gabriel mountains and suggests a change in erosion processes. Data from the San Gabriel mountains are from DiBiase et al. (2010). Normalized channel steepness index, ksn, is plotted here as $m^{0.9}$ to compare with values reported in DiBiase et al. (2010), but elsewhere is reported as m^1.

RANGE-SCALE VARIATIONS IN SLOPE, RELIEF, PRECIPITATION, AND AREA

The most-robust, and somewhat surprising result of our analysis is that catchment-mean relief—as measured in a 2.5-km window around each pixel and averaged throughout the catchment—has a strong positive correlation with precipitation (Fig. 3-6a), local hillslope angle (Fig. 3-6b), and normalized channel steepness, ksn (Fig. 3-6c). To a first order, this suggests that, regardless of the erosional processes at work, relief in a 2.5-km window is a reliable predictor of all other metrics of erosion in this landscape. This is somewhat surprising in consideration of the range of likely exhumation rates, the varied lithology, and the large differences in source-to-sink gradient between range-interior and coastal fluvial networks.

In detail, however, there are strong NE–SW asymmetries in some of the data. The strongest asymmetry is the disproportionate distribution of precipitation on coastal (SW) drainages and the moderate to weak dependence of hillslope and ksn on location (Fig. 3-6d) might reflect this asymmetry. Another, more subtle aspect of the data is that a single linear fit does not appear to adequately capture any of the relationships. Both ksn and local hillslope angle appear to have a change in behavior near 500–750 m of relief; below this value hillslope angle and ksn increase more steeply. When hillslope angle and ksn are plotted together (Fig. 3-6d), it appears that slope increases quickly below a ksn value of ~100, and may become invariant near 25–30° with increasing ksn.

Our data from the Santa Lucia range generally have relationships between metrics of erosion like the San Gabriel mountains (DiBiase et al., 2010), although their data are more scattered. Notably, there is much greater relief in the San Gabriel mountains and the correlation between relief and hillslope angle is much broader in their data (Fig. 3-6b). The general pattern between ksn and slope is quite similar between the two ranges (Fig. 3-6d), but the Santa Lucia range appears less capable of sustaining the higher hillslope angles observed in the San Gabriel mountains. There, the invariance of hillslope in steep drainages and at high relief is thought to mark a shift from transport-limited to detachment-limited erosional processes (DiBiase et al., 2010). If so, the lower-value transition to invariant behavior in the Santa Lucia range may indicate a lower threshold for detachment-limited processes.

DRAINAGE DIVIDE CHARACTERIZATION USING X

A map of χ values for the Santa Lucia range (Fig. 3-7) shows that several drainage divides have moderate to high mismatches in χ values, the most prominent of which is found along the main coastal divide south of the Big Sur River and north of Salmon Creek. This divide traverses both crystalline rock and Franciscan mélange, and the mismatch is most pronounced where the youngest apatite and zircon cooling ages are found along the coast (Fig. 3-2). South of Salmon Creek, and north along the coastal divide from the Big Sur headwaters, χ values are more balanced. A strong mismatch in χ values is also found along the crest of the Sierra de Salinas. Moderate mismatches in χ are noted along a drainage divide that is subparallel to the RRF near Paso Robles (Fig. 3-7), and in a few scattered locations throughout the range. Because there is such strong spatial variation in rates of rock uplift (see below), it is unlikely that these mismatches can be interpreted as indicating only drainage-divide migration.

PATTERNS OF CHANNEL STEEPNESS

We examine the spatial patterns of channel steepness with a map of ksn (Fig. 3-7), and with a coastal transect of χ plots (Fig. 3-8). Several patterns are immediately obvious from the map distribution of ksn: 1) high values of ksn are localized in a band parallel to the SGHF from the Little Sur River to Salmon Creek, regardless of rock type; 2) south of Salmon Creek, high values of ksn are found in a SE-narrowing zone between the Oceanic fault and fault strands subparallel to the Nacimiento fault; 3) NE of the coastal divide and away from the SGHF, high values of ksn are correlated with crystalline rocks; 4) values of ksn are low SW of the SGHF and where channels are developed on sedimentary rocks away from major fault zones; 5) there is little change in ksn across the Reliz-Rinconada fault.

The coastal transect of χ plots (Fig. 3-8) confirms the general trends from the map (Fig. 3-7), and enhances our resolution on the potential correlation between structures and channel steepness. On the NW, channels have low $M\chi$ where developed on Miocene sedimentary rocks and steepen as the rock type changes and drainages become closer to the SGHF. Low values of $M\chi$ are found along the lowest reaches of 3 drainages that cross strands of the SGHF (13, 14, and 15 on Figs. 3-7 and 3-8); the portion of these drainages NE of the SGHF have much higher values of $M\chi$.

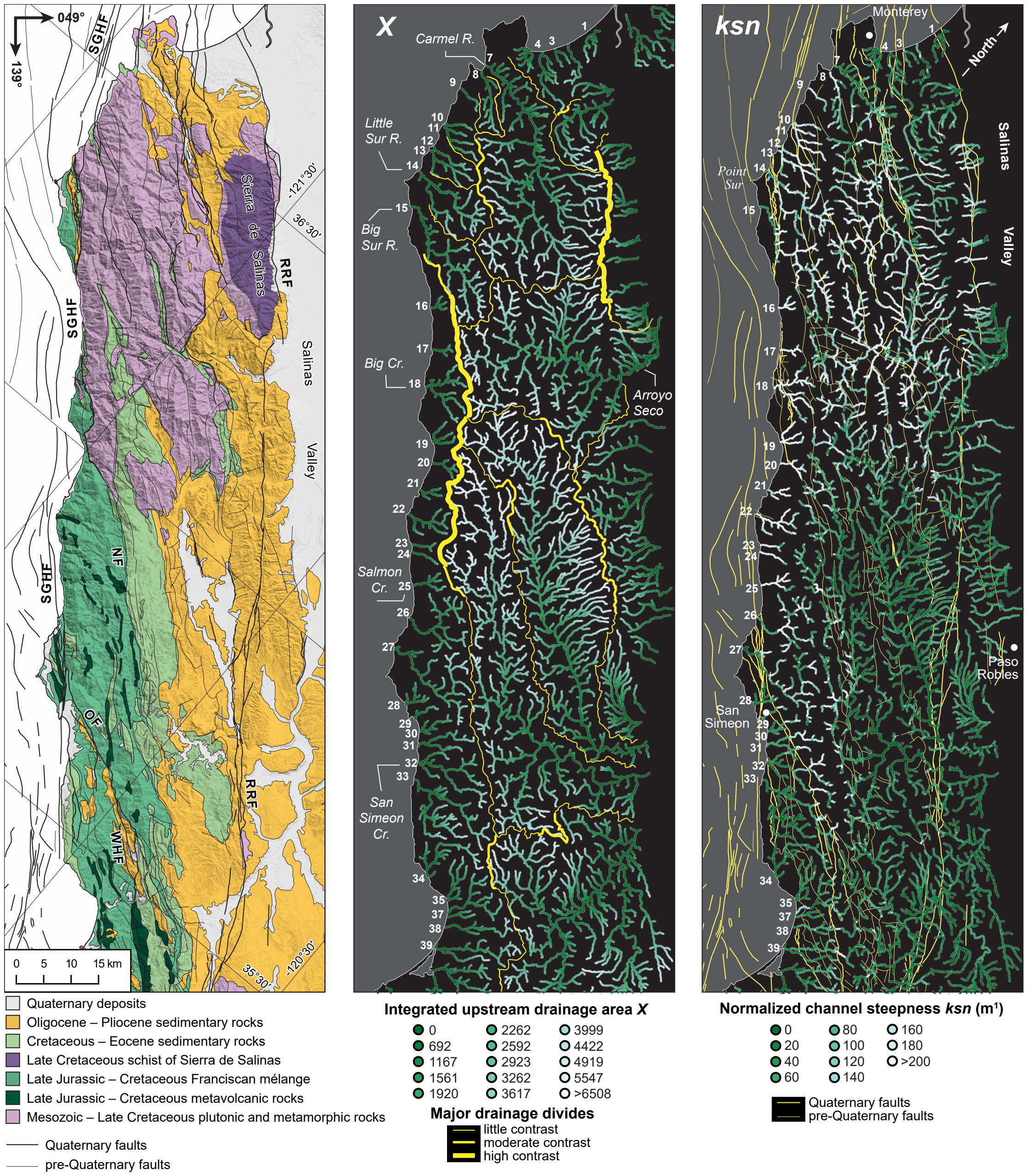

Figure 3-7. Simplified geologic map, values of χ, and values of ksn in the Santa Lucia range indicate that streams are steeper adjacent to the SGHF than elsewhere and that there is locally strong drainage-divide asymmetry. Values of ksn are high in both crystalline rocks and Franciscan mélange along the SGHF, and increase across the Oceanic fault in rocks of similar lithology. Values of ksn also increase SW across a zone of fault strands subparallel to the Nacimiento fault, in a pattern like the post-seismic surface uplift of the 2003 San Simeon earthquake (McLaren et al., 2008). Catchments labeled here are the same as in Fig. 3-7; fault abbreviations same as Fig. 3-1.

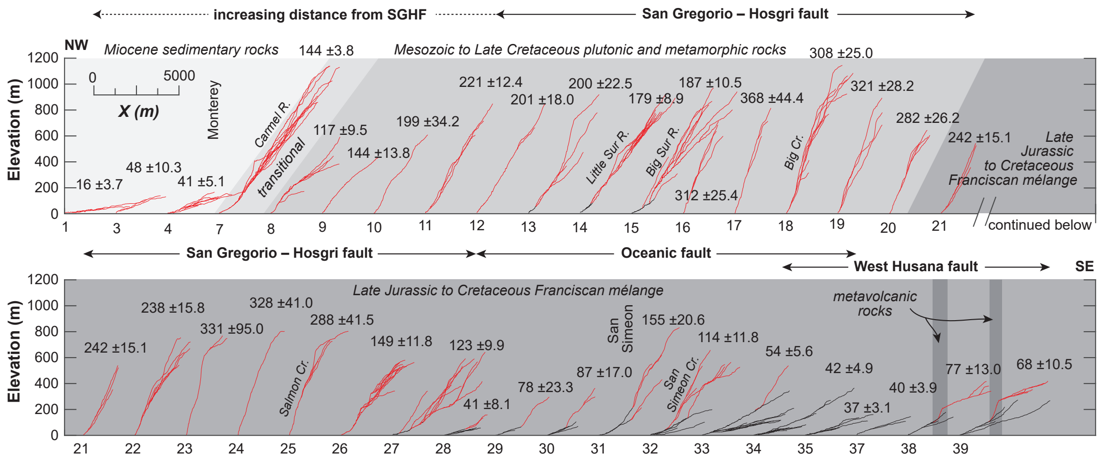

Figure 3-8. Profiles of χ and elevation in a swath along the coast from near Monterey to south of San Simeon. Steeper plots indicate larger uplift-to-erodibility ratios (ksn). Overall, these data suggest increasing uplift with proximity to the SGHF and increasing uplift NE across the Oceanic fault. Each profile is shifted along the axis by a χ-value of 1500; the numbers at the base of each profile indicate its location on Figure 3-13; catchment-mean ksn is indicated at the top of each profile. Red lines indicate profile segments NE of the fault labeled above the profile; black lines indicate profile segments SW of the labeled fault. Except for the slivers of metavolcanic rocks along the West Huasana fault, profiles are steeper across the SGHF and Oceanic faults, even where developed in similar lithologies. Shading and italicized labels indicate dominant lithology.

The change in lithology from crystalline to Franciscan mélange (across the Nacimiento fault) does not appear to substantially affect the values of Mχ; 3 of the 7 steepest drainages are developed on mélange. South of Salmon Creek (25 on Figs. 3-8 and 3-7), values of Mχ decrease substantially, although the dominant lithology does not substantially differ. Here, however, values of Mχ appear to be largely controlled by the Oceanic fault—channels NE of the fault are more steep. The dominant lithology on both sides is Franciscan mélange, although there are local patches of younger sedimentary rocks. Very high values of Mχ along drainages 38 and 39 (Fig. 3-7) separate channels with similar values of Mχ. These steeper segments may be due to uplift along the West Huasana fault, but are more likely the result of local juxtaposition of a narrow band of metavolcanic rocks across fault zone.

DEFORMED MARINE TERRACES

The results of our survey of the lowest-emergent marine terrace at the southeastern end of the Santa Lucia range are shown in Figure 3-9, along with terrace elevations near San Simeon from Hanson et al. (1994) and low-temperature thermochronometry from Salmon Creek. Near Ragged Point, terrace elevations are low SW of the SGHF, highest directly NE of the fault, and

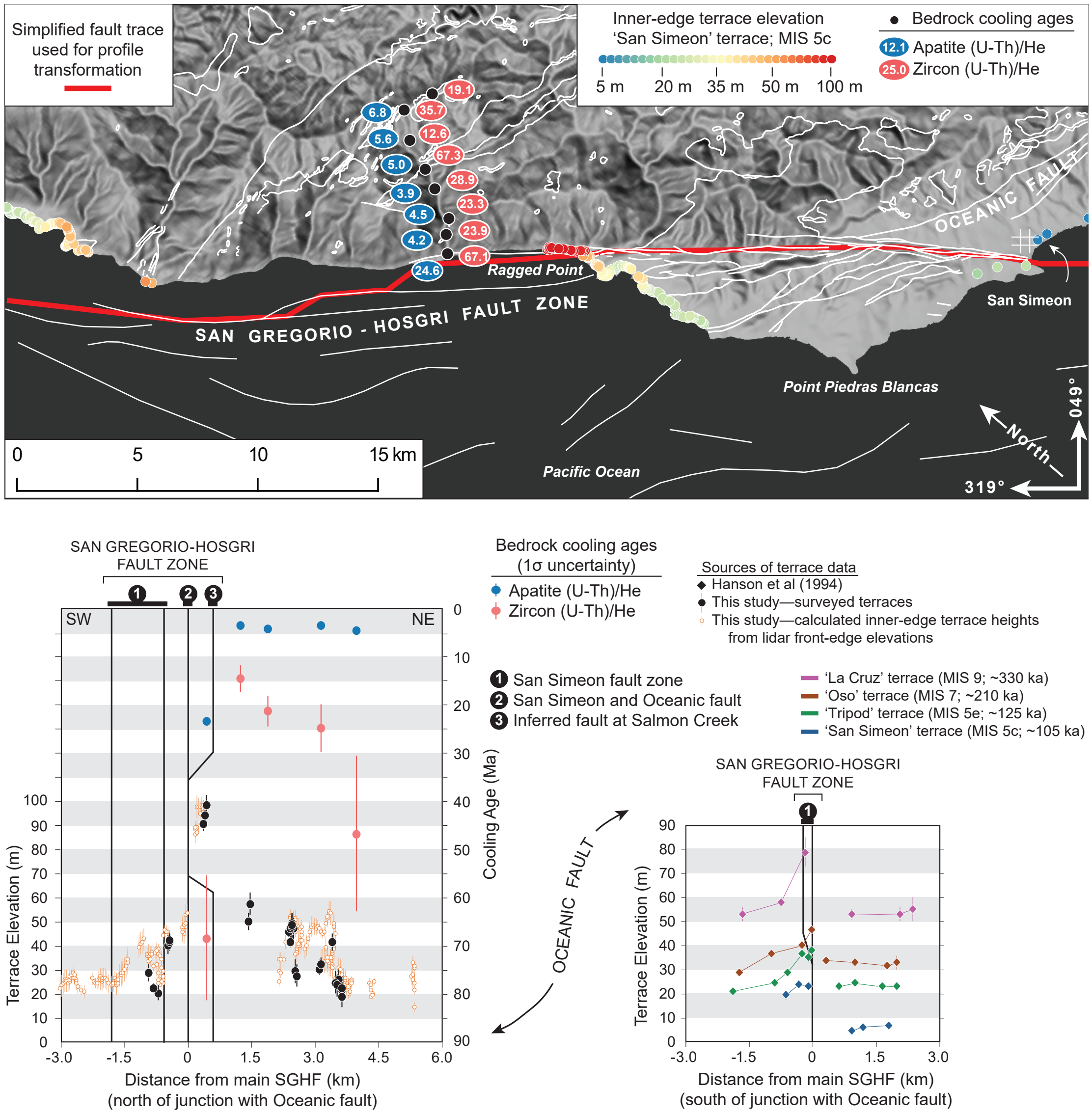

Figure 3-9. Marine terrace elevations and low-temperature thermochronometry near San Simeon indicate that surface uplift and bedrock exhumation are focused NE of the SGHF and Oceanic faults. Terrace data NW of Point Piedras Blancas is from this study and includes surveyed and lidar-based estimates; terrace data near San Simeon are from Hanson et al. (1994). Faults modified from Graymer et al. (2014) and Jennings and Bryant (2010).

decrease gradually in elevation with distance NE of the fault. This pattern of relative elevation change is like that observed between Big Sur and Monterey, 90 km to the NW (Chapter 2), and near Point Año Nuevo, 150 km to the NW (Chapter 1). The pattern of vertical deformation appears to change substantially SE of the junction between the Oceanic and San Simeon fault zones (Fig. 3-9). Near San Simeon, terrace elevations *decrease* to the NE across the San Simeon fault zone (Hanson et al., 1994).

These observations suggest to us that NE-side up vertical deformation may bypass the San Simeon fault zone and be transferred to the Oceanic fault SW of its junction with the SGHF, as suggested by several tectonic models (Lettis et al., 2004; McLaren et al., 2008; Hardebeck, 2010). This interpretation is also consistent with the observed NE increase in M_χ across the trace of the Oceanic fault (Fig. 3-7), higher topographic relief NE of the fault (Fig. 3-1), and known NE-side up co- and post-seismic uplift from the 2003 San Simeon earthquake (McLaren et al., 2008).

DISCUSSION

VARIATIONS IN ESTIMATES OF EXHUMATION RATE

Estimates of exhumation rate are inherently noisy due to uncertainties in the cooling age, closure temperature, and relationship between surface topography and the closure isotherm. In the Santa Lucia range, exhumation rates derived from spectral analysis are the lowest, and rates from individual samples are generally highest (Tables 3-2 and 3-4; Fig. 3-5). We address three possible reasons that may explain these observations below.

CHANGES IN RELIEF

One possibility is that changes in overall topographic relief—coupled with the amplitude of the isothermal surface—have altered the relationship between the free-cooling surface and the closure isotherm. Rates of exhumation derived from AERs can be adjusted for these parameters (Braun, 2002a) using the relief change estimated from spectral analysis (β=1.3 since ~9 Ma) and transect- and rate-specific values of α (Table 3-1). Rates from the Palo Corona and Salmon Creek transect are little affected by this adjustment, but rates from Cone Peak are reduced from ~0.35 to ~0.2 mm/yr. Although it is difficult to perform the same analysis for the Anderson Peak transect, the α and β parameters indicate that the AER is certainly too steep. Together, these data and analyses provide some support for the ~0.2 mm/yr exhumation rate derived from the spectral analysis. In detail, however, the spectral analysis method and the adjustments to the AER rest on the same set of assumptions and do not necessarily constitute independent verification. Additionally, it would require extreme geothermal gradients (>100° C/km) to produce the range of low-elevation apatite cooling ages (as young as 2.2 Ma) with exhumation rates near ~0.2 mm/yr.

SPATIAL GRADIENTS IN ROCK UPLIFT

A more-likely explanation is that the underlying assumptions of both the spectral analysis and AER methods are inadequately met. Both methods aggregate exhumation behavior at large spatial scale into single values of exhumation, and are most applicable to landscapes with nearly uniform uplift and erosion that lack through-going active crustal faults. A good example is the southern Sierra Nevada range where the spectral method has been shown to retrieve known rates of exhumation and relief change (House et al., 1998; Braun, 2002b).

In the Santa Lucia range, patterns in the relative deformation of marine terraces from Monterey to Big Sur (Chapter 2) and northward from Ragged Point (Fig. 3-9) indicate that there is considerably higher rock uplift in a 3-km window NE of the SGHF than at greater distance (Fig. 3-10). In both locations, the terrace elevation increases 3–5x over a 3-km distance; a result that is not tied to age estimates of the terrace. Integrated over several m.y., such a localization of strain would violate the assumption of block

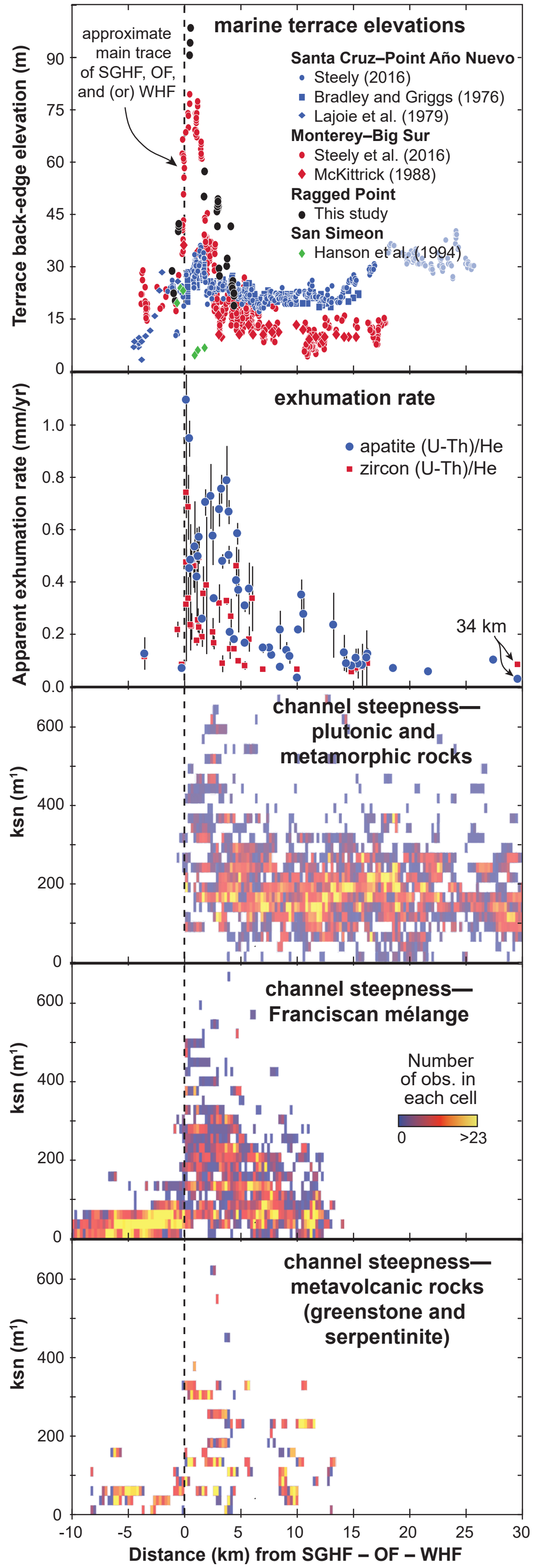

Figure 3-10. Distance and polarity from the San Gregorio–Hosgri, Oceanic, and West Huasana faults are strong predictors of marine terrace elevation, exhumation rate, and normalized channel steepness.

uplift required to use an AER to determine an exhumation rate, and would manifest as decreasing rates of exhumation with distance from the SGHF. Such a pattern is observed in our data where exhumation rates closely mimic the relative change in terrace elevation and are 3–5x higher within 3 km of the fault (Fig. 3-10). These observations indicate that the assumption of block uplift required for spectral analysis is likely unmet at short wavelengths, but may still hold generally true at wavelengths approaching the length of the range.

AMPLITUDE OF CLOSURE ISOTHERMS

Our method of estimating individual-sample exhumation rates does not require any assumption of block uplift and thus likely provides a more-faithful representation of spatial patterns of exhumation than the other two approaches. However, this method does require more assumptions about the thermal structure of the crust than the AER or spectral method. We believe that our method of averaging two estimates of the exhumation rate—one assuming a horizontal closure isotherm and one assuming a closure isotherm that mimics modern topography—dampens the uncertainty in the thermal structure of the crust (Fig. 3-3). Changes to the average geothermal gradient, or substantial long-wavelength variation, will affect both estimates of exhumation rate. Variations of ±5° C in the average geothermal gradient result in exhumation rates +17% or -13% for estimates using non-horizontal closure isotherms.

TIMING OF EXHUMATION IN THE SANTA LUCIA RANGE

LITTLE EXHUMATION DURING THE OLIGOCENE TO LATE MIOCENE

Several lines of evidence suggest that there was relatively little exhumation between the late Oligocene and late Miocene in the Santa Lucia range. Age-elevation relationships of apatite from the Palo Corona transect and zircon from the Anderson Peak transect both indicate low (0.05–0.07 mm/yr) exhumation between ~25 and 11 Ma (Fig. 3-4 and Table 3-4). Our results from spectral analysis of zircon and apatite (Fig. 3-5) indicate that the entire component of exhumation between the present and ~30 Ma can be accrued by exhumation since ~9 Ma and requires no net exhumation from 9–30 Ma. Analysis of sedimentary basins in the central Santa Lucia range and Salinas valley indicate that subsidence was prevalent across much of the Santa Lucia range beginning in the Late Cretaceous (Ruetz, 1979; Grove, 1993) and continuing intermittently through the late Miocene (Graham, 1976; 1978; Dibblee, 1979). Paleogeographic reconstructions of the central California margin between 18 and 9 Ma indicate that much of the Santa Lucia range was submerged below sea level at some point in the Miocene (Graham, 1978; Graham et al., 1989). Plate reconstructions also indicate that the central California margin was probably obliquely divergent in the Oligocene and early to middle Miocene (Atwater and Stock, 1998; Argus and Gordon, 2001).

RAPID EXHUMATION FROM THE LATE MIOCENE THROUGH THE PLIOCENE

In contrast, there has been relatively rapid cooling and exhumation along the SW flank of the Santa Lucia range since the late Miocene. Nearly all apatite cooling ages within 10 km of the SGHF are younger than the late Miocene and most are Pliocene (Table 3-2; Fig. 3-2). Regardless of the exact thermal structure of the crust, these young ages indicate substantial exhumation since the late Miocene.

The precise transition between the older, slower exhumation and the more-rapid, younger exhumation is difficult to determine, but several lines of evidence suggest it is between ~5 and 12 Ma, and most likely sometime after ~8 Ma. When considered together, the age-elevation relationships of apatite and zircon from the Anderson Peak and Salmon Creek transect (Fig. 3-4) suggest that more-rapid exhumation began sometime between 12 and 6 Ma. This result is independent of the exact magnitude of the pseudo-elevation adjustment, and varies depending on whether the youngest three zircon ages from Anderson Peak are interpreted as part of the zircon PRZ or as part of the more-rapid exhumation; both alternatives are consistent with the data. Apatite from the Cone Peak transect may preserve the apatite PRZ at high elevations (Fig. 3-4), and if so, suggests that more-rapid exhumation began ~6 Ma (Ducea et al., 2003), consistent with our new ~7.1 Ma zircon cooling age at the base of the transect. No other late Miocene or younger apatite PRZs were observed in the remaining transects. A plot of exhumation rate through time for all apatite data indicates two possible time periods of more-rapid increases in exhumation rate (Fig. 3-11). Prior to ~15 Ma, all estimates of exhumation rate are below ~0.2 mm/yr. Between ~9–12 Ma, rates appear to nearly double, and then may double again between ~5–7 Ma.

Basin analysis in the nearby Neogene stratigraphy suggests a complicated history of emergence and subsidence in the mid to late Miocene (Graham, 1978; Graham et al., 1989). Local fault-oblique emergent highs are associated with development of the Reliz-Rinconada fault

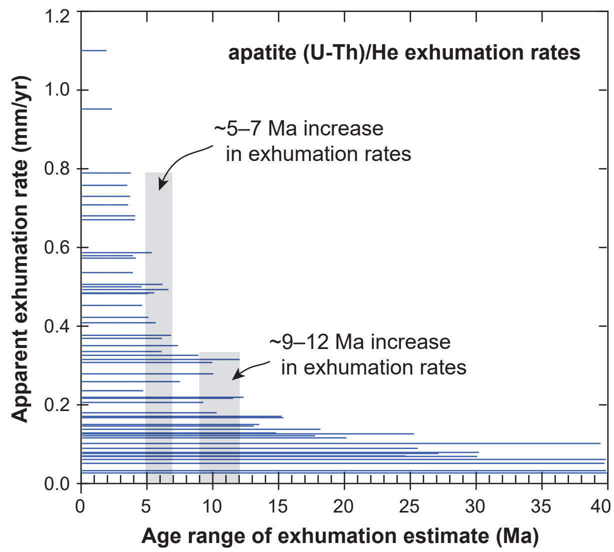

Figure 3-11. Plot of exhumation rates through time in the Santa Lucia range indicate two possible pulses of rate increase. The earlier pulse, at ~9–12 Ma corresponds to the ~11 Ma initiation of the SGHF (Clark, 1998); the younger ~5–7 Ma pulse is remarkably similar to the onset of oblique convergence at this latitude (DeMets and Merkouriev, 2016).

beginning about 15 Ma, but are largely submerged by 9 Ma (Graham, 1978). Most of the Santa Lucia range is predicted to be under >500 m water depth at 9 Ma (Graham, 1978), but there are no direct constraints on the paleogeography of the SW flank of the range because basin deposits—if present—have been eroded. Thus, some uplift along the SW flank of the range between ~12 and 9 Ma is permissible, but not required, and if present, does not appear to have shed sediment into the deep basins to the NE. If there was significant uplift during that time, the nascent range may have remained submerged below sea level and grown with little erosion.

Additional constraints on the timing of exhumation are provided by the age of the San Gregorio-Hosgri fault and reconstructions of relative plate vectors. The SGHF is believed to have initiated at ~11 Ma based on an offset ash bed (Clark, 1998), and this age fits well with the first pulse of more-rapid exhumation noted between ~12–9 Ma (Fig. 3-11). Refinements to relative plate motion reconstructions (Atwater and Stock, 1998; Argus and Gordon, 2001; DeMets and Merkouriev, 2016) indicate that central California experienced transtension prior to ~8 Ma, increasing transpression after ~5.2 Ma, and a period of alternating transtension and transpression between 5.2 and 8 Ma. Within this framework, it seems more likely that exhumation on the NE side of the SGHF began with the onset of transpression sometime since 8 Ma, several m.y. after fault initiation. There is a remarkable correlation between rapid post-6 Ma cooling in the Anderson Peak, Cone Peak, and Salmon Creek transects and the ~5.2 Ma onset of significant transpression predicted by the plate reconstructions of DeMets and Merkouriev (2016) and to a lesser extent by those of Argus and Gordon (2001).

Taken together, permissible ages for the onset of rapid exhumation are from ~6–12 Ma; likely ages are from ~6–8 Ma, and a ~6 Ma age appears to be the most consistent with available constraints. Given that the cumulative slip of many faults comprises the SGHF system (e.g. Dickenson et al., 2005; Langenheim et al., 2013), and that there appears to have been several m.y. of alternating periods of transpression and transtension between 8 and 5.2 Ma (DeMets and Merkouriev, 2016), it is perhaps unsurprising that there is significant variation in the thermochronometric and geologic estimates of when exhumation began.

STEADY RATES OF EXHUMATION SINCE THE PLIOCENE

Estimates of exhumation rate from age-elevation relationships appear to indicate that rates have increased since the latest Pliocene (Table 3-4; this study) or earliest Pleistocene (Ducea et al., 2003). This argument is based on an extrapolation of the exhumation rate required to bring the lowest-elevation sample to the surface since its cooling age, given an assumed geothermal gradient, and an assumption of relatively uniform uplift. For example, if the 0.35 mm/yr exhumation rate calculated for the Cone Peak transect (Table 3-4) had persisted from the lowest-elevation cooling age (2.2 Ma) to the present day, it is only sufficient to exhume 0.77 km of rock. Because the lowest-elevation sample has a closure temperature of ~74° C, the common inference is that rates must have increased since 2.2. However, at least two alternative hypotheses could also explain this discrepancy: 1) a strong spatial variation in geothermal gradient, or; 2) a strong spatial variation un uplift.

The first hypothesis rests on the idea that the geothermal gradient is high enough to shoal the closure depth to the depth predicted by a continuous exhumation rate. At Cone Peak, this requires a geothermal gradient exceeding 75° C/km for either the 2.2 Ma apatite (ID-71) or the ~7.1 Ma zircon (ID-57) cooling age. Similar high gradients are required for the Salmon Creek and Anderson Peak transects. Such geothermal gradients are much higher than predicted for each of these locations (45–52° C/km at the base of Cone Peak and 39° C/km at the base of

Salmon Creek) when topography and exhumation are considered (Table 3-2). Thus, an elevated geothermal gradient along the coast is an unattractive option for the apparent temporal rate increase.

The second hypothesis rests on the idea that if the samples from the bottom of the transect are being advected faster than samples at the top of the transect, the single-value AER will underestimate the actual exhumation rate everywhere along the transect. Spatial gradients in exhumation adjacent to the SGHF are well demonstrated by deformed marine terraces and the pattern of cooling ages along a coastal transect (Chapter 2) and when exhumation rates from the range are analyzed together (Fig. 3-10). These observations provide a compelling mechanism to explain the apparent temporal rate increase. Lower samples—closer to the SGHF—have experienced substantially faster rock uplift than samples at higher elevation that are farther from the SGHF. Thus, age-elevation relationships that suggest a post-Pliocene increase in exhumation rate are not supported over alternative interpretations.

PREDICTING EXHUMATION IN THE CENTRAL CALIFORNIA COAST RANGES

We estimate exhumation rate throughout the range using the relationship between apatite exhumation rate and both distance from the SGHF and local topographic relief (Fig. 3-12). The relationship between exhumation and distance is quite compelling, and is one of the most outstanding features of our dataset; a similar pattern is noted in data from the entirety of the San Andreas fault system (Spotila et al., 2007). An exponential equation describes these data reasonably well (Adj. R^2=0.597) up to the trace of the SGHF, but not on the SW side. Relief is calculated within a 2.5-km window around each sample, and is highly correlated with other metrics of erosion (Fig. 3-6). Although the data are certainly scattered, there is a general trend of increasing exhumation rate with increasing amount of relief (Adj. R^2=0.2447). A nonlinear function that combines an exponential fit for distance and a linear fit for relief produces a much better fit (Adj. R^2=0.727) than either of the single-variable models (Fig. 3-12c). This model is used to interpolate a map of exhumation (Fig. 3-13). Because areas SW of the SGHF do not exhume as rapidly as those on the NE side, areas SW of the fault use only the relief component of the fit.

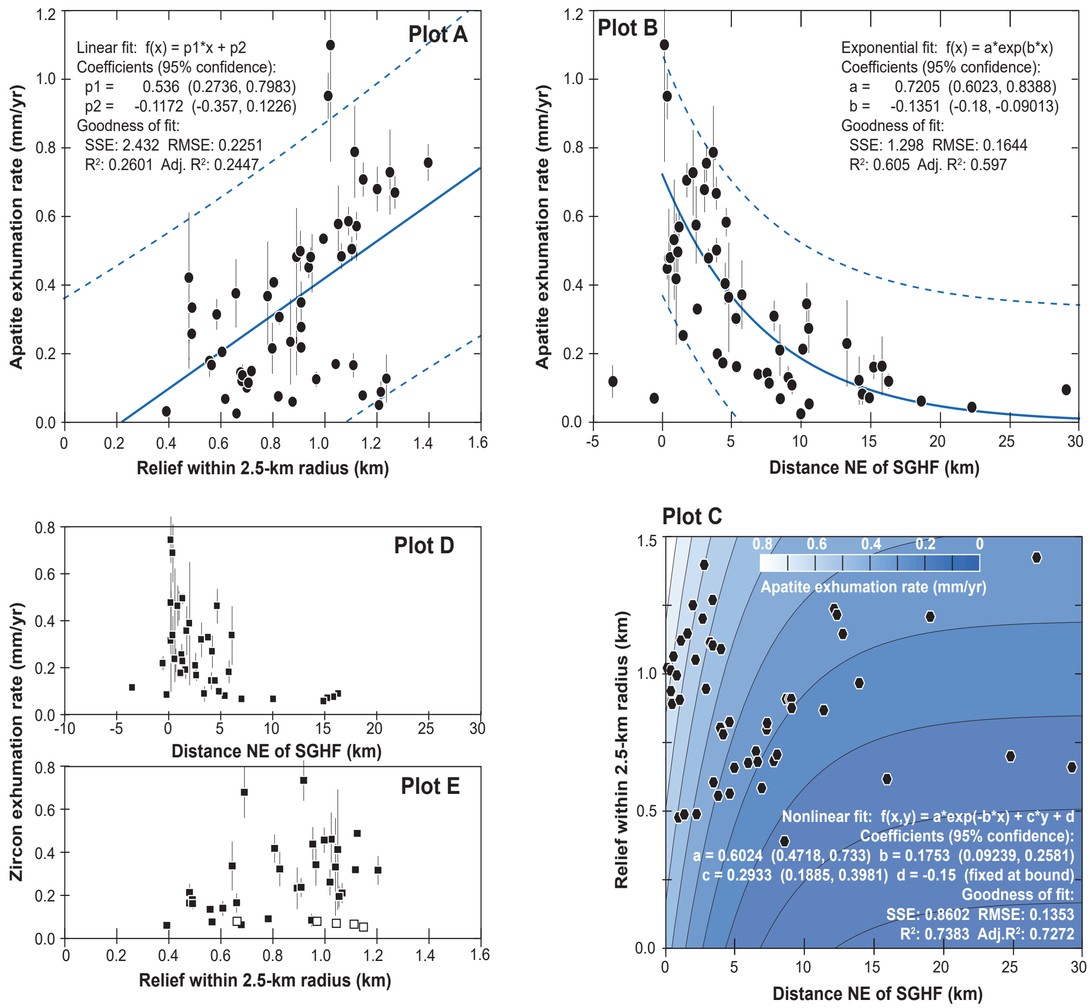

Figure 3-12. Relationships between exhumation rate, topographic relief, and distance to the SGHF for apatite and zircon. **Plot A**—Apatite exhumation rate shows a weak to moderate correlation with topographic relief, but is misleading because almost all of the data above the regression line are within 5 km of the SGHF. **Plot B**—Apatite exhumation rate is strongly correlated with distance from the SGHF; rates NE of the fault decrease rapidly away from the fault. **Plot C**—Contour map of exhumation rate for the nonlinear function that combines exponential decay with distance and linear increase with greater relief. **Plots D and E**—Zircon exhumation rates show similar correlations with relief and distance.

The interpolated model of exhumation rate successfully predicts several important geologic relationships: 1) low exhumation is shown in regions known to preserve Miocene marine sediments or younger Plio-Pleistocene deposits; 2) high exhumation is predicted in the regions with the youngest apatite and zircon cooling ages; 3) moderate exhumation is predicted in the hangingwall of the NE-dipping oblique-reverse Oceanic fault, consistent with post-seismic deformation and detailed geophysical investigation (McLaren et al., 2008; Hardebeck, 2010);

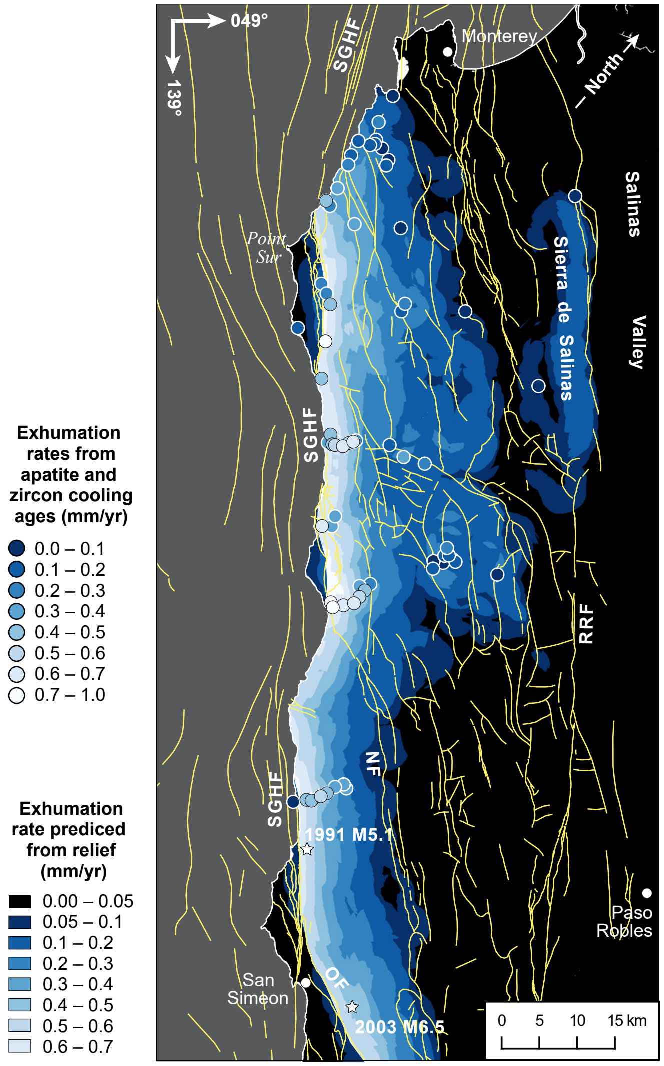

Figure 3-13. Predicted exhumation rate throughout the range using the relationship between apatite exhumation rate and both distance to the SGHF and topographic relief (Fig. 3-12c).

4) the coastal gradient in cooling ages from Monterey to Big Sur is well predicted; 5) the drop in rate SW across the SGHF is well predicted; 6) a general NE crustal tilt (higher exhumation on the SW) and NW-trending antiformal shape are predicted by our model and are well documented by studies of post-Pliocene deformation (Compton, 1966b; Christiansen, 1965; Montgomery, 1993; Page et al., 1998), and; 7) less exhumation is predicted in the Sierra de Salinas than expected from their steep range-front morphology, consistent with studies indicating the Reliz-Rinconada fault is either inactive or active at very low rates in the late Quaternary (Rosenberg and Clark, 2009).

The distribution of the youngest ages is strongly correlated with the regions of highest relief (Fig. 3-12) and appears to indicate both along- and across-strike gradients in exhumation (Fig. 3-13). The highest exhumation rates appear focused near—and NW of—the junction of the SGHF and Nacimiento fault. To the SE of this junction, the Nacimiento fault and the southern SGHF–Oceanic–West Huasana faults define a narrow block of Franciscan mélange with moderate exhumation rates (Fig. 3-13). This narrow block is the topographic expression of the southern Santa Lucia range. North of the junction exists a much wider zone of exhumation between the SGHF and the Sierra de Salinas segment of the Reliz-Rinconada fault. The highest rates of exhumation are in a narrow block of crystalline rocks directly NE of the SGHF and rates decrease to the NE and NW.

LOCALIZATION OF UPLIFT AND EXHUMATION

At least five independent data sets (low-temperature thermochronometry, geologic relationships, estimates of post-Pliocene surface uplift, geomorphic metrics of erosion, and deformed marine terraces) indicate that vertical deformation in the Santa Lucia range is asymmetric, with the greatest amounts of uplift and exhumation on the NE side of the San Gregorio-Hosgri and Oceanic faults.

LOW-TEMPERATURE THERMOCHRONOMETRY

Late Miocene and younger ages from three separate low-temperature thermochronometers (apatite and zircon (U-Th)/He and apatite fission track) are found NE of and near the SGHF whereas the interior and NE part of the range contain older mid-Miocene to Late Cretaceous cooling ages (Fig. 3-2 and Table 3-2). The youngest cooling ages are found directly NE of the SGHF and include many 1.9–4 Ma apatite cooling ages and 7.1–11.5 Ma zircon cooling ages (Table 3-2). Ages this young are unprecedented anywhere along the San Andreas fault system outside of the most transpressional portions of the main plate-boundary fault (Dumitru, 1991; Bürgmann et al., 1994; Spotila et al., 1998, 2007; Niemi et al., 2013). A simple isochron map (Fig. 3-2) shows the overall pattern in cooling ages but does not explicitly adjust for age-elevation relationships and could produce a spurious correlation if the SGHF were simply co-located with the lowest elevations in the range. Rates of exhumation calculated from individual cooling ages remove the effect of elevation and are also strongly correlated with distance from the SGHF (Fig. 3-10).

DISTRIBUTION AND ORIENTATION OF LATE CRETACEOUS–MIOCENE SEDIMENTARY ROCKS

The distribution of Late Cretaceous through Miocene sedimentary rocks in the range provides a first-order constraint on the amount and location of uplift. On the Salinian block, sedimentary rocks are nearly completely absent along the coastal divide adjacent to the SGHF where cooling ages are young (Fig 3-2; Rosenberg and Wills, 2016). The closest sedimentary rocks NE of the SGHF in the central part of the range are Late Cretaceous, floor a thick basin to the NE, and generally dip NE (e.g. Dibblee, 1974). The lack of these rocks along the range crest, their NE dip, and the increasing stratigraphic levels exposed to the NE all suggest a moderate amount of tilt subparallel to the SGHF and sufficient erosion to remove them from high elevations.

PATTERNS OF POST-PLIOCENE SURFACE UPLIFT

Estimates of post-Pliocene range-wide uplift from stratigraphic relationships indicate a NW-trending uplifted core that is subparallel to the SGHF and plunges NW towards Monterey (Christensen, 1965; Page et al., 1998). Substantial stratigraphic relief was also created along the Sierra de Salinas segment of the Reliz-Rinconada fault during this time (Christensen, 1965). A lack of post-Miocene sedimentary rocks along the SW border of the range leaves much of the area closest to the SGHF unconstrained by this method. However, E and SE of San Simeon, the steep SW limb of the uplift is more constrained and approximates the trace of the Oceanic fault (Christensen, 1965). Nearby, analysis of paleocurrent indicators from Plio-Pleistocene rocks between the coast and Paso Robles indicates that there was a coastal divide shedding sediment eastward since at least the late Pliocene (Galehouse, 1967).

GEOMORPHIC METRICS OF EROSION

In a stream-power model of river incision, the value of ksn encodes the ratio between uplift and erodibility, such that higher values of ksn can be attributed to a more durable substrate or higher rates of uplift (e.g. Wobus et al., 2006). We constructed a plot of ksn as a function of distance from the SGHF–OF–WHF for each of the three main lithologies along the coast to explore these parameters at a range-wide scale (Fig. 3-10). The plot is constructed by measuring the distance between each pixel and the bounding fault and plotting the value of ksn for that pixel.

Because this results in >10^4 points, we plot the density of points in bins that measure 0.25 km in distance by 25 m in ksn.

Our analysis indicates that at both range-wide and local scales, ksn is relatively low on the SW side of the SGHF–OF–WHF system, increases substantially directly across the fault, and decreases with distance from the fault. This signal is observed in all three lithologies (Fig. 3-10) and strongly suggests that the increase in ksn is a function of relative uplift, and not the durability of the bedrock substrate. The range-wide pattern of ksn is also noted in map and profile view where abrupt increases are found in every drainage that crosses the Oceanic fault (n=7; Fig. 3-8), and where drainages cross strands of the SGHF (n=3; Fig. 3-8). Such across-fault changes are also noted along fault strands subparallel to the Nacimiento fault (Fig. 3-7), although the presence of a change in lithology makes it less clear that the change is related to differential uplift. The range-wide patterns observed in ksn are nearly identical to the patterns of exhumation rate and marine terrace elevation (Fig. 3-10).

DEFORMED MARINE TERRACES

Lastly, deformed marine terraces along >100 km of the SGHF, from Point Año Nuevo to San Simeon (Figs. 3-1 and 3-10) also indicate that uplift is highly focused NE of the fault (Bradley and Griggs, 1976; Lajoie et al., 1979; Weber, 1990; McKittrick, 1988; Hanson et al., 1994; Chapter 1; Chapter 2). Although there are uncertainties in terrace age along the central California coast, the lateral continuity and similar initial elevation of marine terraces make them an excellent strain marker. Thus, even if the age correlations near Ragged Point (this study), between Big Sur and Monterey (McKittrick, 1988; Chapter 2), or near Santa Cruz (e.g. Weber, 1990; Perg et al., 2001; Chapter 1) prove to be incorrect with additional study, the relative uplift and deformation of an initially horizontal sea-level datum across the SGHF remains a robust result. Differences in the relative deformation pattern of marine terraces near Ragged Point and San Simeon further suggest that surface uplift is partitioned onto the Oceanic fault instead of continuing southeast along the San Simeon fault zone (Fig. 3-10).

STRAIN TRANSFER BETWEEN THE SGHF AND INLAND FAULTS

Our analysis of low-temperature thermochronometry, geomorphic metrics of erosion, and deformed marine terraces suggest that vertical strain is transferred from inland faults to the

SGHF across the Oceanic and Nacimiento faults, and perhaps across faults farther NW in the range.

OCEANIC FAULT

Our predicted values of exhumation rate increase stepwise SE to NW, from low rates near and SE of San Simeon—that are similar to rates of rock uplift determined from deformed marine terraces (Hanson et al., 1994)—to moderate rates across the Oceanic fault, to the highest rates in the range across the Nacimiento fault (Fig. 3-13). Increases in ksn values NE across the Oceanic fault (Figs. 3-7 and 3-8) and changes in the accommodation of vertical strain SE of the junction between the Oceanic and SGH faults (Fig. 3-9) appear to corroborate its role in focusing uplift NE of its trace. The 2003 M6.5 San Simeon earthquake occurred on the Oceanic fault and had a mostly NE-side up reverse sense of slip and broad NE-side up post-seismic deformation (McLaren et al., 2008). Additionally, just NW of the junction between the Oceanic fault and SGHF, an oblique-reverse M5.1 event occurred in 1991 (Hardebeck, 2010). Together, these data provide strong support for a tectonic model where strain is transferred from the West Huasana fault to the SGHF across the Oceanic fault (e.g. Lettis et al., 2004; Hardebeck, 2010).

NACIMIENTO FAULT

Slip transfer along the Nacimiento fault is more difficult to constrain, but strongly suggested by the apparent localization of high exhumation NE of its junction with the SGHF and its similar geometry to the Oceanic fault (Fig. 3-13). Arguments against significant displacement on the Nacimiento fault are based on an overlapping and relatively undisrupted basal unit of the Vaqueros Formation west of Paso Robles (e.g. Dickenson et al., 2005). It is not clear how much displacement might be needed along the Nacimiento fault to account for the higher rates of exhumation NE of the fault junction, but it could be a relatively small amount if it is all converted into uplift. Regardless, there are many sub-parallel and en-echelon fault strands SW of the basal Vaqueros Formation (e.g. Graymer et al., 2014) that could plausibly link the northern end of the West Huasana fault with the Nacimiento fault, bypass the slip constraint, and possibly transfer a few km of slip. Geophysical investigation (Langenheim et al., 2013) suggests a much larger lateral displacement on the West Huasana fault than previously recognized (McLean, 1993; Hall et al., 1995). The transfer of some of this displacement across the oblique Oceanic and Nacimiento faults onto the SGHF may help balance the slip budget and provide a plausible mechanism to explain the observed patterns of uplift and exhumation.

FAULT MESH IN THE NW SANTA LUCIA RANGE

Slip transfer between strands of the Reliz-Rinconada fault and the SGHF has been proposed to account for the NW decrease in slip along the RRF, uplifted crustal blocks in the north-central Santa Lucia range, and discrepancies in late Quaternary slip rates on the SGHF north and south of the Santa Lucia range (Graham, 1978; Dibblee, 1979; Weber, 1990; Dickenson et al., 2005; Langenheim et al., 2013; Johnson et al., 2014). Within the range, several NW-striking faults—most notably the Junipero Serra and Tularcitos faults—cut and offset late Cretaceous through late Miocene strata along steep faults and indicate at least some component of oblique slip after the late Miocene (Compton, 1966b; Dibblee, 1979).

Our oldest apatite cooling age (65.0 ±5.8 Ma) is located adjacent to the NW RRF (ID-56; Fig. 3-2) and strongly suggests that there has been little exhumation there since the late Cretaceous. This observation supports interpretations of decreasing slip along the RRF (e.g. Graham, 1978) and little or no late Quaternary activity (Rosenberg and Clark, 2009). Late Miocene cooling ages at moderate and high elevation from the central part of the range (ID 80–89) are consistent with uplift and exhumation since the late Miocene, but neither require nor preclude slip on individual fault strands. Values of ksn are generally high in the north-central part of the range and are compatible with higher rates of uplift and exhumation, but are inconclusive because the high values could arguably be produced by the presence of more durable crystalline bedrock. Together, our results support the hypothesis of late Miocene strain transfer across the Santa Lucia range, but do not provide conclusive evidence of its pattern or timing.

REGIONAL IMPLICATIONS OF UPLIFT AND EXHUMATION IN THE SANTA LUCIA RANGE

The data presented above show that the San Gregorio–Hosgri fault system exerts a fundamental control on the magnitude and pattern of uplift and exhumation in central California. Rates of bedrock exhumation are substantially higher in a narrow window along the SGHF than along most of the San Andreas fault north of the ‘Big Bend’ (Spotila et al., 2007; Niemi et al., 2013). Rates in the Santa Lucia range are locally higher than those in the Sierra Azul block, an exhuming crustal block along a transpressional bend and stepover of the San Andreas fault near Santa Cruz (Bürgmann et al., 1994; Hilley et al., 2013). These observations are especially surprising given that estimates of the modern strain field in central California from GPS predict the exhumation of the Sierra Azul block, but fail to predict the even-greater exhumation of the southwest Santa Lucia range (d'Alessio et al., 2008; Rolandone et al., 2008; Titus et al., 2011; DeMets et al., 2014). There, permanent and semi-continuous GPS stations appear to indicate that within uncertainty the Santa Lucia range behaves as a relatively coherent block bound by low slip rate (<2 mm/yr) faults with little or no across-range change in fault-perpendicular components of strain (e.g. Titus et al., 2011; DeMets et al., 2014). Such low slip rates are generally confirmed by paleoseismic studies along the major faults of the SGHF: the San Gregorio fault indicates ~4–8 mm/yr (Weber, 1990; Weber et al., 1995); the San Simeon fault zone indicates ~1–3 mm/yr (Hanson et al., 2004); and the Hosgri fault indicates a minimum of 2.6 ±0.9 mm/yr (Johnson et al., 2014).

Given that low late Quaternary slip rates on faults SW of the San Andreas fault are a consistent result, these observations and constraints appear to challenge our assumptions of how strain is distributed along the Pacific–North America plate boundary in three main ways: 1) how can robust evidence of late Quaternary through late Miocene rock uplift and exhumation be reconciled with a modern strain field that does not predict these features, 2) why were coaxial components of plate boundary strain focused in the Santa Lucia range during the late Miocene through Pleistocene instead of along the main San Andreas fault, and 3) what mechanism accounts for long-term (>10^6 yr) differential exhumation within narrow (<3–5 km-wide) zones of crystalline bedrock? The answer to these questions is not immediately clear, but several hypotheses may explain the observations.

RATE CHANGES ALONG THE SGHF AND POSSIBLE LATE QUATERNARY ISOSTATIC UPLIFT OF THE RANGE

One explanation for the discrepancy between the modern strain field and evidence of uplift and exhumation invokes isostatic adjustment of the range in the wake of a recent and rapid decrease in slip rate along the SGHF. Offset geologic markers along the SGHF constrain slip at ~11 Ma and ~8 Ma (Clark, 1998; Dickenson et al., 2005), and in the late Quaternary since ~230 ka (e.g. Weber, 1990). Within these bounds, late Miocene to Pleistocene rates were ~16–18 mm/

yr, substantially higher than those since the late Quaternary. If such high slip rates persisted through 0.5 Ma, for example, the near-constant clockwise rotation of plate vectors during that time (DeMets and Merkouriev, 2016) would have increased the coaxial component of shortening across the range to a maximum at 0.5 Ma. If exhumation and erosion were well matched at that time—as perhaps indicated by the relationship between exhumation and modern metrics of erosion in our data—continued erosion after 0.5 Ma would be met with isostatic uplift at rates of about 4/5 the erosion rate (e.g. Turcotte and Schubert, 2002). Modeling of an instantaneous drop in tectonic uplift during orogenic evolution suggests that high rates of rock uplift persist for several m.y. after the change because of isostatic adjustment (Spotila, 2005).

Isostatic uplift can explain much of the magnitude of marine terrace uplift, but alone does not adequately explain the entire uplift, nor why elevation is so closely tied to the SGHF (Fig. 3-10). The distribution and elevation of marine terraces clearly indicate they are cut and offset by strands of the SGHF since the late Quaternary (Chapter 2; Lajoie et al., 1979; Weber, 1990; Hanson et al., 1994; Dickenson et al., 2005). Thus, there is at least some component—perhaps small—of late Quaternary transpression across the SGHF that is responsible for their deformation. One solution is that the isostatic adjustment utilizes existing faults to accommodate uplift, in a process similar to some Basin and Range faults that experienced increased fault activity as a result of late Quaternary lake recession (Karrow and Hampel, 2010). Together, these two components could explain the pattern of high-elevation marine terraces without requiring that their uplift is tied entirely to high rates of late Quaternary plate-boundary transpression.

POSSIBLE MECHANISM OF STRAIN LOCALIZATION ALONG THE OUTER EDGE OF THE SANTA LUCIA RANGE

At ~6 Ma, when rapid exhumation had begun along the length of the Santa Lucia range adjacent to the SGHF, the range was located near the southern San Joaquin basin (e.g. Powell, 1993). Since then, there has been no location between the southern San Joaquin basin and the transpressional bend near Santa Cruz that has experienced the magnitude of exhumation recorded in the Santa Lucia range as it has been transported to the NW (e.g. Bartow, 1981; Goodman and Malin, 1992). This suggests that the range has acted like the ‘crumple zone’ on modern cars, whereby coaxial components of plate-boundary strain are preferentially focused along the outer edge of the Salinian block instead of being transferred across the range to the San Andreas fault.

One possible mechanism to account for this invokes the late Cretaceous crustal restructuring that juxtaposed the schist of Sierra de Salinas beneath crystalline rocks of the Sierran batholith (Kidder and Ducea, 2006; Chapman et al., 2010; 2012). Within the Santa Lucia range, this is likely manifest as a several km-thick package of schist structurally beneath the entire crystalline core of the range (e.g. Kidder and Ducea, 2006). A shallow and sub-horizontal detachment zone has been inferred beneath the range based on geophysical data (Page et al., 1998) and may represent this discontinuity. The strength of mica schist is substantially less than the crystalline rocks that lie above it (Shea and Kronenberg, 1992) and so the replacement of crystalline rock with weak schist at mid-crustal depths might cause a rheological contrast with surrounding unaltered crust that is large enough to focus compressional deformation along the edge of the range.

MECHANICAL PROBLEM OF A NARROW WINDOW OF HIGH EXHUMATION

The intense localization of vertical strain in a narrow window along the SGHF is also unusual behavior. Rates of exhumation increase rapidly within ~5 km of the SGHF and are highest adjacent to the fault (Fig. 3-10; Chapter 2). Such a pattern is impossible to produce in crystalline rock with block uplift along a single steeply NE-dipping fault because each point in the hangingwall is advected upwards by an equal amount. A model of synclinal folding above a NE-dipping fault might explain the overall pattern, but such a fold requires a ~10 km wavelength and ~1 km amplitude (assuming a 3 Ma apatite age at the fault and a 9 Ma age at 5 km distance). Using typical values of Young's modulus, the elastic thickness of crystalline crust would need to be ~1 km to produce such a fold (e.g. Turcotte and Schubert, 2002).

One alternative is that closely spaced faults divide the NE side of the SGHF into a series of thin crustal zones or lenses that each can have a different exhumation rate. In some locations—such as between Monterey and Point Sur (Fig. 3-2; Chapter 2)—changes in marine terrace elevation and exhumation rate coincide with such fault-bound lenses. Additionally, crystalline rock is nearly always intensely fractured where observed, even where no faults are mapped along the southwest flank of the range. These observations, and the overall high density of faults mapped range-wide (Rosenberg and Wills, 2016), provide some support for this hypothesis.

Neither of these hypotheses are entirely satisfactory if the crust of the Santa Lucia range is composed solely of crystalline rock: the folding of a thin carapace of crystalline rock requires unusual physical parameters; a ~3–5-km-wide shear zone seems more likely—and is locally observed—but requires the presence of a nearly 90 km-long shear zone that has apparently remained elusive after decades of field mapping. However, the presence of weak schist at depth beneath the crystalline rock may ease some of these constraints. In the case of folding, a flexural thickness of ~1–2 km may be entirely possible if schist were located at shallow depth—a permissible option from available geologic constraints (e.g. Kidder and Ducea, 2006; Chapman et al., 2010). Closely spaced faults are also more likely where a thin elastic layer—such as a crystalline 'lid'—overlies a viscous layer—such as weak schist (e.g. Dauteuil and Mart, 1998). The absence of such faults on geologic maps is suspicious, but if displacement on each strand is relatively small, they would be difficult to detect in crystalline rock lacking marker horizons. It is notable that a similar pattern of exhumation—highest adjacent to the main strike-slip fault and decaying with distance without notable shear zones or folds—is found along the SAF in the San Emigdio Mountains, where underplated schist also lies at shallow depth below crystalline rock (Niemi et al., 2013).

CATCHMENT-MEAN EXHUMATION AND ^{10}BE DENUDATION

We use our interpolated map of exhumation rate (Fig. 3-13) to calculate catchment-mean exhumation rate (Fig. 3-14). As with Figure 3-13, there is considerable uncertainty on the actual values of exhumation rate, and so this map is best viewed as depicting the relative differences between catchments. Many of the most-striking features of this dataset are similar to those listed for Figure 3-13, namely that exhumation is largely localized along the San Gregorio-Hosgri and Oceanic faults. It is notable that when averaged in this way, large drainages developed on crystalline rock with high ksn values (e.g. Arroyo Seco, 51; Carmel River, 7) have low catchment-mean exhumation rates.

Our catchment-mean rates of exhumation do not compare favorably with denudation rates (Figs. 3-14 and 3-15a). Denudation rates were calculated for 18 basins in the Santa Lucia

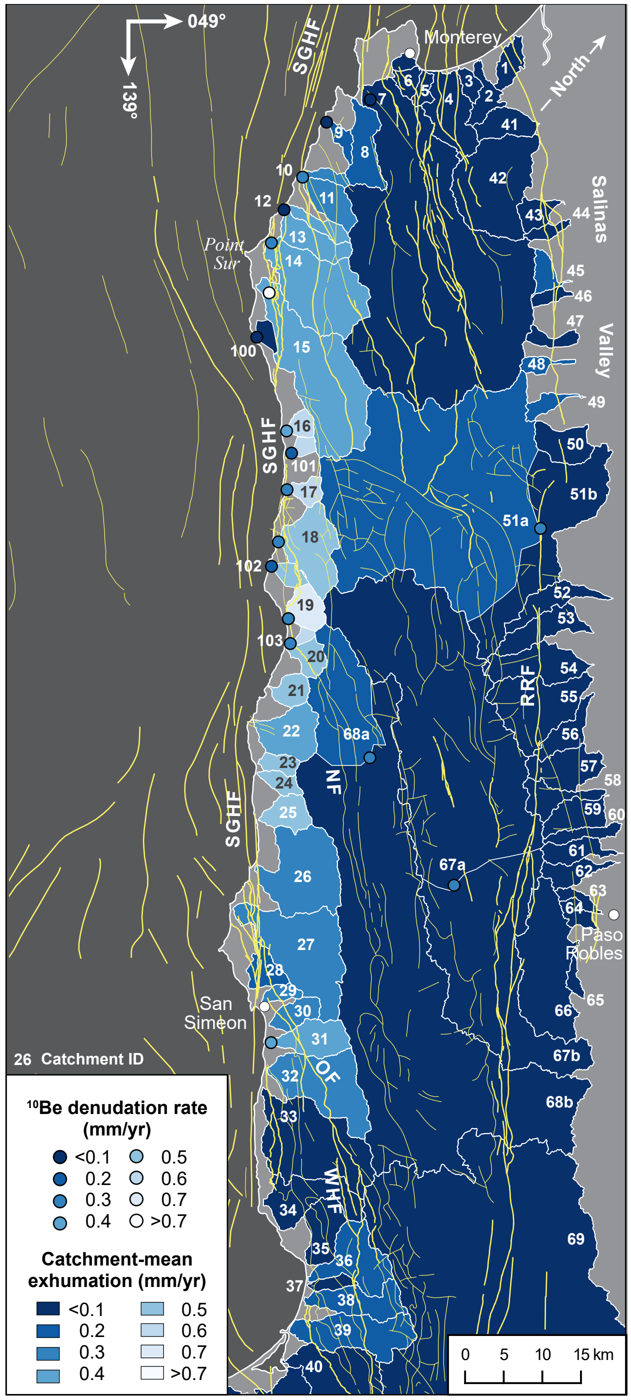

Figure 3-14. Drainage basins >5 km^2 in the Santa Lucia range show systematic differences in catchment-mean exhumation rate as a function of distance from the SGHF but compare poorly with denudation rates from ^{10}Be cosmogenic dating (H. Young, written commun., 2016). The greatest mismatch between exhumation and denudate is found in the steep drainages south of Point Sur and north of the Nacimiento fault. Exhumation rates are calculated from data in Fig. 3-13. Four basins under 5 km^2 (ID 100–103) are shown here because they were sampled for denudation estimates. Fault abbreviations are the same as Fig. 3-1.

range using ^{10}Be cosmogenic radionuclides (Young et al., 2015; H. Young, Stanford University, written commun., 2016). There is no statistical correlation ($p>0.08$) between exhumation and denudation (Fig., 3-15a), and the mismatch can be plainly observed in map view (Fig. 3-14). Denudation rates in the range also do not appear to correlate strongly with topographic metrics of erosion, such as *ksn* or relief (Young et al., 2015). This is a very puzzling result considering how well these metrics agree internally and appear to indicate the range is perhaps near equilibrium between long-term uplift and erosion. Somewhat surprisingly, the magnitude of the discrepancy appears to be well correlated with catchment-mean slope (Fig. 3-15b).

We suspect that the mismatch between denudation and exhumation rates may be explained by biases in the sediment supply related to landslides (e.g. Puchol et al., 2014). Landslide deposits are a large portion of the surficial units throughout the range (e.g. Rosenberg and Wills, 2016) and have been suggested to be the dominant erosional process on the steeper slopes of the range (Ducea et al., 2003). Additionally, our analysis of geomorphic metrics indicates a change in behavior above catchment-mean slopes of ~25° (Fig. 3-6) that could signal an increasing role of landslides in sediment transport (e.g. Binnie et al., 2007; Ouimet et al., 2009; DiBiase et al., 2010). Landslides can bias ^{10}Be cosmogenic denudation rate estimates by introducing large quantities of material with low cosmogenic radionuclide concentration to the fluvial system—which overestimates denudation rate, and through the generation of a grain-size dependency on cosmogenic radionuclide concentration—which underestimates

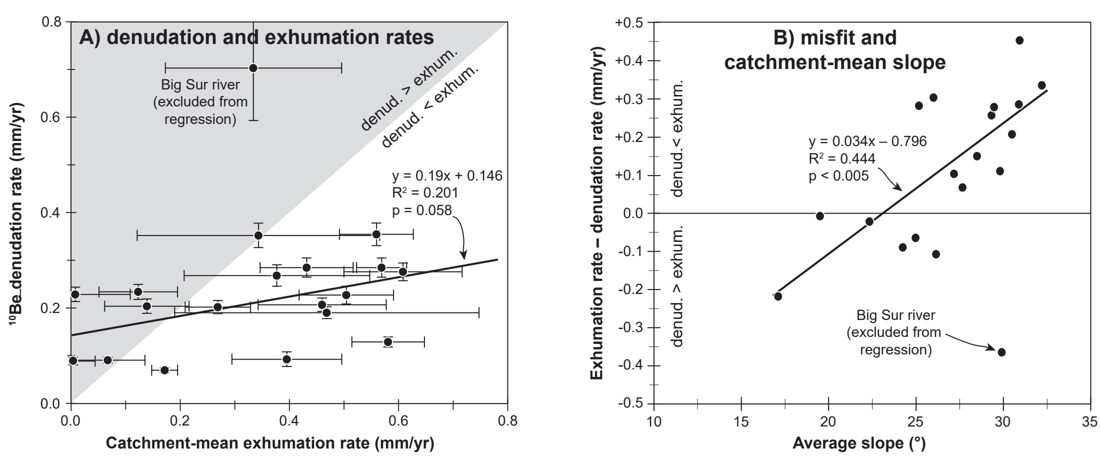

Figure 3-15. Plot A—Catchment-mean exhumation rate shows no statistical correlation ($p>0.05$) with denudation rates measured from cosmogenic ^{10}Be in 18 drainages; denudation rates from H. Young (Stanford University, written commun., 2016). **Plot B—**The misfit between exhumation and denudation has a moderate correlation with catchment-mean slope.

denudation rate downstream of the landslide (Puchol et al., 2014). To a first order, these two processes can explain the correlation between catchment-mean slope and the discrepancy between denudation and exhumation (Fig. 3-15b), as follows.

The high denudation rates of the Big Sur river can be explained by the addition of landslide material from the expansive steep slopes above the main gorge where the river crosses the rapidly exhuming band of rock that forms the main coastal divide (Figs. 3-7 and 3-13). No other river along the coast of the Santa Lucia range crosses this band of rapidly exhuming rock, and the second-youngest apatite cooling age in the range (ID 58; Table 3-2) is from the mouth of this gorge. The addition of low-cosmogenic-concentration material from these slopes may overwhelm the denudation signal from farther upstream. The lower-than-predicted denudation rates for other high-slope catchments may be related to the grain-size dependency effect (e.g. Puchol et al., 2014), whereby low-cosmogenic-concentration grains are often large. Because of this, sampling far downstream of a landslide-dominated landscape—such as our data suggest for catchments with slopes >25°—may bias the results by preferentially analyzing only the high-cosmogenic-concentration fine-grained fraction of sediment. Although this interpretation is tentative, it provides the testable prediction that high-mismatch catchments have sediment-transport processes much different than low-mismatch catchments.

CONCLUSION

We combine new and existing low-temperature thermochronometry of apatite and zircon with geomorphic metrics of erosion, deformed marine terraces, and geologic constraints to describe the Oligocene through modern history of uplift and exhumation for the Santa Lucia range in central California. Rates of long-term exhumation vary widely across the range; the NE part of the range preserves late Cretaceous apatite cooling ages, Oligocene to late Miocene apatite ages characterize the central part of the range, and late Miocene to Pleistocene apatite ages are found along the SW flank of the range. Zircon cooling ages are predominantly late Cretaceous except at low elevations directly NE of the SGHF where they are as young as 7.1 Ma. Deformed marine terraces indicate that at least since the late Quaternary, there has been a ~3-km-wide zone of localized rock uplift NE of the SGHF; within this zone, uplift is 3–5x higher than farther from the fault. A similar pattern is observed in long-term rates of exhumation along an equal-elevation coastal transect (Chapter 2). These data indicate that exhumation has been asymmetric, with generally greater exhumation NE of the SGHF, and an especially localized zone of strain directly NE of the fault.

There was little exhumation during the Oligocene through late Miocene, when much of the central California borderland was undergoing oblique transtension and basin subsidence (e.g. Graham, 1978). The San Gregorio-Hosgri fault initiated ~11 Ma (Clark, 1998), but it was not until several m.y. later, most likely at ~6 Ma, that rapid exhumation began along the SW flank of the range adjacent to the fault. This age corresponds closely to the ~5.2 Ma final shift towards transpression at this latitude (DeMets and Merkouriev, 2016). Initial studies of low-temperature thermochronometry suggested faster exhumation since ~2.3 Ma (Ducea et al., 2003), but a consideration of the strong spatial gradient in vertical strain NE of the SGHF does not require such a rate change.

We develop a range-wide map of exhumation rate using the correlation between topographic relief within a 2.5-km window, distance to the SGHF, and exhumation rates from apatite (U-Th)/He cooling ages. A band of rapid exhumation—at ~0.5–0.9 mm/yr—has been located directly NE of the SGHF since the late Miocene; rates decay NE slowly in the northern half of the range, and rapidly in the southern half. These predictions agree with all known geological and thermochronological constraints, and although there is uncertainty in the exact values of exhumation, the general pattern is likely a robust result.

Metrics of erosion from χ-analysis of river profiles, in combination with our other results, indicate a stepwise increase in uplift and exhumation NW across the Oceanic and Nacimiento faults. We interpret these data as indicating transfer of strain from inland faults such as the West Huasana fault, to the coastal SGHF, in support of the model advocated by Hardebeck (2010). A similar pattern of strain transfer likely exists farther NW between the RRF and SGHF, but our data provide little additional constraint beyond supporting general post-mid to late Miocene exhumation in the core of the range.

REFERENCES

Ahnert, F., 1970. Functional relationships between denudation, relief, and uplift in large mid-latitude drainage basins. American Journal of Science v. 268, p. 243–263.

Alexander, C.S., 1953, The marine and stream terraces of the Capitola-Watsonville area. University of California Publications in Geography, v. 10, p. 1–44.

Anderson, R.S., 1990, Evolution of the northern Santa Cruz mountains by advection of crust past a San Andreas Fault bend. Science, v. 249.4967, p. 397-401.

Anderson, R.S., and Menking, K.M., 1994, The Quaternary marine terraces of Santa Cruz, California: Evidence for coseismic uplift on two faults. Geological Society of America Bulletin, v. 106, n. 5, p. 649-664.

Argus, D.F., Gordon, R.G., 2001, Present tectonic motion across the coast ranges and San Andreas fault system in central California. Geological Society of America Bulletin v. 113, p. 1580– 1592.

Atwater, T., Stock, J., 1998, Pacific– North America plate tectonics of the Neogene southwestern United States: an update. International Geology Review v. 40, p. 375–402.

Bartow, J.A., 1991, The Cenozoic Evolution of the San Joaquin Valley, California. U.S. Geological Survey Professional Paper 1501, 40 pp.

Barth, A.P., Wooden, J.L., Grove, M., Jacobson, C.E., Pedrick, J.N., 2003, U-Pb zircon geochronology of rocks in the Salinas Valley region of California: A re-evaluation of the crustal structure and origin of the Salinian block. Geology, v. 31, p. 517-520.

Binnie, S.A., Phillips, W.M., Summerfield, M.A., Fifield, L.K., 2007. Tectonic uplift, threshold hillslopes, and denudation rates in a developing mountain range. Geology v. 35, p. 743-846.

Bradley, W.C., and Griggs, G.B., 1976, Form, genesis, and deformation of central California wave-cut platforms. Geological Society of America Bulletin, v. 87, p. 433–449.

Braun, J., 2002a, Quantifying the effect of recent relief changes on age-elevation relationships. Earth Planetary Science Letters v. 200, p. 331–343.

Braun, J., 2002b, Estimating exhumation rate and relief evolution by spectral analysis of age-elevation profiles. Terra Nova v. 14, p. 210–214.

Braun, J., 2005, Quantitative constraints on the rate of landform evolution derived from low-temperature thermochronology, in Reiners, P.W., and Ehlers, T.A., eds., Low-temperature thermochronology: techniques, interpretations, and applications: Reviews in Mineralogy and Geochemistry Volume 58, p. 351-374.

Braun, J., van der Beek, P., Batt, G., 2006, Quantitative thermochronology: Numerical methods for the interpretation of thermochronological data. Cambridge University Press, Cambridge, U.K., 258 pp.

Braun, J., van der Beek, P., Valla, P., Robert, X., Herman, F., Glotzbach, C., Pederson, V., Perry, C., Simon-Labric, T., and Prigent, C., 2012, Quantifying rates of landscape evolution and tectonic processes by thermochronology and numerical modeling of crustal heat transport using PECUBE. Tectonophysics, v. 524-525, p. 1-28.

Burbank, D.W., Leland, J., Fielding, E., Anderson, R.S., Brozovic, N., Reid, M.R., Duncan, C., 1996, Bedrock incision, rock uplift and threshold hillslopes in the northwestern Himalayas. Nature v. 379, p. 505–510.

Bürgmann, R., Arrowsmith, R., Dumitru, T., and McLaughlin, R., 1994, Rise and fall of the southern Santa Cruz Mountains, California, from fission tracks, geomorphology, and geodesy. Journal of Geophysical Research, v. 99, p. 20,181-20,202.

Chapman, A. D., Kidder, S., Saleeby, J.B., and Ducea, M.N., 2010, Role of extrusion of the Rand and Sierra de Salinas schists in late Cretaceous extension and rotation of the southern Sierra Nevada and vicinity. Tectonics, v. 29, TC5006.

Chapman, A.D. Saleeby, J.B., Wood, D.J., Piasecki, A., Kidder, S., Ducea, M.N., Farley, K.A., 2012, Late Cretaceous gravitational collapse of the southern Sierra Nevada batholith, California. Geosphere, v. 8, n. 2, p. 314-341. DOI:10.1130/GES00740.1

Christensen, M.N., 1965, Late Cenozoic deformation in the central Coast Ranges of California. Geological Society of America Bulletin, v. 76, p. 1105–1124.

Clark, J.C., 1998, Neotectonics of the San Gregorio fault zone: Age dating controls on offset history and slip rates. American Association of Petroleum Geologists Bulletin, v. 82, p. 884–885.

Clark, J.C., and Rosenberg, L.I., 1999, Southern San Gregorio fault: stepover segmentation vs. through-going tectonics: U.S. Geological Survey, National Earthquake Hazards Reduction Program, Final Technical Report 1434-HQ-98-GR-0007, 50 p., 3 sheets, scale 1:24,000.

Clark, J.C., Dupre, W.R., Rosenberg, L.I., 1997, Geologic map of the Monterey and Seaside 7.5-minute quadrangles, Monterey County, California: a digital database. U.S. Geological Survey Open-File Report 97-30, scale 1:24,000, 1 plate.

Clark, J.C., Brabb, E.E., and Rosenberg, L.I., 2001, Geologic map and map database of the Spreckels 7.5-minute quadrangle, Monterey County, California: U.S. Geological Survey, Miscellaneous Field Studies Map MF-2349, scale 1:24,000.

Colgan, J.P., McPhee, D.K., McDougall, K., and Hourigan, J.K., 2012, Superimposed extension and shortening in the southern Salinas Basin and La Panza Range, California: A guide to Neogene deformation in the Salinian block of the central California Coast Ranges. Lithosphere, v. 4, p. 411–429. DOI:10.1130/L208.1

Compton, R.R., 1960, Charnockitic rocks of the Santa Lucia Range, California. American Journal of Science, v. 258, p. 609-636.

Compton, R.R., 1966a, Granitic and metamorphic rocks of the Salinian block, California Coast Ranges, in Bailey, E.H., editor, Geology of northern California: California Division of Mines and Geology Bulletin 190, p. 277–287.

Compton, R.R., 1966b, Analysis of Pliocene–Pleistocene deformation and stresses in the northern Santa Lucia Range, California. Geological Society of America Bulletin, v. 77, p. 1361-1380.

Cox, A., Engebretson, D.C., 1985, Change in motion of Pacific plate at 5 Myr BP. Nature, v. 313, p. 472–474. DOI:10.1038/313472a0

d'Alessio, M.A., Johanson, I.A., Bürgmann, R., Schmidt, D.A., and Murray, M.H., 2005, Slicing up the San Francisco Bay area; block kinematics and fault slip rates from GPS-derived surface velocities. Journal of Geophysical Research, v. 110, B06403, DOI:10.1029/2004JB003496.

Dauteuil, O., Mart, Y., 1998, Analogue modeling of faulting pattern, ductile deformation, and vertical motion in strike-slip fault zones. Tectonics, v. 17, n. 2, p. 303-410.

DeMets, C., and Merkouriev, S., 2016, High-resolution reconstructions of Pacific-North America plate motion: 20 Ma to present. Geophysical Journal International, v. 207, p. 741-773.

DeMets, C., Marquez-Azua, B., and Cabral-Cano, E., 2014, A new GPS velocity field for the Pacific Plate-Part 2: implications for fault slip rates in western California. Geophysical Journal International, v. 199, p. 1900-1909.

Dibblee, T.W., Jr., 1974, Geologic maps of the Monterey, Salinas, Gonzales, Point Sur, Jamesburg, Soledad and Junipero Serra 15′ quadrangles, Monterey County, California, U.S. Geological Survey Open File Report 74□1021.

Dibblee, T.W., Jr., 1976, The Rinconada and related faults in the southern Coast Ranges, California, and their tectonic significance, U.S. Geological Survey Professional Paper 981, 55 p.

Dibblee, T.W., 1979, Cenozoic tectonics of the northeast flank of the Santa Lucia Mountains from the Arroyo Seco to the Nacimiento River, California, in Graham, S.A., ed, Tertiary and Quaternary geology of the Salinas Valley and Santa Lucia range, Monterey County, California: Pacific Section, SEPM, Pacific Coast paleogeography Field Guide 4, p. 67-76.

DiBiase, R.A., Whipple, K.X., Heimsath, A.M., and Ouimet, W.B., 2010, Landscape form and millennial erosion rates in the San Gabriel Mountains, CA. Earth and Planetary Science Letters, v. 289, p. 134-144.

Dickinson, W.R., 1983, Cretaceous sinistral strike slip along Nacimiento fault in coastal California: The American Association of Petroleum Geologists Bulletin, v. 67, p. 624–645.

Dickinson, W.R., Ducea, M., Rosenberg, L.I., Greene, H.G., Graham, S.A., Clark, J.C., Weber, G.E., Kidder, S., Ernst, G.W., and Brabb, E.E., 2005, Net dextral slip, Neogene San Gregorio–Hosgri fault zone, coastal California; geologic evidence and tectonic implications. Geological Society of America Special Paper 391, 43 p.

Dodson, M.H., 1973, Closure temperature in cooling geochronological and petrological systems. Contributions to Mineral Petrology, v. 40, p. 259-274.

Ducea, M., House, M.A., and Kidder, S., 2003, Late Cenozoic denudation and uplift rates in the Santa Lucia Mountains, California. Geology, v. 31, p. 139–142.

Dumitru, T.A., 1991, Major Quaternary uplift along the northernmost San Andreas fault, King Range, northwestern California. Geology, v. 19, p. 526-529.

Duvall, A., Kirby, E., Burbank, D., 2004, Tectonic and lithologic controls on bedrock channel profiles and processes in coastal California. Journal of Geophysical Research v. 109. DOI:10.1029/2003JF000086.

Ehlers, T.A., 2005, Crustal thermal processes and the interpretation of thermochronometer data, in Reiners, P.W., and Ehlers, T.A., eds., Low-temperature thermochronology: techniques, interpretations, and applications: Reviews in Mineralogy and Geochemistry Volume 58, p. 315-350.

Evernden, J.F., Kistler, R.W., 1970, Chronology of emplacement of Mesozoic batholithic complexes in California and western Nevada. U.S. Geological Survey Professional Paper 623, 42 p.

Farley, K.A. 2000, Helium diffusion from apatite: General behavior as illustrated by Durango Fluorapatite. Journal of Geophysical Research, v. 105, p. 2903-2914.

Farley, K.A., 2002, (U-Th)/He dating: techniques, calibrations, and applications. Reviews of Mineralogy and Geochemistry 47, p. 819-844.

Farley, K. A., Shuster, D. L., Ketcham, R. A., 2011, U and Th zonation in apatite observed by laser ablation ICPMS and implications for the (U–Th)/He system. Geochimica et Cosmochimica Acta, v. 75, 4194–4215.

Flint, J.J., 1974. Stream gradient as a function of order, magnitude, and discharge. Water Resources Research v. 10, p. 969–973.

Fossen, H., Tikoff, B., 1998, Extended models of transpression/transtension and application to tectonic settings, in Holdsworth, R.E., Strachan, R.A., Dewey, J.F., eds., Continental Transpressional and Transtensional Tectonics. Geological Society of London Special Publication, v. 135, p. 15-33.

Furlong, K.P., 1984, Lithospheric behavior with triple junction migration: An example based on the Mendocino triple junction. Physics of Earth and Planetary Interiors, v. 36, p. 213-233.

Gallagher, K., Stephenson, J., Brown, R., Holmes, C., Fitzgerald, P., 2005, Low temperature thermochronology and modeling strategies for multiple samples 1: vertical profiles. Earth Planetary Science Letters v. 237, n. 1-2, p. 193–208.

Galehouse, J.S., 1967, Provenance and paleocurrents of the Paso Robles Formation, California. Geological Society of America Bulletin, v. 78, n. 8, p. 951-978.

Gautheron, C., Tassan-Got, L., 2010, A Monte Carlo approach to diffusion applied to noble gas/helium thermochronology. Chemical Geology, v. 273, n. 3-5, p. 212-224.

Goodman, E.D., Malin, P.E., 1992; Evolution of the southern San Joaquin basin and mid-Tertiary “Transitional” tectonics, central California. Tectonics, v. 11, n. 3, p. 478-498.

Graham, S.A., 1976, Tertiary sedimentary tectonics of the central Salinian block of California. Stanford University Thesis.

Graham, S.A., 1978, Role of Salinian Block in evolution of the San Andreas fault system, California. AAPG Bulletin, v. 62, p. 2214-2231.

Graham, S.A., Stanley, R.G., Bent, J.V., Carter, J.B., 1989, Oligocene and Miocene paleogeography of central California and displacement along the San Andreas fault. Geological Society of America Bulletin, v. 101, p. 711–730.

Graymer, R.W., Langenheim, V.E., Roberts, M.A., and McDougall, K., 2014, Geologic and Geophysical Maps of the Eastern Three-Fourths of the Cambria 30′ × 60′ Quadrangle, Central California Coast Ranges: U.S. Geological Survey Scientific Investigations Map SIM-3287, scale 1:100,000.

Grove, M., Jacobson, C.E., Barth, A.P., and Vucic, A., 2003, Temporal and spatial trends of Late Cretaceous-early Tertiary underplating Pelona and related schist beneath southern California and southwestern Arizona. Geological Society of America Special Paper 374, p. 381-406.

Grove, K., 1993, Latest Cretaceous basin formation within the Salinian Terrane of west-central California. Geological Society of America Bulletin, v. 105, n. 4, p. 307-310.

Groome, W.G., and Thorkelson, D.J., 2009, The three-dimensional thermomechanical signature of ridge subduction and slab window migration. Tectonophysics, v. 464, n. 1-4, p. 70-83.

Greene, H.G., Lee, W.H.K., McCulloch, D.S., and Brabb, E.E., 1973, Fault map of the Monterey Bay region, California. USGS Miscellaneous Field Studies Map MF-518, 4 sheets, 1:200,000 scale.

Guenthner, W.R., Reiners, P.W., Ketcham, R.A., Nasdala, L., and Geister, G., 2013, Helium diffusion in natural zircon: Radiation damage, anisotropy, and the interpretation of zircon (U-Th)/He thermochronology. American Journal of Science, v. 313, p. 145-198. DOI: 10.2475/03.2013.01.

Hack, J.T., 1957. Studies of longitudinal stream profiles in Virginia and Maryland. U.S. Geological Survey Professional Paper, v. 294-B, p. 97.

Hall, C. A., Jr., 1974, Geologic map of the Cambria region, San Luis Obispo County, California, U.S. Geological Survey Miscellaneous Field Studies Map MF-599.

Hall, C. A., Jr., 1976, Geologic map of the San Simeon-Piedras Blancas region, San Luis Obispo County, California, U.S. Geological Survey Field Studies Map MF-784.

Hall, C. A., Jr., 1991, Geology of the Point Sur-Lopez Point region, Coast Ranges, California; a part of the southern California allochthon, Geological Society of America Special Paper 266, 40 pp.

Hall, C. A., Jr., Prior, S.W., 1975, Geologic map of the Cayucos-San Luis Obispo region, San Luis Obispo County, California, U.S. Geological Survey Field Studies Map MF-686.

Hardebeck, J.L., 2010, Seismotectonics and fault structure of the California central coast. Bulletin of the Seismological Society of America, v. 100, n. 3, p. 1031-1050. DOI:10.1785/0120090307

Hanson, K.L., Wesline, J.R., Lettis, W.R., Kelson, K.I., and Mezger, L., 1994, Correlation, ages, and uplift rates of Quaternary marine terraces: south-central coastal California, in Alterman, I.B., McMullen, R.B., Cluff, L.S., and Slemmons, D.B., eds., Seismotectonics of the Central California Coast Ranges, Geological Society of America Special Paper 292, p. 45-71.

Hanson, K.L., and Lettis, W.R., 1994, Estimated Pleistocene slip rate for the San Simeon fault zone, south-central California, in Alterman, I.B., McMullen, R.B., Cluff, L.S., and Slemmons, D.B., eds., Seismotectonics of the Central California Coast Ranges, Geological Society of America Special Paper 292, p. 133-150.

Hanson, K. L., Lettis, W.R., McLaren, M.K., Savage, W.U., Hall, N.T., 2004, Style and rate of quaternary deformation of the Hosgri fault zone, offshore south-central California, in Evolution of Sedimentary Basins/Offshore Oil and Gas Investigations—Santa Maria Province, Keller, M.A., ed., U.S. Geological Survey Bulletin 1995–BB.

Harkins N., Kirby, E., Heimsath, A., Robinson, R., Reiser, U., 2007, Transient fluvial incision in the headwaters of the Yellow River, northeastern Tibet, China, Journal of Geophysical Research, v. 112, F03S04. DOI:10.1029/2006JF000570

Hilley, G.E., Dumitru, T., Gudmundsdottir, M.H., Bürgmann, R., 2008, Exhumation history of the Sierra Azul block of the Santa Cruz mountains revealed using low temperature thermochronology. EOS Transactions, American Geophysical Union 89.53, Abstract T43E-02.

Hourigan, J.K, Reiners, PW., and Brandon, M.T., 2005, U-Th zonation-dependent alpha-ejection in (U-Th)/He chronometry. Geochimica et Cosmochim Acta, v. 69, p. 3349-3365.

Hovius, N., Stark, C.P., Allen, P.A., 1997, Sediment flux from a mountain belt derived by landslide mapping. Geology v. 25, p. 231–234.

Howard, A., 1994, A detachment-limited model of drainage basin evolution. Water Resources Research, v. 30, p. 2261–2285.

Jacobson, C.E. Grove, M., Vucic, A., Pedrick, J.N., Ebert, K.A., 2007, Exhumation of the Orocopia schist and associated rocks of southeastern California: relative roles of erosion, synsubduction tectonic denudation, and middle Cenozoic extension. Geological Society of America Special Paper 419, p. 1-37.

Jacobson, C.E., Grove, M., Pedrick, J.N., Barth, A.P., Marsaglia, K.M., Gehrels, G.E., and Nourse, J.A., 2011, Late Cretaceous–early Cenozoic tectonic evolution of the southern California margin inferred from provenance of trench and forearc sediments. Geological Society of America Bulletin, v. 123, p. 485–506. DOI:10 .1130 /B30238.1

Jennings, C.W., Bryant, W.A., 2010, Fault activity map of California. California Geological Survey, Geologic Data Map No. 6, scale 1:750,000.

Jennings, C.W., with modifications by Gutierrez, C., Bryant, W., Saucedo, G, Wills, C., 2010, Geologic map of California. California Geological Survey, Geologic Data Map No. 2, scale 1:750,000.

Johnson, S.Y., Hartwell, S.R., and Dartnell, P., 2014, Offset of latest Pleistocene shoreface reveals slip rate on the Hosgri strike-slip fault, offshore central California. Bulletin of the Seismological Society of America, v. 104, n. 4, p. 1650-1662.

Jones, R.R., Holdsworth, R.E., Clegg, P., McCaffrey, K.J.W., Tavarnelli, E., 2004. Inclined transpression. Journal of Structural Geology, v. 26, p. 1531-1548.

Karrow, T., Hampel, A., 2010, Slip rate variations on faults in the Basin-and-Range province caused by regression of late Pleistocene Lake Bonneville and Lake Lahontan. International Journal of Earth Sciences, v. 99, n. 8, p. 1941-1953.

Kidder, S., and Ducea, M.N., 2006, High temperatures and inverted metamorphism in the schist of Sierra de Salinas, California, Earth Planetary Science Letters, v. 241, p. 422-437.

Kidder, S., Ducea, M.N., Gehrels, G., Patchett, P.J., and Vervoort, J., 2003, Tectonic and magmatic development of the Salinian Coast Ridge belt, California. Tectonics, v. 22, n.5, 1058.

Kirby, E., Whipple, K.X., 2001. Quantifying differential rock-uplift rates via stream profile analysis. Geology, v. 29, p. 415–418.

Kirby, E., Whipple, K.X., 2012, Expression of active tectonics in erosional landscapes. Journal of Structural Geology, v. 44, p. 54-75. DOI:10.1016/j.jsg.2012.07.009

Kistler, R.W., Champion, D.E., 2001, Rb-Sr whole-rock and mineral ages, K-Ar, 40Ar/39Ar, and U-Pb mineral ages, and strontium, lead, neodymium, and oxygen isotopic compositions for granitic rocks from the Salinian composite terrane, California. U.S. Geological Survey Open-File Report 01-453, 84 p.

Lachenbruch, A.H., and Sass, J.H., 1980, Heat flow and energetics of the San Andreas Fault Zone. Journal of Geophysical Research, v. 85, n. B11, p. 6185-6222.

Lajoie, K.R., Weber, G.E., Mathieson, S.A., and Wallace, J., 1979, Quaternary tectonics of coastal Santa Cruz and San Mateo counties, California, as indicated by deformed marine terraces and alluvial deposits, in Weber, G.E., Lajoie, K.R., and Griggs, G. B., eds., Coastal tectonics and coastal geologic hazards in Santa Cruz and San Mateo counties, California. Geological Society of America Field Trip Guidebook, p. 61-80.

Langenheim, V.E., Jachens, R.C., Graymer, R.W., Colgan, J.P., Wentworth, C.M., and Stanley, R.G., 2013, Fault Geometry and cumulative offsets in the central Coast Ranges, California: Evidence for northward increasing slip along the San Gregorio-San Simeon-Hosgri fault. Lithosphere, v. 5, p. 29-48.

Larsen, I.J., Montgomery, D.R., 2012, Landslide erosion coupled to tectonics and river incision. Nature Geoscience, v. 5, n. 7, p. 468-473. DOI:10.1038/ngeo1479

Lettis, W. R., Hanson, K.L., Unruh, J.R., McLaren, M., Savage, W.U., 2004, Quaternary tectonic setting of south-central coastal California, U.S. Geological Survey Bulletin 1995-AA, 21 pp.

Lori, L.M.A., 2016, Exhumation of the Nacimiento block: a thermochronologic analysis. Missouri University of Science and Technology Thesis, 138 p.

Mancktelow, N.S., Grasemann, B., 1997, Time-dependent effects of heat advection and topography on cooling histories during erosion. Tectonophysics, v. 270, p. 167–195.

Mattinson, J.M., 1978, Age, origin, and thermal histories of some plutonic rocks from the Salinian Block of California. Contributions to Mineralogy and Petrology, v. 67, p. 233-245.

McKittrick, M.A., 1988, Elevated marine terraces near Monterey, California. University of Arizona Thesis, 46 p.

McLaren, M. K., Hardebeck, J.L., van der Elst, N., Unruh, J., Bawden, G.W., Blair, J.L., 2008, Complex faulting associated with the 22 December 2003 Mw 6.5 San Simeon, California earthquake, aftershocks and post-seismic deformation, Bulletin of the Seismological Society of America, v. 98, p. 1659–1680.

Meesters, A.G.C.A., Dunai, T.J., 2002, Solving the production-diffusion equation for finite diffusion domains of various shapes Part 1: Implications for low-temperature (U-Th)/He thermochronology. Chemical Geology, v. 186, p. 333-444.

Merrits, D., and Bull, W.B., 1989, Interpreting Quaternary uplift rates at the Mendocino triple junction, northern California, from uplifted marine terraces. Geology, v. 17, p. 1020-1024.

Montgomery, D.R., 1993, Compressional uplift in the central California Coast Ranges. Geology, v. 21, p. 543-646.

Montgomery, D.R., 2001, Slope distributions, threshold hillslopes, and steady-state topography. American Journal of Science, v. 301, p. 432-454.

Montgomery, D.R., Dietrich, W.E., 1988, Where do channels begin? Nature, v. 366, p. 232-234. DOI:10.1038/336232a0

Montgomery, D.R., Brandon, M.T., 2002. Topographic controls on erosion rates in tectonically active mountain ranges. Earth Planetary Science Letters, v. 201, p. 481–489.

Mudd, S.M., Attal, M., Milodowski, D.T., Grieve, S.W.D., Valters, D.A., 2014, A statistical framework to quantify spatial variation in channel gradients using the integral method of channel profile analysis. Journal of Geophysical Research: Earth Surface, v. 119, p. 138-152. DOI:10.1002/2013JF002981

Naeser, C.W., and Ross, D.C., 1976, Fission-track ages of sphene and apatite of granitic rocks of the Salinian Block, Coast Ranges, California. Journal of Research of the U.S. Geological Survey, v. 4, n. 4, p. 415-420.

Niemi, N.A., Buscher, J.T., Spotila, J.A., House, M.A., Kelley, S.A., 2013, Insights from low-temperature thermochronometry into transpressional deformation and crustal exhumation along the San Andreas fault in the western Transverse Ranges, California. Tectonics, v. 32, p. 1602-1622. DOI: 10.1002/2013TC003377

Nilsen, T.H., 1981, Early Cenozoic stratigraphy, tectonics and sedimentation of the central Diablo Range between Hollister and New Idria. Pacific Section SEPM Field Trip Guide Book.

Ólafsdóttir, K.B., Schulz, M., Mudelsee, M., 2016, REDFIT-X: Cross-spectral analysis of unevenly spaced paleoclimate time series. Computers and Geosciences, v. 91, p. 11-18. DOI:10.1016/j.cageo.2016.03.001

Ouimet, W.B., Whipple, K.X., Granger, D.E., 2009, Beyond threshold hillslopes: channel adjustment to base-level fall in tectonically active mountain ranges. Geology v. 37, p. 579–582.

Page, B.M., Thompson, G.A., Coleman, R.G., 1998, Late Cenozoic tectonics of the central and southern Coast Ranges of California. Geological Society of America Bulletin, v. 110, p. 846–876.

Perg, LA., Anderson, R., Finkel, R.C., 2001, Use of new 10Be and 26Al inventory method to date marine terraces, Santa Cruz, CA, USA. Geology, v. 29, p. 879-882.

Perron, J.T., Royden, L., 2013, An integral approach to bedrock river profile analysis. Earth Surface Processes and Landforms, v. 38, p. 570-576.

Powell, R.E., 1993, Balanced palinspastic reconstruction of pre-late Cenozoic paleogeology, southern California: Geologic and kinematic constrains on evolution of the San Andreas fault system, in Powell, R.E., Weldon, R.J., and Matti, J.C., eds., The San Andreas fault system: Displacement, Palinspastic reconstruction, and geologic evolution, Geological Society of America Memoirs 178, p. 1-106.

Puchol, N., Lave, J., Lupker, M., Blard, P., Gallo, F., France-Lanord, C., ASTER Team, 2014, Grain-size dependent concentration of cosmogenic 10Be and erosion dynamics in a landslide-dominated Himalayan watershed. Geomorphology, v. 224, p. 55-68. DOI:10.1016/j.geomorph.2014.06.019

Reiners, P.W., Brandon, M.T., 2006, Using thermochronology to understand orogenic erosion. Annual Reviews of Earth and Planetary Science, v. 34, p. 419-466.

Reiners, P.W., Spell, T.L., Nicolescu, S., Zanetti, K.A., 2004, Zircon (U-Th)/He thermochronometry: He diffusion and comparisons with 40Ar/39Ar dating. Geochimica Cosmochimica Acta, v. 68, p. 1857-1887.

Reiners, P. W., S. N. Thomson, D. McPhillips, R. A. Donelick, and J. J. Roering, 2007, Wildfire thermochronology and the fate and transport of apatite in hillslope and fluvial environments. Journal of Geophysical Research, v. 112, F04001, DOI:10.1029/2007JF000759.

Reiners, P.W., 2005, Zircon (U-Th)/He thermochronometry, in Reiners, P.W., and Ehlers, T.A., eds., Low-temperature thermochronology: techniques, interpretations, and applications: Reviews in Mineralogy and Geochemistry Volume 58, p. 151-179.

Roering, J.J., Kirchner, J.W., Dietrich, W.E., 1999, Evidence for nonlinear, diffusive sediment transport on hillslopes and implications for landscape morphology. Water Resources Research, v. 35, n. 3, p. 853-970.

Rolandone, F., Bürgmann, R., Agnew, D.C., Johanson, I.A., Templeton, D.C., d'Alessio, M.A., Titus, S.J., DeMets, C, Tikoff, B., 2008, Aseismic slip and fault-normal strain along the central creeping section of the San Andreas fault. Geophysical Research Letters, v. 35, L14305. DOI: 10.1029/2008GL034437

Rosenberg, L., Clark, J.C., 2009, Map of the Rinconada and Reliz fault zones, Salinas River valley, California. U.S. Geological Survey Scientific Investigations Map SIM-3059.

Ross, D.C., 1976, Reconnaissance geologic map of pre-Cenozoic basement rocks, northern Santa Lucia Range, Monterey County, California: U.S. Geological Survey Miscellaneous Field Studies Map MF-750, 7 p., 2 sheets, scale 1:125,000.

Roy, M., Royden, L.H., 2000, Crustal rheology and faulting at strike-slip plate boundaries 2. Effects of lower crustal flow. Journal of Geophysical Research, v. 105, n. B3 p. 5599-5613.

Royden, L.H., Clark, M.K., Whipple, K.X., 2000, Evolution of River Elevation Profiles by Bedrock Incision: Analytical Solutions for Transient River Profiles Related to Changing Uplift and Precipitation Rates. EOS, Transactions American Geophysical Union 81, Fall Meeting Supplement, Abstract T62F-09.

Ruetz, J.W., 1979, Paleocene submarine fan deposits of the Indians Ranch area, Monterey County, California, in Pacific Coast Paleogeography Field Guide #4: Tertiary and Quaternary Geology of the Salinas Valley and Santa Lucia Range, Monterey County, California, Pacific Section Society for Sedimentary Geology, p. 13-24.

Schwanghart, W., Scherler, D., 2014, TopoToolbox 2 – MATLAB-based software for topographic analysis and modeling in Earth surface sciences. Earth Surface Dynamics, v. 2, p. 1-7. DOI:10.5194/esurf-2-1-2014

Saleeby, J.B., 2003, Segmentation of the Laramide slab: Evidence from the southern Sierra Nevada region. Geological Society of America Bulletin, v. 115, n. 6, p. 655-668.

Saleeby, J.B., Farley, K.A., Kistler, R.W., Fleck, R.J., 2007, Thermal evolution and exhumation of deep-level batholithic exposures, southernmost Sierra Nevada, California. Geological Society of America Special Paper 419, p. 39-66.

Sanderson, D., Marchini, R.D., 1984, Transpression. Journal of Structural Geology, v. 6, p. 449-458.

Schmidt, K.M., Montgomery, D.R., 1995. Limits to relief. Science v. 270, p. 617–620.

Shea, W.T., Kronenberg, A.K., 1992, Rheology and deformation mechanisms of an isotropic mica schist. Journal of Geophysical Research, v. 97, n. B11, p. 15201-15237.

Shikakura, Y., Fukahata, Y., Matsu'ura, M., 2012, Spatial relationship between topography and rock uplift patterns in asymmetric mountain ranges based on a stream erosion model. Geomorphology, v. 138, p. 162-170. DOI:10.1016/j.geomorph.2011.09.002

Simpson, G.D., Thompson, S.C., Noller, J.N., Lettis, W.P., 1997, The northern San Gregorio Fault Zone: Evidence for the timing of late Holocene earthquakes near Seal Cove, California. Bulletin of the Seismological Society of America, v. 87, no. 5, p. 1158-1170.

Sorby, A.P., England, P.C., 2004. Critical Assessment of Quantitative Geomorphology in the Footwall of Active Normal Faults, Basin and Range Province, Western USA. EOS Transactions American Geophysical Union 85, Fall Meeting Supplement, Abstract T42B-02.

Snyder, N.P., Whipple, K.X., Tucker, G.E, Merrits, D.J., 2000, Landscape response to tectonic forcing: digital elevation model analysis of stream profiles in the Mendocino triple junction region, northern California. Geological Society of America, Bulletin, v. 112, p. 1250-1263.

Snyder, N.P., Whipple, K.X., Tucker, G.E, Merrits, D.J., 2003, Channel response to tectonic forcing: Field analysis of stream morphology and hydrology in the Mendocino triple junction region, northern California. Geomorphology, v. 53, p. 97–127.

Spotila, J.A., 2005, Applications of low-temperature thermochronometry to quantification of recent exhumation in mountain belts, in Reiners, P.W., and Ehlers, T.A., eds., Low-temperature thermochronology: techniques, interpretations, and applications: Reviews in Mineralogy and Geochemistry Volume 58, p. 449-466.

Spotila, J.A., Farley, K.A., Yule, D., and Reiners, P.W., 2001, Near-field transpressive deformation along the San Andreas fault zone in southern California, based on exhumation constrained by (U-Th)/He dating. Journal of Geophysical Research, v. 106, n. B12, p. 30,909-30,922.

Spotila, J.A., Niemi, N., Brady, R., House, M., Buscher, J., Oskin, M., 2007, Long-term continental deformation associated with transpressive plate motion: the San Andreas fault. Geology, v. 35, p. 967-970.

Stock, J., Dietrich, W.E., 2003, Valley incision by debris flows: Evidence of a topographic signature. Water Resources Research, v. 39, n. 4, 1089. DOI: 10.1029/2001WR001057

Stüwe, K., White, L., and Brown, R., 1994, The influence of eroding topography on steady-state isotherms. Application to fission-track analysis. Earth and Planetary Science Letters, v. 124, p. 63-84.

Sylvester, A.G., 1988, Strike slip faults, Geological Society of America Bulletin, v. 100, n. 11, p. 1666-1703.

Tikoff, B. Fossen, H., 1993, Simultaneous pure and simple shear: the unified deformation matrix. Tectonophysics, v. 217, p. 267-283.

Titus, S.J., Housen, B., Tikoff, B., 2007, A kinematic model for the Rinconada fault system in central California based on structural analysis of en echelon folds and paleomagnetism. Journal of Structural Geology, v. 29, p. 961-982.

Titus, S.J., Dyson, M., DeMets, C., Tikoff, B., Rolandone, F., 2011, Geologic versus geodetic deformation adjacent to the San Andreas fault, central California. Geological Society of America Bulletin, v. 123, n. 5-6, p. 794-820.

Turcotte, D.L., Schubert, G., 2002, Geodynamics, 2nd ed. Cambridge University Press, New York, NY, 456 pp.

Trask, P.D., 1926, Geology of Point Sur quadrangle, California. University of California Publications, Bulletin of the Department of Geological Sciences, v. 16, no. 6, p. 119–186, 1 sheet, scale 1:62,500.

Wiebe, R.A., 1966, Structure and petrology of Ventana Cones area, California. Stanford University Thesis, 95 p.

U.S. Geological Survey and California Geological Survey, 2006, Quaternary fault and fold database for the United States, accessed Dec 1, 2013, from http://earthquakes.usgs.gov/regional/qfaults/

Valla, P.G., van der Beek, P.A., Braun,J., 2011, Rethinking low-temperature thermochronology data sampling strategies for quantification of denudation and relief histories: A case study in the French western Alps. Earth and Planetary Science Letters, v. 307, p. 309-322. DOI:10.1016/j.epsl.2011.05.003

Valensise, G., and Ward, S.N., 1991, Long-term uplift of the Santa Cruz coastline in response to repeated earthquakes along the San Andreas Fault. Bulletin of the Seismological Society of America, v. 81, n. 5, p. 1694-1704.

Vedder, J.G., Brown, R.D., 1968, Structure and stratigraphic relations along the Nacimiento fault in the southern Santa Lucia range and San Rafael Mountains, California, in Dickenson, W.R., and Grantz, A., eds., Proceedings of a conference on Geologic Problems of the San Andreas Fault System. Stanford University Publications in the Geological Sciences 11, p. 242-259.

Weber, G.E., 1990, Late Pleistocene slip rates on the San Gregorio fault zone at Point Ano Nuevo, San Mateo County, California, in Garrison, R.E., Greene, H.G., Hicks, K.R., Weber, G.E., and Wright, T.L., eds., Geology and tectonics of the Central California coast region, San Francisco to Monterey: Pacific Section, American Association of Petroleum Geologists Book GB67, p. 193-203.

Weber, G.E., Nolan, J.M., Zinn, E.N., 1995, Determination of late Pleistocene-Holocene slip rates along the San Gregorio Fault Zone, San Mateo County, California: Final Technical Report, National Earthquake Hazard Reduction Program, Contract No. 1434-93-G-2336, 70 p., 4 oversize map sheets.

Whipple, K.X., 2004, Bedrock rivers and the geomorphology of active orogens. Annual Reviews in Earth and Planetary Science, v. 32, p. 151–185.

Whipple, K.X., Tucker, G.E., 1999, Dynamics of the stream-power river incision model: implications for height limits of mountain ranges, landscape response timescales, and research needs. Journal of Geophysical Research, v. 104, p. 17,661–617,674.

Willett, S.D., McCoy, S.W., Perron, J.T., Goren, L., Chen, C., 2014, Dynamic reorganization of river basins. Science, v. 343, 1248765. DOI:10.1126/science.1238765

Wobus C., Whipple, K.X., Kirby, E., Snyder, N., Johnson, J., Spyropolou, K., Crosby, B., Sheehan, D., 2006, Tectonics from topography: procedures, promise, and pitfalls, in Willett, S.D., Hovius, N., Brandon, M.T., Fisher, D.M., eds, Tectonics, Climate, and Landscape Evolution. Geological Society of America Special Paper 398, p. 55–74.

Young, H., Hilley, G., Blisniuk, K., Kiefer, K., 2015, Millennial-scale Denudation Rates of the Santa Lucia Mountains, CA: implications for landscape thresholds from a steep, high relief, coastal mountain range. EOS Transactions, American Geophysical Union, Abstract #EP53B-1016.

Zeitler, P.K., Herczeg, A.L., McDougal, I., Honda, M., 1987, U-Th-He dating of apatite: a potential thermochronometer. Geochimica et Cosmochimica Acta, v. 51, p. 2865-2868.

CHAPTER 4

DISCRETE MULTI-PULSE LASER ABLATION DEPTH PROFILING WITH A SINGLE-COLLECTOR ICP-MS: SUB-MICRON U-PB GEOCHRONOLOGY OF ZIRCON AND THE EFFECT OF RADIATION DAMAGE ON DEPTH-DEPENDENT FRACTIONATION

ABSTRACT

A discrete multi-pulse method for single-collector ICP-MS laser ablation systems is presented that interrogates isotopic variation as a function of sample depth. The fidelity of the method is assessed with a 183-sample U-Pb analysis session of zircons with known age. By using bursts of 5 laser pulses the method resolves integration-level ages with ~0.55 μm depth resolution and ~6% 2σ age uncertainty. To avoid signal aliasing, isotopic ratios are calculated using total ion counts for each integration, instead of on a cycle-by-cycle basis. Fractionation correction is achieved by constructing a continuous-function, non-parametric 3D surface from which discrete values for any time and sample depth can be calculated. At the sample level (15 integrations for this study), average 2σ uncertainty is ~2.5% for $^{206}Pb/^{238}U$ ages; 95% of samples and ~90% of integrations overlap with their accepted age at 2σ. The data reduction software developed here is designed to be flexible and a discussion of the effects of varying method parameters is provided. Total ablation depth is measured using white light interferometry, ranges between 7 and 10 μm and is found to vary as a function of parent radionuclide concentration, measures of crystal lattice disorganization from Raman spectroscopy, and metrics of radiation damage (alpha dose). These data indicate that radiation damage exerts a fundamental control on laser ablation efficiency, although the exact physical process is unknown at present. Consequently, fractionation correction factors derived for a reference material may not be appropriate for unknowns with vastly different crystal structure.

INTRODUCTION

Ultraviolet laser ablation Inductively Coupled Mass Spectrometry (LA-ICPMS) is an increasingly common tool used to extract isotopic and chemical data from a variety of geochemical reservoir materials. Recent advances within the geochronologic community have led to the development of new methods and instrument designs that enable routine acquisition of large age and/or trace-element data sets with accuracy and precision approaching the ~1-3% level

(Kosler et al., 2002; Gehrels et al., 2008, Frei and Gerdes, 2009). Exact methodological details vary significantly between laboratories, but a single zircon spot analysis typically consists of 10-30 seconds of baseline data collection followed by 20-60 seconds of on-peak data collection, during which time the UV laser is pulsed continuously at a fixed rate between 5 hz and 10 hz depending on individual lab instrumentation and sample delivery methods (e.g. Jackson et al., 2004; Gehrels et al., 2008; Chew et al., 2011). The ablated and aerosolized zircon is exported from the ablation cell by helium carrier gas and mixed with argon sample gas prior to injection into an inductively coupled plasma stream. The isotopic composition of the zircon is then measured using either a single- (quadrupole or sector field) or a multi-collector ICP-MS system.

Typical analytical procedures employing continuously-pulsed laser ablation produce a single age for each targeted grain. However, accurate and precise depth-resolved data have the capacity to answer a wide range of questions which are difficult to resolve with continuous ablation, such as probing fine-scale variations in crystallization age or metamorphic crystal overgrowths (Cottle et al., 2009a), measuring chemical diffusion profiles in experimental petrology (Till et al., 2012), determining concentration gradients through mineral grains (e.g. Blackburn et al., 2011), or reconstructing paleo-ocean temperatures using the micro-stratigraphy of calcareous forams (e.g. Eggins et al., 2003). The reason for this difficulty is that sample aerosol produced by continuously pulsed laser ablation undergoes significant mixing with aerosol ablated during both antecedent and subsequent pulses within the ablation cell and transport tubing. As an outside case, this convolution might produce time-series data with a functional form of a diffusion profile, while the sample contains a chemical step function. Cell design advances in recent years (Eggins, 1998; Woodhead et al, 2004) have targeted improvement of washout efficiency to limit mixing and thereby improve spatial resolution. Improved efficiency, however, results in an increased magnitude of signal transients at frequencies comparable to that of data acquisition cycles, thereby increasing signal aliasing. To combat this, many labs employ some manner of signal smoothing device in the carrier gas delivery system, effectively discarding much of the spatial resolution attained with a faster washout cell.

Several workers have extracted depth-resolved data from continuously-pulsed ablation (e.g. Patton et al., 2010; Tollstrup et al., 2012) by selecting subsets of incoming data, but many difficulties remain. For example, although it is theoretically possible to deconvolve a mixed signal if the response function of the laser cell is known, such approaches are mathematically non-unique. This ambiguity makes assigning a given analysis (age, concentration, or otherwise) to a precise depth difficult, although depending on the analytical precision required this level of ambiguity may be acceptable. Yet other laser ablation techniques have been developed that construct isotopic maps by rastering exposed grain sections or faces (e.g. Farley et al., 2011; Cottle et al., 2009b; Gehrels et al., 2008). These maps can be combined to create pseudo depth profiles by sequentially sectioning through the grain (Farley et al., 2011). However, limitations imposed by laser spot size (~10-30 μm), and the desire to retain as much grain as possible for either future LA-ICP-MS sampling or thermochronometry make sequential grain sectioning an unattractive option. Secondary Ion Mass Spectrometry depth profiling has the capacity to deliver depth resolution better than ~0.5 μm, but can only do so over relatively shallow total depths and has lower throughput than laser ablation (Breeding et al, 2004; Vorhies et al, 2013).

To more robustly tie analyses to depth, we adopt the approach developed by Cottle and coworkers (2009a) that isolates and analyzes small, discrete volumes of material. In this contribution, their single-pulse/multi-collector approach is modified for use with more common and less expensive single collector ICP-MS systems, and contains additional treatment of laser-induced down-hole fractionation. For this type of analysis the use of a single-collector ICP-MS introduces additional complication over a multi-collector system. During short laser activation analyses, the pulsed nature of aerosol delivery and 'plasma flicker' result in signal aliasing and highly variable cycle-by-cycle ratios. One solution is expeditious cycling through the analysis table in order minimize the time delay between subsequent data points. However, rapidity comes at the expense of noise quantization in low count rate signals. Single-collector data acquisition strategies must therefore compromise between rapid sampling to limit signal aliasing and increased dwell times to reduce noise quantization. Multi-collection mitigates these issues to a significant extent; however, the differential response times of mixed mode (faraday – ion counter) collector arrays during very short (single pulse or low-volume) analyses also requires alternate data handling procedures (e.g. Johnston et al, 2009; Cottle et al., 2009a; 2012). One solution that minimizes the inevitable signal aliasing cause by short-period transient signals is to integrate the total counts for each aerosol wave and calculate a single ratio (e.g. Johnston et al, 2009; Cottle et al., 2009a; 2012). Here, this method is generalized for use with a single collector LA-ICP-MS to demonstrate the feasibility of high depth-resolution zircon U-Pb geochronology. While specifically applied to U-Pb analysis, it is important to note that the concept, methods, and software are appropriate for depth resolved analysis of other chemical systems, particularly when coupled to single collector ICP-MS system.

DISCRETE MULTI-PULSE DEPTH PROFILE METHOD

INSTRUMENTATION

Sample ablation is achieved with a PhotonMachines Analyte 193H, a 193-nm ArF excimer laser system fitted with a Helex 2-volume sample chamber for improved washout of analyte aerosols (after Eggins et al, 2005). Material is ablated in a He-gas atmosphere, mixed with Ar carrier gas after exiting the sample chamber and transported through a ten-conduit, ~1.5 m - long tuned-length Teflon 'Squid' signal smoothing device. The Squid effectively attenuates peak signal intensity and lengthens delivery time of the analyte resulting in a well-mixed and smooth signal. For high concentration ions such as ^{238}U, the attenuated signal lowered peak count rates below the threshold for the digital/analog cutoff in this study. We use a spot size of 34 µm, energy stabilized laser fluence of 4.0 Jcm^{-2}, and repetition rate of 10 hz, which are the standard operating parameters for the Plasma Analytical facility at the University of California, Santa Cruz.

Isotopic data were collected with a ThermoScientifc ElementXR single-collector magnetic sector ICPMS; analytical parameters and conditions are summarized in Table 4-1. For U-Pb analyses the ElementXR is operated in electrostatic mode allowing rapid peak-hopping within the range of collected ions. Data are collected on ^{202}Hg, ^{204}Pb, ^{206}Pb, ^{207}Pb, ^{208}Pb, ^{232}Th, ^{235}U, and ^{238}U for a total run cycle time of 120 ms, 102 ms of which are on-peak; the remainder represents total dead time during peak hops between ions. Approximately half of this settling time is required to shift from ^{238}U back to ^{202}Hg, so although a small amount of settling time reduction could be gained by eliminating ^{202}Hg, ^{208}Pb, ^{232}Th, and ^{235}U the proportional change would not necessarily balance losing the ability to independently measure ^{235}U, Th-Pb ages, or to perform a ^{202}Hg correction if necessary. However, the needs of each analyst will vary and for some types of determinations, this may be an acceptable trade-off; the choice of ions and dwell times for this study is intended only to represent one of many possible parameter selections.

Table 4-1. ICP-MS and laser ablation analytical parameters used in this study.

ThermoScientific ElementXR single-collector magnetic sector ICPMS	
Isotopes (ms dwell time)	^{202}Hg (15), ^{204}Pb (15), ^{206}Pb (15), ^{207}Pb (30), ^{208}Pb (15), ^{232}Th (3), ^{235}U (6), and ^{238}U (3)
Collection mode	Electrostatic peak hopping
Collector type	Discrete-dynode electron multiplier with automatic digital/analog cutoff
Carrier gas and flow rate	0.75 L/min He gas to Helex cell, 0.75 L/min Ar gas upon exit from Helex
Auxillary gas flow rate	~1 L/min
Cooling gas flow rate	18 L/min
Forward RF power	1200 W
Baseline data acquisition	30 seconds
On-peak signal acquisition	82.5 seconds
Sample washout time	20 seconds
Burst cycles per sample	15
Photon Machines 193H ArF Excimer Laser	
Wavelength	193 nm
Fluence	4.0 J cm^{-2}
Spot size	34μm
Sample cell	Two-volume Helex cell
Sample delivery	3mm ID, ~1.5 m-length, 10-conduit tuned-length Tygon 'squid' sample smoothing plenum
Repetition rate	Burst of 5 laser pulses at 10 hz
Repeat delay between bursts	5 seconds

Topography of ablated laser pits was measured with a Zygo NewView 7200 white-light vertical-scanning interferometer—a non-contact 3D surface mapping tool that utilizes sophisticated image acquisition hardware and processing software to extract topographic maps from complex surfaces. The optics are such that interference fringes appear only on those parts of the surface that are in focus. A vertical-scanning piezoelectric stage system with 1nm vertical reproducibility is used to change the focal plane elevation. For a given elevation, a subset of the pixels will reflect fringes, which are registered as in-focus. A sequence of images, gathered at different elevations, is then processed to create a nm-resolution topographic map of the target. All measurement was carried out with a 100X Mirau objective and 0.5X field zoom lens resulting in a horizontal resolution of 224 nm and a sub 1 nm vertical resolution.

Raman spectra for each ablated grain were collected using a Horiba Scientific LabRAM HR Evol over a range of wavenumbers from 900-1200 cm^{-1} with a 633 nm green diode laser. Measurements were calibrated by analyzing the M146 zircon standard of Nasdala et al (2004) who showed that for zircon, increasing alpha-dosage results in a systematic shift and broadening of the diagnostic Raman spectra peak related to the v_3 Zr-SiO_4 stretching bond and is indicative of increasing amounts of crystal lattice disorganization. Zircons with little disorganization have sharp, narrow peaks at 1007 cm^{-1}, whereas zircons with high levels of disorganization have much broader peaks near 997 cm^{-1} (Nasdala et al, 2004; Guenthner et al, 2013).

SAMPLE PREPARATION AND ANALYTICAL METHOD

Individual zircon grains and grain fragments were mounted on 2” double-sided sticky tape and fixed with Struers Epofix epoxy using a 1” internal diameter ring form. After curing, samples were polished just enough to expose most grains in successive steps with 600- and 1500-grit paper, and then with 9-, 3-, and 1-μm diamond suspension on a Struers LabPol polishing station. In this study, grains were sectioned and polished to demonstrate method performance under idealized mounting conditions. Mounting euhedral grains directly on double-sided sticky tape or indium would facilitate analysis of chemical gradient at grain margins and allow their removal for other subsequent analyses. Prior to installation in the Helex 2 cell, the 1” round was washed in 1% HNO_3 and rinsed with MilliQ water to remove surface contaminants. No scanning electron microscopy or cathodoluminescence imaging was performed prior to analysis and no laser pre-ablation passes were performed prior to data acquisition.

The discrete multi-pulse method presented here differs from conventional continuously-pulsed laser sampling approaches and thus the nomenclature differs from typical studies. One analysis ‘session’ is composed of all the individual ‘samples’ analyzed for a given purpose. In this study, our session contains 183 samples of either idiomorphic grains or fragments of larger gem-quality zircons and includes both reference materials and unknowns. Each ‘sample’ is composed of many ‘integrations’ which are discrete analyses that increase in depth from first to last. The number of integrations for each sample ultimately defines the total depth, is a free parameter to be chosen by the analyst, and will vary depending on the specific needs of the session. The choice of 15 integrations per sample for this study was motivated by achieving depths of 8-10 μm, but is only meant to demonstrate one possible parameter choice. Each ‘integration’ is achieved by operating the laser for a set number of pulses, followed by a washout delay before the next sequence is initiated (Fig. 4-1). The number of pulses that comprise a single integration is another free parameter and determines the overall depth resolution of the technique; fewer pulses (up to a single pulse) yield finer resolution but sacrifice total counts and the ability to effectively quantify the shrinking amount of aerosol. For multi-collector systems which can

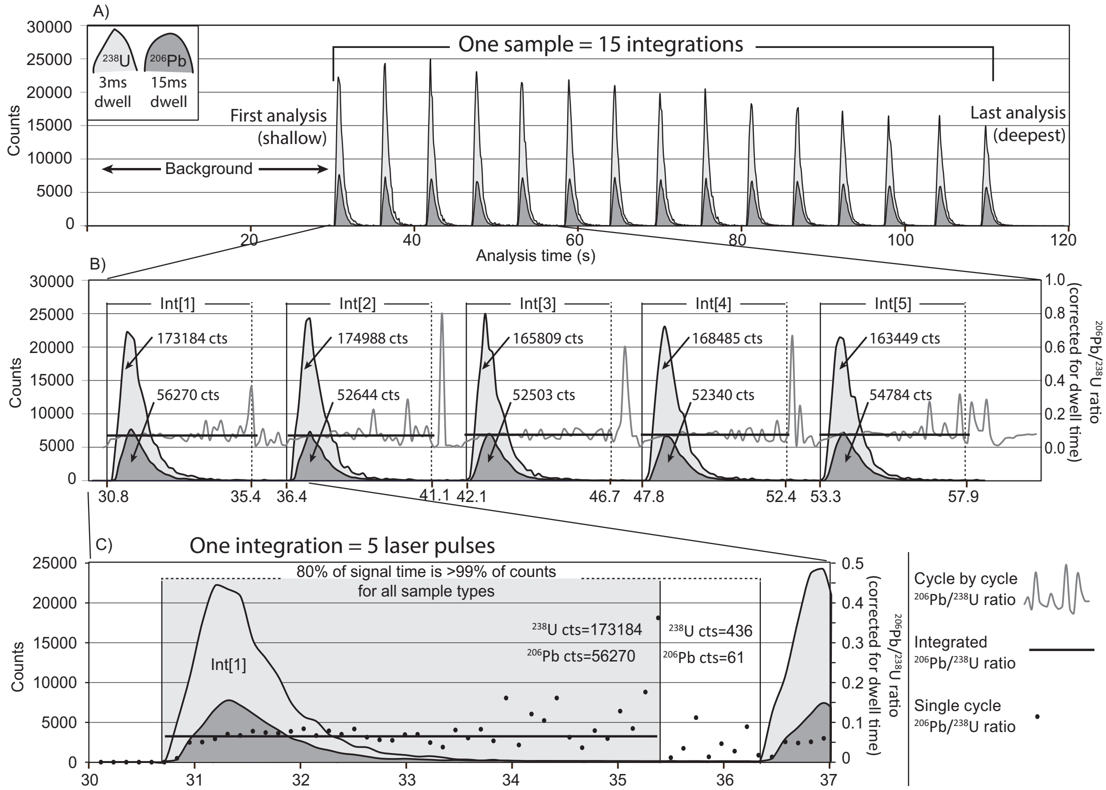

Figure 4-1. A) The ^{206}Pb and ^{238}U isotope spectra for an entire sample (first SLM reference zircon analysis): 30 seconds of baseline collection followed by 15 integrations of five laser pulses each, each with a five second pause before the subsequent integration; traces are scaled to show total counts. B) Expanded spectra of first five integrations diagraming the beginning and end of each cycle, the total counts used for each area (using ~4.5s of time), the cycle-by-cycle ^{206}Pb /^{238}U ratio, and the ratio calculated for each integration by summing the total counts of each isotope and correcting for dwell time. C) Expansion of the first integration to highlight the effects of signal aliasing on cycle-by-cycle ratios for short-duration analyses and the greater stability of the integrated counts approach. Faster cycling (and more ratio data points) could be gained by decreasing dwell times, but this leads to excessive noise due to quantization in low count-rate ion channels.

capture data on all ion channels simultaneously, a single pulse is enough data to produce results with acceptable uncertainty (e.g. Cottle et al., 2009a; 2012). However, for single-collector systems which must cycle through an analysis table, the comparable time scales of signal transience and ICP sampling for single-pulse analysis severely limits ratio precision. Thus, for this study we balanced the need for analyzing a broad range of concentrations against ultimate depth resolution with five pulses/integration. This choice resulted in acceptable uncertainty for all but the lowest count rate signals (<~20 ppm ^{238}U) and reasonable depth resolution. A future session that requires smaller uncertainty or is analyzing mostly low-concentration grains could increase the pulses/integration at the expense of depth resolution. Conversely, if ultimate depth resolution is of greatest importance, a careful optimization study must be performed to determine the necessary parameters. In any case, our choices for the free parameters of total number of integrations and pulses/integration are only meant to represent one possibility and to document a baseline case for future analysts.

The required delay between subsequent bursts of the laser, i.e. between integrations, varies as a function of cell and transport tubing geometry. For the UCSC Helex 2 with a Teflon Squid, the rise time to peak ion intensity is ~0.6s and background levels are reached by ~3s of initial signal in-growth. For all ion channels >99% of the integrated signal occurs within ~4.5s; we thus use a 5 second delay after ablation ceases to allow all of the signal to pass through the system prior to initiation of the next laser burst (integration). Baseline data acquisition is acquired by triggering ElementXR data collection 30 seconds prior to laser activation. For this experiment session, each sample consisted of 15 integrations, each with five laser pulses (0.5 s) and a five second delay for a cumulative signal acquisition time of 82.5 s followed by a 20 s washout prior to the subsequent sample baseline collection (Fig. 4-1). With a 34 μm spot size, this method resulted in discrete analyses with approximately 0.5 μm depth resolution (see below for detailed discussion of depth data).

To assess the precision and accuracy of the method and our choice of parameters, we performed a 183-sample round-robin analysis with a variety of zircons of known age and radiogenic parent concentrations (Table 4-2). A sample-standard bracketing approach is used to enable correction for mass bias and fractionation that occurs during the ablation, transport, ionization, and detection processes. We advocate the use of a primary and secondary reference material (RM) located after every five unknowns in order to assess the precision and accuracy of the corrections being applied. Additionally, several analyses of primary RM at the beginning and end of an analysis session is prudent as many data reduction packages use smoothing or averaging functions, which can be highly sensitive to outlier data near end points. Our choice of primary RM was motivated by the need for a readily available and homogenous zircon of known concentration. The 564.1 ± 1.4 Ma Sri Lanka zircon 'SLM' has been analyzed at the Arizona LaserChron center (n>150) in reference to the nearly identical aged 'SL2' zircon RM of Gehrels et al. (2008) by M. Grove (Stanford University, written commun., 2012). Although the

Table 4-2. Ages and concentrations of zircons used in this study.

Sample	Accepted Age ± 2σ	Method	^{238}U(ppm)	^{232}Th (ppm)	Source
SLM	564.1 ± 1.4	LA-ICPMS	~750	n.a.	M. Grove (Pers. Comm)
M146	567 ± 4	IMP	923 ± 17	411 ± 9	Nasdala et al (2004)
Plesovice	337.1 ± 0.4	ID-TIMS	465-1106 (755 avg)	37-188 (76 avg)	Slama et al (2008)
VP10	1198.4 ± 7.7	ID-TIMS	n.a.	n.a.	J. Wooden (Pers. Comm)
AS3	1099.1 ± 0.2	ID-TIMS	~200-1600	~140-1100	Paces and Miller (1993); Schmitz et al. (2003)
Mud Tank	732 ± 5	ID-TIMS	6-36	n.a.	Black and Gulson (1978)
WF1	n.p.d.	Q-ICPMS	26 ± 8	15 ± 7	In house Sri Lanka megacryst
WF2	n.p.d.	Q-ICPMS	1755 ± 61	775 ± 11	In house Sri Lanka megacryst
WF6	n.p.d.	Q-ICPMS	588 ± 6	58 ± 7	In house Sri Lanka megacryst
WF10	n.p.d.	Q-ICPMS	287 ± 4	276 ± 2	In house Sri Lanka megacryst

Notes: Accepted ages are a combination of ^{206}Pb/^{238}U, Concordia ages, and ^{207}Pb/^{206}Pb ages. LA-ICPMS-Laser ablation inductively-coupled plasma mass spectrometry; IMP-Ion Microprobe; ID-TIMS-Isotope dilution-thermal ionization mass spectrometry; Q-ICPMS-Quadrapole-inductively coupled plasma-mass spectrometry

use of a reference material dated by LA-ICPMS is less ideal than a reference material dated by ID-TIMS, it is adequate for the purposes of our method development. This assertion is validated by ages of well-characterized secondary reference zircons within uncertainty of their accepted values, i.e. if the age of 'SLM' were incorrect, it would be unable to produce correct ages for the secondary RMs. Analysts applying this method to geological questions should use a well characterized (ID-TIMS) primary RM as this decreases the external uncertainty of each analysis.

DATA REDUCTION—ICPMS DATA

Existing data reduction software packages typically calculate isotope ratios on a cycle-by-cycle basis, which contributes to signal noise because of aliasing effects related to periodic sampling of a highly transient signal (Fig. 4-1). Recent methods which calculate ratios from integrated total counts also require new data reduction techniques (e.g. Johnston et al., 2009; Cottle et al., 2012) as previous software is unable to make these calculations. Although our methods are similar to those of Cottle and coworkers (2012), the addition of robust down-hole fractionation corrections which are not necessary for single-pulse techniques and the automation of integration selection necessitated development of a new data reduction software package. Further, we operate within a multi-use analytical facility and wished to design a program with the flexibility to work with any sampling strategy (continuous or discrete) and for any type of isotopic inquiry. Thus, the LabVIEW-based data reduction program detailed below is a highly flexible process with peak- and edge-detection algorithms, multi- or single-cycle integration capability, and statistically rigorous uncertainty propagation. LabVIEW is a user-friendly programming environment with easily-deployable and intuitive graphical user interfaces, visualization tools, and mathematical models. Furthermore, LabVIEW code can be compiled as an executable that runs with a free runtime engine for ease of distribution. Data are stored in a proprietary streaming binary file format (*.tdms) for efficiency; these files can be opened in Excel with the TDMS file add-in. The software is available from the authors upon request.

INTEGRATION SELECTION AND PROGRAMMATIC 'EDGE' DETECTION

Our data processing approach utilizes programmatic detection of the start of ‘parcels’ or waves of ablated aerosol in the intensity time series. Alternative approaches could use absolute timing between integrations, or even couple ICPMS time-stamps with the laser log file, if available. However, slight fluctuations in the timing of the laser system can occur, which, for continuously-pulsed operation are insignificant, but for tightly-spaced methods such as this, slight fluctuations can result in systematically analyzing the wrong section of the time series. Also, although coupling laser log files and time-stamps is a robust means of defining when laser pulses are delivered (when these files are available), there are slight stochastic fluctuations in the transport of the aerosol which could be on the order of single analysis cycles and possibly result in ‘missing’ the first cycle of incoming data. Thus, although it represents an additional step in the processing of the data, simply detecting when each packet arrives is perhaps a more generalized and flexible procedure for assigning integrations.

Single-channel algorithms can produce spurious ‘edges’ as a result of random background counts in low dwell time channels. We therefore use an algorithm based on signal gain across multiple ion channels. A potential sample start is generated when the ^{238}U signal is either above a user-specified rate-of-change compared to the running average of the five previous data points, or greater than a user-specified threshold value. Start position is confirmed if three of the four other isotope channels (^{206}Pb, ^{207}Pb, ^{208}Pb, ^{232}Th) are greater than limits of detection (any on-peak signal that exceeds 3 standard deviations of the mean background signal). Remaining starts are filtered based on a user-set minimum distance between integrations (5.5 s for this study). The resulting start locations are displayed and the user can adjust parameters as necessary to optimize the automatic detection algorithm. Occasionally, the user may have to manually select the start location for a difficult-to-detect parcel.

Once sample starts have been selected, background lengths and offsets are applied based on user settings and individual samples are shown with automatically calculated integration starts and ends. Because of the discrete data cycles with a single-collector ICPMS, selection of the entire 5.5s integration window could double-sample data at the start or end with a neighboring integration. Thus, the user is able to choose what percent of the integration cycle is used for the calculation of ages, but this value is not allowed to vary throughout the session in order to maintain consistency. For this session, >99% of all counts occur before 4.5s and so we use this as our analysis window. This choice results in the software analyzing 39 to 41 cycles of data for each integration, with slight variations due to quantization of individual data cycles. All programmatically detected integration windows are visually inspected to ensure they capture the data correctly. For the 2745 individual integrations of our round-robin analysis <1% of calculated integration starts had to be changed and the entire process from raw data to selected and checked data took about 10 minutes.

BACKGROUND SUBTRACTION, COUNTING UNCERTAINTY, AND RATIO CALCULATION

After automated selection of background and integration time slices, the average per-cycle baseline for each isotope $\hat{B}_{jk}$ is calculated by dividing the total background counts by the number of run-table cycles over the baseline acquisition, n:

$$\hat{B}_{jk} = \sum\nolimits_{i=1}^{n} \left(r_{ij} \times t_j^{dwell} \right) \Big/ n \Big|_{j=1}^{q} \Bigg|_{k=1}^{r}$$

Where r_{ij}, is the count rate of the i^{th} cycle of the j^{th} isotope, and t_j^{dwell} is the per-cycle count time for the j^{th} isotope evaluated over all samples k → r (see Table 4-3 for equation definitions). Total baseline corrected on-peak counts for each integration, C_{jlk}^{bc} are evaluated over all isotopes, j → q, all integrations l → s for each sample, and all samples k → r:

$$C_{jlk}^{bc} = \sum\nolimits_{i=1}^{n} \left(r_{ij} \times t_j^{dwell} - \hat{B}_{jk} \right) \Big|_{j=1}^{q} \Bigg|_{l=1}^{s} \Bigg|_{k=1}^{r}$$

Table 4-3. Definition of variables used.

Variable Notation	Definition
$i \rightarrow n$	ICP-MS run cycle over which data is collected
$j \rightarrow q$	Range of isotopes over which data is collected
$k \rightarrow r$	Samples of the analytical session
$l \rightarrow s$	Integrations of each sample
$m \rightarrow v$	Isotope pairs (e.g. j_1=^{206}Pb, j_2=^{238}U)
$\hat{B}_{jk}$	Per-cycle background intensity
t_j^{dwell}	Dwell time for each isotope
t	Time during analytical session
r_{ij}	Count rate for ith cycle of the jth isotope
C_{jlk}^{bc}	Background-corrected total counts
E_{jlk}^{bc}	Poisson counting error for background-corrected counts
R_{mlk}^{obs}	Observed ratio of isotope pairs j_1 and j_2
$R_{mlk}^{\exp}$	Expected ratio of isotope pairs j_1 and j_2 for primary standards
f_{mlk}	Fractionation correction factor for primary standards
$f_m\left(l,t\right)$	Discrete-value fractionation correction function for primary standards
$\Phi_m\left(l,t\right)$	Continuous 3-D fractionation correction surface
Φ_{mlk}	Discrete value fractionation correction for all samples
Ψ_{mlk}	Fractionation-corrected isotopic ratios
E_{mlk}^{R}	Poisson-based error of each isotope ratio
$\hat{\theta}_{mk}$	Goodness-of-fit function for Ψ -induced error
δ_{mlk}	Cumulative internal uncertainty for all samples, integrations, and isotopic ratios

Internal count uncertainty for background-corrected counts E_{jlk}^{bc} is estimated by summing in quadrature the Poisson counting uncertainty from the baseline and on-peak signals:

$$E_{jlk}^{bc} = \sqrt{\left[\sum_{i=1}^{n}\left(r_{ij} \times t_j^{dwell}\right)\right] - n\hat{B}_{jk}}\Bigg|_{j=1}^{q}\Bigg|_{l=1}^{s}\Bigg|_{k=1}^{r}$$

Background-corrected isotopic ratios R_{mlk}^{obs} are evaluated over all isotope pairs, *m,* comprising total counts on isotopes j_1 and j_2, for each integration and sample with:

$$R_{mlk}^{obs} = C_{j_1kl}^{bc} \Big/ C_{j_2kl}^{bc}\Big|_{m=1}^{v}\Big|_{l=1}^{s}\Big|_{k=1}^{r}$$

The $^{207}Pb/^{235}U$ ratio was calculated using the measured ^{207}Pb and calculating ^{235}U using the canonical $^{238}U/^{235}U$ ratio of 137.88 (Jaffey et al, 1971) because of high analytical uncertainty associated with the low count rate ^{235}U signal.

CORRECTION FACTOR CALCULATION

An isotope ratio correction factor, f_{mlk}, is calculated for each isotopic ratio m, of each integration l for the primary standards as the ratio of the observed to expected values. For the round-robin data described below, each primary reference material (RM) analysis yields f_{mlk} values for each of the 15 integrations over all isotopic ratios:

$$f_{mlk} = R_{mlk}^{obs} / R_{mlk}^{\exp} \Big|_{m=1}^{v} \Big|_{l=1}^{s} \Big|_{k=1}^{primary-stds}$$

Because analyses are unevenly spaced during the analytical session we chose to convert the discrete fractionation correction values into a functional form with two variables (analytical session time, t, and integration, l) that is valid over all discrete observations of the primary RM for each ratio, m:

$$f_{mlk} \rightarrow f_m(l,t)\Big|_{m=1}^{v}$$

This conversion is essential to correctly smooth observed values and interpolate values to be applied to intervening 'unknown' samples. These discrete correction factors from primary RMs are then mapped into a continuous three dimensional estimator of fractionation correction, $\Phi_m(l,t)$:

$$f_m(l,t)\Big|_{m=1}^{v} \rightarrow \Phi_m(l,t)\Big|_{m=1}^{v}$$

We use a three-step smoothing method applied to the discrete primary RM correction factors to construct this surface. First, all integrations and ratios for an individual RM $f_m(t)\Big|_{l=1}^{s}$ are smoothed using a 7-term Henderson filter. Second, smoothed fractionation correction values for each integration are smoothed across the entire analytical session $f_m(l)\Big|_{k=1}^{primary\_stds}$ with a 15-term Spencer filter. Finally, a 2-D cubic spline of all smoothed discrete primary RM f values is used to construct the interpolated fractionation correction surface. The resulting three-dimensional surface is a non-parametric estimator of fractionation over all integrations at any time during the analytical session (Fig. 4-2). We then assign discrete fractionation correction values for each analysis based on its location on the surface:

$$\Phi_m\left(l,t\right)\Big|_{m=1}^{v} \rightarrow \Phi_{mlk}$$

The fractionation-corrected isotope ratios, Ψ_{mlk} , are calculated from these discrete values and the observed ratios with:

$$\Psi_{mlk} = R_{mlk}^{obs} / \Phi_{mlk}\Big|_{m=1}^{v}\Big|_{l=1}^{s}\Big|_{k=1}^{r}$$

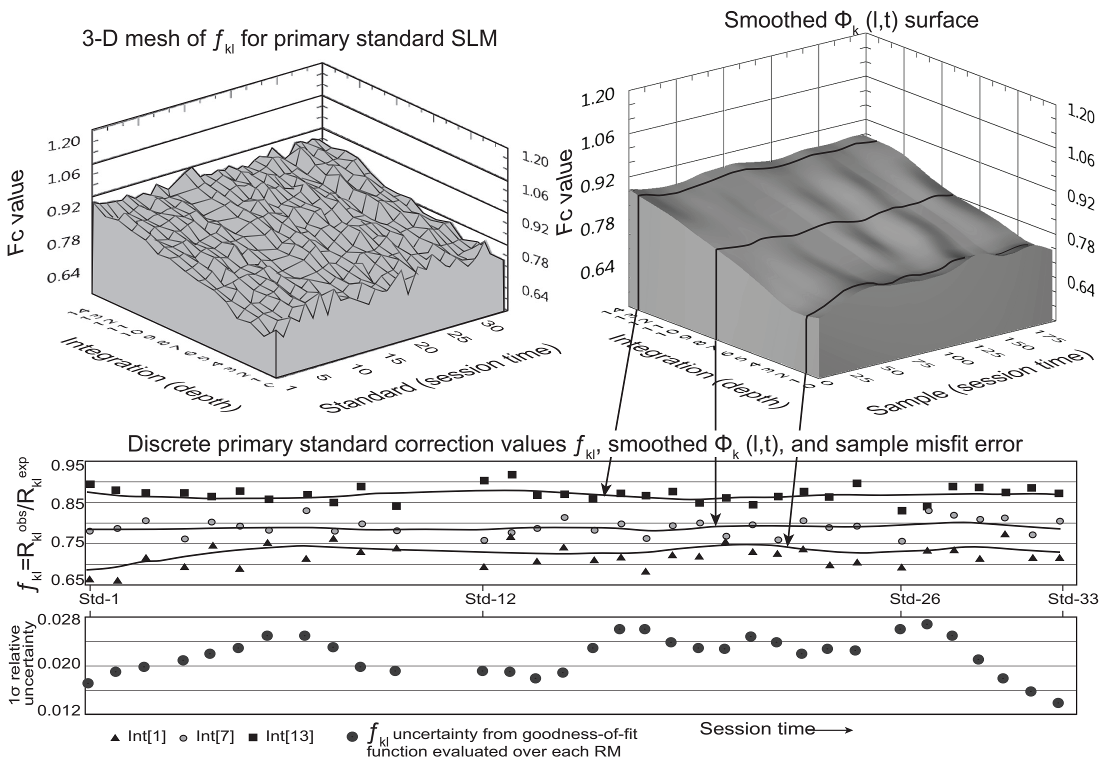

Figure 4-2. Left-side plot shows calculated correction factor mesh (f_{mlk}) as a function of integration and session placement for our reference zircon, SLM. The closest corner of the mesh is the first integration of the first standard analyzed, and the farthest corner is the last (deepest) integration of the last standard analyzed. Note the high variance in the first integrations of all samples, and the general down-hole trend towards unity. Right-side plot is the smoothed 3D fractionation correction surface $\Phi_m\left(l,t\right)$ for $^{206}Pb/^{238}U$. Cross-section lines at integrations 1, 7, and 13 are shown below to visually asses the fit between the f_{mlk} values (triangles, circles, and squares) and the resulting smoothed surface. Although there is a higher degree of variance in the early integrations, our smoothing method appears to adequately capture the longer-wavelength variations. Longer gaps in data near Std-12 and Std-26 are the result of programming the next batch of analyses. Lowest plot is the relative uncertainty for each sample from fractionation correction. These values are calculated for each RM sample and then a 1D cubic spline allows interpolation for intervening unknown samples (see text for discussion). In essence, samples have low uncertainty where measured ratios agree with the smoothed correction surface and high uncertainty where they differ more.

Correction factor values for the $^{206}Pb/^{238}U$ and $^{207}Pb/^{235}U$ systems show the greatest degree of depth-dependent fractionation, as typically reported (Patton et al, 2010). The $^{207}Pb/^{206}Pb$ system is usually assumed to have no depth dependency, which our data corroborate, although the magnitude of the correction is slightly less than unity and likely reflects instrumental mass bias.

The combination of moving average and 2-D cubic spline methods described above minimizes the uncertainty residual for secondary reference materials (M146 for this study). Furthermore, these methods are non-parametric and make no assumptions about the functional form of down-hole fractionation, only that it varies smoothly. Many alternative smoothing models exist, but a rigorous statistical analysis of these approaches is beyond the scope of this contribution. Data reduction and statistical treatment of laser ablation ICP-MS is the focus of substantial interest and debate at the present time (Jackson, 2009; Cottle et al, 2009; Patton et al, 2010; Horstwood et al., 2010; McLean et al., 2011). A key feature of this data reduction user interface is the flexibility to implement improved mathematical and statistical models of fractionation as the science progresses.

COMMON PB CORRECTION

Zircon can incorporate small amounts of common (non-radiogenic) Pb isotopes at the time of formation or during subsequent recrystallization or metamictization which results in an apparent age that can vary significantly from the true age. Several methods are available to estimate the contribution of this initial common Pb. All, except a ^{204}Pb-based correction, rely on the assumption of concordance of at least two of the decay systems and are therefore less preferred (Anderson, 2002). However, if the measured ^{204}Pb signal is not statistically above background levels, a correction using this method only serves to add noise, and may bias the data. Therefore, we implement a logical algorithm based on signal strength relative to the limits of detection to determine which correction is most appropriate for each sample (Fig. 4-3). For all common Pb corrections, the starting Pb composition is estimated by calculating two-stage Stacey and Kramers (1975) Pb composition at the uncorrected $^{206}Pb/^{238}U$ age. Both ^{207}Pb- and ^{208}Pb-based corrections utilize the uncorrected $^{206}Pb/^{238}U$ age as an initial age and iteratively solve for common Pb components until the change in age is $\ll 1\sigma$ uncertainty of the age, usually less than 5 iterations. Uncertainty in the common Pb composition is propagated in quadrature and included in the final external uncertainty.

UNCERTAINTY PROPAGATION, FINAL AGE CALCULATIONS, AND STATISTICAL MEASURES

The fundamental basis of our uncertainty propagation method is the Poisson counting uncertainty on the summed total counts for each isotope, E_{jlk}^{bc}, which is added in quadrature to form the absolute uncertainty of each ratio, E_{mlk}^{R}:

$$E_{mlk}^{R} = R_{mlk}^{obs} \times \sqrt{\left(\frac{E_{j_1lk}}{C_{j_1lk}}\right)^2 + \left(\frac{E_{j_2lk}}{C_{j_2lk}}\right)^2} \Bigg|_{m=1}^{v} \Bigg|_{l=1}^{s} \Bigg|_{k=1}^{r}$$

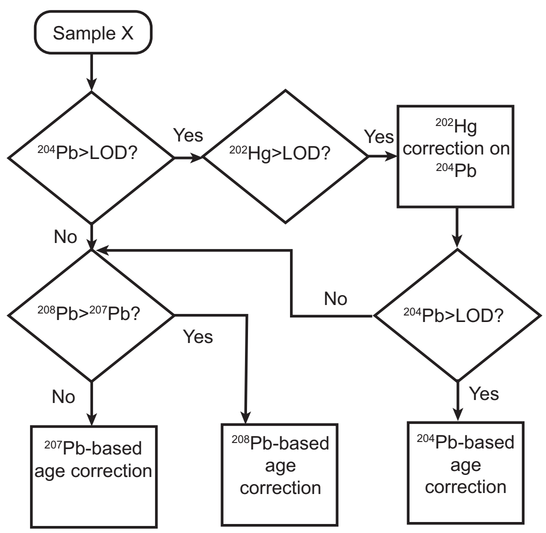

Figure 4-3. Algorithm workflow for the correction of common Pb used in this study. Although the correction methods are not equivalent, each has distinct criteria that must be met for appropriate use. Limits of detection (LOD) are defined as any signal greater than the 3σ uncertainty band of the background value.

Fractionation correction introduces a significant source of uncertainty due to the smoothing and interpolation process and must be included in the total uncertainty budget. We estimate its magnitude by calculating a goodness-of-fit function using the root mean square deviation, $\hat{\theta}_{mk}$ which, for unbiased estimators is equivalent to the standard error:

$$\hat{\theta}_{mk} = \sqrt{\frac{\sum_{l=1}^{s}\left(\Phi_{mlk} - f_{mlk}\right)^2}{s}}\Bigg|_{m=1}^{v}\Bigg|_{k=1}^{primary\_stds}$$

This formulation is valid for primary standards where f_{mlk} is defined, and provides an uncertainty estimate for each sample based on the goodness-of-fit between the final smoothed and interpolated fractionation correction surface and the values which perfectly transformed the observed ratio to the expected (Fig. 4-2). In a similar manner to that employed for Φ_{mlk} values, the discrete values for primary standards are mapped into a continuous time-series, smoothed with a 9-term Henderson filter, and values for intervening 'unknown' samples are interpolated with a 1-D cubic spline. Total relative internal uncertainty, δ_{mlk} is calculated by adding in quadrature the fractionation correction uncertainty of each sample to each integration's ratio uncertainty from Poisson counting statistics:

$$\delta_{mlk} = \sqrt{\left(\frac{E^{R}_{mlk}}{R^{obs}_{mlk}}\right)^2 + \left(\frac{\hat{\theta}_{mk}}{\Phi_{mlk}}\right)^2}\Bigg|_{m=1}^{v}\Bigg|_{l=1}^{s}\Bigg|_{k=1}^{r}$$

Sample-standard bracketing and the use of moving averages introduce correlated uncertainty, which if unaccounted for can produce spurious underestimation of weighted mean uncertainties (Mclean et al, 2011). For continuously-pulsed laser ablation methods which typically do not treat correlated uncertainty, new data reduction protocols have been developed that minimize this effect and are available at www.plasmage.org. The method presented here fundamentally differs from typical data reduction packages and intrinsically captures and propagates much of this uncertainty correlation by employing multiple time-series smoothing and interpolation methods and distributing the goodness-of-fit uncertainty function to unknown samples. In effect, locations where RMs have large uncertainties from counting statistics or excessive variance in correction factors at the sample level, those large uncertainties are propagated to the nearby unknowns over a reasonable length window in the smoothing process. However, as our understanding of the underlying processes which govern data point variation during laser ablation analyses improves, refined uncertainty models can be incorporated into existing data reduction packages.

For most zircons in this study, the internal uncertainty budget is dominated by correction factor uncertainty with the remainder from ion counting statistics (Fig. 4-2C). For low concentration (<~30 ppm ^{238}U) or young (Miocene) samples, isotope counting statistics can play a sub-equal role in the total uncertainty (Table 4-4). Final ages are calculated using the decay constants of Jaffey et al (1971) and the corrected Ψ_{mlk} isotope ratios. External age uncertainties propagate the uncertainty of the reference zircon, decay constants, and uncertainties from common Pb corrections when applied, typically resulting in an additional ~0.2-0.4% 2σ. This amount is propagated in quadrature with internal uncertainties and provided as a separate estimate.

At the sample level we calculate a weighted mean age using each sample's 15 integrations weighted by their inverse-square uncertainty, and a sample-level Reduced χ^2 statistic (MSWD value). The Reduced χ^2 assesses the degree that observed scatter about the weighted mean is consistent with the ascribed uncertainty of individual data; sample-level values near unity indicate that the majority of 1σ uncertainty envelopes for each integration overlap the weighted mean of that sample. The average for all samples in our round-robin session is 1.2, indicating to a first order that individual integration uncertainties are adequately estimated by our uncertainty model. The ability to assess this metric for each of our samples provides a built-in check that correlated error is being adequately propagated, and is a unique feature of this discrete depth-profiling method. However, session-level Reduced χ^2 for each sample type (15 samples) averages 7.5 and indicates that the typical standard error formulation for weighted means is significantly underestimated (Table 4-4). Although the exact cause of this underestimation is unclear at the present time, it is a common observation (Gehrels et al, 2008; Patton et al., 2010) and may be due to unaccounted uncertainty correlation in the typical standard error calculation (Mclean et al, 2011). Therefore, we employ a method similar to Patton et al (2010) and apply an additional uncertainty, added in quadrature to the standard error calculation that captures and propagates correlated uncertainty from the integration-level to the sample-level. We calculate this additional uncertainty by iteratively adding uncertainty to our primary RM

Table 4-4. Average session-level ages, uncertainties, and metrics for each zircon type and isotopic system.

Sample	Weighted session-level mean ±2σ	Original session-level MSWD	Added sample-level error (%1σ)	Amended MSWD	Average sample-level error (%2σ)	Average sample-level MSWD	Average integration-level error (%2σ)	% integration overlap with accepted value at 2σ	% samples overlap with accepted value at 2σ
$^{206}Pb/^{238}U$ system									
SLM	562.9 ±0.42%	4.90	1.02	1.00	2.35	0.54	5.85	98.9	100.0
WF6	535.8 ±0.45%	2.00	1.02	0.26	2.44	0.68	6.01	91.9	100.0
VP10	1155.6 ±1.63%	17.88	1.02	2.96	2.49	0.72	6.12	74.8	73.3
AS3	1137.5 ±0.96%	5.36	1.02	0.98	2.79	1.43	5.94	66.7	86.7
WF10	539.1 ±0.61%	2.06	1.02	0.39	2.55	0.86	6.22	94.8	100.0
WF2	528.6 ±1.10%	8.35	1.02	1.39	2.49	0.82	5.87	90.5	100.0
Plesovice	333.4 ±1.96%	36.11	1.02	4.19/2.84	2.60	1.01	6.00	81.4	80.0
M146	564.3 ±0.91%	4.95	1.02	0.80	2.51	0.89	5.82	93.8	100.0
UNK-1	18.2 ±1.88%	1.20	1.02	0.66	7.54	3.38	13.61	79.0	93.3
WF1	585.6 ±0.98%	1.65	1.02	0.58	3.50	1.76	7.98	86.7	100.0
Mud Tank	729.7 ±2.38%	2.67	1.02	1.30	5.94	2.65	12.59	74.8	100.0
$^{207}Pb/^{235}U$ system									
SLM	563.2 ±0.31%	2.32	0.65	1.00	1.79	0.18	9.45	100.0	93.9
WF6	537.3 ±0.53%	2.54	0.65	0.56	1.93	0.20	10.74	93.3	93.3
VP10	1173.7 ±1.23%	19.89	0.65	3.71	1.79	0.09	14.57	95.7	53.3
AS3	1123.2 ±0.56%	3.34	0.65	0.67	1.89	0.26	9.79	99.5	46.7
WF10	542.8 ±0.72%	1.67	0.65	0.61	2.57	0.27	14.84	100.0	92.9
WF2	530.7 ±1.06%	9.35	0.65	2.28	1.90	0.32	8.09	98.6	66.7
Plesovice	342.6 ±1.02%	2.85	0.65	0.59	2.60	0.50	11.05	98.6	66.7
M146	567.5 ±0.83%	4.50	0.65	1.27	2.00	0.32	8.91	99.5	80.0
UNK-1	18.1 ±10.21%	2.36	0.65	2.06	39.56	1.24	38.83	54.3	53.3
WF1	585.9 ±1.46%	1.37	0.65	0.86	5.20	8.19	36.72	100.0	100.0
Mud Tank	753.5 ±4.96%	3.33	0.65	2.82	15.61	0.47	77.55	98.6	73.3
$^{208}Pb/^{232}U$ system									
SLM	558.6 ±0.63%	2.95	1.45	1.00	3.73	0.40	10.64	97.6	90.9
WF6	520.9 ±0.93%	2.76	1.45	0.50	3.62	0.40	10.37	85.2	100.0
VP10	1138.7 ±2.04%	15.40	1.45	2.39	3.63	0.45	10.35	85.2	40.0
AS3	1109.1 ±1.76%	8.07	1.45	1.61	3.95	0.63	9.85	88.6	80.0
WF10	527.0 ±0.92%	3.58	1.45	0.55	3.45	0.31	10.37	93.8	100.0
WF2	528.9 ±1.11%	4.98	1.45	0.79	3.44	0.32	9.99	98.6	86.7
Plesovice	333.4 ±2.95%	7.47	1.45	0.81	5.07	0.97	13.63	85.2	80.0
M146	560.6 ±0.97%	4.29	1.45	0.59	3.51	0.34	10.35	95.7	93.3
UNK-1	18.1 ±3.99%	3.08	1.45	1.75	10.45	1.80	18.86	73.8	86.7
WF1	566.0 ±1.53%	1.30	1.45	0.50	6.24	3.03	14.86	84.3	93.3
Mud Tank	698.9 ±6.23%	2.53	1.45	1.98	17.55	4.21	27.71	66.7	80.0
$^{207}Pb/^{206}Pb$ system									
SLM	556.7 ±0.99%	0.97	0.00	0.97	5.54	9.44	6.53	49.4	100.0
WF6	528.8 ±1.84%	0.84	0.00	0.84	7.80	17.23	6.86	39.5	100.0
VP10	1203.4 ±0.78%	1.41	0.00	1.41	2.84	2.06	6.71	82.9	100.0
AS3	1100.7 ±0.71%	1.52	0.00	1.52	2.36	1.75	6.11	86.7	100.0
WF10	531.3 ±4.78%	2.72	0.00	2.72	12.20	28.54	8.06	34.3	100.0
WF2	530.9 ±2.43%	2.92	0.00	2.92	5.51	10.24	6.21	46.2	93.3
Plesovice	340.3 ±9.53%	6.37	0.00	6.37	16.00	54.01	7.54	15.7	93.3
M146	575.8 ±1.94%	1.61	0.00	1.61	5.53	10.15	6.35	46.2	100.0
UNK-1	NA	NA	NA	NA	NA	NA	NA	NA	NA
WF1	408.1 ±19.25%	NA	NA	NA	NA	NA	NA	NA	NA
Mud Tank	NA	NA	NA	NA	NA	NA	NA	NA	NA

sample-level means until the session-level Reduced χ^2 value becomes unity; this resulted in an additional 1.02% 1σ uncertainty for sample-level means (Table 4-4). Reduced χ^2 values for each sample type after application of the additional uncertainty are near unity and result in mean 2σ uncertainties of ~2.5% for each weighted sample mean.

RESULTS

ACCURACY AND PRECISION OF U-PB AGES

We conducted a round-robin analysis of 10 zircon types selected to cover a wide range of ages (~18 Ma to ~1200 Ma) and uranium concentrations (~10 ppm to >1500 ppm) (Table 4-2). Each zircon type was analyzed 15 times throughout the session, and the primary RM was analyzed prior to every 5 'unknowns'. Each sample-level analysis contains a 15-age depth profile as the laser ablates successively deeper layers of the zircon grain. In total, 225 individual ages were collected for each 'unknown' zircon type and 495 ages for our RM. Combining all 225 integrations for each zircon type and calculating ages using Isoplot (Ludwig, 2003) results in better than 2% precision and accuracy for zircons with known ages (Fig. 4-4) and have Reduced χ^2 values significantly less than unity. Discordance is generally absent throughout our samples, however, three anomalously young Plesovice samples are clearly discordant (colored black on Fig. 4-4), and 1-2 samples in both VP-10 and AS-3 are also discordant. The Mud Tank samples appear generally concordant, but due to very low concentration of radiogenic nuclides Isoplot was unable to generate an age from these data. Two samples of the Unknown-1 zircon account for all of the observed discordance and suggest possible inheritance.

At the integration level, $^{206}Pb/^{238}U$ ages nearly all overlap with their respective weighted mean at 1σ confidence and for Phanerozoic-age samples, also overlap with the accepted age (Fig. 4-5). It is noteworthy that the first integration of each analysis is typically aberrant in age, falling outside of both sample and session variance. Because most samples are shards of zircons and not whole grains, it is unlikely this observation is due to chemical diffusion as we drill through outer to inner zones, but instead, is most likely caused by early-stage ablation processes or surface contamination; therefore, ages from the first integration are excluded from sample means and Reduced χ^2 statistics. The calculated internal uncertainty for each integration-level $^{206}Pb/^{238}U$ age is typically ~6% 2σ (Fig. 4-5; Table 4-4) but increases when analyzing low-concentration and/or young grains; individual integration uncertainties for the

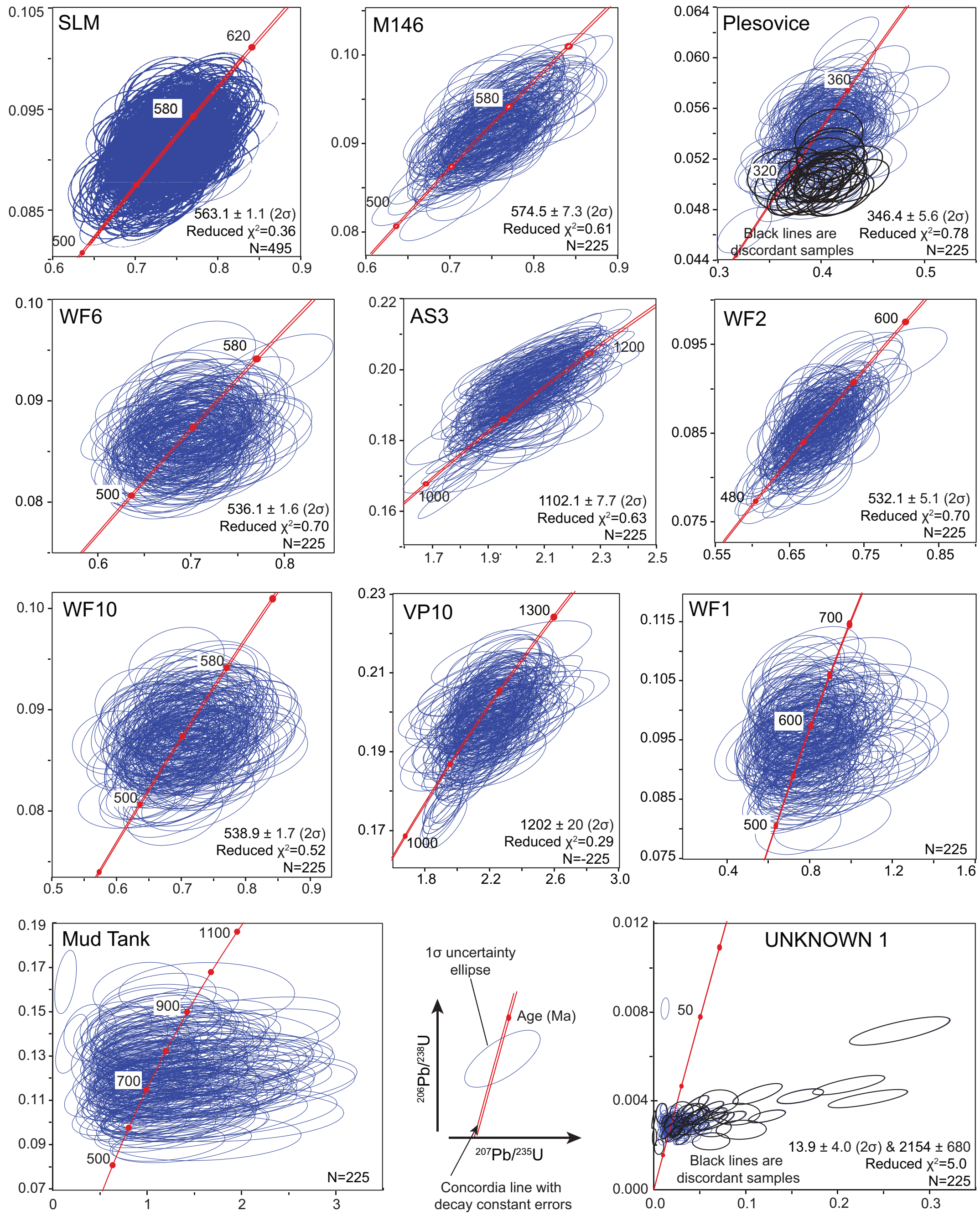

Figure 4-4. Concordia plots for all integrations of each sample type. Grains which displayed entirely discordant ages are in black. Uncertainty ellipses depict 1σ confidence limit.

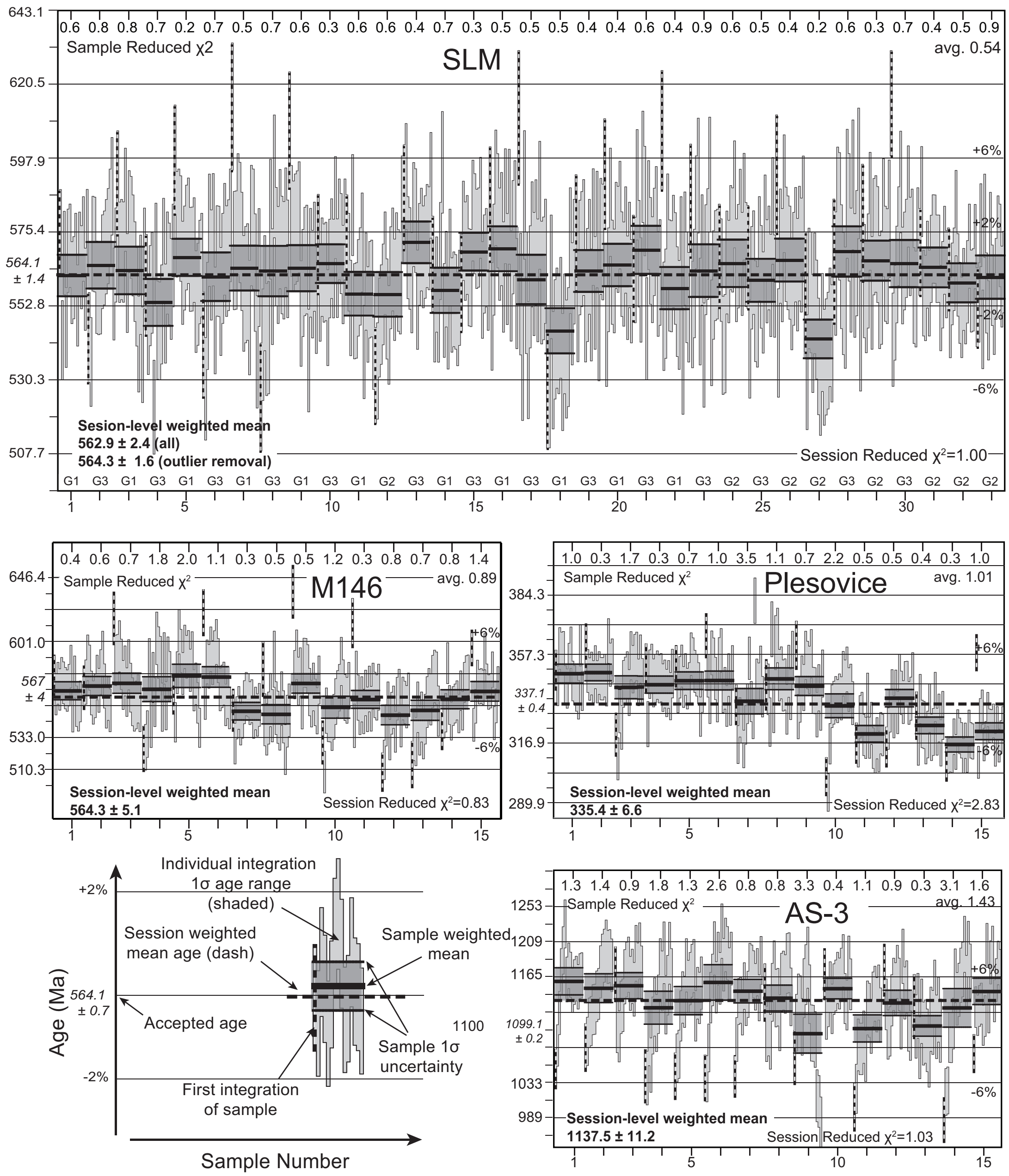

Figure 4-5. Whisker plots of $^{206}Pb/^{238}U$ age for each sample type. Shaded outline represents individual integration ages at 1σ uncertainty and dashed vertical lines are the first integration of each sample. Sample weighted means (thick horizontal lines) and 1σ uncertainty (shaded box) do not include the first integration of each sample. The dashed black line through the entire session represents the session weighted mean of all samples and its value is indicated in bold with 2σ uncertainty. Note that two samples of our primary reference zircon do not overlap the session mean at 2σ; this is discussed in the text. Reduced χ^2 values for each sample shown across top axis do not include the first integration; session-level Reduced χ^2 using weighted sample means in lower right. G1...G2...G3 on SLM refer to the grain ablated for that sample and correspond to Raman spectra labels in Figure 4-7. Y-axis scales are constructed such that major divisions are 2% widths of the known age which is indicated in italics. Because no reference ages were previously determined for the WildFish zircons, these plots do not have this feature.

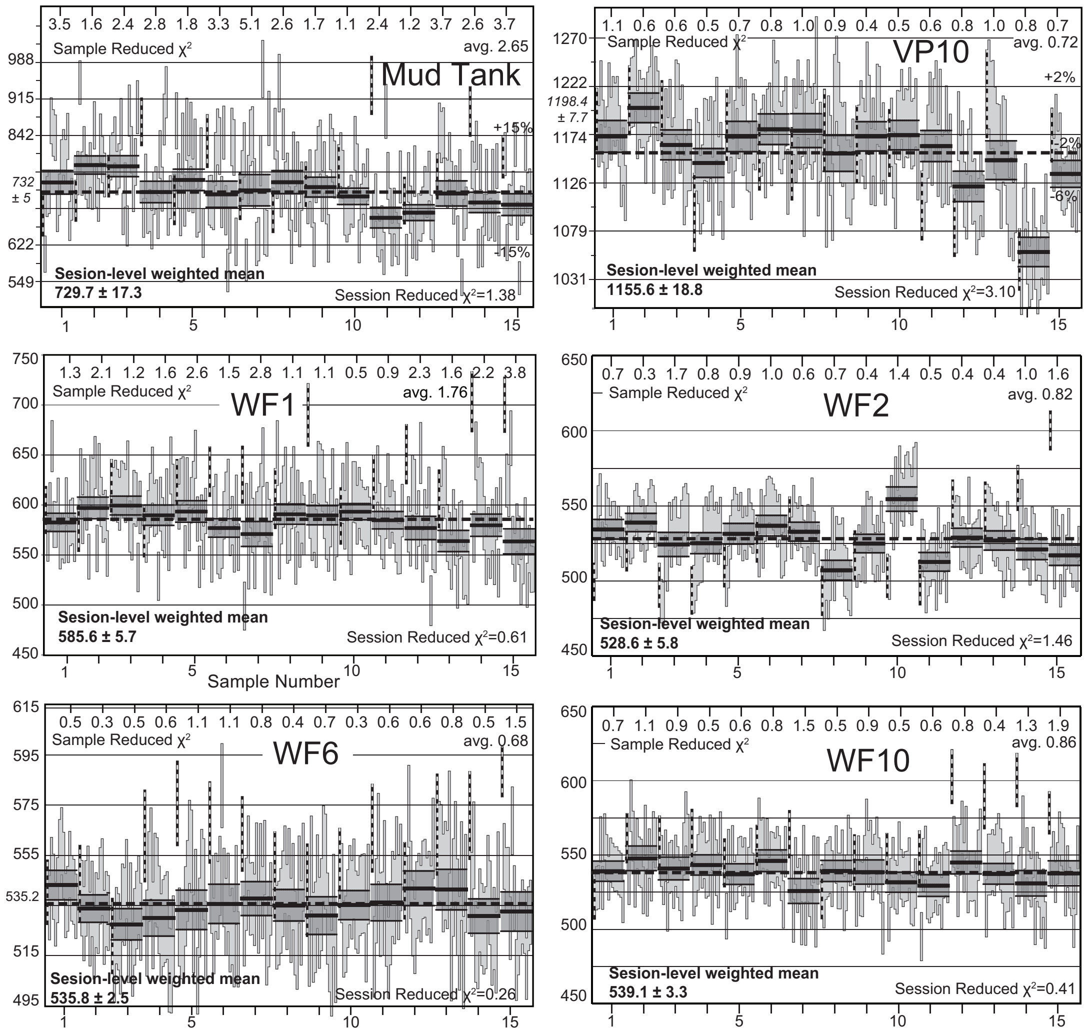

Figure 4-5, continued. See previous page for full caption.

Miocene-age Unknown-1 zircon and the <30 ppm uranium Mud Tank and WF1 zircons are ~8-12%. Integration-level uncertainties for the $^{207}Pb/^{206}Pb$ system vary but are typically ~5-7% 2σ for Proterozoic samples, and 6-8% for Phanerozoic samples depending on radiogenic nuclide concentrations. Average ages and uncertainties for each zircon type and isotopic system are shown in Table 4-4.

The primary reference zircon is included in Figure 4-5 because the ability to accurately and precisely reproduce ages at the integration and sample level for these zircons provides a bounding limit to the accuracy and precision of unknowns. Excluding the first integration of each sample results in an average Reduced χ^2 value for each sample of 0.54 indicating this method may actually overestimate the uncertainty at this level. Aside from two samples (18 and 27) that do not overlap the session-level mean at 2σ, sample-level weighted mean ages overlap the accepted age of the standard within 1σ uncertainty. Including these two outlier samples, all individual integration-level ages overlap the accepted value of the reference material at the 2σ level, and 85% at the 1σ level. Although this level of agreement is expected from the RM, it still provides a first-order check that the data reduction method is capable of reproducing meaningful ages. The two aberrant samples were not discarded in this analysis, but a 2σ-outlier removal protocol can be employed by the software.

Average internal uncertainties for each $^{206}Pb/^{238}U$ weighted sample mean (14 integrations) are thus about 2.5% 2σ, except for the Miocene-age sample (~7.5%), Mud Tank (~6%), and WF1 (~3.5%). Aside from Plesovice and VP-10, all weighted sample means overlap with accepted values at the 2σ level, and many within 1σ. Our method of assigning additional correlated uncertainty to the weighted sample means is validated by session-level Reduced χ^2 values near or below unity for each sample type (Fig. 4-5). Two exceptions to this are Plesovice and VP-10, both of which have noticeable discordant grains or zones. For Plesovice the Reduced χ^2 value drops from 4.19 to 2.83 if the three discordant grains (PLES-11, -14, and -15) are excluded from analysis; the still-large Reduced χ^2 value is puzzling but might reflect the presence of two age populations. Overall, the precision and accuracy of individual sample ages using this method is near the low side of standard laser ablation protocols (~1-3%; Kosler et al., 2002; Gehrels et al., 2008, Frei and Gerdes, 2009) or single-pulse/multi-collector methods (e.g. Cottle et al., 2012) but with the added benefit of capturing discrete depth-resolved ages at the sub-sample level.

SURFACE METRICS

DATA REDUCTION

Typical 193nm excimer laser ablation pits display a 'top-hat' profile with steep pit walls and flat pit bottoms. However, because surface metrics are obtained with the epoxy disc resting on its bottom face whereas ablation occurs with the top face horizontal, surface tilt is introduced. To correct this tilt and calculate pit depths and volumes, a custom code was written in LabView. Unlike an SEM, vertical-scanning interferometers have difficulty measuring steeply-dipping features which results in data for the upper surface and the pit bottom but not always the intervening pit walls (Fig. 4-6a). All of the 183 imaged ablation pits displayed a narrow rim of concavity near the outside edge indicating an abrupt change in slope from the flat bottom to steep walls. We therefore measure the average pit bottom depth in a ~300 μm^2 area near the center and exclude the narrow rim of steeper topography around the edges. Total volumes for each ablation pit are calculated using the radius of the surface aperture (R), the radius of the pit bottom to the edge of flat topography (r), and the depth of the sample (d) (Fig. 4-6d).

The uncertainty of our depth measurements is calculated using the typical standard error formulation with N=number of observations (pixels) in the ~300 μm^2 area that we average for the pit depth. This formulation results in 2σ uncertainties of ~4-6nm (<0.1%) which seems reasonable for relatively flat-bottom pits of equal elevation and sub-nm vertical precision of the instrument. Uncertainty for volume calculations must include the uncertainty in defining the

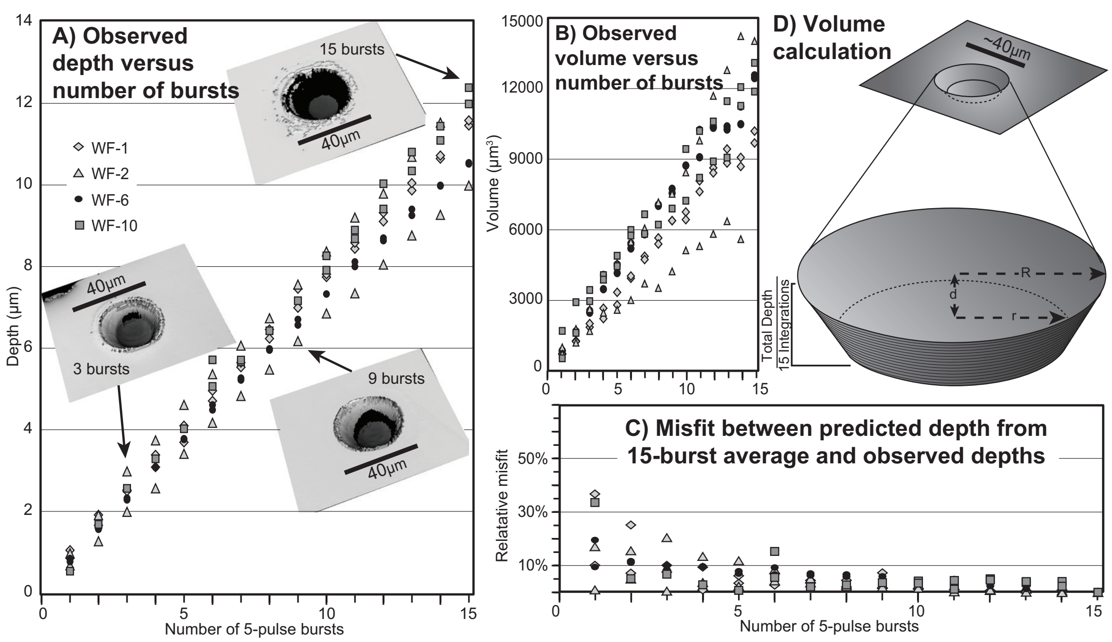

Figure 4-6. A) Depths measured by interferometry for 8 zircon grains to determine linearity of ablation rate with depth. Data were collected using the same instrument parameters in Table 4-1, with the exception of laser fluence set at 5.1 Jcm^{-2}, resulting in pits which are slightly deeper than those of the round robin analysis. Shaded relief plots of ablation pits document the evolution of pit morphology and the increasing difficulty of the interferometer to measure the steeply-dipping pit walls. Regression statistics for the depth data are found in Table 4-5. B) Volume data also show a relatively linear relationship but are more scattered. This may be due to the greater sensitivity of volume to the aspect ratio of the ablation pit. C) Misfit is calculated as the absolute value of the per-cycle misfit normalized to the predicted depth and suggests that some, but not all, grains appear to have early-stage non linearity followed by relatively linear ablation rate that is reasonably characterized by the long term average. D) Model depicting the idealized geometry and variables used to calculate total ablation volumes. Because the area of the pit bottom is less than the area of the top, volumes decrease as a function of ablated depth.

edges of the surface aperture and the exact size of the pit bottom. Based on our experience measuring these parameters, we assign a nominal uncertainty of ±2 pixels (0.448 μm) in both the top and bottom radii. With these values, our uncertainty budget for volume calculations is clearly dominated by the uncertainty in radii, yet still yields an average 2σ uncertainty of ~15% for each sample. Individual integration volume uncertainties vary as a result of their changing surface areas but range between ~12 and 18%.

LINEARITY OF ABLATION DEPTH WITH TIME

In order to characterize the functional form of ablation depth with time, we ablated and measured successively deeper pits from 1 burst of 5 pulses (one integration) to 15 bursts of 5 pulses (15 integrations) on eight different zircon grains. These data are shown on Figure 4-6 and indicate generally linear relationships between depth, volume, and number of integrations, with fit coefficients (R^2) for ordinary least squares regression all >0.98. Because these data are an autocorrelated time-series, a generalized least squares regression of each sample type is used to evaluate the probability that the y-intercept is non-zero, a result which may indicate non-linear behavior (statistical measures are located in the Supplementary Material). All of the regressions yield statistically significant non-zero intercepts (p values <0.001), but the removal of the first integration from the analysis results in 3 of the 5 regressions being indistinguishable from zero (p values >0.3). These results suggest that some amount of non-linear behavior occurs in the first 1-2 bursts. An analysis of the residual between the observed depth and that predicted by a simple average of the 15-integration total (Fig. 4-6c) supports an interpretation of slight non-linearity during the first few bursts. Overall, however, these data show that calculating an ablation rate from the final depth is a reasonable approximation unless additional data are acquired to improve the fit (such as depth measurement between each laser burst). For some, but not all samples, this will slightly underestimate the 'true' depth of the first integration by up to ~35%, and by less than ~20% for the subsequent 1-2 integrations; integrations from 2-15 are generally <10% different than predicted.

SAMPLE DEPTHS AND VOLUMES

Average depth after 15 integrations for all samples is 8.3 μm (2 SD = 1.6 μm) and average volume is 7770 $μm^3$ (2 SD = 1636 $μm^3$), but these values vary significantly by sample type such that samples with higher concentrations of radionuclides are generally deeper. This correlation

Table 4-5. Depth, volume, concentrations, and thermochronometric ages and metrics for each sample type.

Sample	Average depth ±2SD	Average depth per integration	Average volume ±2SD	Average ^{238}U (ppm) ±2σ	Range ^{238}U (ppm) ±2σ	Average ^{232}Th (ppm) ±2σ	eU (ppm)	(U-Th)/He age	Average alpha dose (α/g) ±2σ
WF1	7.26 ±0.63	~0.48	7697 ±838	35 ±5	24-54	23 ±4	41 ±6	~440 [2]	6.1E+16 ±15.5%
UNK-1	7.52 ±0.29	~0.50	7233 ±638	242 ±57	71-449	367 ±117	329 ±83	18.2	2.0E+16 ±24.8%
Mud Tank	7.59 ±0.96	~0.51	7004 ±657	8 ±1	6-10	4 ±1	9 ±1	~300 [3]	8.9E+15 ±10.0%
WF2	7.85 ±0.77	~0.52	7916 ±774	1350 ±37	1230-1476	707 ±19	1516 ±41	~440 [2]	2.3E+18 ±2.7%
M146	8.11 ±0.48	~0.54	7981 ±566	894 ±34	806-993	364 ±14	980 ±37	443 ±20 [1]	1.5E+18 ±3.8%
Plesovice	8.2 ±0.75	~0.55	7645 ±535	573 ±60	371-837	52 ±8	586 ±62	Unk.	NA
WF10	8.39 ±0.27	~0.56	7509 ±704	245 ±8	220-271	224 ±8	298 ±10	~440 [2]	4.4E+17 ±3.3%
VP10	8.64 ±0.57	~0.58	7424 ±2438	352 ±143	66-1086	225 ±87	405 ±163	Unk.	NA
WF6	8.92 ±0.18	~0.59	8271 ±837	504 ±23	410-563	166 ±7	543 ±24	~440 [2]	8.1E+17 ±4.5%
SLM	8.95 ±0.73	~0.60	8402 ±1403	729 ±70	444-908	138 ±14	761 ±73	~440 [2]	1.1E+18 ±9.6%
AS3	9.4 ±1.56	~0.62	9296 ±2321	719 ±241	310-1413	428 ±138	819 ±273	~900 [4]	2.8E+18 ±33.4%

[1] (U-The)/He age for M146 is average of four individual dates from Nasdala et al. (2004).

[2] Other Sri Lanka zircons were assigned a representative date consistent with the compilation of Sri Lanka (U-Th)/He ages in Nasdala et al. (2004).

[3] (U-Th)/He age estimated from biotite Rb/Sr and apatite fission track data reported in Green et al. (2006).

[4] Cooling through ~175° C at ~900 Ma is estimated from forward modeled date-eU correlations in Guenthner et al. (2013).

is discussed in greater detail below. Assuming relatively constant rates of ablation, the average depth per integration is ~0.55 μm using a nominal 34 μm spot size and 4 Jcm^{-2} laser fluence (Table 4-5). Average volume of ablated material per integration changes systematically with depth as a function of the different surface area of the pit opening and the pit bottom (Fig. 4-6d). The average ratio of top radius to bottom radius is 1.5:1 (pit walls of ~50° for average depth) equating to ~735 μm^3 for the first integration and ~340 μm^3 for the last integration. This change in volume results in a systematic decrease from ~3.4 to ~1.5 ng of zircon per integration from top to bottom (4.65 g/cm^3 density), and an average of ~36 ng of ablated zircon per sample.

EFFECTIVE URANIUM AND ALPHA DOSE

We calculate an approximate ^{238}U concentration for each sample by dividing total measured isotope counts by the calculated volume and scale this relative concentration using a value of 750 ppm for our average SLM zircon data (M.Grove, Stanford University, written commun., 2012); ^{232}Th concentration is calculated using the measured $^{232}Th/^{238}U$ ratio. Effective uranium (eU) is calculated as [U] + 0.235[Th] which weights each isotope for its overall contribution to ^{4}He production. Average values of [U], [Th], and eU are shown in Table 4-5 and in general there is good agreement between our calculated values and accepted values.

The depth measurements collected in this study indicate that depth does not vary uniformly amongst all analyses but instead carries a strong dependence on eU (Fig. 4-7). The reason for this is not entirely clear, but recent work has also shown that artificial annealing of radiation-damaged zircons reduces age dispersion in the U-Pb system (Allen and Campbell, 2012). Radiogenic ^{4}He that accumulates when zircon or apatite are below their closure temperatures as the result of parent nuclide decay (alpha dosage) is one proxy for accumulated radiation damage and has been shown to have complicated effects on the crystal lattice of these minerals (Meldrum et al., 1998; Nasdala et al., 2004; Shuster et al., 2006; Guenthner et al., 2013). Thus, in order to evaluate how radiation damage may affect ablation depth, alpha dosage is calculated for each sample.

$$\alpha / g = \frac{8\left(C_{238}\right)\left(e^{\lambda_{238}t}-1\right)+7\left(C_{235}\right)\left(e^{\lambda_{235}t}-1\right)+6\left(C_{232}\right)\left(e^{\lambda_{232}t}-1\right)}{V_z \times \rho_z}$$

Where ($1.55136*10^{-10}yr^{-1}$), ($9.8485*10^{-10}$ yr^{-1}), ($4.9475*10^{-11}$ yr^{-1}), C_x are the parent nuclide contents in total atoms, t is thermochronologic age when the sample passed through the zircon closure temperature (~175-220° C; Reiners, 2005), V_z is the volume of the zircon, and ρ_z is the density of zircon (assumed to be 4.65 g/cm^3). Values of t are known or reasonably estimated for all of the samples but VP-10 and Plesovice and are found in Table 4-5. In short, because of the varying effects of eU on measured zircon (U-Th)/He dates for a population of grains that have all experienced the same thermal history (Guenthner et al., 2013), we choose to use the 'average' thermochronologic age (~440 Ma; Nasdala et al., 2004) for all of the Sri Lankan zircons used in this study instead of measuring individual (U-Th)/He ages. Individual ages for these grains would vary substantially because of their radically different radionuclide concentrations and would be unrepresentative of experiencing a similar thermal history. Despite these drawbacks, each sample type occupies a relatively narrow range of depth-dosage space (Fig. 4-7) and as

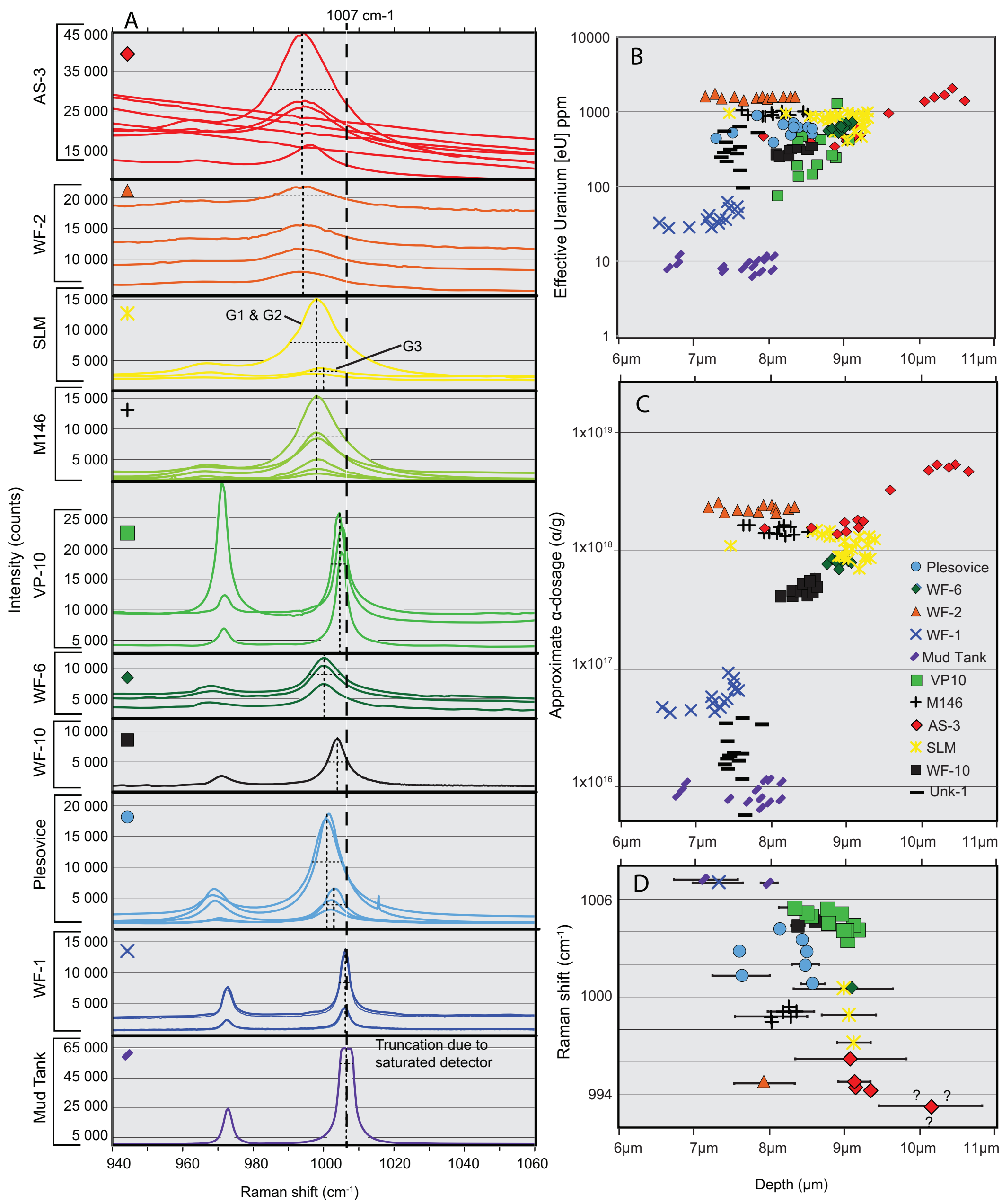

Figure 4-7. A) Raman spectra for all analyzed grains of each zircon type. Vertical long dash is the crystalline 1007 cm^{-1} peak and vertical and horizontal short dash lines are each sample's primary peak and Full-Width Half-Max (FWHM), respectively. For SLM, grains G1 and G2 have similar spectra and correction factors but differ from G3 in both of these measures. B) Effective Uranium (eU) for each sample as a function of ablation depth. Note the positive correlation in the population and within many zircon types. C) Approximate alpha dosage as a function of ablation depth. Although data are scattered, there appears to be a marked break in slope near a dosage of ~10^{18} α/g and may correspond to changes in damage accommodation and annealing observed at these dosage levels by others (Guenthner et al., 2013). D) Range of Raman spectra peak shifts for each ablated grain (increasing lattice distortion from top to bottom). The range of depth values result from multiple ablation pits on a particular grain.

an entire population have a Spearman rank correlation of 0.62 ($p<0.001$) indicating a relatively high degree of correlation between total ablation depth and production of ^{4}He.

RAMAN SPECTROSCOPY

Increasing amounts of crystal lattice disorganization in zircon occur when the grain can no longer anneal and results in a systematic shift and broadening of the diagnostic Raman spectra peak related to the v_3 Zr-SiO_4 stretching bond (Nasdala et al, 2004; Guenthner et al, 2013). Therefore, to further characterize the relationship between radiation damage and ablation depth representative Raman spectra were collected for each ablation pit over between 900 and 1200 cm^{-1}. Spectra within each zircon type (Fig. 4-7) are relatively similar and indicate consistent levels of crystallinity with a primary peak between 995 and 1007 cm^{-1} and a variable but broader secondary peak near 970 cm^{-1}. Two exceptions are the reference zircon, SLM, and Plesovice, which each appear to display a range of primary peak Raman shifts. Between zircon types, however, there are systematic variations in primary peak Raman shift and peak width that correlate with increasing alpha dosage as expected from previous results. Zircons with low alpha-doses display sharp and narrow peaks centered at 1007 cm^{-1} and those with the highest relative alpha-doses have broad peaks near 995-997 cm^{-1}, or in the case of the most extreme alpha-dosage AS-3 samples, no discernible peaks at all. These results are similar to other studies which more clearly link radiation damage and alpha dose to systematic changes in crystallinity (Meldrum et al., 1998; Nasdala et al., 2004; Guenthner et al., 2013). However, our data also show that ablation depth is correlated with both changes in Raman spectra and alpha dose, (Fig. 4-7), although the causal relationship is unclear at the present time and is the focus of current inquiry.

DISCUSSION

ANOMALOUS INITIAL ANALYSES

Similar to many laser ablation studies, our data indicate that early-stage isotopic ratios are anomalous even after fractionation correction (Fig. 4-5) which leads most workers to discard the first several seconds of on-peak data (Gehrels et al., 2008; Frei and Gerdes, 2009; Patton et al., 2010). At typical laser repetition rates, removal of five seconds of analysis time eliminates between 25-50 laser pulses which is as much as 2/3 of each sample’s integrations. This work confirms the work of Cottle and coworkers (2012) that only the first several laser pulses (<5) generally yield anomalous data and should be excluded. However, in a typical constant-rate analysis, signal convolution makes eliminating just this small fraction nearly impossible. Methods which either raster the sample area prior to analysis (e.g. Chew et al., 2011) or apply several 'pre-ablation' laser pulses to each site appear to reduce this problem (e.g. Cottle et al., 2009a). The trade-off between material lost for a 'pre-ablation' cleansing pass versus simply discarding the first integration should be systematically evaluated if maximum depth resolution is required.

Several potential hypotheses could explain anomalous early integration isotopic ratios: 1) surface contamination; 2) differential ingrowth of isotopic signals, or; 3) initial laser ablation processes. Our discretized method explicitly treats ingrowth and decay of transient signals by calculating ratios based on total counts and effectively eliminates the highly variable isotopic ratios that occur as a result of aliasing. Most workers, ourselves included, carefully wash and prepare epoxy resin discs prior to analysis, thus making surface contamination unlikely, but not improbable. Furthermore, surfaces contaminated with common Pb in great enough abundance to significantly affect isotopic ratios would consistently produce ages too old, a feature that our data do not corroborate. Consequently, we favor the idea that initial ablation processes are responsible for anomalous behavior during the first few laser pulses of each analysis, perhaps related to scattering of incident photons off the polished surface. Other studies have correlated unstable laser energy with these early periods of anomalous ratios (Cottle et al., 2012), but the laser used in this study contains a fluence monitor feedback loop that samples a portion of each laser pulse and adjusts energy levels accordingly, so this explanation seems less likely but cannot be ruled out.

FACTORS AFFECTING PRECISION AND ACCURACY

These results demonstrate the ability of this method to determine U-Pb ages from ~1.5-3.4 ng of ablated zircon with an average depth resolution of ~0.55 μm and 2σ uncertainties of ~6% for the $^{206}Pb/^{238}U$ system. Although we must ablate more zircon than single-pulse methods designed for multi-collector instruments (e.g. Cottle et al., 2009a; 2012), final precision and accuracy is comparable at the sample-level and depth resolution could be enhanced by increasing spot size and decreasing pulses/integration to maintain adequate ion signal. The predominant source of age dispersion in this method arises from fractionation correction and thus, the two main factors that influence the precision and accuracy of our analyses are the homogeneity of the reference zircon and the applicability of correction factors derived from that reference to unknown samples. Fundamentally, the accuracy and precision for unknown samples cannot supersede the ability to reproduce accurate and precise ages for the reference zircon and these characteristics bear directly on its homogeneity.

A close inspection of Figure 4-3 shows that Φ_{mlk} varies substantially between analyses of our reference zircon (as much as ~8% for the first and second integrations). To a first order, this high-frequency session variation results from systematically analyzing three different grains of SLM (G1, G2, G3 in Figs. 4-5 and 4-7). Two of the grains G1 and G2 have similar correction factors and similar Raman spectra, whereas G3 consistently has slightly different correction factors and noticeably less shifted Raman peaks (Fig. 4-7). The smoothing of these variations in the interpolation process results in values which adequately correct the ‘average’ reference zircon, but still show some residual high-frequency variation in age (Fig. 4-5) and may contribute to the over-dispersion of data about the known age which must be subsequently corrected for. This heterogeneity in reference behavior would have presented a serious challenge (or been misinterpreted as long-term instrumental drift) had the different grains not been relatively scattered throughout the analysis session and highlights the need for consistency in reference zircon behavior.

The second factor that controls the precision and accuracy of our method is the applicability of correction factors from a reference zircon to unknown samples. For example, age discrepancies between samples analyzed by laser ablation and those analyzed by ID-TIMS are commonly observed (e.g. Gehrels et al, 2008) but can be significantly, although not entirely, reduced by thermal annealing of zircons prior to ablation (Allen and Campbell, 2012). Similar matrix effects, correlated to high levels of uranium (and thus radiation damage), are also observed during SIMS analysis (White and Ireland, 2012). Our depth data, alpha-dosage, and Raman spectroscopy indicate that ablation depth generally increases with crystal lattice disorganization and provides a simple explanation for observed age biases, ie, if the pit depth of an ‘unknown’ sample is significantly deeper or shallower than the pits of the reference zircon, the reference-derived fractionation correction values may be a poor match for the unknown. This phenomenon would only be noticeable when a mismatch occurs between the damage profile of reference zircons and samples of known age. Thus, if primary and secondary standards share a similar damage profile the derived correction factors may appear to perform adequately, but for 'unknowns' with substantially different damage profiles ages may be over-dispersed, inaccurate, or have unrealistically low uncertainty estimates.

For our samples with known ages, M146 is the most reproducible sample and has nearly identical Raman spectra, relative alpha-dosage, and ablation depth to our reference zircon. However, Mud Tank, Plesovice, VP10, and AS-3 all differ significantly in two or more of these three variables and all have greater dispersion of integration-level $^{206}Pb/^{238}U$ ages, or have mean sample ages different than accepted values (Figs. 4-5 and 4-7). Although no ID-TIMS data yet exist for the Wild Fish zircons, WF6 is very similar in character to the reference zircon and has the lowest session-level Reduced χ^2, suggesting that the derived correction factors are well matched for this sample. In contrast, WF1 is most similar in character to Mud Tank and displays similarly high magnitude integration-level age dispersion. These results seem to indicate a strong correlation between the accuracy and precision of ages and the degree of similarity in ablation depth/crystal lattice disorganization between sample types and the reference zircon. An alternative explanation is that increased discoloration resulting from high levels of parent radionuclides causes greater coupling of the laser to the zircon and leads to higher ablation efficiencies. However, because it is radiation-damage induced crystal lattice defects which create discoloration in zircon, and we cannot at present discern between these two processes, it is largely irrelevant which is ultimately responsible for the correlation with ablation depth. Overall, it is clear that parent nuclide concentration plays a fundamental role in determining laser ablation efficiency and consequently may ultimately control the accuracy and precision of any laser ablation method.

Several method improvements could potentially alleviate or lessen these age biases: 1) anneal both unknown and reference zircons in an attempt to ensure similar damage profiles and ablation characteristics (e.g. Allen and Campbell, 2012); 2) use multiple reference zircons with variable damage profiles and ablation characteristics and match these characteristics to unknowns, or; 3) use one reference zircon of a known damage level and scale the correction factors to match the damage profile of 'unknown' samples. The annealing method is by far the easiest to employ and has clearly demonstrated reductions in age bias (Allen and Campbell, 2012). However, double-dating methods (U-Pb and (U-Th)/He) typically first obtain a U-Pb age before ^{4}He-extraction (Reiners et al., 2005) and would clearly have to be modified since the annealing process (~850° C for 48 hours) would undoubtedly release most, if not all ^{4}He from the grain. Both the first and second methods require independent knowledge of the level of crystal lattice disorganization, either by using Raman spectroscopy, or measuring ablation pit depths and alpha-dosage. For samples in a double-dating application, the effective alpha dosage can be accurately determined in conjunction with the (U-Th)/He age, but further work is needed to robustly assess these last two methods. Clearly, a fourth alternative is to accept the precision and accuracy limitations of current methods and is a reasonable option where utmost age resolution is not required.

CONCLUSION

A discrete multi-pulse depth-profiling method for single-collector ICP-MS laser ablation systems is presented that is applicable to any arbitrary geochemical system that seeks to interrogate isotopic variation as a function of sample depth. This study uses U-Pb analysis of zircon as a case study and resolves ages at the integration-level (~0.55 μm depth resolution and ~6% 2σ age uncertainty) using five laser pulses and calculating ratios from total integrated counts. The total count approach provides better stability and accuracy than cycle-by-cycle ratios, especially when signal transience is high. At the sample-level (15 integrations) depths are 7-10 μm and average 2σ uncertainty is ~2.5% for $^{206}Pb/^{238}U$ ages. Fractionation correction is achieved through iterative smoothing and interpolation of a continuous-function, non-parametric 3D surface from which discrete values for any time and sample depth can be calculated. This method offers a high degree of flexibility and is validated by Reduced χ^2 values near unity for both sample- and session-level weighted mean ages.

We identify several previously unrecognized factors which appear to contribute to the accuracy and precision of laser ablation U-Pb zircon ages by combining surface topography of ablation pits, Raman spectroscopy, and metrics of radiation damage. High positive correlation exists between measures of radiation damage (alpha dosage), crystal lattice distortion (shifted and broadened v_3 Zr-SiO_4 spectra peaks) and ablation pit depths. We interpret these results to indicate that ablation efficiency is controlled by the accumulation of radiation damage in the zircon crystal lattice. Consequently, significant damage variation within a reference zircon can potentially translate to excessive variance in fractionation-correction values and will decrease accuracy and precision. Additionally, fractionation-correction values derived from a reference material will either over- or under-correct intervening 'unknown' samples if their damage profiles are significantly different. This second issue is undetectable if primary and secondary reference materials have similar damage profiles, yet contributes significantly to age dispersion.

REFERENCES

Allen, C.A., Campbell, I.H., 2012, Identification and elimination of a matrix-induced systematic uncertainty in LA–ICP–MS 206Pb/238U dating of zircon. Chemical Geology, v. 332–333, 157-165. http://dx.doi.org/10.1016/j.chemgeo.2012.09.038.

Anderson, T., 2002, Correction of common lead in U–Pb analyses that do not report 204Pb. Chemical Geology, v. 192, 59-79.

Black, L.P., Gulson, B.L., 1978, The age of the Mud Tank carbonatite, Strangways Range, Northern Territory. BMR Journal of Australian Geology and Geophysics, v. 3, 227–232.

Blackburn, T., Bowring, S.A., Schoene, B., Mahan, K., Dudas, F., 2011, U-pb thermochronology: Creating a temporal record of lithosphere thermal evolution. Contributions to Mineralogy and petrology/Beitrage Zur Minerologie Und Petrologie. Berlin and New York NY 162(3):479-500.

Breeding, C.M., Ague, J.J., Grove, M., and Rupke, A.L., 2004, Isotopic and chemical alteration of zircon by metamorphic fluids: U-Pb age depth-profiling of zircon crystals from Barrow's garnet zone, northeast Scotland. American Mineralogist, v. 89, 1067–1077.

Chew, D.M., Sylvester, P.J., and Tubrett, M.N, 2011, U-Pb and Th-Pb dating of apatite by LA-ICPMS. Chemical Geology, v. 280, n. 1, p. 200-216.

Cottle, J.M., Kylander-Clark, A., Vrijmoed, J.C., 2012, U-Th/Pb Geochronology of Detrital zircon and monazite by Single Shot Laser Ablation Inductively Coupled Plasma Mass Spectrometry (SS-LA-ICPMS), Chemical Geology, v. 332, 136-147. doi: 10.1016/j.chemgeo.2012.09.035

Cottle, J.M., Horstwood, M.S.A, Parrish, R.R., 2009a. A new approach to single shot laser ablation analysis and its application to in situ Pb/U geochronology, Journal of Analytical Atomic Spectrometry, v. 24, 1355-1363. doi: 10.1039/b821899d.

Cottle, J.M., Jessup, M.J., Newell, D.L., Horstwood, M.S., Noble, S.R., Parrish, R.R., Walters, D.J., and Searle, M.P., 2009b, Geochronology of granulitized eclogite from the Ama Drime Massif: Implications for the tectonic evolution of the South Tibetan Himalaya. Tectonics, v. 28, TC1002.

Eggins, S.M., Kinsley, L.P.J., Shelley, J.M.G., 1998, Deposition and element fractionation processes during atmospheric pressure laser sampling for analysis by ICP-MS. Appl. Surf. Sci. v. 127–129, 278–286.

Eggins, S., De Deckker, P., Marshall, J., 2003, Mg/Ca variation in planktonic foraminifera tests; implications for reconstructing palaeo-seawater temperature and habitat migration. Earth Planet Sci. Lett., v. 212, n. 3-4, 291-306.

Ewing, R.C., Meldrum, A., Wang, I., Weber W.J., and Corrales, I.R., 2003, Radiation effects in zircon. *In* J.M. Hanchar and P.W.O. Hoskin. *Eds*., Zircon, 53, p. 378–420. Reviews in Mineralogy and Geochemisty, Mineralogical Society of America, Chantilly, Virginia.

Farley, K. A., Shuster, D. L., Ketcham, R. A., 2011, U and Th zonation in apatite observed by laser ablation ICPMS and implications for the (U–Th)/He system. Geochim. Cosmochim. Acta, v. 75, 4194–4215.

Flowers, R. M., 2009 Exploiting radiation damage control on apatite (U–Th)/He dates in cratonic regions. Earth Planet. Sci. Lett., v. 277, 148–155.

Frei, D., Gerdes, A., 2009, Precise and accurate in situ U-Pb dating of zircon with high sample throughput by automated LA-SF-ICP-MS. Chemical Geology, v. 261, n. 3-4, 261-270.

Green, P. F., Crowhurst, P. V., Duddy, I. R., Japsen, P., and Holford, S. P., 2006, Conflicting (U-Th)/He and fission track ages in apatite: Enhanced He retention, not anomalous annealing behavior: Earth and Planetary Science Letters, v. 250, n. 3–4, p. 407–427, http://dx.doi.org/10.1016/j.epsl.2006.08.022

Gehrels, G., Valencia, V.A. and Ruiz, J., 2008, Enhanced precision, accuracy, efficiency, and spatial resolution of U-Pb ages by laser ablation–multicollector–inductively coupled plasma–mass spectrometry. Geochemistry, Geophysics, and Geosystems, v. 9, n.3, Q03017. doi:10.1029/2007GC001805

Guenthner, W.R., Reiners, P.W., Ketcham, R.A., Nasdala, L., and Geister, G., 2013, Helium diffusion in natural zircon: Radiation damage, anisotropy, and the interpretation of zircon (U-Th)/He thermochronology, American Journal of Science, v. 313, p. 145-198. doi 10.2475/03.2013.01.

Horstwood, M., Gehrels, G., Bowring, J., 2010, Improving consistency in laser ablation geochronology. EOS (2010), Transactions, American Geophysical Union, v. 91, n. 28, 247. doi:10.1029/2010EO280003.

Jaffey, A.H., Flynn, K.F., Glendenin, L.E., Bentley, W.C. and Essling, A.M., 1971, Precision measurement of the half-lives and specific activities of U235 and U238. Physical Reviews C, v. 4, 1889-1906. doi: 10.1103/PhysRevC.4.1889

Jackson, S.E., 2009, Correction of fractionation in LA-ICP-MS elemental and U-Pb analysis. Geochimica et Cosmochimica Acta, v. 73, p. A579.

Johnston, S., Gehrels, G., Valencia, V., Ruiz, J., 2009, Small volume U-Pb zircon geochronology by laser ablation multicollector-ICP-MS. Chemical Geology, v. 259, n. 3–4, 218–229.

Košler, J., Fonneland, H., Sylvester, P., Turbrett, M., Pedersen, R-B., 2002. U-Pb dating of detrital zircons for sediment provenance studies—a comparison of laser ablation ICPMS and SIMS techniques. Chemical Geology, 182: 605-618, doi: 10.1016/S0009-2541(01)00341-2

Ludwig, K.R., 2003. Isoplot/Ex Version 3.00: a Geochronological Toolkit for Microsoft Excel. Berkeley Geochronology Center, Berkeley, CA.

McLean, N. M., Bowring, J.F., Bowring, S.A., 2011, An algorithm for U-Pb isotope dilution data reduction and uncertainty propagation, Geochem. Geophys. Geosyst., v. 12, Q0AA18, doi:10.1029/2010GC003478.

Meldrum, A., Boatner, L.A., Weber, W.J., Ewing, R.C., 1998, Radiation damage in zircon and monazite. Geochimica et Cosmochimica Acta, v. 62, n. 14, 2509–2520.

Nasdala, L., Reiners, P.W., Garver, J.I., Kennedy, A.K., Stern, R.A., Balan, E., Wirth, R., 2004, Incomplete retention of radiation damage in zircon from Sri Lanka. American Mineralogist, v. 89, 219–231.

Paces, J.B., Miller, J.D., 1993, Precise U–Pb ages of Duluth Complex and related mafic intrusions, northeastern Minnesota: geochronological insights into physical, petrogenetic, paleomagnetic, and tectonomagmatic processes associated with the 1.1 Ga midcontinent rift system. J. Geophys. Res. V. 98, 13997– 14013.

Paton, C., J. D. Woodhead, J. C. Hellstrom, J. M. Hergt, A. Greig, and R. Maas (2010), Improved laser ablation U/Pb zircon geochronology through robust downhole fractionation correction, Geochem. Geophys. Geosyst., v. 11, Q0AA06, doi:10.1029/2009GC002618.

Reiners, P.W., 2005, Zircon (U-Th)/He thermochronometry. In Reiners, P.W., and Ehlers, T.A., eds., Low-temperature thermochronology: Techniques, interpretations, and applications. Reviews in Mineralogy and Geochemistry, v. 58, p.49-93

Reiners, P., Campbell, I., Nicolescu, S., Allen, C., Hourigan, J., Garver, J., Mattinson, J., Coman, D., 2005, (U-Th) / (He-Pb) double dating of detrital zircons. American Journal of Science, v. 305, p. 259-311.

Schmitz, M.D., Bowring, S.A., Ireland, T.R., 2003, Evaluation of Duluth Complex anorthositic series (AS3) zircon as a U–Pb geochronological standard, new high-precision isotope dilution thermal ionization mass spectrometry results. Geochimica et Cosmochimica Acta, v. 67 n. 19, 3665–3672.

Shuster, D. L., Flowers, R. M., Farley, K. A., 2006, The influence of natural radiation damage on helium diffusion kinetics in apatite. Earth Planet. Sci. Lett., v. 249, 148–161.

Sláma, J. et al., 2008, Plešovice zircon -- A new natural reference material for U–Pb and Hf isotopic analysis. Chemical Geology, v. 249: 1–35. doi: 10.1016/j.chemgeo.2007.11.005.

Stacey, J.S., Kramers, J.D., 1975, Approximation of terrestrial lead isotope evolution by a two-stage model. Earth Planet. Sci. Lett., v. 26, 207– 221.

Till, C.B., Grove, T.L., Withers, A.C., 2012, The beginnings of hydrous mantle wedge melting. Contributions to Mineralogy and Petrology, v. 163, n. 4, 669-688.

Tollstrup, D.L., Liewen, X., Winpenny, J.B., Chin, E., and Lee, C.T., 2012, A trio of laser ablation in concert with two ICP-MSs; simultaneous, pulse-by-pulse determination of U-Pb discordant ages and a single spot Hf isotope ratio analysis in complex zircons from petrographic thin sections. Geochemistry, Geophysics, Geosystems, v. 13, n. 3, Q03017.

Vorhies, S.H., Ague, J.I., Schmitt, A.K., 2013, Zircon growth and recrystallization during progressive metamorphism, Barrovian zones, Scotland. American Mineralogist, v. 98, 219–230.

White, L. T., Ireland, T. R., 2012, High uranium matrix effect in zircon and its implications for SHRIMP U-Pb age determinations. Chemical Geology, v. 306-307, 78-91. doi:http://dx.doi.org/10.1016/j.chemgeo.2012.02.025

Woodhead, J., Hergt, J., Shelley, M., Eggins, S., Kemp, R., 2004, Zircon Hf-isotope analysis with an excimer laser, depth profiling, ablation of complex geometries, and concomitant age estimation. Chemical Geology, v. 209, 121–135.

SUPPLEMENTARY MATERIAL FOR CHAPTER 4

STATISTICAL MEASURES OF ABLATION RATE

Eight ablation rate experiments were conducted on four different types of zircon grains. For each experiment an increasing number of bursts of five laser pulses (up to 15) were delivered to the grain in a sequential order. The 15 ablation pits for each experiment were then measured by vertical scanning interferometry. Ordinary and generalized least squares regression analysis were performed on the combined depth data from two experiments on WF1, WF6, and WF10; WF2 was treated as two distinct regressions due to significantly different behavior for each of the experiments. The results are summarized below. A second analysis was performed in which the depth of the first integration was subtracted from all subsequent data points for each experiment and the number of bursts was reduced by 1. A regression of this modified data set helps to determine whether linear behavior occurs after the first integration regardless of its (potentially non linear) behavior. Four data points were removed from WF10 (first four of second experiment) because the laser energy was observed to be highly variable during these analyses and resulted in abnormal depths. For all other analyses the laser energy was stabilized at 4 ± 0.1 J cm^{-2}.

ORDINARY LEAST-SQUARES REGRESSION

WF1

Coefficients:

	Value	Std.Error	t-value	p-value
(Intercept)	0.26820	0.05628	4.765	5.27e-05 ***
sample	0.74968	0.00619	121.114	< 2e-16 ***

Signif. codes: 0 ‘***’ 0.001 ‘**’ 0.01 ‘*’ 0.05 ‘.’ 0.1 ‘ ’ 1
Residual standard error: 0.1465 on 28 degrees of freedom
Multiple R-squared: 0.9981, Adjusted R-squared: 0.998
F-statistic: 1.467e+04 on 1 and 28 DF, p-value: < 2.2e-16

WF2A

Coefficients:

	Value	Std.Error	t-value	p-value
(Intercept)	0.027457	0.054108	0.507	0.62
sample	0.669543	0.005951	112.508	<2e-16 ***

Signif. codes: 0 ‘***’ 0.001 ‘**’ 0.01 ‘*’ 0.05 ‘.’ 0.1 ‘ ’ 1
Residual standard error: 0.09958 on 13 degrees of freedom
Multiple R-squared: 0.999, Adjusted R-squared: 0.9989
F-statistic: 1.266e+04 on 1 and 13 DF, p-value: < 2.2e-16

WF2B

Coefficients:

	Value	Std.Error	t-value	p-value
(Intercept)	0.463604	0.078894	5.876	7.52e-05 ***
sample	0.790081	0.009266	85.270	< 2e-16 ***

Signif. codes: 0 '***' 0.001 '**' 0.01 '*' 0.05 '.' 0.1 ' ' 1
Residual standard error: 0.1398 on 12 degrees of freedom
Multiple R-squared: 0.9984, Adjusted R-squared: 0.9982
F-statistic: 7271 on 1 and 12 DF, p-value: < 2.2e-16

WF6

Coefficients:

	Value	Std.Error	t-value	p-value
(Intercept)	0.255341	0.041902	6.094	1.65e-06 ***
sample	0.699231	0.004625	151.174	< 2e-16 ***

Signif. codes: 0 '***' 0.001 '**' 0.01 '*' 0.05 '.' 0.1 ' ' 1
Residual standard error: 0.1091 on 27 degrees of freedom
Multiple R-squared: 0.9988, Adjusted R-squared: 0.9988
F-statistic: 2.285e+04 on 1 and 27 DF, p-value: < 2.2e-16

WF10

Coefficients:

	Value	Std.Error	t-value	p-value
(Intercept)	0.08683	0.12968	0.67	0.51
sample	0.80295	0.01302	61.65	<2e-16 ***

Signif. codes: 0 '***' 0.001 '**' 0.01 '*' 0.05 '.' 0.1 ' ' 1
Residual standard error: 0.2601 on 21 degrees of freedom
Multiple R-squared: 0.9945, Adjusted R-squared: 0.9942
F-statistic: 3801 on 1 and 21 DF, p-value: < 2.2e-16

GENERALIZED LEAST-SQUARES REGRESSION

WF1

Generalized least squares fit by maximum likelihood

AIC	BIC	logLik
-26.1853	- 21.981	16.09268

Coefficients:

	Value	Std.Error	t-value	p-value
(Intercept)	0.2681952	0.05627949	4.76542	1e-04
sample	0.7496839	0.00618992	121.11369	0e+00

WF2A

Generalized least squares fit by maximum likelihood

AIC	BIC	logLik
-22.78199	-20.65784	14.39099

Coefficients:

	Value	Std.Error	t-value	p-value
(Intercept)	0.0274571	0.05410794	0.50745	0.6203
sample	0.6695429	0.00595108	112.50779	0.0000

WF2B

Generalized least squares fit by maximum likelihood

AIC	BIC	logLik
-11.52819	-9.611021	8.764096

Coefficients:

	Value	Std.Error	t-value	p-value
(Intercept)	0.4636044	0.07889386	5.87631	1e-04
sample	0.7900813	0.00926561	85.27026	0e+00

WF6

Generalized least squares fit by maximum likelihood

AIC	BIC	logLik
-42.2988	-38.19691	24.1494

Coefficients:

	Value	Std.Error	t-value	p-value
(Intercept)	0.2553412	0.04190177	6.0938	0
sample	0.6992309	0.00462533	151.1742	0

WF10

Generalized least squares fit by maximum likelihood

AIC	BIC	logLik
26.63403	30.63064	-10.31701

Coefficients:

	Value	Std.Error	t-value	p-value
(Intercept)	0.5179641	0.14020057	3.69445	0.001
sample	0.7661615	0.01535272	49.90395	0.000

GENERALIZED LEAST-SQUARES REGRESSION AFTER

SUBTRACTION OF THE FIRST INTEGRATION

WF1

Generalized least squares fit by maximum likelihood

AIC	BIC	logLik
-0.998889	2.997725	3.499444

Coefficients:

	Value	Std.Error	t-value	p-value
(Intercept)	0.0934670	0.08845864	1.05662	0.3004
sample	0.7473473	0.01038894	71.93681	0.0000

WF2A

Generalized least squares fit by maximum likelihood

AIC	BIC	logLik
-19.98708	-18.06991	12.99354

Coefficients:

	Value	Std.Error	t-value	p-value
(Intercept)	0.0329670	0.05832321	0.56525	0.5823
sample	0.6687187	0.00684971	97.62725	0.0000

WF2B

Generalized least squares fit by maximum likelihood

AIC	BIC	logLik
-17.86366	-16.16881	11.93183

Coefficients:

	Value	Std.Error	t-value	p-value
(Intercept)	0.3899615	0.06181059	6.30898	1e-04
sample	0.7789396	0.00778740	100.02559	0e+00

WF6

Generalized least squares fit by maximum likelihood

AIC	BIC	logLik
-40.73897 -	36.85145	23.36948

Coefficients:

	Value	Std.Error	t-value	p-value
(Intercept)	0.1996721	0.04225828	4.72504	1e-04
sample	0.6943873	0.00497379	139.60920	0e+00

WF10

Generalized least squares fit by maximum likelihood

AIC	BIC	logLik
57.57445	61.34874	-25.78722

Coefficients:

	Value	Std.Error	t-value	p-value
(Intercept)	0.1076050	0.27349014	0.393451	0.6975
sample	0.7622629	0.03185058	23.932469	0.0000

APPENDIX A. DETAILED METHOD DESCRIPTIONS

This section is divided into two parts: Part 1 provides the detailed method for our measurement of marine terraces, uncertainty calculations, and compares our results with previously published terrace elevations near Santa Cruz, CA to evaluate the validity of the method; Part 2 provides the detailed method and uncertainty calculations for our low-temperature thermochronometric analyses. Detailed analytical data can be found in Appendices B and C.

PART 1—MARINE TERRACES ALONG THE CENTRAL CALIFORNIA COAST

OVERVIEW

Flights of wave-cut marine terraces have been cut into the rugged Big Sur and Santa Cruz coastline over the past several hundred ka (Alexander, 1953; Bradley and Griggs, 1976; Lajoie et al., 1979; McKittrick, 1988; Weber, 1990). The elevation of contiguous terrace levels was presumably similar during their formation but now varies considerably. These variations provide an opportunity to examine the latest Pleistocene to recent time-integrated record of vertical deformation.

This study was undertaken to document the height of the lowest-emergent marine terrace from near San Simeon at the south end of the Big Sur coast northward through Santa Cruz to Point Ano Nuevo. The lowest terrace level was chosen specifically because reconnaissance work in Big Sur revealed that only a single marine terrace is preserved in most locations and it can be continuously tracked and correlated with the first emergent terrace near Monterey. The first emergent terrace near Santa Cruz and Monterey was resurveyed owing to advances in surveying techniques since the 1950s and 1970s when it was last measured (Alexander, 1953; Bradley and Griggs, 1976), and also to help validate our method. Additional constraints and elevation data are provided by continuous lidar coverage along the California coast through the California Coastal Conservancy Coastal Lidar Project (http://coast.noaa.gov/dataviewer) and the 3DEP program at the U.S. Geological Survey.

The elevation of the bedrock terrace surface was measured from Point Ano Nuevo through Aptos on the northern side of Monterey Bay (February, 2016) and from downtown Monterey through Ragged Point at the southern end of the Big Sur coastline (September, 2014 to March, 2015). Altogether this resulted in the collection of 1,025 elevation measurements of the bedrock surface (Fig. A-1). An additional ~3,500 measurements of the terrace surface elevation along its front edge (nearest the ocean) were made using lidar; these measurements are a maximum

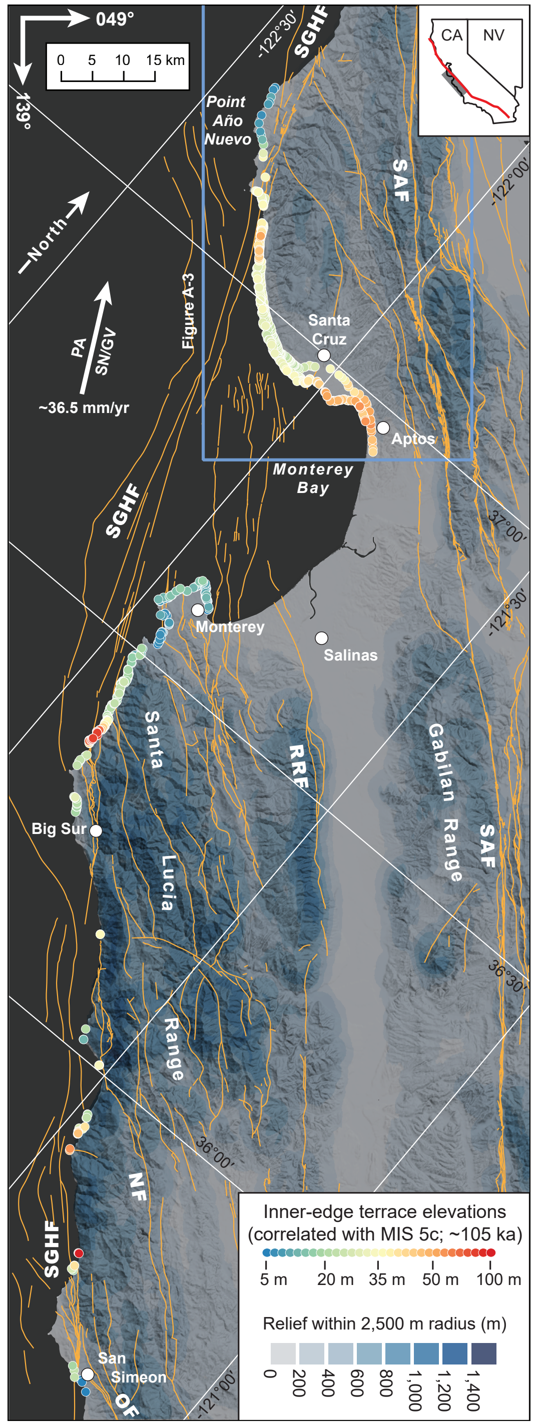

Figure A-1. Focused zones of surface uplift and exhumation are found along the San Gregorio-Hosgri fault (SGHF) in central coastal California. Oblique mercator projection is rotated so that the long edge of the map is parallel to the N41°W trace of the main San Andreas fault (SAF). Ovals are the youngest (U-Th)/He ages found along the SGHF or SAF outside of this figure; blue (apatite) and red (zircon); D_CONE_1 from Cone Peak (CP) transect of Ducea et al. (2003); GAB5 from Spotila et al. (1998); remainder from this study. Blue rectangle is pooled apatite fission track age from Bürgmann et al. (1994). Slip history constraints are from Weber (1990), Clark (1998), Dickenson et al. (2005), and d'Alessio et al. (2005). Terrace elevations are from this study (n=1,025), Alexander (1953), n=26; Bradley and Griggs (1976), n=151; Lajoie et al. (1979), n=15; and Hanson et al. (1994) n=6. Faults are from the Quaternary fault and fold database (USGS, 2006). General outcrop of Coast Ridge Belt (CRB) shown with light shading, after Kidder et al. (2003). Relative plate vector and rate is from DeMets and Merkouriev (2016). NF-Nacimiento fault; OF-Oceanic fault; RRF-Reliz-Rinconada fault.

estimate of the bedrock surface because they include the colluvial or alluvial deposits above the bedrock surface and were not used in our analysis.

DATA COLLECTION

Directly surveying the bedrock surface of marine terraces is challenging due to steep cliffs, varying thickness of sedimentary deposits, and limited access to coastal bluffs. Because of this, terraces were first identified on lidar and using Google Earth. Each site was visited and the elevation of the bedrock terrace surface was measured using a laser rangefinder (Laser Tech TruPulse 360B) coupled with a survey grade GPS receiver (Trimble GPS Pathfinder ProXH) and a rugged tablet computer (Trimble Yuma). These three components communicate wirelessly and determine the position and elevation of the laser rangefinder target. This is accomplished by using the sight distance, angular declination, and azimuth from the laser rangefinder and applying this offset to the GPS location of the user. Given the non-reflective character of most rock types, the functional limit of the laser rangefinder was less than about 500 m; for this dataset, the average sight distance was ~132 m. For each data point collected, two additional parameters were recorded: the vertical offset between the GPS receiver and the laser rangefinder, and the laser rangefinder sight distance.

DIFFERENTIAL GPS PROCESSING

After collection in the field, a differential correction was calculated and applied to the GPS location using the GPS Pathfinder Office software from Trimble. Base stations were selected based on their proximity to the survey and include stations P534, P231, P172, and P173 from the CORS (Continuously Operated Reference Station) network maintained by the National Geodetic Survey.

Location uncertainty for the GPS receiver is a function of many factors, including satellite coverage, number of data points recorded for each location, and the quality of differential correction. At 1σ, vertical (elevation) uncertainties average ~0.6 m (range from 0.1–3.1 m) and horizontal uncertainties average ~0.45 m (range from 0.1–2.9 m). These uncertainties do not include those introduced by the laser rangefinder offset, which is discussed below.

MEASUREMENT UNCERTAINTY

A full accounting of the uncertainties introduced by the laser rangefinder would require the addition of two 3-dimensional error ellipsoids: the ellipsoid of the rangefinder (with axis orientations determined by the inclination and azimuth of the sighting), and the orthogonal ellipsoid of the GPS receiver. In order to simplify the uncertainty estimate, it is assumed that the difference between using error ellipsoids and a simple quadratic addition is significantly less than the uncertainty itself; therefore a simpler quadratic summation is used to estimate the combined uncertainty from the GPS measurement and the laser rangefinder offset.

Table A-1. Specifications and typical values for the Laser Tech TruPulse 360B laser rangefinder.

Parameter	Value
Distance accuracy to typical targets	±0.3 m
Distance accuracy to distant or weak targets	±0.3–1 m
Inclination accuracy (typical)	±0.25°
Azimuthal accuracy (typical)	±1°
Maximum range to non-reflective targets	1,000 m
Working range to bedrock targets (this project)	~500 m

Uncertainties for the laser rangefinder offset can be estimated from the product specifications provided by the manufacturer (Laser Tech). The provided specifications are not clearly defined as either 1σ or 2σ and no further information was available; thus, 2σ values are assumed and 1σ values are used in uncertainty calculations.

Table A-2. Parameters used in uncertainty calculations.

Parameter	Description
D_m	Measured offset distance
I_m	Measured offset inclination
Eh_a	Horizontal uncertainty perpendicular to the offset azimuth
Ez_i	Vertical uncertainty perpendicular to the sight line
Eh_{dm}	Horizontal uncertainty parallel to the offset azimuth
Ezm	Total measurement elevation uncertainty estimate
Eh	Total horizontal uncertainty estimate; average of ~1.2 m 1σ
E_a	Azimuthal measurement uncertainty (1σ=0.5°)
E_i	Inclination measurement uncertainty (1σ=0.125°)
E_d	Distance measurement uncertainty (1σ=0.5 m at 1,000 m)
E_{gps_h}	Horizontal uncertainty estimate from GPS measurement (1σ); average 0.45 m
E_{gps_v}	Vertical uncertainty estimate from GPS measurement (1σ); average 0.6 m

HORIZONTAL UNCERTAINTY

Horizontal uncertainty is estimated by quadratic summation of the radial GPS uncertainty and the directional components of the offset uncertainty. The azimuth-parallel uncertainty must be transformed into the horizontal plane, but the azimuth-perpendicular component does not. The uncertainty perpendicular to the offset azimuth is given by:

$$Eh_a = \sqrt{(D_m \tan(E_a))^2 + (E_{gps\_h})^2}$$

and the uncertainty along the offset azimuth is:

$$Eh_{dm} = \sqrt{(D_m E_d \cos(I_m))^2 + (E_{gps\_h})^2}$$

These formulations provide a simple estimate of the horizontal error ellipse. However, it proved difficult to extract inclination values from the Trimble software or the laser rangefinder and this information is available for only ~300 of the >1,000 survey points. Using these ~300 data points as a test case, the average horizontal azimuth-perpendicular component of uncertainty is ~1.5 m whereas the average azimuth-parallel component is only 0.09 m. Thus, because the azimuth-parallel component is such a small fraction of either the azimuth-perpendicular component or the GPS component, it was not used in the final horizontal uncertainty calculation, which is given by:

$$Eh = Eh_a$$

This results in an overestimation of the azimuth-parallel component of uncertainty which is acceptable for this analysis. Average horizontal uncertainty (Eh_a) for the dataset is ~1.2 m 1σ.

VERTICAL UNCERTAINTY

Vertical uncertainty is estimated by quadratic summation of the GPS uncertainty and the uncertainty associated with the laser rangefinder offset. The vertical uncertainty perpendicular to the line of sight can be estimated by:

$$Ez_i = D_m \sin(E_i)$$

This results in 1σ vertical uncertainties of ~0.21 m/100 m of measured distance. Combined with the GPS uncertainty, the total vertical uncertainty estimate is:

$$Ezm = \sqrt{(Ez_{gps\_v})^2 + (Ez_i)^2}$$

Average vertical uncertainty for the entire dataset is ~0.7 m at 1σ.

TERRACE BACK-EDGE MODEL

OVERVIEW

During sea-level highstands, if a coastline is not overwhelmed with sediment, a front of erosion caused by wave abrasion migrates landward to create a gently sloping bench that terminates at a steep coastal cliffline. The location of this prominent break-in-slope—called a shoreline angle, back edge, or inner edge—is important because it marks paleohorizontal along the coastline and can be tied to the mean sea level at the time of its formation. These characteristics make the back edge of a marine terrace an excellent strain marker that can be used to document patterns of deformation since its formation. As sea level changes, however, these back edges are abandoned, erosional processes begin degrading the hillslope, and the back edge and terrace are covered by colluvial material.

Many studies in coastal California have used the elevation of marine terrace back edges to infer horizontal (e.g. Weber, 1990) or vertical (e.g. Bradley and Griggs, 1976) deformation. Most all of these studies determine elevations directly at or very near the original back edge of the terrace. These studies typically take advantage of natural exposures that reveal the original elevation of the bedrock terrace surface. Without such exposures, boreholes or geophysical techniques must be used to determine the thickness of colluvial cover above the bedrock surface. The advantage of determining the elevation of the bedrock surface at or near the back edge is that elevations at this location they have their greatest paleohorizontal meaning. However, limited access because of private property and relatively few natural outcrops make these measurements difficult.

An additional concern with measuring back-edge elevations at the back edge is that the spacing between measurements is often great. Wide spacing may be acceptable for a regional study, but a higher fidelity recorder is required in order to test the history of vertical deformation across individual fault strands.

An alternative, used in this study, is to measure the elevation of the bedrock surface where it is abundantly exposed—along the modern sea cliffs. This provides the benefit of high measurement density, data can be collected rapidly, and areas difficult or impossible to reach can still be surveyed using modern equipment. The drawback to this method is that each surveyed point is located somewhere downslope of (and below) the terrace back edge; thus each measurement must be 'adjusted' to remove the change in elevation resulting from the gently sloping marine terrace surface.

The method developed in this study to provide this adjustment consists of five main steps, each of which are detailed below:

1) Define the terrace back edge using lidar and previous mapping, where applicable
2) Determine the distance between each data point and the back edge
3) Develop a statistically robust model of the bedrock paleoslope
4) Use the back-edge distance and the paleoslope model to determine a correction for each data point
5) Robustly propagate uncertainty

BACK EDGE LOCATION AND DISTANCE

The location of the back edge was developed using a combination of lidar from the 2009–2011 California Coastal Conservancy Coastal Lidar Project and, near Santa Cruz, rectified geologic maps that focus on marine terraces (Alexander, 1953; Bradley and Griggs, 1976). The basic method was to draw a line in GIS at the base of the break in slope above the first extensive marine terrace. Near Santa Cruz, this correlates with the Highway 1 terrace; near Monterey this correlates generally with 'Terrace 1' of McKittrick (1988). Where there are both maps and lidar, the mapped location of the terrace back edge was always within several m of the break in slope observed on lidar. This correlation provides confidence that mapping the back edge using lidar in areas without existing detailed maps works well. Although the two different methods are in good agreement, the back edge mapped from lidar was used for all calculations because of its inherently higher spatial resolution. Once the back edge was mapped for the length of the study area, the distance to the nearest back edge was calculated for each data point needing adjustment.

MODELING THE BEDROCK PALEOSLOPE

Aside from distance, the single largest factor that affects the magnitude back-edge adjustment is the paleoslope of the bedrock surface. Paleoslopes were determined for all terrace levels along the coast north of Santa Cruz by Bradley and Griggs (1976). The data for the Highway 1 (MIS 5c) terrace (Table A-3) was analyzed to develop a robust model of the bedrock paleoslope for this time period that was subsequently applied to all survey and front-edge measurements.

Table A-3. Original bedrock paleoslope data for the 'Highway 1' terrace level from Bradley and Griggs (1976). Onshore-slope widths were provided by the original authors, but offshore widths were not and were estimated from their scaled profiles. The original authors provided unit-less slope which has been converted here to degree slope and elevation change.

Profile no.	Width (m)	Change in elevation (m)	Slope (°)	Offshore width (m)	Change in elevation (m)	Slope (°)
10	396	6.73	0.97	1029	7.20	0.40
11	427	14.94	2.00	1073	7.51	0.40
12	427	7.26	0.97	773	6.96	0.52
13	530	10.60	1.15	270	2.70	0.57
14	305	9.76	1.83	245	3.19	0.74
15	366	10.61	1.66	184	3.13	0.97
16	335	7.71	1.32	315	3.15	0.57
18	427	8.11	1.09	223	2.23	0.57
19	244	8.30	1.95	606	6.06	0.57
21	305	9.46	1.78	495	8.42	0.97
26	360	11.88	1.89	1640	11.48	0.40
18	213	3.20	0.86	– – –	– – –	– – –
19	305	3.05	0.57	– – –	– – –	– – –
21	213	3.41	0.92	– – –	– – –	– – –
17	287	9.76	1.95	– – –	– – –	– – –
20	293	8.50	1.66	– – –	– – –	– – –
22	30	1.89	3.60	– – –	– – –	– – –
23	11	0.59	3.09	– – –	– – –	– – –
24	53	2.49	2.69	– – –	– – –	– – –

A two-slope model was created that divides the paleoslope into an onshore and offshore segment. The transition from onshore to offshore was calculated by using the mean onshore segment length for profiles that contained both on and offshore segments. Slopes for each segment were calculated using a mean, weighted by segment length such that longer segments contribute more to the average (Table A-4). This seemed especially important for the longer-length offshore segments which have lower slopes in general.

Table A-4. Parameters and values used in the back-edge model.

Parameter	Description
z	Original elevation (from survey or lidar)
Ez_m	Elevation measurement uncertainty (1σ)
Ez	Elevation uncertainty, model and measurement (1σ)
Ez_s	Elevation uncertainty, back-edge model
z'	'Corrected' back-edge elevation
d	Distance from measurement to back edge
d_o	Transition from onshore to offshore (m); 374.7 ±78.3 1σ
d_{ol}	Lower bound; 296.4
d_{ou}	Upper bound; 453.0
S_{on}	Onshore slope (weighted by length); 1.412° ±0.467°
S_{off}	Offshore slope (weighted by length); 0.518° ±0.175°

EXTRAPOLATING THE RANGE OF BACK-EDGE ELEVATIONS

For each measurement point, the back-edge elevation is estimated using the values in Table A-4 with:

$$z'(d) = \begin{cases} d < (d_{ol});\, z + d\tan(S_{on}) \\ d < (d_{ou'});\, z + (d_{ol})\tan(S_{on}) + \dfrac{(d - d_{ol})\left[\tan(S_{off}) + \tan(S_{on})\right]}{2} \\ d \geq (d_{ou});\, z + (d_{ol})\tan(S_{on}) + \dfrac{(d_{ou} - d_{ol})\left[\tan(S_{off}) + \tan(S_{on})\right]}{2} + (d - d_{ou})\tan(S_{off}) \end{cases}$$

Uncertainty about this corrected value is estimated using the same form of the above equation but calculating an upper and lower bound using the 1σ deviation about the slope value. The difference between these bounds is the uncertainty for that point, which is then added in quadrature for each piecemeal equation.

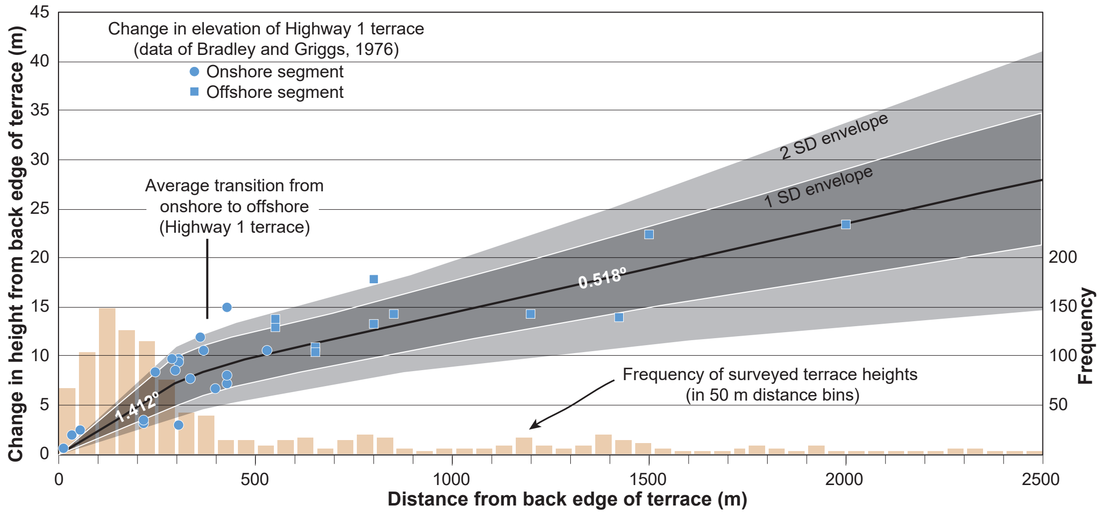

Figure A-2. Comparison of our bedrock slope model with observed values of the 'Highway 1' terrace observed between Santa Cruz and Point Ano Nuevo, CA.

Figure A-2 shows the original data points from Bradley and Griggs (1976) and our bedrock paleoslope model. Of the original 33 data points, 22 are captured within our 1σ envelope using this method. At 2σ, 5 data points lie outside of our envelope, indicating that there is some misfit (largely a result of 3 high-slope/short-width points). Figure A-2 also contains a histogram of surveyed data points which indicates that most of the survey corrections are restricted to the onshore portion of the model.

Uncertainties introduced by the back-edge correction are substantial and largely mask the uncertainties associated with measurement. The majority of our data have back-edge distances of less than ~400 m, corresponding to uncertainties of less than about 5 m. Total uncertainty is estimated with:

$$Ez = \sqrt{Ez_m^{\ 2} + Ez_s^{\ 2}}$$

ELEVATION DATA FROM PREVIOUS WORKERS

Additional constraints come from the results of previous works in the region who documented terraces near San Simeon, south of Ragged Point (Hanson et al., 1994); near Monterey (McKittrick, 1988), and from Aptos northward (Alexander, 1953; Bradley and Griggs, 1976; Lajoie et al., 1979). These data were compiled from their original sources, digitized, and used to help validate our method in areas where the data sets overlap.

Much of the previous data in the Santa Cruz and Monterey area lack georeferenced elevation points. The method used to extract data from these reports is in general similar, but varies depending on how the authors presented their data. In general, maps and terrace-elevation profiles were scanned at 600 dpi and georeferenced using QGIS. A line feature class was digitized from the back edge of terraces and terrace points were transformed from their profile plot back to their near-original location at the back edge of the terrace. The details of this transformation vary and are discussed below.

ALEXANDER (1953)

Terraces were mapped on a geologic map with abundant geographic reference lines. Terrace elevations were provided on a coast-parallel profile without a definite distance axis, but with abundant and clear depiction of drainages and relative terrace widths. The geologic map was georeferenced and the back-edge of terraces matched well with lidar terrace scarps. Because the number of data were few and the cartographic representation on the profiles was so good, elevation data from the profile could be directly added to a series of points in GIS.

BRADLEY AND GRIGGS (1976)

Terraces were mapped on a geologic map with no geographic reference lines but abundant drainages. Terrace elevations were provided on a coast-parallel plot with a defined distance axis and the locations of drainages were well marked. After georeferencing, the back edge of terraces matched well with lidar scarps and drainages were well located. The elevation profile was georeferenced with a custom reference frame such that the digitization of each elevation data point yielded an elevation measurement and a distance measurement. The profile (and its data points) were then divided into segments defined by drainages marked on the profile and geologic map. The distance between the drainages was measured on the map and this value was used to scale the distance measured between the drainages on the profile. This effectively allows the profile terrace points to have a non-uniform scaling between the profile and the back edge. Data transformed to the back edge in this way were transformed onto the mapped terrace extents and not into drainages where they were assuredly not measured. This gives us confidence that our transformation places the points in a position that is likely near their original location.

LAJOIE ET AL. (1979)

Data from this study were georeferenced and transformed onto a coast-parallel transect in Gutmonsdotir et al. (2013); and the transformed data were graciously made available by Maria Gutmonsdotir. Using the trend and location of the coast-parallel transect line from Gutmonsdotir et al. (2013) and the back-edge locations from lidar, the coast-parallel data were transformed to the back edge. Transformed data fall on terrace surfaces and gaps in data are co-located with gaps in the terrace, lending confidence in the transformation process.

MCKITTRICK (1988)

Terrace elevations were provided on a coast-parallel plot with abundant geographic and geologic annotation; no map of the terraces was provided. Similar to the Bradley and Griggs (1976) data, the elevation profile was georeferenced into a custom reference frame that allowed distance and elevation values to be extracted. The profile was then divided into segments based on faults that cross the profile as it wraps around the irregular coast near Monterey, CA. A continuous line was constructed for the terrace back edge from lidar and distances between the profile segments were measured on the map. The map measurements allowed a non-uniform scaling for each segment which was important given the complexity of the coastline. Terrace elevation points from the profile were then transformed onto the back edge. The presumed MIS 5c back edge was used for all terrace levels described by McKittrick (1988). This simplification introduces positional (geographic) uncertainty in older terrace data points since older terraces had back edges that were presumably farther inland. However, it was beyond the scope of this study to map these older terrace levels in detail and they are not the focus of this work.

HANSON ET AL. (1994)

Terrace deposits, back edges, and the elevation of terrace back edges where measured, were provided on a geologic map. However, no geographic reference lines or points were noted; the map was georeferenced using stream intersections and coastline features. After georeferencing, mapped back edges were all coincident with lidar scarps and drainages were well located. Terrace heights and locations were digitized directly from the map.

DISTANCE TO THE SAN GREGORIO-HOSGRI FAULT

The distance from each data point to the San Gregorio-Hosgri fault was the last geospatial calculation to be completed. Simplified traces of the SGHF were constructed in GIS using the USGS Quaternary fault and fold database (USGS, 2006). The distance from each point to the nearest part of the simplified fault trace was calculated, with the convention that positive values are east or northeast of the SGHF.

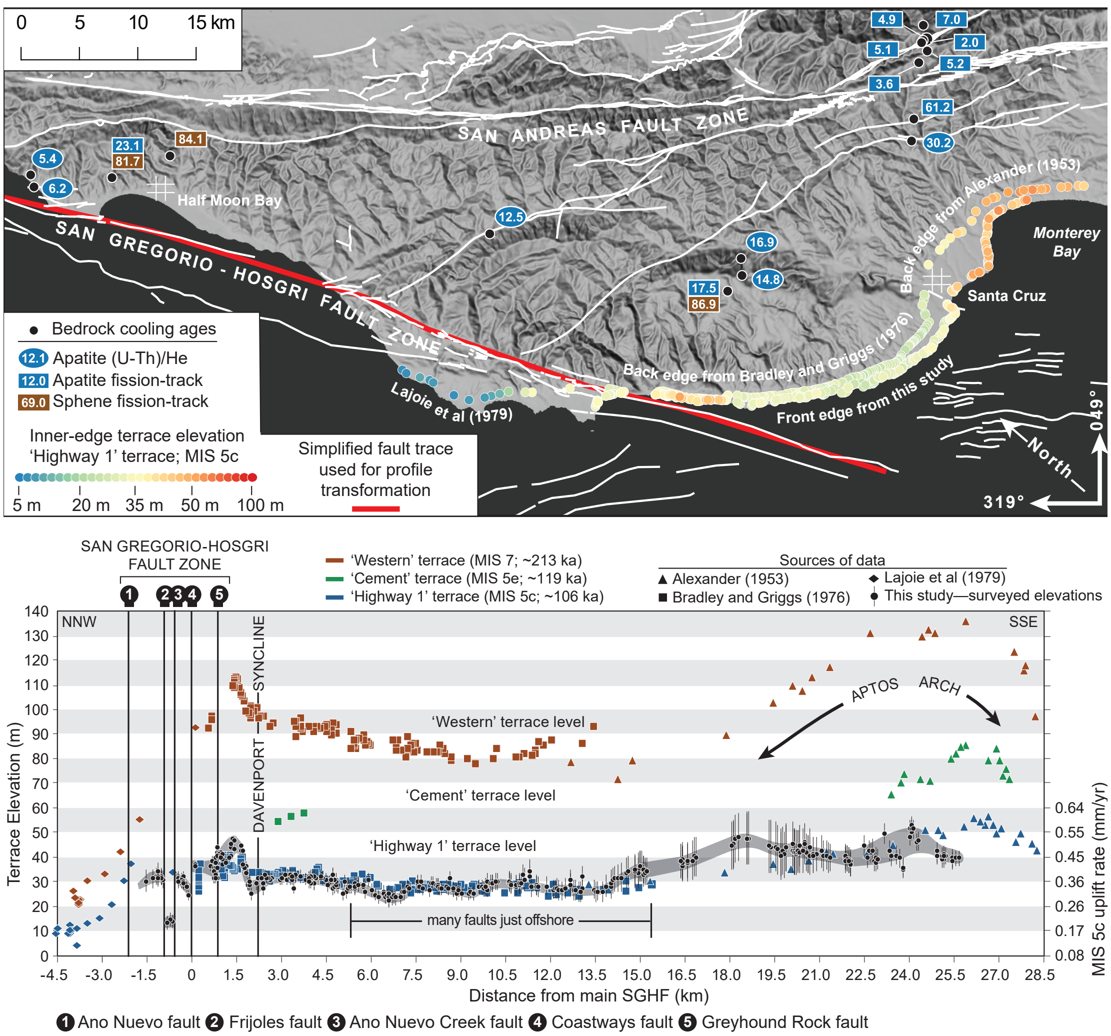

Figure A-3. Uplifted marine terraces near Santa Cruz, CA and their relationship to bounding strike-slip faults. Oblique mercator projection is rotated so that the top edge of the map is parallel to the N41°W trace of the main San Andreas fault (SAF). Apatite (U-Th)/He ages are from C. Baden (Stanford University, written commun., 2016); apatite fission-track ages from the upper-right portion of the map are from Bürgmann et al. (1994); apatite and sphene fission track ages are from Naeser and Ross (1976).

COMPARISON OF RESULTS NEAR SANTA CRUZ, CA WITH PREVIOUS ESTIMATES OF TERRACE ELEVATION

To validate our surveying method we compare elevations of the lowest-emergent marine terrace from Aptos northward through Santa Cruz to Point Año Nuevo (Fig. A-3). The general character of the marine terraces is evident in both our new data and previous surveys, and shows the slight uplift near the SGHF and larger uplift near the SAF described by previous workers (Bradley and Griggs, 1976; Anderson, 1990; Valensise and Ward, 1992; Anderson and Menking, 1994). The excellent agreement between our data and that of Bradley and Griggs (1976) suggests that our method of measurement and back-edge adjustment produce elevations similar to those measured directly at the back edge. This correlation provides confidence in our elevations farther south near Big Sur.

The fault-perpendicular offset between the crest of the 'Aptos Arch' in the data of Alexander (1953) and our elevation data is noticeable and most likely attributed to the significant differences in the locations of observation; Alexander (1953) measured several km farther inland and north of our coastal bluff measurements. This difference serves as a cautionary statement. Although our method appears to replicate elevations at the back edge, the presence of a horizontally varying vertical deformation field—such as that demonstrated for this stretch of coastline by many authors (e.g. Anderson and Menking, 1994)—means that terrace back edges and coastal bluffs may experience different amounts of uplift if the terrace is wide relative to the variation in uplift.

The increased resolution of our new data, and the fault-perpendicular profile transformation help to define several features of the vertical deformation field that were difficult to observe in the older data sets that used a coast-parallel or fault-parallel transformation. 1) The 'Aptos Arch' appears to be a composite feature, possibly created by two sub-parallel anticlines. This is a permissible feature in all terrace levels of the Alexander (1953) data and is noted, with much scatter, in our new data. 2) The Davenport Syncline (Brabb, 1997) is well expressed in the terrace elevations, appears to be flanked to the SW by an anticline, and is likely a developing structural feature. 3) Terrace elevations drop considerably across the SGHF zone as a whole, and do so in discrete steps across individual faults—such as the 10–15 m drop across the Coastways fault—as noted by previous workers in this area (e.g. Weber and Allwardt, 2001).

REFERENCES USED IN PART 1

Alexander, C.S., 1953, The marine and stream terraces of the Capitola-Watsonville area. University of California Publications in Geography, v. 10, p. 1–44.

Brabb, E.E., 1997, Geologic map of Santa Cruz County, California: A digital database. U.S. Geological Survey Open-File Report 97-489, 1-sheet, 15 pp., 1:62,500 scale.

Bradley, W.C., Griggs, G.B., 1976, Form, genesis, and deformation of central California wave-cut platforms. Geological Society of America Bulletin, v. 87, p. 433–449.

Bürgmann, R., Arrowsmith, R., Dumitru, T., and McLaughlin, R., 1994, Rise and fall of the southern Santa Cruz Mountains, California, from fission tracks, geomorphology, and geodesy. Journal of Geophysical Research, v. 99, p. 20,181-20,202.

Hanson, K.L., Wesline, J.R., Lettis, W.R., Kelson, K.I., Mezger, L., 1994, Correlation, ages, and uplift rates of Quaternary marine terraces: south-central coastal California, in Alterman, I.B., McMullen, R.B., Cluff, L.S., and Slemmons, D.B., eds., Seismotectonics of the Central California Coast Ranges, Geological Society of America Special Paper 292, p. 45-71.

Lajoie, K.R., Weber, G.E., Mathieson, S.A., Wallace, J., 1979, Quaternary tectonics of coastal Santa Cruz and San Mateo counties, California, as indicated by deformed marine terraces and alluvial deposits, in Weber, G.E., Lajoie, K.R., and Griggs, G. B., eds., Coastal tectonics and coastal geologic hazards in Santa Cruz and San Mateo counties, California. Geological Society of America Field Trip Guidebook, p. 61-80.

McKittrick, M.A., 1988, Elevated marine terraces near Monterey, California. University of Arizona Thesis, 46 p.

Naeser, C.W., and Ross, D.C., 1976, Fission-track ages of sphene and apatite of granitic rocks of the Salinian Block, Coast Ranges, California. Journal of Research of the US Geological Survey, v. 4, n. 4, p. 415-420.

Simms, A.R., Rouby, H., Lambeck, K., 2016, marine terraces and rates of vertical tectonic motion: The important of glacio-isostatic adjustment along the Pacific coast of central North America. Geological Society of America Bulletin, v. 128, n. 1-2, p. 81-93.

U.S. Geological Survey and California Geological Survey, 2006, Quaternary fault and fold database for the United States, accessed Dec 1, 2013, from http://earthquakes.usgs.gov/regional/qfaults/

Weber, G.E., 1990, Late Pleistocene slip rates on the San Gregorio fault zone at Point Ano Nuevo, San Mateo County, California, in Garrison, R.E., Greene, H.G., Hicks, K.R., Weber, G.E., and Wright, T.L., eds., Geology and tectonics of the Central California coast region, San Francisco to Monterey: Pacific Section, American Association of Petroleum Geologists Book GB67, p. 193-203.

Weber, G.E., Allwardt, A.O., 2001, The geology from Santa Cruz to Point Ano Nuevo—the San Gregorio fault zone and Pleistocene marine terraces. U.S. Geological Survery Bulletin, v. 2188, p. 1-32.

PART 2—(U-TH)/HE THERMOCHRONOMETRY

ANALYTICAL PROCEDURES

MINERAL SEPARATION, GRAIN MEASUREMENT, AND ALIQUOT PREPARATION

Standard (U-Th)/He analytical procedures involve crushing the rock sample and separating mineral species using a variety of mechanical, magnetic, and heavy liquid techniques. The high-density non-magnetic fraction of minerals <500 μm are then placed beneath a microscope and only clear, euhedral, and inclusion free zircon and apatite grains are picked. Each picked grain is measured and photographed under 100x magnification along its width and length, then flipped on a different edge, measured, and re-photographed. The tip height of zircon grains is also recorded. Each grain is then enclosed within an ~1 mm-long Nb-foil tube. Each sample generally consists of 4–6 of these single-grain aliquots for each analysis type.

DETERMINATION OF ^{4}HE CONTENT

Each foil-wrapped grain is placed on a copper planchet in the helium extraction cell and heated with a diode laser to ~1100–1300° C for 3 minutes (apatite) or 7 minutes (zircon) under ultra-high vacuum. Evolved 4He gas is spiked with a calibrated ^{3}He/^{4}He tracer, cooled to 16° K in a cryogenic trap, and then re-evolved to be analyzed by a noble gas mass spectrometer, constituting an isotope dilution experiment. Re-extraction heating steps are performed on each zircon grain (at least once) until the evolved fraction is <1.5% of the total. Line blanks (background signal of the mass spectrometer), cold blanks (background signal of the cryogenic trap), hot blanks (heating of a crimped Nb foil tube, followed by analysis as if it were an unknown), and ^{3}He/^{4}He standards (analysis of calibrated tracer gas) are performed twice before an analysis session, once after every five unknowns, and twice at the end of the session in order to track instrument drift. Background values from the hot blank analyses are used for baseline subtraction for unknowns. Mineral grain standards for apatite (Durango apatite) and zircon (Fish Canyon Tuff) are analyzed as unknowns to document the external reproducibility of the method because measurement uncertainties are typically much lower than the uncertainties associated with geologic materials.

GRAIN DISSOLUTION

After extraction of ^{4}He, minerals are spiked a with gravimetrically calibrated radiogenic ^{229}Th/^{236}U spike and dissolved, preceding analysis on an ICP-MS to determine bulk U and

Th content. Apatite grains are dissolved in Wheaton vials with concentrated HNO_3 for ~1 hour at ~70° C; only the apatite grain is dissolved during this process. Zircon dissolution requires greater effort because of the resiliency of the mineral to chemical dissolution. However, the dissolution of the Nb foil is undesirable because it becomes a major constituent of the solution and dampens Th sensitivity in the mass spectrometer. To combat this issue, we chemically 'unpacked' each grain using a procedure modified from Seth Burgess at Stanford University. In short, each grain was placed in a teflon cap and the Nb foil tube was dissolved in ~ 10s with a mixture of HF and HNO_3 acid at room temperature. The acid/Nb solution was pipetted into a waste container and the remaining zircon grain was rinsed with MilliQ water 3 times. After rinsing, the grain was transferred to a 2.5 ml teflon cap using the pipette. Concentrated HF was added to the grain before it was placed in a stainless steel Parr pressure digestion vessel with 14 other packed grains, and heated at 210° C for 72 hours. The zircons were dried down, redissolved in concentrated HNO_3, placed back in the pressure digestion vessel, and heated to 180° C for 24 hours. The grains were then dried down again and redissolved once more in a dilute solution of HCl before analysis on the ICP-MS.

DETERMINATION OF ^{238}U AND ^{232}TH CONTENT

An isotope dilution experiment is performed (separately for each mineral type) that utilizes the known contents of the radiogenic tracer to calculate the content of the unknown species. A series of acid blanks (procedural blanks that underwent the same dissolution steps but without any mineral), spike blanks (several procedural blanks with different contents of calibrated radiogenic spike), and spike 'normals' (analysis with calibrated radiogenic spike and a known content of ^{238}U and ^{232}Th—the 'normal' solution) are analyzed before, during, and after a session of unknowns. The acid blank values are used for baseline subtraction and determination of instrument drift (an uncommon occurrence with our instrumentation). The spike blanks are used to construct a session-specific calibration curve between measured isotope count rates on the ICP-MS and tracer content. The spike normals are used to check that the spike calibration curve correctly calculates the (known) content of normal solution.

AGE CALCULATION AND FT CORRECTION

Once contents have been measured for both parent and daughter isotopes, initial ages can be calculated. Because ^{4}He is ejected up to ~20 μm from where it is produced, there is a depleted zone near the grain boundary that must be accounted for (Farley, 2002; Hourigan et al., 2005). Many methods are available to accomplish this task and vary predominantly in their geometric representations of the mineral grain. For the rapidly exhumed samples in this study, the corrected age is relatively insensitive to this choice (e.g. Gautheron and Tassan-Got, 2012). The calculation of ages and uncertainties from raw helium, ICP-MS, and grain measurement data is carried out by the HeDR program written in LabView by J. Hourigan. It uses the production-diffusion equation of Meesters and Dunai (2002) to quickly estimate ages, and the algorithms described in Hourigan et al. (2005) for the determination of Ft correction. Analytical uncertainties are determined formally for each step of the process and are added in quadrature to the estimate of uncertainty; typical aliquot uncertainty is ~1–2% 1σ.

Sample-level ages are calculated once a quality assurance check is performed for all aliquot ages and analytical data to identify spurious results. Sample level ages are the weighted mean of all aliquot ages and are weighted by the inverse square error. In this manner, analyses which have greater uncertainty than others are 'penalized' and contribute less to the final age. The final uncertainty is the weighted standard error and is ~13% 1σ for all of our samples, but varies depending on the dispersion of aliquot ages.

SYSTEMATIC BIAS AND ADJUSTMENT OF APATITE AGES

As a check, several mineral standards of known age are measured as unknowns. In this way, the reproducibility of these standards is a good indicator of the overall reproducibility of the unknowns. Typical reproducibility of Durango apatite is <2–4% at 2σ and 5–10% for Fish Canyon Tuff zircon. Replicate analyses (n=15) of the Durango apatite during the January–February 2016 analysis sessions revealed a slight 5% systematic bias in our methods. The replicate analyses have a weighted mean of 33.02 ±0.39 Ma (2σ) whereas the accepted age for the Durango apatite is 31.44 ±0.18 Ma (2σ) (McDowell et al., 2005). All sample-level apatite analyses from these sessions are thus multiplied by 0.9521 in order to correct for this bias. Additional uncertainty from this correction is 1.312% (2σ) and is added in quadrature to the total external uncertainty for each analysis at the sample level. Replicate Durango apatite during the 2009 and April 2016 session overlapped with the accepted age within uncertainty and no further adjustments were made.

DEVIATIONS AND EXCEPTIONS

The procedures and data reduction methods outlines above were employed for the majority of samples. However, several issues occurred during January–February 2016 as a result of instrumental malfunction and (or) user oversight that required deviation from standard protocol or additional calculations in the data reduction workflow. Each issue and the resulting changes to the data reduction workflow are discussed below. Affected samples in the tabular data are marked with an *.

DISAGGREGATION OF ZIRCONS DURING CHEMICAL UNPACKING

ISSUE

Whole zircons were packed into Nb-foil tubes prior to helium extraction and were then dissolved in concentrated HNO_3 and HF acid. After this chemical unpacking about 10% of zircons were fractured into two or more pieces. Zircons that were composed of 2–3 large fragments were easy to pipette into the microcapsule for dissolution. However, several grains were broken into smaller pieces that were not possible to migrate into the microcapsules, or it was not possible to tell if all of the constituent pieces were migrated. The loss of any amount of zircon at this stage would cause an aberrantly old age because the helium from the missing piece was measured, but the fragment responsible for that helium would remain unanalyzed.

SOLUTION

Aliquots that had multiple fragments were noted and several of these had geologically impossible ages (pre Cretaceous); these aliquots were excluded from further analysis. Most multiple-fragment aliquots had ages similar to other aliquots from the same sample and were included in sample-level averages.

OVERHEATING OF APATITE DURING DISSOLUTION IN FEBRUARY, 2016

ISSUE

Apatite grains and their Nb-foil packets are placed into a polypropylene Wheaton vial with concentrated HNO_3 and set on a hotplate for ~1 hour in order to dissolve the apatite. The hot-plate is usually set at ~60–70% heat through the use of a variac power supply. Both sessions of apatites were dissolved on a hotplate without a variable power supply and thus were heated to a much higher temperature than is typical. Above ~70° C, polypropylene becomes unstable in concentrated HNO_3 but the typical duration in this unstable region is short. However, the duration within this unstable zone was greatly increased for two main reasons: (1) the higher temperature imposed by the unregulated hotplate, and (2) the decision to let the apatites dissolve for nearly 2 hours to ensure complete dissolution in the very tightly crimped packets. The result was that nearly all of the Wheaton vials in the February analysis session underwent significant acid attack and contained small blebs and nodules of plastic floating in solution. This occurred in a few of the January analysis session vials, but its cause was not considered until much later.

The most significant concern imposed by the floating plastic debris was accidental aspiration and clogging during analysis on the ICP-MS. Although several ideas were brought forth to combat the issue, the simplest-sounding idea was to use small wads of borosilicate glass wool to push the plastic to the bottom of the vial, thus keeping the upper part free of large particles. This plan was implemented and was largely successful at moving the plastic particles downward. Borosilicate glass, however, apparently contains trace amounts of ^{238}U and ^{232}Th, a fact that was unknown before using it as a filter medium. The result was that every blank, standard, spike, norm, and unknown was accidentally doped with an unknown quantity of ^{238}U and ^{232}Th. This issue was discovered after analysis of the first blank on the ICP-MS; completion of the ICP-MS analysis was suspended until a remedy was found.

A calibration experiment was performed and found an approximately linear correlation between measured amounts of ^{29}Si (an isotope of the glass wool matrix) and the amount of ^{238}U and ^{232}Th; there was no additional ^{229}Th or ^{236}U as a result of the glass wool. This relationship permitted quantification of the 'additional' ^{238}U and ^{232}Th in each sample that was accidentally added during the filtration step. We proceeded with the ICP-MS analysis but modified the instrumental parameters to also collect ^{11}B and ^{29}Si. Additionally, we analyzed a new set of acid blanks and a series of 12 calibration samples that had varying amounts of glass wool added to them. These calibration samples permitted quantification of ^{238}U and ^{232}Th during the analysis session and covered nearly the entire range of ^{29}Si values measured for the doped samples.

SOLUTION

Excess ^{238}U and ^{232}Th was calculated and removed through a 6 step process: (1) calculation of means for each isotope for each sample; (2) correction for session instrument drift; (3)

baseline subtraction; (4) linear regression of ^{238}U and ^{232}Th against ^{29}Si for all samples that did not originally contain ^{238}U or ^{232}Th (acid blanks, spike blanks, and the 12 calibration samples); (5) calculation and subtraction of excess ^{238}U and ^{232}Th as a function of the measured ^{29}Si for each sample, and; (6) uncertainty propagation. Each step is detailed below. Apatite aliquots that underwent this additional process are marked with a single * and their ε-value (see below) is provided.

Another complicating factor was that small particles or strands of the glass wool were apparently aspirated during analysis. Surface tension of sample solution on this detritus prolonged the time needed for sample washout and uptake. Because of this, the first few analysis runs of many samples still contained washout solution. To combat this, we lengthened the washout time (from 20 s to 60 s), but the problem persisted. In order to effectively remove these aberrant data, we removed the first 4 runs (of 15 total) for all samples.

Table A-5. Definitions of variable notation.

Variable notation	Definition	Variable notation	Definition
$i \rightarrow p$	ICP-MS run cycle over which data is collected	m	Slope of weighted least squares linear regression
$j \rightarrow k$	Range of isotopes over which data is collected	b	Intercept of weighted least squares linear regression
$k \rightarrow r$	Samples of the analytical session	dm	68.3% confidence interval of the slope
X_{jki}	ICP-MS counts measured	db	68.3% confidence interval of the intercept
σC_{jk}	Standard deviation of mean counts	E_{jk}^{C}	Uncertainty of the average for each isotope and sample
$\hat{B}_j$	Baseline-corrected counts	E_j^f	Uncertainty of the instrumental-drift correction factor
C_{jk}	Average counts	E_{jk}^{D}	Uncertainty of the drift-corrected value
D_{jk}	Instrumental-drift-corrected mean counts	E_j^B	Uncertainty of the baseline correction
D_{jk}^{bc}	Baseline- and drift-corrected mean counts	E_{jk}^{Dbc}	Uncertainty of the drift- and baseline corrected value
D_{jk}^{Si}	Baseline-, drift-, and excess U- and Th-corrected mean counts	E_{jk}^{Si}	Uncertainty on the amount of 'excess' ^{238}U and ^{232}Th
f_j^t	Instrumental-drift correction factor	E_{jk}^{Dbcsi}	Total internal uncertainty
f_j^{Si}	^{29}Si-based correction factor for excess ^{238}U and ^{232}Th	ε_k	Ratio of 'excess' ^{238}U and ^{232}Th to measured values, weighted for ^{4}He production

Mean values for each isotope

A simple mean for each isotope was calculated using the last 11 analysis runs, where C_{jk} is the mean count for each isotope $j \rightarrow q$ for each sample $k \rightarrow r$ evaluated over analysis runs $i \rightarrow p$.

$$_{jk} \quad \sum \quad \frac{_{jki}}{} \Big|_{j=1}^{q} \Big|_{k=1}^{r}$$

The standard error of the mean, E_{jk}, was calculated and forms the basis for the propagation of uncertainty:

$$E_{jk}^{C} = \frac{\sigma C_{jk}}{\sqrt{p-5}} \Big|_{j=1}^{q} \Big|_{k=1}^{r}$$

Instrument drift

Instrumental drift over the course of a long analysis session (~13 hours) is common during ICP-MS analyses. For our purposes this drift is generally neglected because we calculate ratios of isotopes that are similar in their mass/charge and are affected by instrumental drift in nearly the same way. Because the workflow for removing excess ^{238}U and ^{232}Th requires taking ratios to an isotope with drastically different properties (^{29}Si), instrumental drift cannot be neglected. For this analysis session the sensitivity of ^{29}Si changed by ~20% over the course of the session in the opposite sense as a similar magnitude change in ^{238}U and ^{232}Th. Unaccounted for, these changes would cause ratios to vary significantly for replicate analyses.

To correct for this drift, two acid blanks and a ‘tune’ solution composed of a mixture of leftover apatite samples and standards were analyzed at the start, in the middle, and at the end of the session. Instrumental drift for ^{29}Si was calculated using all of these analyses. Drift in uranium and thorium isotopes was calculated from the tune solution only because count rates were too low in the acid blanks to be useful. Initial exploration of the data suggested that the long term drift for ^{229}Th, ^{232}Th, ^{235}U, ^{236}U, and ^{238}U were identical within uncertainty. Thus, the relative changes through time for each of the isotopes was combined into a single least-squares weighted linear regression model with 15 data points that best fits the equation:

$$C_j = m_j^t \times t + b_j^t \Big|_{j=Si}^{UTh}$$

Where m^t and b^t are the linear fit parameters as a function of time during the analysis session and the equation is evaluated over isotopes j=^{29}Si and j=^{229}Th+^{232}Th+^{235}U+^{236}U+^{238}U but only for replicate acid blanks and 'tune' analyses, as discussed above. The regression model for ^{29}Si contains 9 data points. The intercept of the regression at the start of the analysis session and the slope was used to form a 'correction factor' for each time point in the regression that follows the form:

$$f_j^t = \frac{m_j^t}{b_j^t}\Big|_{j=Si}^{UTh}$$

The result is a linear correction factor as a function of time throughout the analysis session. Uncertainty is calculated as the squared summation of the 68.3% confidence interval on the slope and intercept values by:

$$E_j^f = \sqrt{dm_j^2 + db_j^2}\Big|_{j=Si}^{UTh}$$

Each sample was then divided by the correction factor to remove the component of instrumental drift at the time of the analysis through:

$$D_{jk} = \frac{C_{jk}}{(f_j^t \times t)+1}\Big|_{j=Si}^{q}\Big|_{k=1}^{r}$$

Where D_{jk} is the de-trended mean for each isotope (excluding ^{43}Ca, ^{51}V, and ^{147}Sm) and is evaluated for all samples. Uncertainty is propagated by combining the uncertainties from the mean counts and the correction factor with:

$$E_{jk}^D = \sqrt{(E_{jk}^C)^2 + (E_j^f)^2}\Big|_{j=Si}^{q}\Big|_{k=1}^{r}$$

Baseline subtraction

Once all samples were corrected for long-term drift instrument drift, baseline values using replicate analyses of un-doped acid blanks (ab) were calculated for each isotope:

$$\hat{B}_j = \frac{\sum_k^{ab} D_j}{ab}\Big|_{j=1}^{q}$$

Uncertainty was calculated using the standard error of the mean:

$$E_j^B = \frac{\sigma \hat{B}_j}{\sqrt{ab-1}}\Big|_{j=1}^{q}$$

This baseline value was then subtracted from all samples to produce the baseline- and drift-corrected values for each isotope and sample. For those samples that did not undergo a drift correction this step produces the simple baseline-corrected value.

$$D_{jk}^{bc} = D_{jk} - \hat{B}_j \Big|_{j=1}^{q} \Big|_{k=1}^{r}$$

Uncertainty was propagated by combining the absolute uncertainties for the de-trended mean and the baseline correction with:

$$E_{jk}^{Dbc} = \frac{\sqrt{(D_{jk} \times E_{jk}^{D})^2 + (\hat{B}_j \times E_j^{B})^2}}{D_{jk}^{bc}} \Bigg|_{j=1}^{q} \Bigg|_{k=1}^{r}$$

Ratios of ^{238}U and ^{232}Th to ^{29}Si

A simple weighted mean ratio model was developed for ^{238}U and ^{232}Th that used every analysis which did not contain ^{238}U or ^{232}Th before the addition of the borosilicate glass wool (doped acid blanks, doped spike blanks, and the 12 calibration samples; k=$noUTh$) with:

$$f_j^{Si} = \frac{\sum_{k=1}^{r} \left(\frac{D_j^{bc}}{D_{Si}^{bc}} \times w_{jk} \right)}{\sum_{k=1}^{r} w_{jk}} \Bigg|_{j=232Th}^{238U} \Bigg|_{k=1}^{noUTh}$$

The range of ^{29}Si values used in the regression was similar to the range of values for the remaining samples. This overlap ensures that regression values do not need to be extrapolated beyond the limit of the data. Uncertainty df_j^{si} was calculated as the weighted uncertainty of the mean for each of the two correction isotopes.

Calculation and subtraction of excess ^{238}U and ^{232}Th

The regression model was used to calculate an amount of ^{238}U and ^{232}Th for each sample based on the measured amount of ^{29}Si. These ‘excess’ amounts were then subtracted from the measured values for all samples with:

$$D_{jk}^{Si} = D_{jk}^{bc} - (f_j^{Si} \times D_{Sik}^{bc}) \Big|_{j=232Th}^{238U} \Big|_{k=1}^{r}$$

Uncertainty on the amount of 'excess' ^{238}U and ^{232}Th was propagated with:

$$E_{jk}^{Si} = \sqrt{\left(df_{jk}^{Si}\right)^2 + \left(E_{Sik}^{Dbc}\right)^2}\Bigg|_{j=232Th}^{238U}\Bigg|_{k=1}^{r}$$

Final uncertainty for the drift-, baseline-, and excess ^{238}U- and ^{232}Th-correction is given by:

$$E_{jk}^{Dbcsi} = \frac{\sqrt{\left(D_{jk}^{bc} \times E_{jk}^{Dbc}\right)^2 + \left(D_{jk}^{Si} \times E_{jk}^{Si}\right)^2}}{D_{jk}^{Si}}\Bigg|_{j=232Th}^{238U}\Bigg|_{k=1}^{r}$$

A 'noise to signal' calculation is made to provide a means of screening ages that have corrections similar to or greater in magnitude as the corrected values. Values of ^{232}Th are multiplied by 0.235 in order to account for differences in ^{4}He productivity.

$$\varepsilon_k = \frac{\left(f_{238Uk}^{Si} + 0.235 \times f_{232Thk}^{Si}\right) \times D_{Sik}^{bc}}{D_{238Uk}^{Si} + 0.235 \times D_{232Thk}^{Si}}$$

After all corrections were performed, the data were returned to the 'typical' data reduction routine for completion of the remaining steps.

Validation of the solution

Each step in the process described above adds substantial uncertainty to the 'corrected' analyses. Replicate analyses of Durango apatite that underwent the correction process (33.24 ±3.9 Ma, MSWD=0.02) are nearly indistinguishable from replicate Durango apatite that did not (32.98 ±0.47 Ma, MSWD=3.9) providing confidence that the corrections produce accurate and precise ages. These analyses have an average ε value of 9.75% indicating relatively low ratios of noise (doped uranium and thorium) to signal (original uranium and thorium) when corrected for ^{4}He productivity. The average ε value for all other analyses is ~29% and we use the value of 50% as a cutoff for rejecting ages. Aliquots with >50% ε (n=6) have corrections that are more than half of the original value and are often tens of millions of years outside the range of remaining sample ages. These aliquots are not used in sample averages.

REFERENCES USED IN PART 2

Farley, K.A. 2000, Helium diffusion from apatite: General behavior as illustrated by Durango Fluorapatite. Journal of Geophysical Research, v. 105, p. 2903-2914.

Farley, K.A., 2002, (U-Th)/He dating: techniques, calibrations, and applications. Reviews in Mineralogy and Geochemistry, v. 47, p. 819-844.

Gautheron, C., Tassan-Got, L., 2010, A Monte Carlo approach to diffusion applied to noble gas/helium thermochronology. Chemical Geology, v. 273, n. 3-4, p. 212-224.

Hourigan, J.K, Reiners, PW., Brandon, M.T., 2005, U-Th zonation-dependent alpha-ejection in (U-Th)/He chronometry. Geochimica et Cosmochim Acta, v. 69, p. 3349-3365.

McDowell, F.W., McIntosh, W.C., and Farley, K.A., 2005, A precise Ar-40–Ar-39 reference age for the Durango apatite (U–Th)/He and fission-track dating standard. Chemical Geology v. 214, p. 249-263.

Meesters, A.G.C.A., Dunai, T.J., 2002, Solving the production-diffusion equation for finite diffusion domains of various shapes Part 1. Implications for low-temperature (U-Th)/He thermochronology. Chemical Geology, v. 186, p. 333-344.

Reiners, P.W., Spell, T.L., Nicolescu, S., Zanetti, K.A., 2004, Zircon (U-Th)/He thermochronometry: He diffusion and comparisons with 40Ar/39Ar dating. Geochimica Cosmochimica Acta, v. 68, p. 1857-1887.

Stüwe, K., White, L., Brown, R., 1994, The influence of eroding topography on steady-state isotherms. Application to fission-track analysis. Earth and Planetary Science Letters, v. 124, p. 63-74.

APPENDIX B. ANALYTICAL DATA FOR NEW (U-TH)/HE ANALYSES

Table B-1. Analytical data for new apatite (U-Th)/He thermochronometry. All data processed at the University of California Helium Thermochronology Laboratory; see Table 3-2 for sources of data. Light gray shading indicates aliquots likely affected by wildfire; italicized age is the average of remaining aliquots. Strike-through indicates aliquots not included in the final age. (*) Indicates additional lab procedures, as desribed for apatite in Appendix A. Mean ages weighted by the inverse square error.

Sample	Aliquot	Width 1 (μm)	Width 2 (μm)	Length (μm)	Sphere ER (μm)	Est. T_c (° C)	Mass (μg)	Ft	U (ppm)	Th (ppm)	^{4}He (mol x 10^{-14})	Ind. cooling age ±1σ (Ma)	ε (noise to signal ratio)*	Weighted mean sample age ±1σ (Ma)
09DO07	a	71.1	82.4	128.4	39.6	58.8	11.70	0.670	1.6	3.0	0.07	6.6 ±0.3	– – –	6.1 ±1.8
	b	94.8	101.2	243.3	54.2	64.8	36.20	0.752	10.6	25.0	1.34	5.5 ±0.1	– – –	
	c	104.5	113.2	243.0	59.2	60.3	44.60	0.773	5.1	8.7	1.56	11.7 ±0.3	– – –	
	d	98.7	110.5	226.8	56.6	69.3	38.50	0.761	9.4	23.2	0.77	3.3 ±0.1	– – –	
	e	100.0	120.8	290.5	61.6	67.8	54.90	0.780	3.6	9.2	0.62	4.6 ±0.1	– – –	
09DO08	a	105.3	102.0	236.1	56.6	60.3	39.30	0.764	6.9	11.5	1.61	10.3 ±0.2	– – –	10.2
	b	84.5	83.8	117.5	41.7	55.8	12.90	0.684	3.5	6.2	0.25	10.3 ±0.2	– – –	
	c	149.0	145.8	223.6	74.5	64.8	75.40	0.816	4.2	7.2	2.05	10.2 ±0.1	– – –	
AS004	a	185.3	192.4	308.6	97.0	66.3	22.80	0.845	9.4	3.1	1.54	14.5 ±0.6	– – –	25.3 ±3.2
	b	231.4	237.1	400.4	121.4	65.3	45.50	0.876	8.3	0.7	4.53	24.5 ±1.0	– – –	*27.6*
	c	168.8	172.7	297.6	88.8	59.8	18.00	0.833	9.4	2.0	2.27	28.2 ±0.9	– – –	
	d	160.5	162.2	214.5	79.1	56.3	11.60	0.813	8.8	2.5	1.68	34.9 ±1.7	– – –	
	e	255.5	263.4	313.0	124.0	64.8	43.69	0.878	10.9	4.5	6.98	28.1 ±10.6	0.23	
	f	195.3	204.3	261.5	97.5	62.8	21.65	0.845	5.9	3.4	1.47	22.1 ±9.5	0.45	
	g	133.1	163.3	263.5	77.4	64.8	11.98	0.808	31.5	14.2	2.07	11.3 ±4.4	0.29	
AS005	a	134.8	162.4	315.9	80.2	68.3	14.50	0.810	39.9	63.4	2.66	7.6 ±0.2	– – –	6.6 ±1.0
	b	126.8	137.6	208.5	67.4	68.8	7.55	0.775	55.0	109.9	1.23	4.8 ±0.1	– – –	
	c	201.2	219.0	262.0	101.3	69.3	23.96	0.848	15.4	21.8	2.43	10.7 ±3.5	0.19	
	d	203.6	213.2	251.5	99.6	75.3	22.63	0.844	24.7	49.0	1.75	4.6 ±1.4	0.10	
	e	164.7	194.3	223.5	86.5	69.3	14.91	0.822	24.6	44.7	1.80	7.7 ±2.4	0.20	
AS006	a	96.1	107.9	169.1	52.5	51.3	3.64	0.727	70.1	3.1	3.45	33.8 ±1.5	– – –	15.2 ±5.4
	b	111.9	134.1	187.5	62.2	62.3	5.88	0.767	96.6	4.6	2.36	9.9 ±0.3	– – –	*26.9*
	c	102.5	109.3	186.2	55.2	62.3	4.33	0.739	62.6	2.5	0.86	7.8 ±0.3	– – –	
	d	120.7	153.0	202.5	68.8	56.3	7.84	0.788	39.0	0.6	3.62	27.5 ±11.9	0.34	
	e	94.9	141.7	215.0	62.1	55.8	6.24	0.766	66.1	2.2	4.07	23.5 ±9.7	0.25	
	f	116.2	125.9	176.5	60.6	55.8	5.37	0.761	33.9	0.9	1.74	22.9 ±10.4	0.41	
	g	161.3	163.7	187.5	76.7	63.8	10.27	0.808	69.1	4.3	3.83	12.1 ±4.8	0.11	
AS007	a	125.6	125.7	258.4	67.4	65.3	8.45	0.784	29.4	0.8	0.81	7.6 ±0.3	– – –	8.9 ±1.1
	b	87.8	88.0	126.7	43.9	53.3	2.03	0.678	11.1	1.2	0.14	16.2 ±1.9	– – –	
	c	119.7	127.6	159.0	60.1	62.3	5.04	0.759	23.7	1.2	0.45	9.0 ±0.3	– – –	
	d	150.3	152.7	284.0	79.9	67.3	13.51	0.816	15.4	1.0	0.77	8.2 ±3.6	0.35	
	e	151.6	151.6	231.0	76.7	66.8	11.02	0.801	40.0	72.9	2.23	8.2 ±2.5	0.17	
	f	134.8	143.7	207.0	70.0	66.8	8.32	0.784	15.2	25.8	0.52	6.9 ±2.6	0.42	
	g	~~166.1~~	~~174.0~~	~~246.5~~	~~85.0~~	~~59.3~~	~~14.75~~	~~0.825~~	~~4.2~~	~~0.9~~	~~0.79~~	~~27.2 ±20.4~~	~~0.74~~	

Sample	Aliquot	Width 1 (µm)	Width 2 (µm)	Length (µm)	Sphere ER (µm)	Est. T_c (° C)	Mass (µg)	Ft	U (ppm)	Th (ppm)	^{4}He (mol x 10^{-14})	Ind. cooling age ±1σ (Ma)	ε (noise to signal ratio)*	Weighted mean sample age ±1σ (Ma)
AS008	a	146.4	155.6	259.1	78.3	64.3	12.20	0.812	92.9	11.8	6.28	12.2 ±0.3	– – –	15.3 ±2.3
	b	130.9	160.5	325.5	79.3	60.3	14.30	0.814	86.6	6.6	11.60	20.7 ±0.6	– – –	*20.8*
	c	86.1	88.8	157.3	45.8	59.3	2.49	0.691	91.8	2.6	0.67	7.7 ±0.3	– – –	
	d	105.1	107.5	227.9	57.4	55.3	5.33	0.749	86.8	3.6	3.99	21.0 ±0.8	– – –	
	e	133.1	146.5	239.0	72.5	66.8	9.69	0.798	100.8	8.2	3.10	7.2 ±2.8	0.10	
	f	139.3	139.3	242.0	72.4	58.3	9.73	0.798	116.9	10.1	11.10	22.1 ±8.5	0.09	
	g	123.4	178.1	333.5	81.9	62.8	15.71	0.820	54.3	1.9	6.23	16.2 ±6.4	0.10	
	h	165.4	205.6	287.5	94.2	63.3	20.50	0.842	109.4	3.5	20.10	19.4 ±7.4	0.05	
AS010	a	166.9	166.9	376.6	91.0	59.3	21.70	0.836	39.4	9.2	12.70	30.8 ±1.2	– – –	30.2 ±0.7
	b	107.4	146.6	300.2	69.7	55.8	10.00	0.790	28.6	4.9	3.73	29.1 ±1.1	– – –	*31.4*
	c	110.9	118.0	215.9	60.5	53.3	5.86	0.760	20.2	1.2	1.56	31.5 ±1.5	– – –	
	d	163.7	215.6	326.5	98.4	61.8	24.36	0.849	19.6	0.6	5.81	26.2 ±10.9	0.29	
	e	161.3	174.7	358.5	90.7	57.3	20.95	0.836	22.2	4.3	8.87	40.0 ±15.7	0.21	
	f	144.8	200.5	354.0	92.6	65.3	21.85	0.840	17.5	0.7	2.54	14.4 ±6.1	0.32	
	g	134.1	172.3	237.0	77.7	57.3	11.50	0.805	22.8	29.5	4.60	30.7 ±10.8	0.31	
AS011	a	149.5	182.6	271.2	85.2	60.3	15.50	0.827	29.7	0.7	4.94	23.7 ±1.0	– – –	25.6 ±6.4
	b	116.9	142.4	200.1	65.8	59.8	6.97	0.779	11.7	0.3	0.54	15.5 ±0.9	– – –	
	c	122.3	127.3	209.7	64.4	52.3	6.77	0.774	14.7	0.5	1.87	44.1 ±2.9	– – –	
	d	125.9	178.5	223.0	76.3	61.8	10.70	0.807	11.2	2.3	0.85	15.4 ±7.1	0.46	
	e	164.7	172.3	276.0	86.6	63.3	16.23	0.830	12.6	-0.9	1.54	17.0 ±7.4	0.29	
	~~f~~	~~99.7~~	~~121.4~~	~~232.0~~	~~59.5~~	~~61.3~~	~~5.87~~	~~0.747~~	~~6.4~~	~~13.5~~	~~0.24~~	~~10.6 ±6.0~~	~~0.69~~	
AS012	a	87.4	92.9	173.3	47.8	52.3	2.92	0.702	22.8	2.7	0.61	23.2 ±1.5	– – –	14.8 ±5.7
	b	91.0	96.4	143.2	47.4	58.8	2.61	0.701	54.7	1.2	0.49	9.0 ±0.5	– – –	*25.0*
	c	67.7	69.4	111.7	35.2	48.3	1.09	0.608	10.3	1.7	0.10	26.8 ±5.3	– – –	
	d	108.0	119.3	195.5	59.0	57.3	5.22	0.755	99.6	4.8	3.78	17.5 ±7.0	0.14	
	~~e~~	~~95.9~~	~~101.4~~	~~155.0~~	~~50.2~~	~~46.3~~	~~3.12~~	~~0.709~~	~~-4.7~~	~~-5.3~~	~~0.01~~	~~-1.9 ±-2.7~~	~~1.13~~	
	~~f~~	~~94.6~~	~~103.2~~	~~194.0~~	~~52.6~~	~~50.3~~	~~3.92~~	~~0.733~~	~~6.8~~	~~-3.6~~	~~0.36~~	~~39.2 ±41.1~~	~~0.81~~	
AS016	a	137.6	117.0	176.8	63.0	68.8	59.30	0.766	172.0	112.0	2.18	4.5 ±0.2	– – –	5.5 ±0.3
	b	108.7	101.6	158.9	53.1	63.8	36.40	0.727	495.5	230.1	4.59	5.8 ±0.3	– – –	
	c	174.7	147.0	215.6	79.0	70.3	116.00	0.810	167.4	116.6	5.51	5.6 ±0.2	– – –	
	d	182.7	171.3	253.8	88.3	71.8	165.00	0.829	179.1	154.0	9.20	5.8 ±0.2	– – –	
AS020	a	112.7	116.3	191.4	59.1	67.8	5.20	0.740	96.8	392.9	1.71	4.3 ±0.1	– – –	3.7 ±0.4
	b	119.0	135.8	192.3	64.3	72.8	6.47	0.765	38.5	78.7	0.42	2.8 ±0.1	– – –	
	c	157.1	158.9	185.0	74.9	72.8	4.12	0.721	40.9	131.1	0.43	3.7 ±0.2	– – –	
	d	102.4	106.6	182.5	54.4	70.3	3.19	0.704	6.6	16.1	0.03	2.7 ±0.3	– – –	
	e	92.7	105.2	157.0	50.5	65.8	9.57	0.793	20.6	62.5	0.58	4.0 ±1.2	0.30	
AS022	a	116.0	129.7	183.3	61.8	70.8	5.73	0.755	33.7	80.4	0.39	3.1 ±0.1	– – –	4.0 ±0.3
	b	103.6	120.8	210.5	59.2	67.8	5.49	0.744	33.8	90.7	0.54	4.4 ±0.1	– – –	
	c	163.7	170.2	227.5	82.3	72.8	2.87	0.694	29.4	63.3	0.21	4.4 ±0.2	– – –	
	d	167.8	178.8	253.5	86.9	74.3	1.73	0.649	59.5	62.8	0.18	4.0 ±0.3	– – –	
	e	89.2	98.3	157.4	48.4	66.3	13.14	0.811	28.2	91.7	1.01	3.5 ±1.0	0.17	
	f	74.5	82.3	135.9	40.7	63.3	15.76	0.820	20.5	65.7	0.94	3.7 ±1.1	0.15	

Sample	Aliquot	Width 1 (µm)	Width 2 (µm)	Length (µm)	Sphere ER (µm)	Est. T_c (° C)	Mass (µg)	Ft	U (ppm)	Th (ppm)	^4He (mol x 10^{-14})	Ind. cooling age ±1σ (Ma)	ε (noise to signal ratio)*	Weighted mean sample age ±1σ (Ma)
AS023	a	152.3	171.6	222.5	80.0	74.3	12.09	0.806	17.3	53.3	0.55	3.5 ±1.1	0.33	3.7 ±0.4
	b	123.8	144.4	211.3	68.3	72.3	17.55	0.825	15.6	44.4	0.66	3.2 ±1.0	0.19	
	c	173.3	174.3	280.4	89.0	73.8	6.40	0.760	11.7	35.5	0.24	4.4 ±1.5	0.41	
	~~d~~	~~123.8~~	~~126.5~~	~~197.5~~	~~63.8~~	~~66.8~~	~~7.87~~	~~0.774~~	~~7.7~~	~~27.1~~	~~0.27~~	~~5.8 ±2.2~~	~~0.51~~	
AS024	a	150.5	173.7	337.8	87.2	74.3	18.40	0.818	38.1	186.8	2.71	4.0 ±0.1	– – –	4.1 ±0.2
	b	105.5	108.0	174.3	54.8	65.8	4.12	0.720	29.4	133.3	0.46	4.7 ±0.2	– – –	
	c	130.3	138.9	213.9	68.7	70.8	3.61	0.709	47.7	218.3	0.53	3.9 ±0.1	– – –	
	d	158.5	159.9	271.2	82.4	73.8	8.03	0.772	33.0	181.9	0.98	3.8 ±1.1	0.16	
	e	100.9	102.3	169.0	52.4	69.3	14.24	0.808	18.4	102.1	0.75	2.8 ±0.8	0.19	
AS025	a	92.0	88.2	164.5	47.3	65.3	2.76	0.695	75.0	54.8	0.36	3.9 ±0.2	– – –	3.9 ±0.9
	b	138.2	52.0	270.4	53.6	71.8	11.80	0.808	57.3	0.0	0.63	2.1 ±0.9	0.19	
	c	135.8	162.6	298.1	79.6	78.3	13.70	0.852	19.7	1.6	0.26	2.1 ±1.0	0.29	
AS027	a	76.4	100.5	125.7	44.0	60.8	2.04	0.672	57.3	61.9	0.32	6.0 ±0.4	– – –	6.8 ±1.3
	b	96.7	110.9	213.6	55.7	61.3	4.77	0.734	10.9	15.1	0.24	8.8 ±0.4	– – –	
	c	71.2	79.2	115.8	38.1	60.3	1.36	0.623	10.6	18.5	0.03	4.7 ±0.4	– – –	
	d	70.6	74.2	108.6	36.5	60.8	1.18	0.609	10.0	16.6	0.02	4.2 ±0.5	– – –	
AS029	a	66.7	79.9	168.9	40.1	59.8	1.88	0.636	16.1	39.6	0.09	5.6 ±0.6	– – –	5.6 ±0.6
AS030	a	175.5	194.4	302.9	95.0	74.3	21.50	0.838	15.7	26.7	1.04	4.8 ±0.1	– – –	5.0 ±0.2
	b	106.0	142.8	184.4	62.5	66.8	5.92	0.760	52.5	84.2	0.95	5.4 ±0.2	– – –	
	c	135.1	142.0	243.6	72.2	69.8	9.69	0.791	28.2	37.1	0.76	4.9 ±0.2	– – –	
AS031	a	85.0	91.1	161.0	46.2	63.8	2.58	0.687	26.0	25.3	0.14	4.6 ±0.8	– – –	3.9 ±0.5
	b	93.0	114.0	192.6	54.5	67.3	6.12	0.767	28.3	20.9	0.32	3.8 ±0.2	– – –	
	~~e~~	~~140.6~~	~~145.8~~	~~217.0~~	~~72.3~~	~~85.8~~	~~9.22~~	~~0.796~~	~~31.6~~	~~11.3~~	~~0.08~~	~~0.6 ±0.8~~	~~0.23~~	
AS032	a	173.8	216.1	297.2	98.6	76.3	23.40	0.846	51.2	40.1	2.69	4.1 ±0.1	– – –	4.5 ±0.4
	b	74.4	87.3	154.4	42.8	61.3	2.09	0.669	109.9	40.2	0.47	5.2 ±0.2	– – –	
	c	106.4	111.9	203.7	57.5	67.3	5.03	0.745	35.8	24.3	0.38	4.5 ±0.2	– – –	
AS033	a	102.9	98.8	174.5	52.4	66.8	3.68	0.715	35.2	80.5	0.30	3.8 ±0.1	– – –	4.2 ±0.9
	b	107.0	95.9	146.0	50.6	70.8	3.11	0.711	25.5	30.0	0.09	2.2 ±0.4	– – –	
	c	91.2	82.7	171.7	46.3	61.8	2.69	0.680	17.6	46.6	0.17	5.9 ±0.3	– – –	
	d	85.6	79.5	123.9	41.6	66.8	1.75	0.659	32.6	16.1	0.05	2.4 ±0.7	– – –	
	~~e~~	~~146.1~~	~~157.1~~	~~238.0~~	~~77.2~~	~~74.3~~	~~11.33~~	~~0.804~~	~~10.1~~	~~14.1~~	~~0.22~~	~~3.2 ±1.4~~	~~0.53~~	
AS040	a	128.8	142.1	178.2	66.2	58.8	6.77	0.775	93.9	86.0	5.75	17.7 ±0.4	– – –	18.2 ±3.0
	b	125.2	128.9	158.7	61.3	54.8	5.31	0.759	64.0	47.7	4.27	25.9 ±0.6	– – –	
	c	122.8	137.5	216.8	67.1	61.8	2.66	0.682	116.8	104.8	1.76	12.6 ±0.3	– – –	
	d	136.2	147.5	209.6	71.3	62.3	7.61	0.778	69.7	63.3	3.57	13.1 ±4.5	0.16	
	e	152.0	186.0	236.6	83.8	53.3	8.74	0.788	38.2	54.6	11.60	60.7 ±19.6	0.16	
	f	83.7	84.1	182.2	45.4	53.8	14.00	0.820	60.2	51.6	7.64	16.9 ±5.7	0.09	

Sample	Aliquot	Width 1 (µm)	Width 2 (µm)	Length (µm)	Sphere ER (µm)	Est. T_c (° C)	Mass (µg)	Ft	U (ppm)	Th (ppm)	^{4}He (mol x 10^{-14})	Ind. cooling age ±1σ (Ma)	ε (noise to signal ratio)*	Weighted mean sample age ±1σ (Ma)
AS041	a	117.3	119.6	217.7	62.3	54.8	6.32	0.759	78.5	115.7	7.38	26.7 ±0.5	– – –	20.1 ±3.4
	b	96.1	102.0	186.4	52.3	57.3	3.79	0.717	77.6	116.4	2.06	13.3 ±0.2	– – –	
	c	119.3	127.6	257.2	66.4	56.3	3.42	0.720	47.6	52.8	1.95	24.3 ±0.5	– – –	
	d	83.9	91.8	174.7	46.9	50.3	8.12	0.773	46.5	69.8	6.98	32.4 ±10.4	0.16	
	e	86.7	97.3	168.9	48.3	53.3	2.79	0.686	68.4	125.0	2.21	21.7 ±7.2	0.30	
	f	105.8	106.0	147.0	52.4	55.3	2.96	0.696	49.8	78.0	1.33	17.4 ±6.3	0.38	
AS042	a	81.6	96.0	161.2	46.6	52.3	2.63	0.689	63.8	56.3	1.75	23.1 ±0.4	– – –	27.2 ±3.1
	b	83.5	91.8	161.3	46.1	49.3	2.57	0.686	89.5	79.0	3.67	35.4 ±0.7	– – –	
	c	88.0	89.4	206.7	48.6	53.3	2.77	0.704	113.5	146.4	3.42	21.8 ±0.5	– – –	
	d	101.6	106.5	123.7	49.5	51.3	3.14	0.710	100.9	128.0	4.38	27.6 ±0.6	– – –	
	e	95.8	105.0	150.2	50.6	52.3	3.37	0.696	77.2	150.1	3.96	27.6 ±8.6	0.18	
AS043	a	123.9	125.2	175.3	61.9	57.3	5.64	0.761	29.9	24.8	1.61	19.3 ±0.4	– – –	17.7 ±0.8
	b	123.8	102.6	164.7	56.7	56.8	4.37	0.741	45.3	37.9	1.60	16.7 ±0.4	– – –	
	c	106.3	107.4	162.9	54.0	56.3	3.85	0.729	41.2	33.8	1.27	17.0 ±0.4	– – –	
	d	150.6	167.5	213.4	78.1	62.8	11.18	0.808	35.0	30.5	3.01	14.6 ±5.1	0.22	
AS044	a	119.4	112.8	161.4	57.5	58.8	4.51	0.746	65.4	38.9	1.77	13.0 ±0.2	– – –	13.5 ±0.4
	b	109.6	95.8	172.4	53.0	56.8	3.77	0.726	76.8	45.9	1.90	14.6 ±0.4	– – –	
	c	110.8	103.9	142.6	52.6	57.3	3.40	0.722	52.6	42.1	1.12	13.4 ±0.3	– – –	
	d	120.0	133.1	204.8	64.8	58.3	6.79	0.772	72.4	46.1	4.42	18.6 ±6.7	0.21	
	e	167.5	169.9	228.5	83.0	62.8	13.47	0.819	70.3	48.0	7.81	16.0 ±5.5	0.07	
AS045	a	184.8	182.4	346.6	97.0	65.8	24.20	0.842	78.4	93.2	16.70	15.0 ±0.3	– – –	13.1 ±1.0
	b	90.5	96.1	131.1	46.3	56.8	2.36	0.686	77.2	99.0	1.02	11.6 ±0.3	– – –	
	c	89.5	88.1	136.7	45.0	56.3	2.23	0.679	69.6	67.5	0.82	11.6 ±0.3	– – –	
	d	171.9	182.2	189.1	81.8	63.8	12.28	0.816	37.8	29.5	3.40	13.9 ±4.9	0.18	
	e	134.4	134.8	229.2	69.7	61.8	8.60	0.784	54.8	69.1	3.37	12.9 ±4.2	0.12	
AS046	a	120.6	116.2	201.0	61.3	61.3	5.84	0.758	57.5	55.0	1.87	11.0 ±0.2	– – –	10.7 ±0.3
	b	136.4	116.7	215.0	65.5	62.3	7.13	0.773	183.2	158.6	7.03	10.6 ±0.2	– – –	
	c	102.9	94.3	167.1	51.0	58.8	3.36	0.715	227.2	161.9	3.57	10.3 ±0.2	– – –	
AS047	a	122.2	124.0	220.3	64.4	56.3	6.92	0.767	54.4	77.4	4.94	23.6 ±0.4	– – –	24.6 ±0.6
	b	123.6	126.8	203.0	64.2	55.8	6.59	0.766	57.0	85.3	5.38	25.4 ±0.5	– – –	
	c	98.7	111.3	246.2	57.6	54.3	5.63	0.741	69.2	100.2	5.23	24.9 ±0.4	– – –	
AS049	a	183.6	168.0	300.9	91.1	60.3	19.30	0.829	11.3	27.8	4.22	27.2 ±0.4	– – –	52.1 ±12.2
	b	155.0	137.5	339.9	80.1	52.3	15.10	0.811	10.4	12.7	5.51	61.8 ±1.7	– – –	
	c	169.0	169.0	142.1	72.4	52.3	2.10	0.668	57.5	80.2	3.32	56.8 ±1.2	– – –	
	d	173.1	157.3	348.5	89.0	52.3	19.70	0.831	6.2	4.6	5.08	77.8 ±1.5	– – –	
	e	148.5	160.9	247.8	79.1	59.8	12.29	0.809	7.6	9.1	1.19	22.6 ±8.4	0.31	
	~~f~~	~~139.6~~	~~163.3~~	~~249.2~~	~~77.9~~	~~53.8~~	~~11.84~~	~~0.804~~	~~7.2~~	~~12.9~~	~~2.62~~	~~49.4 ±19.2~~	~~0.47~~	
AS050	a	106.1	94.3	216.1	54.2	62.3	4.50	0.732	67.4	29.1	1.02	7.7 ±0.3	– – –	7.5 ±0.3
	b	126.1	117.1	239.0	64.7	64.8	7.32	0.773	34.9	15.5	0.91	7.7 ±0.3	– – –	
	c	74.3	85.9	118.7	40.3	59.3	1.58	0.649	17.5	8.8	0.07	6.2 ±1.2	– – –	
	d	97.2	90.6	153.8	48.2	61.3	2.81	0.700	67.7	52.2	0.59	6.9 ±0.3	– – –	
	~~e~~	~~121.7~~	~~140.4~~	~~271.8~~	~~70.4~~	~~60.8~~	~~9.67~~	~~0.790~~	~~48.4~~	~~21.2~~	~~3.44~~	~~15.5 ±0.5~~	– – –	

Sample	Aliquot	Width 1 (µm)	Width 2 (µm)	Length (µm)	Sphere ER (µm)	Est. T_c (° C)	Mass (µg)	Ft	U (ppm)	Th (ppm)	^{4}He (mol x 10^{-14})	Ind. cooling age ±1σ (Ma)	ε (noise to signal ratio)*	Weighted mean sample age ±1σ (Ma)
AS051	a	106.0	97.2	172.7	52.6	61.8	3.69	0.723	16.1	11.8	0.21	7.6 ±1.8	– – –	5.1 ±1.6
	b	102.7	104.4	168.5	53.1	61.3	3.74	0.728	19.3	5.9	0.25	8.1 ±0.7	– – –	
	c	208.7	217.9	293.6	105.4	78.8	27.67	0.856	8.8	4.8	0.45	3.5 ±0.2	– – –	
	d	113.5	109.5	180.6	57.1	64.3	4.65	0.745	12.0	5.0	0.16	6.5 ±0.8	– – –	
	~~e~~	~~100.7~~	~~97.2~~	~~203.0~~	~~53.1~~	~~73.8~~	~~4.12~~	~~0.724~~	~~31.0~~	~~28.0~~	~~0.10~~	~~1.6 ±0.3~~	– – –	
AS052	a	141.5	139.1	289.4	75.3	68.8	11.81	0.805	57.8	2.1	1.80	6.0 ±0.2	– – –	6.1 ±0.2
	b	118.5	104.9	260.1	61.2	68.3	6.73	0.763	10.6	1.3	0.13	4.4 ±0.7	– – –	
	c	193.2	162.9	351.4	94.8	72.3	23.09	0.842	22.1	9.1	1.58	6.2 ±0.2	– – –	
	d	128.2	132.1	212.8	66.8	66.8	7.46	0.781	12.3	2.7	0.26	6.3 ±0.4	– – –	
	e	120.5	120.5	167.2	59.7	67.3	5.03	0.756	8.3	1.8	0.08	4.6 ±1.1	– – –	
AS053	a	131.6	151.4	214.3	71.5	64.8	8.88	0.792	9.7	5.7	0.39	9.3 ±0.6	– – –	9.2 ±0.4
	b	171.3	158.6	232.6	82.0	67.3	13.11	0.818	34.9	19.5	2.07	9.0 ±0.3	– – –	
	c	127.3	126.9	267.4	68.5	65.3	8.95	0.784	48.4	29.2	1.71	8.1 ±0.3	– – –	
	d	117.2	123.7	314.9	67.1	63.3	9.47	0.778	25.2	22.0	1.22	10.0 ±0.3	– – –	
	e	106.4	109.1	202.9	56.9	60.8	4.88	0.741	14.6	14.3	0.36	10.2 ±0.7	– – –	
AS056	a	74.0	84.1	134.5	40.9	47.3	1.74	0.653	10.3	6.6	0.31	42.7 ±5.1	– – –	65.0 ±5.8
	b	116.8	131.2	258.4	66.7	50.3	8.23	0.780	107.1	24.0	24.23	61.3 ±2.0	– – –	
	c	94.6	97.0	258.9	53.6	47.3	4.92	0.732	82.9	6.1	11.68	70.3 ±2.2	– – –	
	d	88.9	103.6	158.6	49.5	46.3	3.04	0.708	40.6	25.1	4.34	79.4 ±3.2	– – –	
	e	88.7	93.1	190.1	48.9	48.3	3.25	0.709	101.8	5.2	6.61	51.0 ±2.0	– – –	
AS058	a	123.6	146.4	259.8	71.6	79.8	9.81	0.788	3.8	6.7	0.03	1.4 ±0.3	– – –	1.8 ±0.4
	b	117.9	119.2	218.5	62.3	76.8	6.36	0.757	4.4	10.4	0.03	1.5 ±0.3	– – –	
	c	99.8	102.0	253.5	55.9	75.3	5.34	0.733	3.8	6.9	0.02	1.4 ±0.4	– – –	
	d	113.9	120.4	252.9	63.4	72.3	7.19	0.761	2.7	5.3	0.03	2.8 ±0.6	– – –	
	~~e~~	~~93.3~~	~~119.5~~	~~284.6~~	~~59.5~~	~~66.8~~	~~6.68~~	~~0.748~~	~~8.2~~	~~15.0~~	~~0.16~~	~~5.1 ±0.5~~	– – –	
AS059	a	72.5	79.8	222.8	43.1	53.3	2.68	0.673	27.2	2.0	0.42	15.4 ±0.6	– – –	12.7 ±4.3
	b	105.5	92.3	189.2	52.4	60.3	3.83	0.720	51.4	56.4	0.89	9.2 ±0.4	– – –	

Table B-2. Analytical data for new zircon (U-Th)/He thermochronometry. All data processed at the University of California Helium Thermochronology Laboratory; see Table 3-2 for sources of data. Strike-through indicates aliquots not included in the final age. (*) Indicates disaggregation of grain during chemical unpacking, as desribed for zircon in Appendix A. Mean ages weighted by the inverse square error. Light gray shading indicates aliquots with re-extraction values of 5–10%; dark gray shading indicates aliquots with re-extraction values of 10–20%.

Sample	Aliquot	Width 1 (µm)	Width 2 (µm)	Length (µm)	Tip (µm)	Sphere ER (µm)	Est. T_c (° C)	Mass (µg)	Ft	U (ppm)	Th (ppm)	^4He (mol x 10^{-14})	Ind. cooling age ±1σ (Ma)	Weighted mean sample age ±1σ (Ma)
09DO01	a	103.8	94.9	213.9	29.7	61.1	182.8	7.99	0.798	1942.8	346.5	126.0	17.9 ±0.2	15.8 ±3.2
	b	124.4	134.8	327.0	68.0	80.5	192.3	18.50	0.845	1690.7	456.9	197.0	13.0 ±0.3	
	c	75.2	90.0	256.4	37.5	53.5	187.3	6.49	0.772	2834.1	287.2	71.40	9.0 ±0.3	
09DO02	a	77.1	69.4	180.5	38.7	45.2	175.8	3.21	0.731	841.6	273.3	22.70	19.6 ±0.3	14.9 ±7.2
	b	63.9	76.0	158.7	32.4	42.5	181.8	2.61	0.716	113.0	32.7	1.16	9.5 ±0.1	
09DO04	a	162.1	121.9	275.2	71.1	80.9	197.3	16.60	0.844	106.4	53.0	6.86	7.6 ±0.1	8.0 ±1.0
	b	150.6	133.6	273.4	64.3	82.9	196.3	17.60	0.848	77.2	38.8	6.31	9.1 ±0.2	
09DO05	a	68.7	74.2	154.7	33.1	43.1	178.3	2.63	0.720	804.8	181.7	12.10	13.9 ±0.2	11.5 ±1.5
	b	77.7	92.1	196.1	40.0	51.8	186.8	4.75	0.764	328.1	101.7	6.15	8.9 ±0.1	
	c	79.1	58.0	172.5	34.8	41.8	179.3	2.69	0.711	355.3	119.9	4.71	11.8 ±0.2	
	d	67.5	68.4	159.5	34.8	41.6	177.8	2.43	0.709	141.7	71.2	2.03	13.7 ±0.2	
09DO06	a	86.8	61.3	161.0	31.7	43.9	170.8	2.94	0.724	526.8	193.6	19.70	29.8 ±0.8	23.6 ±3.2
	b	79.6	85.7	167.4	28.1	49.9	177.3	4.11	0.756	1283.0	283.8	47.80	20.9 ±0.4	
	c	51.4	60.8	135.2	23.6	34.8	170.3	1.51	0.659	492.2	146.3	5.65	19.8 ±0.3	
	d	64.1	68.5	171.5	30.8	41.8	169.8	2.66	0.711	948.1	313.6	31.60	30.0 ±0.7	
09DO07	a	60.0	64.4	128.4	20.7	37.8	162.8	1.81	0.683	390.2	147.6	18.50	64.4 ±1.3	56.8 ±5.2
	b	69.6	60.3	159.0	29.3	40.3	164.8	2.34	0.702	378.1	143.9	18.90	51.2 ±0.6	
	c	74.6	52.5	149.6	24.2	38.6	162.8	2.14	0.689	397.5	158.4	21.40	61.3 ±1.0	
09DO08	a	57.0	54.6	120.0	23.6	33.9	165.8	1.28	0.650	533.5	218.5	9.21	34.8 ±0.6	36.3 ±1.7
	b	50.7	52.6	132.0	20.7	32.7	164.8	1.29	0.639	421.5	159.1	7.46	36.1 ±0.7	
	c	60.1	58.4	157.2	24.9	37.7	165.8	2.02	0.682	467.1	197.1	15.80	41.0 ±0.6	
	d	45.9	55.1	139.7	22.2	32.1	163.8	1.30	0.632	499.0	231.2	8.93	36.2 ±0.4	
	e	81.4	69.8	206.1	30.0	48.2	172.8	4.39	0.747	394.0	121.9	22.60	30.0 ±0.7	
AS004	a	81.8	86.0	323.9	60.1	55.3	165.8	7.97	0.779	486.8	69.5	142.60	83.5 ±2.1	78.1 ±3.8
	b	102.8	122.8	335.6	66.5	71.6	171.8	14.50	0.827	458.6	39.9	218.90	71.4 ±1.7	
	c	106.6	116.9	324.6	63.2	71.2	170.8	13.93	0.826	585.9	71.0	299.10	79.0 ±1.3	
AS006	a	73.6	75.3	221.6	30.1	48.4	162.8	4.68	0.749	402.2	68.6	62.42	77.9 ±1.3	86.4 ±8.6
	b	81.1	102.5	320.9	38.3	60.3	165.8	10.43	0.796	305.6	41.2	152.70	106.4 ±2.6	
	c	94.2	107.6	281.3	42.7	64.6	167.8	10.58	0.808	511.3	100.1	227.60	91.0 ±1.4	
	~~d~~	~~74.6~~	~~99.4~~	~~323.4~~	~~38.6~~	~~57.2~~	~~164.8~~	~~9.38~~	~~0.785~~	~~262.6~~	~~61.9~~	~~160.10~~	~~142.7 ±2.8~~	
AS008	a	90.4	93.5	356.3	40.3	61.9	165.8	11.89	0.800	245.5	70.7	155.30	113.5 ±1.7	90.6 ±12.7
	b	93.5	103.8	252.8	35.7	62.5	167.8	9.26	0.803	462.4	90.0	168.90	85.9 ±1.5	
	c	96.3	97.0	307.8	44.6	63.3	168.8	10.78	0.805	429.7	75.8	176.10	82.9 ±2.4	
	d	98.3	99.7	262.2	40.3	63.1	169.8	9.50	0.804	1286.5	219.8	380.30	68.1 ±1.1	

Sample	Aliquot	Width 1 (µm)	Width 2 (µm)	Length (µm)	Tip (µm)	Sphere ER (µm)	Est. T_c (° C)	Mass (µg)	Ft	U (ppm)	Th (ppm)	^{4}He (mol x 10^{-14})	Ind. cooling age ±1σ (Ma)	Weighted mean sample age ±1σ (Ma)
AS010	a	104.9	114.2	412.3	61.9	72.9	168.8	18.40	0.829	240.5	89.6	229.0	105.1 ±3.9	108.5 ±5.9
	b	93.5	94.2	255.7	65.7	57.7	164.8	6.88	0.786	426.5	126.5	145.0	107.1 ±1.6	
	c	80.8	83.9	287.7	54	53.8	163.8	6.80	0.771	279.7	134.6	91.71	102.7 ±1.8	
	d	97.7	100.4	321.4	43.9	65.1	165.8	11.99	0.810	233.2	66.9	170.20	128.3 ±3.5	
	~~e~~	~~132.7~~	~~134.1~~	~~335.0~~	~~36.4~~	~~84.7~~	~~184.3~~	~~23.70~~	~~0.852~~	~~12.1~~	~~3.7~~	~~4.32~~	~~30.4 ±1.4~~	
AS016	a	102.5	136.9	316.9	59.9	74.1	182.8	15.46	0.832	107.0	28.0	20.92	26.3 ±0.5	27.1 ±4.2
	b	108.3	111.8	277.3	77.2	66.1	176.8	9.82	0.813	196.2	46.3	33.32	37.0 ±0.7	
	c	98.7	110.0	265.8	48.2	65.4	183.8	10.17	0.810	159.7	46.3	14.35	18.8 ±0.3	
	d	95.9	108.3	247.3	42.1	63.6	179.8	9.23	0.806	770.6	97.0	84.56	26.3 ±0.5	
AS017	a	112.1	115.9	367.9	50.5	74.9	189.3	18.16	0.834	2365.6	373.2	288.30	14.3 ±0.2	19.5 ±9.5
	b	81.5	92.2	185.9	30.4	53.0	172.8	5.08	0.770	1138.8	43.2	88.50	36.2 ±0.6	
	c	69.8	83.9	174.0	26.3	47.3	183.3	3.78	0.745	1602.1	96.2	25.43	10.2 ±0.2	
AS018	a	109.0	152.7	321.3	47.0	80.5	183.3	20.00	0.845	668.3	165.9	192.0	29.6 ±1.0	27.6 ±2.6
	b	109.0	152.7	321.3	47.0	80.5	182.8	20.02	0.845	441.8	98.3	131.70	30.8 ±0.7	
	c	118.6	145.5	337.2	45.4	83.2	185.3	22.20	0.850	671.4	128.5	188.0	26.1 ±0.8	
	d	118.6	145.5	337.2	45.4	83.2	182.3	22.20	0.850	394.4	80.1	144.90	34.2 ±0.7	
	e	104.2	108.0	323.6	37.6	69.4	180.8	14.31	0.821	352.6	79.2	68.16	28.7 ±0.5	
	f	100.4	108.3	286.1	35.8	67.1	184.3	12.10	0.815	513.3	131.9	55.0	18.9 ±0.8	
	g	100.4	108.3	286.1	35.8	67.1	185.3	12.05	0.815	364.6	64.8	34.57	17.0 ±0.4	
AS019	a	99.4	102.8	251.4	30.4	64.0	180.8	10.02	0.807	201.2	36.8	21.61	23.4 ±0.5	25.1 ±4.6
	b	99.4	123.4	265.5	36.5	69.2	184.8	12.37	0.821	139.3	26.5	15.60	19.4 ±0.4	
	c	92.8	113.1	179.5	36.3	59.1	176.3	6.40	0.792	330.9	38.5	29.43	31.4 ±0.6	
AS020	a	104.2	135.8	296.1	50.9	74.1	185.3	15.01	0.832	461.1	127.0	67.66	20.3 ±0.3	20.0 ±0.5
	b	64.6	80.5	249.7	35.7	47.5	177.3	4.89	0.745	199.2	23.4	7.67	18.9 ±0.5	
	c	65.3	85.6	214.9	31.8	47.9	176.8	4.48	0.746	263.3	69.9	10.28	20.2 ±0.4	
AS022	a	145.1	201.5	378.3	94.2	100.9	196.3	34.35	0.875	47.4	16.1	11.79	14.1 ±0.2	20.5 ±3.4
	b	133.1	195.3	463.9	108.1	99.3	191.8	38.65	0.872	53.2	26.2	21.62	19.9 ±0.4	
	c	92.5	119.3	272.4	65.3	64.2	181.8	9.51	0.807	79.5	27.0	7.92	22.1 ±0.4	
	d	103.8	120.0	290.9	73.0	68.3	180.8	11.21	0.818	185.2	62.8	27.62	27.7 ±0.5	
AS024	a	177.4	183.6	317.1	66.0	104.4	197.3	34.70	0.879	117.7	36.8	26.60	12.7 ±0.5	11.7 ±0.4
	b	100.1	100.4	300.4	42.7	65.2	188.8	11.40	0.811	1478.0	102.8	88.40	11.7 ±0.4	
	c	76.7	93.9	241.9	30.9	54.7	185.8	6.68	0.776	258.0	60.0	8.30	10.8 ±0.3	
	d	73.9	95.6	192.8	31.9	51.7	183.8	4.98	0.764	541.2	140.8	13.90	11.7 ±0.3	
	~~e~~	~~107.6~~	~~122.8~~	~~249.3~~	~~40.9~~	~~70.4~~	~~197.3~~	~~11.97~~	~~0.812~~	~~11.7~~	~~62.8~~	~~0.84~~	~~6.0 ±0.1~~	
AS025	a	174.3	185.0	364.9	52.2	109.1	201.3	44.30	0.885	171.7	17.6	33.20	8.9 ±0.2	12.2 ±1.2
	b	97.0	123.4	282.2	69.5	66.7	187.3	10.50	0.814	250.9	41.6	16.90	13.9 ±0.3	
	c	67.4	74.6	198.8	44.0	44.5	178.8	3.28	0.729	650.9	33.3	11.94	14.0 ±0.3	
	d	76.7	113.8	197.9	36.5	55.8	186.3	6.06	0.781	547.2	45.5	15.40	10.8 ±0.5	
	e	78.7	100.1	235.6	41.4	55.9	186.3	6.61	0.781	484.2	67.6	15.10	10.8 ±0.3	
AS026	a	111.1	114.8	245.5	50.0	68.6	180.3	10.61	0.818	323.8	120.2	46.91	28.2 ±0.4	19.1 ±5.0
	b	76.7	101.4	193.8	35.2	53.6	188.3	5.31	0.771	665.8	168.3	12.80	8.2 ±0.1	
	c	97.0	97.7	186.4	31.1	58.1	179.3	6.38	0.787	988.9	399.8	69.14	23.3 ±0.4	
	d	70.8	74.3	176.8	30.2	45.4	177.8	3.34	0.732	492.2	174.7	11.23	15.8 ±0.3	

Sample	Aliquot	Width 1 (µm)	Width 2 (µm)	Length (µm)	Tip (µm)	Sphere ER (µm)	Est. T_c (° C)	Mass (µg)	Ft	U (ppm)	Th (ppm)	^{4}He (mol x 10^{-14})	Ind. cooling age ±1σ (Ma)	Weighted mean sample age ±1σ (Ma)
AS027	a	130.0	145.5	289.2	48.8	83.7	178.3	19.71	0.850	97.0	31.6	50.99	53.4 ±1.2	35.7 ±6.9
	b	124.1	136.2	331.0	74.9	80.3	180.8	18.16	0.844	126.1	51.5	42.54	36.9 ±0.6	
	c	130.0	135.5	263.6	63.0	78.0	185.8	14.71	0.839	180.7	73.1	28.66	21.6 ±0.4	
	d	106.3	112.4	264.3	48.0	68.1	177.8	11.13	0.817	185.2	72.5	36.23	36.2 ±0.7	
AS029	a	76.7	92.8	236.6	33.6	54.1	182.8	6.35	0.773	422.7	166.9	17.61	14.3 ±0.3	12.9 ±1.4
	b	66.7	93.9	194.3	33.0	49.0	181.3	4.38	0.750	406.8	151.1	10.33	13.1 ±0.2	
	c	83.2	103.5	241.6	41.0	58.4	183.3	7.48	0.789	114.0	34.4	6.06	15.5 ±0.4	
	d	56.4	62.2	196.5	25.9	39.0	180.3	2.64	0.691	419.2	232.7	4.35	9.2 ±0.2	
AS030	a	103.8	126.9	356.9	46.6	74.8	180.8	18.06	0.833	261.0	82.8	76.59	33.4 ±0.6	67.3 ±17.2
	b	109.3	109.3	278.9	53.4	68.5	174.3	11.54	0.818	85.7	31.9	24.69	51.5 ±1.0	
	c	120.0	122.4	371.1	50.3	79.1	172.8	20.76	0.841	355.2	162.8	309.0	82.2 ±1.5	
	d	120.3	122.4	333.2	56.4	77.4	170.8	17.67	0.838	273.0	153.4	244.10	97.5 ±1.6	
AS031	a	156.5	178.8	314.8	63.8	98.4	189.3	29.89	0.872	82.1	30.7	31.62	25.0 ±0.4	28.9 ±5.3
	b	114.8	116.9	268.2	63.4	70.2	177.3	11.46	0.823	27.9	7.5	6.31	41.3 ±0.8	
	c	83.2	127.2	256.4	42.9	63.4	176.8	9.80	0.805	276.8	79.0	44.09	34.8 ±0.5	
	d	105.9	147.9	242.9	53.5	72.9	185.8	12.50	0.829	63.1	18.3	7.33	19.3 ±0.3	
AS032	a	128.3	153.7	306.9	79.1	83.1	189.8	18.47	0.850	547.5	34.6	80.37	16.9 ±0.3	23.3 ±3.1
	b	128.9	129.6	403.4	69.7	83.8	185.8	24.11	0.851	368.8	63.1	106.70	24.9 ±0.5	
	c	93.2	97.7	338.5	46.0	63.4	181.3	11.74	0.804	307.7	131.2	39.43	22.7 ±0.4	
	d	102.8	126.9	305.9	63.4	71.3	180.8	13.43	0.825	287.7	124.1	57.04	29.9 ±0.6	
AS033	a	74.6	101.4	229.4	40.4	54.5	185.3	6.17	0.775	311.9	78.0	9.81	11.4 ±0.3	24.0 ±7.1
	b	81.8	106.9	260.0	33.5	59.8	170.8	8.75	0.793	386.6	137.9	89.80	56.6 ±1.1	
	c	120.0	145.1	344.0	61.8	83.0	190.8	21.18	0.849	318.5	95.9	51.12	15.3 ±0.2	
	d	74.3	88.4	196.4	33.8	50.5	176.8	4.62	0.758	419.7	133.3	19.13	22.3 ±0.4	
	e	64.3	68.4	173.2	29.1	42.0	180.8	2.75	0.714	316.7	56.5	3.64	10.3 ±0.3	
	f	91.8	109.7	237.8	46.3	61.9	173.8	8.24	0.800	349.5	135.7	60.50	44.1 ±1.3	
	g	94.9	128.3	241.6	44.5	66.8	186.8	10.30	0.815	626.8	137.0	44.70	14.8 ±0.3	
AS045	a	129.3	130.0	383.7	56.7	84.1	175.3	24.10	0.851	721.7	249.5	631.0	72.2 ±2.0	84.0 ±4.5
	b	133.4	146.8	412.6	70.8	90.0	174.3	28.98	0.860	568.7	196.1	742.40	88.6 ±1.5	
	c*	80.1	101.1	321.4	41.0	59.6	167.8	10.00	0.793	670.0	239.1	252.0	79.7 ±2.2	
	d	101.8	106.6	246.2	52.1	64.0	167.8	8.92	0.806	367.3	113.3	137.0	88.5 ±2.4	
AS046	a	126.5	165.4	300.6	54.1	87.0	178.3	22.20	0.856	1264.6	202.8	779.0	57.2 ±1.4	67.4 ±9.6
	b	69.8	88.0	215.1	35.2	49.8	164.8	4.80	0.755	1485.8	404.1	264.10	84.3 ±1.3	
	c	84.9	87.0	268.1	36.1	56.3	167.8	7.55	0.781	866.1	238.8	213.40	71.8 ±1.1	
	d	85.6	97.3	212.2	40.3	56.2	170.8	6.14	0.781	1272.9	384.2	175.10	49.2 ±0.8	
	~~e*~~	~~90.4~~	~~109.7~~	~~236.8~~	~~38.9~~	~~61.9~~	~~161.8~~	~~8.53~~	~~0.800~~	~~303.1~~	~~87.4~~	~~221.0~~	~~181.7 ±5.3~~	
	~~f*~~	~~101.1~~	~~119.3~~	~~335.1~~	~~48.8~~	~~71.3~~	~~162.8~~	~~15.10~~	~~0.836~~	~~360.0~~	~~-450.6~~	~~404.0~~	~~225.3 ±44.1~~	
	~~g*~~	~~87.3~~	~~89.1~~	~~217.5~~	~~33.9~~	~~55.5~~	~~159.8~~	~~6.23~~	~~0.779~~	~~140.3~~	~~32.2~~	~~77.50~~	~~195.4 ±5.3~~	
	~~h*~~	~~108.3~~	~~109.3~~	~~315.7~~	~~40.3~~	~~70.6~~	~~158.8~~	~~13.10~~	~~0.821~~	~~135.0~~	~~46.2~~	~~326.0~~	~~371.8 ±7.9~~	
	~~i*~~	~~89.1~~	~~94.6~~	~~346.4~~	~~45.1~~	~~61.5~~	~~159.8~~	~~10.60~~	~~0.798~~	~~183.9~~	~~34.6~~	~~215.0~~	~~238.2 ±10.8~~	

Sample	Aliquot	Width 1 (µm)	Width 2 (µm)	Length (µm)	Tip (µm)	Sphere ER (µm)	Est. T_c (° C)	Mass (µg)	Ft	U (ppm)	Th (ppm)	^{4}He (mol x 10^{-14})	Ind. cooling age ±1σ (Ma)	Weighted mean sample age ±1σ (Ma)
AS047	a	108.3	134.4	365.6	50.1	78.2	175.3	20.20	0.840	824.6	282.4	519.0	62.8 ±1.7	67.1 ±2.2
	b	95.9	116.6	395.3	55.7	70.3	171.8	16.69	0.822	692.3	265.6	390.90	69.1 ±1.3	
	c	80.8	88.7	220.9	35.3	53.7	167.8	5.79	0.771	825.0	250.1	145.0	67.2 ±1.5	
	~~d~~	~~101.4~~	~~125.9~~	~~320.7~~	~~45.1~~	~~72.5~~	~~161.8~~	~~15.50~~	~~0.829~~	~~138.1~~	~~29.7~~	~~265.0~~	~~256.4 ±8.9~~	
AS048	a	121.7	127.9	258.4	38.7	76.0	180.8	15.00	0.836	337.0	68.1	79.50	33.1 ±1.1	16.4 ±2.9
	b	92.8	119.3	298.7	47.6	67.1	185.8	12.11	0.815	626.0	144.0	57.21	16.2 ±0.3	
	c	95.9	100.1	301.3	41.7	64.0	186.8	10.97	0.807	581.0	126.5	40.36	13.7 ±0.3	
	d	93.2	93.2	227.0	42.1	58.1	183.8	6.90	0.787	148.9	66.6	7.24	14.9 ±0.2	
	e	75.6	82.5	188.6	31.6	49.3	181.8	4.25	0.753	102.7	26.5	2.40	12.7 ±0.4	
	~~f~~	~~108.7~~	~~126.2~~	~~247.3~~	~~49.7~~	~~70.6~~	~~158.8~~	~~11.50~~	~~0.824~~	~~13.2~~	~~1.7~~	~~26.90~~	~~370.9 ±15.9~~	
AS049	a	131.4	160.9	437.6	77.2	93.3	175.8	32.90	0.865	409.7	130.4	567.30	82.8 ±2.2	87.5 ±2.4
	b	138.2	149.2	356.6	83.4	88.1	173.8	23.52	0.858	155.9	35.3	162.50	89.7 ±1.4	
	c	96.3	101.8	356.8	49.7	65.8	168.8	13.24	0.812	650.0	149.0	348.10	86.4 ±1.9	
	~~d~~	~~66.7~~	~~73.6~~	~~202.7~~	~~37.2~~	~~44.8~~	~~158.8~~	~~3.49~~	~~0.731~~	~~346.8~~	~~41.6~~	~~77.90~~	~~155.4 ±5.6~~	
AS050	a	101.3	108.1	312.2	58.5	67.1	178.8	10.50	0.811	525.9	170.4	82.12	31.3 ±0.7	29.7 ±3.9
	b	77.2	99.9	321.1	43.1	58.1	179.8	8.72	0.787	440.4	62.4	37.44	22.1 ±0.5	
	c	108.5	112.4	414.9	68.9	73.2	180.3	16.37	0.828	494.1	82.6	123.70	32.6 ±0.5	
AS051	a	76.2	71.6	203.1	29.1	47.4	171.8	3.77	0.740	336.0	62.2	17.18	32.3 ±0.6	31.0 ±2.1
	b	80.6	63.7	279.1	33.9	47.9	174.3	5.14	0.744	305.6	74.9	16.91	25.1 ±0.5	
	c	93.4	96.7	283.3	39.0	61.8	177.8	8.89	0.797	386.1	125.7	47.85	29.8 ±0.7	
	d	74.4	74.7	220.3	28.9	48.5	172.3	4.30	0.746	410.2	79.0	24.27	32.4 ±0.8	
	e	74.9	60.2	220.4	31.5	43.9	169.3	3.42	0.721	438.6	135.2	22.57	35.7 ±0.7	
AS052	a	112.5	120.4	355.5	41.9	76.1	183.8	17.58	0.834	176.6	65.6	37.92	24.8 ±0.5	32.7 ±3.6
	b	106.6	106.8	345.9	43.9	70.3	178.8	14.09	0.821	309.5	102.2	72.87	34.7 ±1.0	
	c	90.0	84.5	393.6	30.7	59.8	173.8	11.88	0.793	234.1	68.0	54.42	42.4 ±0.8	
	d	89.2	85.4	318.6	41.2	58.3	175.8	8.65	0.787	369.6	106.2	48.32	33.1 ±0.7	
	e	98.1	107.2	405.6	49.0	69.1	180.3	15.45	0.819	315.0	97.5	67.71	29.1 ±0.5	
AS053	a	75.7	70.3	481.3	37.9	51.4	172.8	10.20	0.760	479.9	258.3	79.35	34.8 ±0.6	37.7 ±6.8
	b	120.6	133.0	389.1	48.6	82.8	178.8	22.44	0.847	385.9	140.1	212.80	49.0 ±0.9	
	c	96.3	77.9	255.7	36.8	55.9	178.8	6.56	0.777	352.5	126.5	23.77	22.4 ±0.4	
	d	96.5	102.4	296.2	50.1	64.1	174.3	10.03	0.805	602.6	248.0	131.50	45.2 ±0.7	
AS056	a	146.1	146.1	436.7	48.9	95.4	176.8	36.90	0.868	722.8	156.7	1040.0	78.3 ±1.4	67.5 ±3.3
	b	110.8	127.9	268.8	38.2	73.8	173.8	14.40	0.831	1807.9	459.8	784.0	62.8 ±1.3	
	c	90.4	98.2	346.7	29.3	63.2	170.8	12.70	0.805	1457.2	293.9	543.0	63.7 ±1.1	
	d	69.2	73.3	300.3	22.8	48.5	165.8	6.37	0.749	1166.7	275.9	223.0	69.6 ±1.2	
	e	120.5	130.6	283.9	56.7	76.8	174.8	15.20	0.838	1424.4	176.1	644.0	63.0 ±1.0	
AS057	a	108.5	95.6	223.4	36.8	62.5	194.3	8.40	0.803	316.0	55.8	7.67	6.4 ±0.1	7.1 ±0.7
	b	101.9	94.8	248.9	46.2	61.6	190.3	8.42	0.799	87.8	37.5	3.22	9.1 ±0.2	
	c	91.1	67.4	186.8	29.9	48.5	189.3	4.19	0.750	504.0	70.9	5.39	6.1 ±0.1	
	d	70.8	83.5	237.9	29.2	50.2	188.3	5.47	0.757	557.3	144.8	9.48	7.1 ±0.1	
	e	84.9	72.4	155.8	33.9	46.4	189.3	3.16	0.739	1035.7	88.7	7.54	5.6 ±0.1	

Sample	Aliquot	Width 1 (µm)	Width 2 (µm)	Length (µm)	Tip (µm)	Sphere ER (µm)	Est. T_c (° C)	Mass (µg)	Ft	U (ppm)	Th (ppm)	^{4}He (mol x 10^{-14})	Ind. cooling age ±1σ (Ma)	Weighted mean sample age ±1σ (Ma)
AS058	a	108.1	132.0	396.3	64.7	77.9	196.3	18.42	0.836	50.3	24.8	3.90	8.3 ±0.2	11.7 ±2.3
	b	93.7	82.6	357.9	56.9	58.8	188.8	9.12	0.787	45.4	23.7	1.86	9.3 ±0.2	
	c	145.1	134.0	351.3	90.1	84.8	193.8	16.80	0.845	42.8	18.2	4.38	12.1 ±0.3	
	d	114.2	81.6	283.7	61.2	60.3	190.3	7.46	0.789	44.7	20.6	1.35	8.5 ±0.2	
	e	171.7	132.0	489.7	119.9	94.3	191.8	28.57	0.862	30.6	13.1	8.27	18.4 ±0.4	
AS059	a	105.1	110.7	420.0	58.7	72.3	176.8	16.95	0.826	135.2	41.0	50.12	45.4 ±1.0	45.4 ±1.0

APPENDIX C. MEASUREMENTS OF MARINE TERRACES

The following tables provide the surveyed elevations, locations, and back-edge calculations for the lowest-emergent marine terrace from Point Año Nuevo, north of Santa Cruz, CA to south of Ragged Point, near San Simeon, CA. A detailed description of the method is provided in Appendix A.

Table C-1. Names, dates, and survey prefixes for elevation surveys.

Survey	Name	Date
am	Andrew Molera	6/17/2014
bx	Bixby Bridge	9/16/2014
bxc	Bixby Creek	6/17/2014
lm	Limekiln Creek	6/18/2014
my	Monterey	3/4/2015
sc	Santa Cruz	2/22/2016

Table C-2. Locations, elevations, and back-edge calculations for marine terraces.

Survey station	Latitude (WGS84)	Longitude (WGS84)	Meas. terrace height (m)	GPS vert. unc. 1σ (m)	Horiz. offset (m)	Meas. vert. unc. 1σ (m)	Dist. to inner edge (m)	Model terrace height (m)	Model unc. 1σ (m)	Total vert. unc. 1σ (m)	Dist. to SGHF (km)
am_5	36.28001	-121.85476	10.34	0.80	26.7	0.80	227	15.9	1.85	2.02	-3.516
am_6	36.27982	-121.85448	11.02	0.70	15.5	0.70	206	16.1	1.68	1.82	-3.513
am_7	36.27973	-121.85437	11.16	0.50	18.7	0.50	197	16.0	1.61	1.68	-3.512
am_8	36.27909	-121.85351	11.70	0.60	16.8	0.60	153	15.5	1.25	1.39	-3.505
am_9	36.27884	-121.85328	13.99	0.50	22.7	0.50	159	17.9	1.30	1.39	-3.510
am_10	36.27820	-121.85276	12.74	0.80	25.7	0.80	193	17.5	1.57	1.77	-3.524
am_11	36.27688	-121.85098	13.26	0.70	32.1	0.70	182	17.7	1.48	1.64	-3.474
am_12	36.27649	-121.85075	14.71	0.50	21.6	0.50	192	19.4	1.57	1.64	-3.478
am_13	36.27622	-121.85063	11.87	0.50	50.9	0.51	201	16.8	1.64	1.72	-3.483
am_14	36.27627	-121.85065	14.81	0.70	24.1	0.70	199	19.7	1.62	1.77	-3.481
am_15	36.27538	-121.84966	14.63	0.50	24.3	0.50	173	18.9	1.41	1.50	-3.452
am_16	36.27423	-121.84840	14.41	0.60	34.9	0.61	138	17.8	1.13	1.28	-3.415
am_17	36.27354	-121.84796	11.47	0.60	22.3	0.60	133	14.7	1.09	1.24	-3.418
am_18	36.27233	-121.84691	16.56	1.00	31.4	1.00	107	19.2	0.87	1.33	-3.400
am_19	36.27188	-121.84644	14.87	0.70	22.9	0.70	127	18.0	1.04	1.25	-3.388
am_21	36.27086	-121.84563	13.04	1.10	31.3	1.10	128	16.2	1.04	1.52	-3.379
am_22	36.26998	-121.84552	11.10	0.90	22.1	0.90	156	14.9	1.27	1.56	-3.421
am_23	36.26835	-121.84408	12.02	0.40	179.8	0.56	102	14.5	0.83	1.00	-3.412
am_24	36.26753	-121.84347	12.83	0.20	125.2	0.34	133	16.1	1.09	1.14	-3.421
am_25	36.26664	-121.84274	10.79	0.20	88.4	0.28	153	14.6	1.25	1.28	-3.429
am_26	36.26503	-121.84236	12.52	0.30	244.0	0.61	191	17.2	1.56	1.67	-3.514
am_27	36.28039	-121.86053	16.06	0.50	2.3	0.50	735	28.0	2.70	2.74	-3.863
am_28	36.28063	-121.86198	6.52	0.50	123.9	0.57	864	19.6	2.88	2.93	-3.939
am_29	36.28011	-121.86040	10.13	0.50	36.4	0.51	726	21.9	2.68	2.73	-3.876
am_30	36.28068	-121.86234	8.79	0.40	161.0	0.53	897	22.1	2.93	2.98	-3.958
am_31	36.28008	-121.85973	15.24	0.40	0.0	0.40	667	26.5	2.62	2.65	-3.834
am_32	36.28114	-121.86000	17.71	0.30	120.7	0.40	687	29.2	2.64	2.67	-3.771
am_33	36.28057	-121.85636	15.99	0.30	308.8	0.74	360	24.4	2.45	2.56	-3.577
am_34	36.28064	-121.85656	11.15	0.30	291.1	0.70	378	19.8	2.46	2.56	-3.585
am_35	36.28035	-121.85571	12.14	0.50	362.0	0.94	305	19.6	2.42	2.60	-3.551
bx_1	36.37328	-121.90594	68.47	1.10	217.8	1.20	110	71.2	0.90	1.50	0.993
bx_2	36.37335	-121.90627	65.52	1.00	225.6	1.12	137	68.9	1.12	1.58	0.976
bx_3	36.37344	-121.90658	64.25	1.10	234.3	1.21	163	68.3	1.33	1.80	0.961

Survey station	Latitude (WGS84)	Longitude (WGS84)	Meas. terrace height (m)	GPS vert. unc. 1σ (m)	Horiz. offset (m)	Meas. vert. unc. 1σ (m)	Dist. to inner edge (m)	Model terrace height (m)	Model unc. 1σ (m)	Total vert. unc. 1σ (m)	Dist. to SGHF (km)
bx_4	36.37784	-121.90472	61.23	1.10	231.4	1.21	86	63.3	0.70	1.40	1.402
bx_5	36.37816	-121.90481	62.32	1.10	267.0	1.25	101	64.8	0.82	1.49	1.419
bx_6	36.37768	-121.90443	64.22	1.10	217.4	1.20	57	65.6	0.47	1.29	1.411
bx_7	36.37808	-121.90441	59.49	0.60	317.0	0.92	64	61.1	0.52	1.05	1.441
bx_8	36.37820	-121.90377	60.30	0.60	269.3	0.84	21	60.8	0.17	0.86	1.493
bx_9	36.38063	-121.90151	32.68	0.60	67.3	0.62	196	37.5	1.60	1.71	1.822
bx_10	36.38072	-121.90151	32.29	0.60	76.4	0.62	199	37.2	1.62	1.74	1.829
bx_11	36.38088	-121.90151	30.57	0.60	92.4	0.63	203	35.6	1.66	1.77	1.840
bx_12	36.38194	-121.90164	23.72	0.60	203.8	0.75	231	29.4	1.88	2.03	1.907
bx_13	36.38271	-121.90215	32.35	0.60	290.0	0.87	237	38.2	1.93	2.12	1.927
bx_14	36.38299	-121.90248	30.43	0.60	321.0	0.92	260	36.8	2.12	2.31	1.924
bx_15	36.38418	-121.90263	38.82	0.60	454.0	1.16	257	45.2	2.10	2.40	1.999
bx_16	36.38020	-121.90190	39.73	0.80	7.9	0.80	175	44.0	1.43	1.64	1.765
bx_17	36.38130	-121.90140	33.46	0.70	139.6	0.76	208	38.6	1.70	1.86	1.878
bx_18	36.38009	-121.90230	34.33	1.10	32.1	1.10	158	38.2	1.29	1.70	1.729
bx_19	36.38007	-121.90222	35.53	1.20	25.6	1.20	156	39.4	1.27	1.75	1.733
bx_20	36.38496	-121.90175	28.32	0.60	325.0	0.93	174	32.6	1.42	1.70	2.115
bx_21	36.38485	-121.90212	28.79	0.60	339.0	0.95	207	33.9	1.69	1.94	2.082
bx_22	36.38533	-121.90124	28.62	0.60	287.1	0.87	129	31.8	1.05	1.36	2.176
bx_23	36.38765	-121.90300	32.22	0.60	125.5	0.66	179	36.6	1.46	1.60	2.221
bx_24	36.38712	-121.90144	32.37	0.60	93.1	0.63	80	34.3	0.65	0.91	2.290
bx_25	36.38783	-121.90225	34.37	0.50	58.3	0.52	110	37.1	0.90	1.04	2.285
bx_26	36.38756	-121.90306	30.19	0.50	132.3	0.58	188	34.8	1.53	1.64	2.211
bx_27	36.38767	-121.90176	33.62	1.00	134.4	1.04	78	35.5	0.64	1.22	2.308
bx_28	36.38779	-121.90234	33.54	0.80	81.3	0.82	119	36.5	0.97	1.27	2.277
bx_29	36.38675	-121.90192	31.33	0.80	173.1	0.89	136	34.7	1.11	1.42	2.231
bx_30	36.38764	-121.90361	26.64	1.00	14.2	1.00	228	32.3	1.86	2.11	2.179
bx_31	36.38779	-121.90358	31.55	1.00	8.1	1.00	219	36.9	1.79	2.05	2.192
bx_32	36.38502	-121.90291	28.70	0.70	306.0	0.97	272	35.4	2.22	2.42	2.040
bx_33	36.39024	-121.90422	18.58	0.80	154.8	0.87	230	24.2	1.88	2.07	2.322
bx_34	36.39016	-121.90484	16.09	0.80	172.0	0.88	286	23.1	2.33	2.49	2.274
bx_35	36.39015	-121.90473	16.10	0.80	165.9	0.88	276	22.9	2.25	2.42	2.282
bx_36	36.39163	-121.90442	19.21	0.80	306.4	1.04	227	24.8	1.85	2.13	2.408
bx_37	36.39168	-121.90442	15.75	0.80	313.0	1.05	227	21.3	1.85	2.13	2.412
bx_38	36.38930	-121.90462	26.18	0.90	60.1	0.91	269	32.8	2.19	2.38	2.228
bx_39	36.39415	-121.90381	18.09	0.90	555.0	1.51	163	22.1	1.33	2.01	2.630
bx_40	36.39442	-121.90420	16.02	0.90	585.0	1.56	187	20.6	1.53	2.18	2.622
bx_41	36.39550	-121.90559	27.34	0.90	716.0	1.80	281	34.3	2.29	2.92	2.604
bx_42	36.41195	-121.91573	8.29	1.10	137.9	1.14	149	12.0	1.22	1.67	3.084
bx_43	36.41198	-121.91567	8.22	1.10	133.2	1.14	146	11.8	1.19	1.65	3.089
bx_44	36.41189	-121.91532	10.01	0.90	103.6	0.93	112	12.8	0.91	1.30	3.107
bx_45	36.41189	-121.91532	11.32	0.90	103.6	0.93	112	14.1	0.91	1.30	3.107
bx_46	36.41261	-121.91498	12.74	0.90	88.2	0.92	116	15.6	0.95	1.32	3.182
bx_47	36.41269	-121.91554	13.05	0.80	134.0	0.85	165	17.1	1.35	1.59	3.149
bx_48	36.41257	-121.91477	13.66	0.90	72.0	0.91	99	16.1	0.81	1.22	3.193
bx_49	36.41236	-121.91453	13.79	1.00	42.8	1.00	68	15.5	0.56	1.15	3.194
bx_50	36.40097	-121.91060	15.33	0.60	83.6	0.63	197	20.2	1.61	1.73	2.651
bx_51	36.40057	-121.91046	15.96	0.60	110.2	0.65	241	21.9	1.97	2.07	2.632
bx_52	36.40025	-121.90989	11.08	0.60	172.0	0.71	283	18.1	2.31	2.41	2.648
bx_53	36.40007	-121.90988	11.54	0.60	184.2	0.72	303	19.0	2.42	2.53	2.636
bx_54	36.39963	-121.90866	12.40	0.60	299.8	0.89	300	19.8	2.42	2.58	2.689
bx_55	36.39726	-121.90581	14.95	0.60	659.0	1.56	306	22.4	2.42	2.88	2.715
bx_56	36.39728	-121.90604	15.32	0.60	642.0	1.52	327	23.1	2.43	2.87	2.700
bx_57	36.39625	-121.90569	17.66	0.60	747.0	1.74	290	24.8	2.37	2.93	2.651
bx_58	36.39056	-121.90445	7.41	0.60	1330.0	2.96	246	13.5	2.01	3.58	2.329
bx_59	36.39221	-121.90418	19.24	0.60	224.0	0.77	195	24.0	1.59	1.77	2.465
bx_60	36.39220	-121.90419	18.74	0.60	224.5	0.78	196	23.6	1.60	1.78	2.465
bx_61	36.39311	-121.90340	16.25	0.50	128.4	0.57	117	19.1	0.95	1.11	2.584
bx_62	36.39301	-121.90392	16.39	0.50	132.7	0.58	161	20.4	1.31	1.44	2.541
bx_63	36.39391	-121.90364	19.03	0.50	39.1	0.51	156	22.9	1.27	1.37	2.625
bx_64	36.39443	-121.90404	20.50	0.40	28.6	0.41	173	24.8	1.41	1.47	2.634
bx_65	36.39424	-121.90399	20.16	0.40	12.2	0.40	175	24.5	1.43	1.48	2.624
bx_66	36.39297	-121.90345	16.38	0.50	144.0	0.59	120	19.3	0.98	1.14	2.570
bx_67	36.39063	-121.90539	15.01	0.50	419.0	1.04	329	22.9	2.43	2.64	2.270
bx_68	36.39424	-121.90388	13.62	0.80	0.0	0.80	165	17.7	1.35	1.57	2.631
bx_70	36.39545	-121.90530	23.69	0.40	166.2	0.54	257	30.0	2.10	2.16	2.620
bx_71	36.39532	-121.90447	30.92	0.40	98.8	0.45	187	35.5	1.53	1.59	2.668

Survey station	Latitude (WGS84)	Longitude (WGS84)	Meas. terrace height (m)	GPS vert. unc. 1σ (m)	Horiz. offset (m)	Meas. vert. unc. 1σ (m)	Dist. to inner edge (m)	Model terrace height (m)	Model unc. 1σ (m)	Total vert. unc. 1σ (m)	Dist. to SGHF (km)
bx_72	36.39534	-121.90473	28.54	0.40	117.3	0.48	210	33.7	1.71	1.78	2.651
bx_73	36.39930	-121.90750	18.12	0.40	618.0	1.41	249	24.3	2.03	2.47	2.745
bx_74	36.39589	-121.90605	20.98	0.70	272.1	0.92	320	28.7	2.43	2.59	2.601
bx_75	36.39929	-121.90734	17.20	0.50	546.0	1.29	240	23.1	1.96	2.35	2.755
bx_76	36.39941	-121.90815	14.85	0.50	610.0	1.42	284	21.9	2.32	2.72	2.708
bx_77	36.41710	-121.91702	7.99	0.40	120.4	0.48	286	15.0	2.33	2.38	3.362
bx_78	36.41718	-121.91717	9.55	0.30	127.1	0.41	302	17.0	2.42	2.46	3.358
bx_79	36.41743	-121.91625	12.15	0.30	43.6	0.32	243	18.1	1.98	2.01	3.439
bx_80	36.41744	-121.91624	11.68	0.30	43.2	0.31	243	17.7	1.98	2.01	3.440
bx_81	36.41814	-121.91564	11.16	0.30	51.1	0.32	252	17.4	2.06	2.08	3.532
bx_82	36.41842	-121.91563	10.30	0.30	80.0	0.35	273	17.0	2.23	2.25	3.552
bx_83	36.41717	-121.91663	8.75	0.50	89.4	0.54	257	15.1	2.10	2.16	3.394
bx_84	36.41849	-121.91557	10.43	0.40	26.5	0.40	274	17.2	2.24	2.27	3.561
bx_85	36.41847	-121.91560	10.00	0.40	29.2	0.41	275	16.8	2.24	2.28	3.558
bx_86	36.41908	-121.91523	10.35	0.40	45.9	0.41	310	17.9	2.42	2.46	3.626
bx_87	36.41922	-121.91520	11.50	0.40	62.1	0.42	322	19.2	2.43	2.46	3.639
bx_88	36.42027	-121.91496	12.45	0.40	62.5	0.42	413	21.4	2.46	2.50	3.730
bx_89	36.42143	-121.91494	12.99	0.40	67.7	0.43	477	22.5	2.48	2.52	3.814
bx_90	36.42112	-121.91498	12.60	0.60	76.9	0.62	495	22.3	2.49	2.57	3.790
bx_91	36.42243	-121.91477	11.55	0.50	38.6	0.51	399	20.4	2.46	2.51	3.897
bx_92	36.42280	-121.91470	12.36	0.50	79.8	0.53	372	20.9	2.46	2.52	3.929
bx_93	36.42661	-121.91562	9.75	0.50	157.2	0.61	234	15.5	1.91	2.00	4.137
bx_94	36.42691	-121.91593	10.61	0.50	201.1	0.67	252	16.8	2.06	2.16	4.137
bx_95	36.42650	-121.91483	11.77	0.50	109.0	0.55	165	15.8	1.35	1.46	4.185
bx_96	36.42615	-121.91450	10.44	0.50	63.8	0.52	138	13.8	1.13	1.24	4.182
bx_97	36.42581	-121.91438	9.64	0.50	25.4	0.50	141	13.1	1.15	1.26	4.166
bx_98	36.42543	-121.91436	9.60	0.50	18.7	0.50	163	13.6	1.33	1.42	4.140
bx_99	36.42525	-121.91436	9.00	0.50	37.5	0.51	177	13.4	1.44	1.53	4.127
bx_100	36.43073	-121.91895	14.28	0.80	246.4	0.96	124	17.3	1.01	1.40	4.204
bx_101	36.43071	-121.91895	15.88	0.80	250.2	0.97	123	18.9	1.00	1.39	4.202
bx_102	36.43148	-121.91822	16.05	0.80	162.3	0.88	75	17.9	0.61	1.07	4.307
bx_103	36.43061	-121.91889	15.77	0.80	259.9	0.98	118	18.7	0.96	1.37	4.199
bx_104	36.43665	-121.92007	22.37	0.60	47.7	0.61	66	24.0	0.54	0.81	4.550
bx_105	36.43518	-121.91972	21.04	0.80	158.6	0.87	95	23.4	0.78	1.17	4.469
bx_106	36.43678	-121.92097	13.04	0.90	82.1	0.92	142	16.5	1.16	1.48	4.497
bx_107	36.43678	-121.92095	14.20	0.90	79.6	0.92	140	17.7	1.14	1.46	4.498
bx_108	36.43876	-121.92208	15.38	1.00	64.5	1.01	184	19.9	1.50	1.81	4.563
bx_109	36.43901	-121.92231	14.75	0.80	44.1	0.81	179	19.2	1.46	1.67	4.565
bx_110	36.43904	-121.92193	14.60	0.80	15.2	0.80	152	18.3	1.24	1.48	4.592
bx_111	36.43859	-121.92208	14.07	0.80	44.6	0.81	199	19.0	1.62	1.81	4.550
bx_112	36.44053	-121.92395	10.67	0.50	218.0	0.69	218	16.0	1.78	1.91	4.560
bx_113	36.44119	-121.92393	12.58	0.50	145.3	0.59	187	17.2	1.53	1.64	4.609
bx_114	36.44125	-121.92397	9.90	0.50	139.1	0.59	185	14.5	1.51	1.62	4.611
bx_115	36.44166	-121.92338	12.18	0.50	100.6	0.55	116	15.0	0.95	1.09	4.680
bx_116	36.44207	-121.92371	14.31	0.50	48.1	0.51	116	17.2	0.95	1.08	4.687
bx_117	36.44247	-121.92394	13.06	0.50	16.4	0.50	110	15.8	0.90	1.03	4.700
bx_118	36.44414	-121.92527	18.73	0.60	164.8	0.70	163	22.7	1.33	1.50	4.728
bx_119	36.44368	-121.92470	16.62	0.60	94.0	0.63	120	19.6	0.98	1.17	4.735
bx_120	36.44315	-121.92422	16.37	0.50	32.3	0.51	98	18.8	0.80	0.95	4.729
bx_121	36.44326	-121.92455	14.07	0.60	61.5	0.62	118	17.0	0.96	1.14	4.715
bx_122	36.44851	-121.92827	11.27	0.50	177.6	0.63	166	15.4	1.35	1.49	4.834
bx_123	36.44814	-121.92883	12.51	0.50	209.9	0.68	226	18.1	1.84	1.96	4.770
bx_124	36.44820	-121.92869	12.42	0.50	199.5	0.66	214	17.7	1.75	1.87	4.784
bx_125	36.44839	-121.92794	14.07	0.50	144.2	0.59	166	18.2	1.35	1.48	4.848
bx_126	36.44827	-121.92861	10.56	0.50	194.5	0.66	204	15.6	1.66	1.79	4.794
bx_127	36.44846	-121.92717	9.85	0.50	97.2	0.54	98	12.3	0.80	0.97	4.906
bx_128	36.44852	-121.92738	10.07	0.50	113.8	0.56	115	12.9	0.94	1.09	4.896
bx_129	36.44841	-121.92795	17.02	0.50	145.5	0.59	164	21.1	1.34	1.46	4.849
bx_130	36.44779	-121.92696	11.58	0.50	43.1	0.51	104	14.1	0.85	0.99	4.873
bx_131	36.44740	-121.92688	11.68	0.60	50.8	0.61	121	14.7	0.99	1.16	4.851
bx_132	36.44757	-121.92687	10.97	0.60	38.4	0.61	110	13.7	0.90	1.08	4.863
bx_133	36.44728	-121.92704	9.88	0.60	70.3	0.62	141	13.4	1.15	1.31	4.830
bx_134	36.44804	-121.92881	12.01	0.60	44.1	0.61	235	17.8	1.92	2.01	4.764
bx_135	36.44833	-121.92886	12.48	0.60	11.5	0.60	209	17.6	1.71	1.81	4.781
bx_136	36.44777	-121.92701	11.79	0.50	182.4	0.64	109	14.5	0.89	1.10	4.868
bx_137	36.44778	-121.92703	10.68	0.50	182.3	0.64	111	13.4	0.91	1.11	4.867
bx_138	36.44699	-121.92687	10.62	0.50	239.6	0.72	144	14.2	1.17	1.38	4.821

Survey station	Latitude (WGS84)	Longitude (WGS84)	Meas. terrace height (m)	GPS vert. unc. 1σ (m)	Horiz. offset (m)	Meas. vert. unc. 1σ (m)	Dist. to inner edge (m)	Model terrace height (m)	Model unc. 1σ (m)	Total vert. unc. 1σ (m)	Dist. to SGHF (km)
bx_139	36.44835	-121.92791	14.00	0.50	88.6	0.54	166	18.1	1.35	1.46	4.847
bx_140	36.44827	-121.92691	10.99	0.50	179.3	0.64	82	13.0	0.67	0.92	4.910
bx_141	36.44868	-121.92944	13.43	0.50	38.8	0.51	205	18.5	1.67	1.75	4.766
bx_142	36.44853	-121.92936	13.14	0.50	25.4	0.50	213	18.4	1.74	1.81	4.761
bx_143	36.44889	-121.92920	11.93	0.60	12.6	0.60	174	16.2	1.42	1.54	4.797
bx_144	36.44916	-121.92909	11.81	0.70	19.8	0.70	146	15.4	1.19	1.38	4.824
bx_145	36.44935	-121.92936	11.97	0.60	39.2	0.61	152	15.7	1.24	1.38	4.820
bx_146	36.45002	-121.92900	12.64	0.70	97.3	0.73	84	14.7	0.69	1.00	4.892
bx_147	36.45219	-121.92932	12.70	1.20	108.1	1.22	110	15.4	0.90	1.52	5.025
bx_148	36.45278	-121.92959	14.41	0.60	162.9	0.70	146	18.0	1.19	1.38	5.049
bx_149	36.45344	-121.92788	14.95	0.90	51.9	0.91	87	17.1	0.71	1.15	5.213
bx_150	36.45330	-121.92755	22.60	0.90	23.8	0.90	56	24.0	0.46	1.01	5.225
bx_151	36.45344	-121.92819	17.55	0.90	70.9	0.91	104	20.1	0.85	1.25	5.192
bx_152	36.45358	-121.92689	24.29	0.50	48.7	0.51	83	26.3	0.68	0.85	5.291
bx_153	36.45376	-121.92689	24.73	1.70	64.3	1.71	101	27.2	0.82	1.89	5.304
bx_154	36.45504	-121.92562	10.77	0.80	177.8	0.89	274	17.5	2.24	2.41	5.483
bx_155	36.45574	-121.92598	9.90	0.80	259.9	0.98	313	17.5	2.42	2.62	5.508
bx_156	36.45473	-121.92522	12.19	0.80	141.5	0.86	255	18.5	2.08	2.25	5.487
bx_157	36.45445	-121.92513	11.95	0.80	111.7	0.84	231	17.6	1.88	2.06	5.474
bx_158	36.45411	-121.92532	11.97	0.80	73.3	0.82	191	16.7	1.56	1.76	5.437
bx_159	36.45381	-121.92558	14.17	0.80	64.7	0.81	149	17.8	1.22	1.46	5.397
bx_160	36.45389	-121.92584	13.02	0.80	82.4	0.82	148	16.7	1.21	1.46	5.386
bx_161	36.45379	-121.92659	18.18	0.70	150.0	0.77	113	21.0	0.92	1.20	5.326
bx_162	36.45388	-121.92610	14.38	0.70	104.5	0.74	138	17.8	1.13	1.35	5.367
bx_163	36.45613	-121.92582	9.73	0.60	35.1	0.61	292	16.9	2.38	2.46	5.547
bx_164	36.45610	-121.92572	9.17	0.60	26.5	0.60	283	16.1	2.31	2.39	5.551
bx_165	36.45622	-121.92528	11.24	0.50	16.0	0.50	243	17.2	1.98	2.04	5.590
bx_166	36.45650	-121.92512	11.95	0.50	48.6	0.51	228	17.6	1.86	1.93	5.621
bx_168	36.45616	-121.92545	12.06	0.60	4.2	0.60	259	18.4	2.11	2.20	5.574
bx_169	36.45846	-121.92581	9.68	0.50	259.0	0.76	233	15.4	1.90	2.05	5.713
bx_170	36.45848	-121.92584	8.91	0.50	261.8	0.76	234	14.7	1.91	2.05	5.713
bx_171	36.45967	-121.92601	9.88	0.50	395.0	1.00	217	15.2	1.77	2.03	5.786
bx_172	36.45982	-121.92674	8.47	0.50	425.0	1.05	274	15.2	2.24	2.47	5.748
bx_173	36.46092	-121.92750	7.83	0.50	562.0	1.32	240	13.7	1.96	2.36	5.773
bx_174	36.46249	-121.92825	11.18	0.40	179.0	0.56	222	16.7	1.81	1.90	5.834
bx_175	36.46258	-121.92825	8.14	0.40	170.5	0.55	219	13.5	1.79	1.87	5.840
bx_176	36.46383	-121.92853	10.70	0.40	72.2	0.43	224	16.2	1.83	1.88	5.910
bx_177	36.46381	-121.92872	10.14	0.40	88.2	0.44	241	16.1	1.97	2.02	5.896
bx_178	36.46227	-121.92830	12.49	0.50	207.2	0.67	233	18.2	1.90	2.02	5.815
bx_179	36.46266	-121.92818	9.14	0.40	166.9	0.54	211	14.3	1.72	1.80	5.851
bx_180	36.46424	-121.92898	8.91	0.40	36.8	0.41	266	15.5	2.17	2.21	5.909
bx_181	36.46661	-121.93006	7.79	0.30	305.6	0.73	268	14.4	2.19	2.31	6.005
bx_182	36.46671	-121.92975	7.01	0.30	304.0	0.73	258	13.4	2.10	2.23	6.033
bx_183	36.46528	-121.92912	12.25	0.30	137.5	0.42	281	19.2	2.29	2.33	5.974
bx_184	36.46602	-121.92951	8.30	0.30	226.5	0.58	271	15.0	2.21	2.29	6.000
bx_185	36.46674	-121.93115	9.40	0.30	367.0	0.86	252	15.6	2.06	2.23	5.939
bx_186	36.46791	-121.93170	12.45	0.30	503.0	1.14	131	15.7	1.07	1.56	5.985
bx_187	36.46107	-121.92754	12.66	0.40	352.0	0.87	230	18.3	1.88	2.07	5.781
bx_188	36.46680	-121.93117	10.86	0.30	318.0	0.76	244	16.9	1.99	2.13	5.942
bx_189	36.46864	-121.93331	10.97	0.30	44.8	0.32	118	13.9	0.96	1.01	5.927
bx_190	36.46940	-121.93386	13.30	0.30	53.7	0.32	114	16.1	0.93	0.98	5.943
bx_191	36.49352	-121.94195	8.41	0.50	32.5	0.51	37	9.3	0.30	0.59	7.112
bx_192	36.49378	-121.94194	9.86	0.50	60.2	0.52	62	11.4	0.51	0.72	7.131
bx_193	36.49319	-121.94250	8.85	0.50	54.0	0.51	53	10.2	0.43	0.67	7.051
bx_194	36.49270	-121.94309	9.18	0.50	121.7	0.57	53	10.5	0.43	0.71	6.975
bx_195	36.49289	-121.94349	8.56	0.50	147.6	0.60	48	9.7	0.39	0.71	6.961
bx_196	36.49271	-121.94328	9.38	0.50	136.4	0.58	46	10.5	0.38	0.69	6.963
bx_197	36.48931	-121.94435	13.57	0.60	423.0	1.10	95	15.9	0.78	1.35	6.647
bx_198	36.48929	-121.94438	13.94	0.60	426.0	1.11	99	16.4	0.81	1.37	6.643
bx_199	36.50718	-121.94179	13.22	1.00	673.0	1.78	207	18.3	1.69	2.45	8.098
bx_200	36.50183	-121.93967	8.39	0.80	124.3	0.85	85	10.5	0.69	1.09	7.862
bx_201	36.50140	-121.93938	8.39	0.80	101.8	0.83	41	9.4	0.33	0.90	7.851
bxc_1	36.36901	-121.90277	71.56	0.90	378.0	1.22	93	73.9	0.76	1.44	0.906
bxc_2	36.36888	-121.90294	66.26	0.90	394.0	1.25	112	69.0	0.91	1.54	0.885
bxc_4	36.37245	-121.90488	71.17	0.70	422.0	1.16	98	73.6	0.80	1.41	1.007
bxc_5	36.36273	-121.90351	67.90	0.70	680.0	1.64	380	76.6	2.46	2.96	0.407
bxc_6	36.36189	-121.90471	65.56	0.60	790.0	1.83	338	73.6	2.43	3.04	0.264

Survey station	Latitude (WGS84)	Longitude (WGS84)	Meas. terrace height (m)	GPS vert. unc. 1σ (m)	Horiz. offset (m)	Meas. vert. unc. 1σ (m)	Dist. to inner edge (m)	Model terrace height (m)	Model unc. 1σ (m)	Total vert. unc. 1σ (m)	Dist. to SGHF (km)
bxc_7	36.36276	-121.90377	70.16	0.70	679.0	1.64	394	79.0	2.46	2.96	0.391
bxc_8	36.35913	-121.90417	66.44	1.20	107.8	1.22	66	68.1	0.54	1.34	0.102
bxc_9	36.35775	-121.90616	46.87	1.30	333.4	1.49	161	50.8	1.31	1.99	-0.132
bxc_10	36.36119	-121.90448	67.59	0.60	249.1	0.81	262	74.0	2.14	2.29	0.230
bxc_11	36.35750	-121.90574	52.60	1.10	316.8	1.30	124	55.7	1.01	1.65	-0.122
bxc_12	36.35604	-121.90539	58.65	0.80	263.2	0.99	143	62.2	1.17	1.53	-0.203
bxc_13	36.35613	-121.90618	57.31	0.80	352.0	1.11	200	62.2	1.63	1.97	-0.251
bxc_15	36.35605	-121.90570	62.46	0.80	308.9	1.05	167	66.6	1.36	1.72	-0.224
bxc_16	36.33867	-121.89270	26.30	0.90	761.0	1.89	50	27.5	0.41	1.93	-0.596
bxc_17	36.33619	-121.89381	14.45	0.90	282.0	1.09	113	17.2	0.92	1.43	-0.851
bxc_18	36.33581	-121.89364	16.51	0.90	303.0	1.12	119	19.4	0.97	1.48	-0.868
bxc_19	36.33623	-121.89364	14.84	0.90	268.9	1.07	98	17.3	0.80	1.34	-0.837
bxc_20	36.32712	-121.89637	18.92	0.90	342.0	1.17	186	23.5	1.52	1.92	-1.732
bxc_21	36.32676	-121.89568	18.23	0.90	272.6	1.08	121	21.2	0.99	1.46	-1.730
bxc_22	36.32654	-121.89542	18.80	0.80	240.2	0.96	102	21.3	0.83	1.27	-1.738
bxc_23	36.32361	-121.89598	13.79	1.10	232.4	1.21	192	18.5	1.57	1.98	-2.045
bxc_24	36.32094	-121.89440	14.80	1.30	150.0	1.34	125	17.9	1.02	1.68	-2.242
bxc_26	36.31802	-121.89418	19.86	1.10	182.0	1.17	163	23.9	1.33	1.77	-2.519
lc_1	36.00841	-121.51889	30.73	0.50	345.0	0.90	14	31.1	0.11	0.91	4.888
lc_2	36.00810	-121.51924	31.47	0.60	345.0	0.96	23	32.0	0.19	0.98	4.842
lc_3	35.78106	-121.33301	81.97	0.70	345.0	1.03	302	89.4	2.42	2.63	0.322
lc_4	35.78117	-121.33146	91.55	0.70	345.0	1.03	201	96.5	1.64	1.94	0.431
lc_5	35.78112	-121.33213	86.95	0.80	345.0	1.10	250	93.1	2.04	2.32	0.384
lc_6	35.75690	-121.31983	15.85	0.70	345.0	1.03	119	18.8	0.97	1.41	-0.744
lc_7	35.75777	-121.32255	15.45	0.70	345.0	1.03	255	21.7	2.08	2.32	-0.844
lc_8	35.75735	-121.32402	18.74	0.80	345.0	1.10	394	27.5	2.46	2.70	-0.971
lc_9	35.76360	-121.32422	29.28	0.50	345.0	0.90	432	38.4	2.47	2.63	-0.483
lc_10	35.76364	-121.32366	31.07	0.50	345.0	0.90	402	39.9	2.46	2.62	-0.445
lc_11	35.76337	-121.32351	32.10	0.50	345.0	0.90	370	40.7	2.46	2.62	-0.457
lc_12	35.88850	-121.46313	51.63	0.40	345.0	0.85	172	55.9	1.40	1.64	1.431
lc_13	35.88637	-121.46177	44.93	0.50	345.0	0.90	137	48.3	1.12	1.44	1.403
lc_14	35.91479	-121.47146	39.39	0.30	345.0	0.81	222	44.9	1.81	1.98	2.418
lc_15	35.91528	-121.47218	33.57	0.30	345.0	0.81	276	40.4	2.25	2.39	2.394
lc_16	35.91461	-121.47102	39.80	0.30	345.0	0.81	194	44.6	1.58	1.78	2.440
lc_17	35.91353	-121.46981	41.54	0.30	345.0	0.81	152	45.3	1.24	1.48	2.465
lc_18	35.91320	-121.46977	42.34	0.30	345.0	0.81	172	46.6	1.40	1.62	2.447
lc_19	35.91321	-121.46977	42.75	0.30	345.0	0.81	172	47.0	1.40	1.62	2.448
lc_20	35.91195	-121.46978	38.54	0.30	345.0	0.81	248	44.7	2.02	2.18	2.370
lc_21	35.91234	-121.46961	39.95	0.20	345.0	0.78	214	45.2	1.75	1.91	2.407
lc_22	35.91265	-121.46959	40.99	0.20	345.0	0.78	191	45.7	1.56	1.74	2.427
lc_23	35.91310	-121.46969	42.66	0.20	345.0	0.78	169	46.8	1.38	1.58	2.448
lc_24	35.91976	-121.47439	16.51	0.60	345.0	0.96	607	27.2	2.56	2.74	2.503
lc_25	35.91979	-121.47389	14.68	0.60	345.0	0.96	573	25.1	2.53	2.71	2.542
lc_26	35.92196	-121.46874	21.38	0.50	345.0	0.90	337	29.4	2.43	2.60	3.062
lc_27	35.92259	-121.46840	23.92	0.40	345.0	0.85	305	31.4	2.42	2.57	3.127
lc_28	35.92663	-121.46815	34.18	0.40	345.0	0.85	210	39.4	1.71	1.91	3.393
lc_29	35.93858	-121.47602	13.65	0.60	345.0	0.96	523	23.6	2.50	2.68	3.535
lc_30	35.93771	-121.47619	11.84	0.70	345.0	1.03	580	22.3	2.54	2.74	3.468
lc_31	35.93814	-121.47617	10.85	0.70	345.0	1.03	555	21.1	2.52	2.72	3.497
lc_32	35.94235	-121.47813	9.87	0.70	345.0	1.03	482	19.5	2.48	2.69	3.607
lc_33	35.94276	-121.47820	10.98	0.90	345.0	1.17	465	20.4	2.48	2.74	3.628
lc_34	35.94312	-121.47896	6.83	1.30	345.0	1.50	511	16.7	2.50	2.91	3.592
lc_35	36.00756	-121.51939	31.86	1.00	345.0	1.25	76	33.7	0.62	1.40	4.796
lc_36	36.02186	-121.56967	12.18	0.70	345.0	1.03	82	14.2	0.67	1.23	2.107
lc_37	36.02190	-121.57022	10.50	0.80	345.0	1.10	101	13.0	0.82	1.37	2.070
lc_38	36.03535	-121.57903	18.63	1.30	345.0	1.50	64	20.2	0.52	1.59	2.336
lc_39	36.15335	-121.66787	33.61	0.60	345.0	0.96	119	36.5	0.97	1.37	2.839
lc_40	36.15362	-121.66806	32.79	0.60	345.0	0.96	106	35.4	0.87	1.29	2.836
my_3	36.61113	-121.89626	3.09	0.10	133.7	0.31	136	6.4	1.11	1.15	18.641
my_4	36.61363	-121.89653	5.36	0.10	410.0	0.90	220	10.8	1.79	2.01	18.801
my_5	36.61371	-121.89643	4.60	0.10	418.0	0.92	232	10.3	1.89	2.10	18.814
my_6	36.61404	-121.89706	5.01	0.50	153.8	0.60	195	9.8	1.59	1.70	18.794
my_7	36.61535	-121.89863	6.08	0.10	0.0	0.10	210	11.3	1.71	1.72	18.780
my_24	36.62087	-121.90669	3.28	1.00	138.1	1.04	107	5.9	0.87	1.36	18.623
my_25	36.62121	-121.90732	3.42	1.00	171.8	1.07	126	6.5	1.03	1.48	18.604
my_26	36.62141	-121.90762	3.81	1.00	194.0	1.09	135	7.1	1.10	1.55	18.598
my_27	36.62052	-121.90594	4.25	1.00	130.6	1.04	86	6.4	0.70	1.25	18.649

Survey station	Latitude (WGS84)	Longitude (WGS84)	Meas. terrace height (m)	GPS vert. unc. 1σ (m)	Horiz. offset (m)	Meas. vert. unc. 1σ (m)	Dist. to inner edge (m)	Model terrace height (m)	Model unc. 1σ (m)	Total vert. unc. 1σ (m)	Dist. to SGHF (km)
my_28	36.62145	-121.90792	4.30	1.00	220.0	1.11	128	7.5	1.04	1.52	18.580
my_29	36.62155	-121.90913	6.39	0.90	327.0	1.15	109	9.1	0.89	1.45	18.504
my_30	36.62103	-121.90915	3.34	0.70	0.0	0.70	52	4.6	0.42	0.82	18.466
my_31	36.62123	-121.90792	4.42	1.00	112.4	1.03	106	7.0	0.87	1.34	18.565
my_33	36.62166	-121.90991	5.64	1.40	97.5	1.42	107	8.3	0.87	1.66	18.458
my_34	36.62201	-121.91036	4.00	0.90	0.0	0.90	145	7.6	1.18	1.49	18.453
my_35	36.62303	-121.91161	6.08	1.20	101.7	1.22	258	12.4	2.10	2.43	18.440
my_36	36.62261	-121.91139	5.94	1.00	52.9	1.01	219	11.3	1.79	2.05	18.425
my_37	36.62227	-121.91114	6.94	1.00	14.5	1.00	187	11.5	1.53	1.82	18.419
my_38	36.62216	-121.91052	8.02	1.00	42.5	1.00	163	12.0	1.33	1.67	18.453
my_39	36.62325	-121.91238	8.08	0.60	209.0	0.75	240	14.0	1.96	2.10	18.404
my_40	36.62308	-121.91341	7.96	0.50	120.7	0.57	148	11.6	1.21	1.33	18.321
my_41	36.62317	-121.91415	8.09	0.70	54.2	0.71	92	10.4	0.75	1.03	18.277
my_42	36.62364	-121.91464	6.65	0.80	30.9	0.80	74	8.5	0.60	1.00	18.277
my_43	36.62413	-121.91499	6.02	0.50	23.6	0.50	81	8.0	0.66	0.83	18.288
my_44	36.62425	-121.91524	5.07	0.50	15.8	0.50	76	6.9	0.62	0.80	18.279
my_45	36.62642	-121.91494	7.23	0.50	258.1	0.75	280	14.1	2.28	2.41	18.454
my_46	36.62645	-121.91480	6.72	0.70	263.5	0.91	290	13.9	2.37	2.53	18.467
my_47	36.62665	-121.91652	5.43	1.50	0.0	1.50	260	11.8	2.12	2.60	18.363
my_50	36.62684	-121.91772	5.47	1.20	109.2	1.22	224	11.0	1.83	2.20	18.294
my_51	36.62736	-121.91807	6.62	1.20	159.0	1.25	249	12.8	2.03	2.38	18.308
my_52	36.62795	-121.91894	6.66	1.30	260.5	1.42	253	12.9	2.06	2.50	18.290
my_53	36.62759	-121.91931	3.63	0.80	64.2	0.81	201	8.6	1.64	1.83	18.239
my_54	36.62760	-121.92010	5.61	0.90	10.9	0.90	164	9.7	1.34	1.61	18.186
my_55	36.62803	-121.92032	4.84	0.90	62.3	0.91	193	9.6	1.57	1.82	18.201
my_56	36.63200	-121.92211	5.37	0.50	0.0	0.50	155	9.2	1.26	1.36	18.362
my_57	36.63123	-121.92203	7.29	0.50	84.8	0.53	127	10.4	1.04	1.17	18.313
my_58	36.62997	-121.92081	6.73	0.50	253.0	0.75	190	11.4	1.55	1.72	18.307
my_59	36.63379	-121.92307	4.86	0.50	170.5	0.62	167	9.0	1.36	1.50	18.425
my_60	36.63571	-121.92795	4.08	0.50	35.0	0.51	187	8.7	1.53	1.61	18.228
my_61	36.63553	-121.92751	4.30	0.50	75.3	0.53	187	8.9	1.53	1.61	18.245
my_62	36.63568	-121.92614	4.87	0.50	183.7	0.64	226	10.4	1.84	1.95	18.350
my_63	36.63633	-121.92858	6.03	0.50	27.2	0.50	231	11.7	1.88	1.95	18.229
my_64	36.63654	-121.92922	5.33	0.50	38.9	0.51	236	11.1	1.93	1.99	18.200
my_65	36.63703	-121.92965	4.81	0.50	104.3	0.55	278	11.7	2.27	2.33	18.206
my_66	36.63812	-121.92994	3.54	0.50	222.0	0.70	397	12.4	2.46	2.56	18.264
my_67	36.63737	-121.93411	5.11	0.50	50.4	0.51	372	13.7	2.46	2.51	17.926
my_68	36.63723	-121.93462	5.30	0.50	30.5	0.50	373	13.9	2.46	2.51	17.880
my_69	36.63825	-121.93696	4.57	0.50	223.0	0.70	560	14.9	2.53	2.62	17.793
my_70	36.63859	-121.93681	4.94	0.50	227.5	0.70	586	15.5	2.54	2.64	17.828
my_71	36.63568	-121.93726	4.77	0.40	110.4	0.47	358	13.1	2.45	2.49	17.589
my_74	36.63489	-121.93909	4.95	0.40	108.1	0.46	446	14.2	2.47	2.51	17.408
my_75	36.63482	-121.94041	4.60	0.40	225.8	0.64	555	14.9	2.52	2.60	17.312
my_76	36.63323	-121.93876	4.55	0.50	0.0	0.50	362	13.0	2.45	2.50	17.311
my_77	36.63114	-121.93748	4.80	0.20	149.9	0.38	229	10.4	1.87	1.91	17.250
my_78	36.63008	-121.93684	4.36	0.20	277.7	0.64	148	8.0	1.21	1.37	17.218
my_79	36.63212	-121.93845	3.62	0.20	12.0	0.20	318	11.3	2.43	2.43	17.253
my_80	36.63177	-121.93774	4.69	0.20	86.3	0.28	252	10.9	2.06	2.07	17.277
my_81	36.63117	-121.93747	4.74	0.20	147.6	0.38	228	10.4	1.86	1.90	17.253
my_82	36.63270	-121.93858	4.10	0.20	59.9	0.24	334	12.0	2.43	2.44	17.286
my_83	36.62835	-121.93777	5.51	0.40	83.1	0.44	134	8.8	1.09	1.18	17.030
my_84	36.63060	-121.93723	5.06	0.40	171.8	0.55	206	10.1	1.68	1.77	17.228
my_85	36.63057	-121.93711	4.77	0.40	172.1	0.55	196	9.6	1.60	1.69	17.234
my_86	36.62958	-121.93762	3.27	0.40	53.6	0.42	183	7.8	1.49	1.55	17.128
my_87	36.62671	-121.93911	4.33	0.40	294.0	0.76	231	10.0	1.88	2.03	16.821
my_88	36.62664	-121.93885	6.21	0.40	292.0	0.75	209	11.4	1.71	1.86	16.834
my_89	36.62340	-121.94109	6.18	0.60	0.0	0.60	326	14.0	2.43	2.50	16.450
my_90	36.62599	-121.93945	6.00	0.70	323.0	0.99	280	12.9	2.28	2.49	16.747
my_91	36.62589	-121.93935	4.98	0.70	317.0	0.98	267	11.6	2.18	2.39	16.746
my_92	36.62453	-121.94015	5.86	0.70	151.3	0.77	283	12.8	2.31	2.43	16.595
my_93	36.62419	-121.94011	5.99	0.70	124.0	0.75	269	12.6	2.19	2.32	16.573
my_94	36.62397	-121.94011	5.88	0.70	107.6	0.74	261	12.3	2.13	2.25	16.557
my_95	36.62220	-121.94141	5.68	0.40	60.6	0.42	353	13.9	2.44	2.48	16.342
my_96	36.61198	-121.94668	6.33	0.40	75.4	0.43	294	13.6	2.40	2.44	15.251
my_97	36.61288	-121.94616	8.64	0.40	184.5	0.57	254	14.9	2.07	2.15	15.351
my_98	36.61348	-121.94593	6.07	0.40	252.0	0.68	260	12.5	2.12	2.23	15.409
my_99	36.60674	-121.95883	6.55	0.50	0.0	0.50	341	14.6	2.44	2.49	14.046

Survey station	Latitude (WGS84)	Longitude (WGS84)	Meas. terrace height (m)	GPS vert. unc. 1σ (m)	Horiz. offset (m)	Meas. vert. unc. 1σ (m)	Dist. to inner edge (m)	Model terrace height (m)	Model unc. 1σ (m)	Total vert. unc. 1σ (m)	Dist. to SGHF (km)
my_100	36.60781	-121.95835	7.10	0.50	125.5	0.57	373	15.7	2.46	2.53	14.154
my_101	36.60916	-121.95830	6.50	0.50	273.0	0.78	456	15.9	2.47	2.59	14.255
my_102	36.60226	-121.96088	9.77	0.60	58.9	0.61	233	15.5	1.90	2.00	13.585
my_103	36.60150	-121.96091	6.81	0.50	30.4	0.50	206	11.9	1.68	1.75	13.529
my_104	36.59411	-121.96241	10.17	0.70	0.0	0.70	135	13.5	1.10	1.31	12.898
my_105	36.59426	-121.96193	10.20	0.70	45.9	0.71	102	12.7	0.83	1.09	12.942
my_106	36.59368	-121.96247	9.58	0.70	48.3	0.71	122	12.6	1.00	1.22	12.863
my_107	36.59240	-121.96294	10.70	0.70	196.0	0.82	172	14.9	1.40	1.63	12.739
my_108	36.59206	-121.96348	8.93	1.20	246.8	1.32	228	14.6	1.86	2.28	12.679
my_109	36.58805	-121.96409	7.68	0.70	0.0	0.70	120	10.6	0.98	1.20	12.350
my_110	36.58841	-121.96364	7.47	0.60	56.8	0.61	106	10.1	0.87	1.06	12.406
my_111	36.58992	-121.96368	7.85	0.60	211.7	0.76	219	13.2	1.79	1.94	12.512
my_112	36.59005	-121.96380	9.24	0.50	224.0	0.70	236	15.1	1.93	2.05	12.513
my_113	36.58753	-121.96421	7.38	0.60	58.1	0.61	127	10.5	1.04	1.20	12.305
my_114	36.58345	-121.96739	8.81	0.80	236.8	0.95	56	10.2	0.46	1.06	11.796
my_118	36.58365	-121.97108	7.37	0.70	225.7	0.86	200	12.3	1.63	1.84	11.557
my_119	36.58291	-121.97126	6.84	0.70	186.1	0.81	130	10.0	1.06	1.33	11.492
my_120	36.57663	-121.97555	7.20	0.60	46.4	0.61	246	13.3	2.01	2.10	10.750
my_121	36.57669	-121.97562	7.89	0.60	46.8	0.61	251	14.1	2.05	2.14	10.749
my_123	36.57719	-121.97350	7.19	0.70	121.0	0.75	54	8.5	0.44	0.87	10.930
my_124	36.57657	-121.97141	6.96	0.60	309.0	0.90	94	9.3	0.77	1.18	11.029
my_125	36.57583	-121.97131	8.66	0.60	340.0	0.95	32	9.4	0.26	0.99	10.983
my_126	36.57638	-121.97226	8.37	0.60	239.0	0.80	17	8.8	0.14	0.81	10.957
my_130	36.56146	-121.95479	9.47	0.50	74.5	0.53	94	11.8	0.77	0.93	11.087
my_131	36.56724	-121.95031	5.46	0.60	12.6	0.60	113	8.2	0.92	1.10	11.806
my_133	36.56711	-121.95046	5.26	0.50	13.7	0.50	113	8.0	0.92	1.05	11.787
my_135	36.56644	-121.95115	5.03	0.50	108.1	0.55	45	6.1	0.37	0.66	11.692
my_136	36.56594	-121.95066	3.03	0.50	144.9	0.59	76	4.9	0.62	0.86	11.690
my_137	36.56451	-121.95051	3.57	0.50	302.0	0.83	114	6.4	0.93	1.24	11.598
my_138	36.56277	-121.95054	8.49	0.40	496.0	1.15	81	10.5	0.66	1.33	11.471
my_139	36.56714	-121.94685	5.25	0.40	322.9	0.81	97	7.6	0.79	1.13	12.036
my_140	36.56639	-121.94498	4.78	0.40	499.0	1.16	127	7.9	1.04	1.56	12.111
my_141	36.56116	-121.93459	7.31	0.40	0.0	0.40	71	9.1	0.58	0.70	12.448
my_142	36.56108	-121.93384	8.39	0.40	67.8	0.43	70	10.1	0.57	0.71	12.493
my_146	36.56020	-121.93284	7.00	0.40	21.7	0.40	69	8.7	0.56	0.69	12.499
my_147	36.55901	-121.93214	6.04	0.50	34.8	0.51	70	7.8	0.57	0.76	12.462
my_148	36.55857	-121.93187	5.52	0.40	58.3	0.42	56	6.9	0.46	0.62	12.449
my_149	36.54485	-121.93110	4.69	0.50	27.4	0.50	107	7.3	0.87	1.01	11.522
my_150	36.54483	-121.93092	4.80	0.40	34.3	0.41	100	7.3	0.82	0.91	11.533
my_151	36.54495	-121.93140	4.17	0.40	30.9	0.41	126	7.3	1.03	1.11	11.508
my_152	36.54469	-121.93158	4.62	0.40	29.1	0.41	103	7.2	0.84	0.93	11.478
my_153	36.54456	-121.93189	4.20	0.40	33.9	0.41	99	6.6	0.81	0.90	11.447
my_154	36.54441	-121.93263	4.03	0.40	88.3	0.44	105	6.6	0.86	0.97	11.386
my_156	36.54240	-121.93289	6.16	0.70	49.4	0.71	58	7.6	0.47	0.85	11.224
my_157	36.54275	-121.93307	5.68	0.80	9.6	0.80	79	7.6	0.64	1.03	11.237
my_158	36.54324	-121.93313	6.33	0.90	50.5	0.91	89	8.5	0.73	1.16	11.268
my_159	36.54437	-121.93331	3.88	0.60	0.0	0.60	142	7.4	1.16	1.30	11.336
my_160	36.54371	-121.93319	4.80	0.50	74.9	0.53	101	7.3	0.82	0.98	11.298
my_161	36.54429	-121.93308	4.70	0.50	22.9	0.50	120	7.7	0.98	1.10	11.346
my_162	36.54445	-121.93281	4.18	0.50	46.1	0.51	117	7.1	0.95	1.08	11.377
my_163	36.53992	-121.93242	5.01	0.50	50.5	0.51	101	7.5	0.82	0.97	11.080
my_164	36.54067	-121.93248	5.53	0.50	132.7	0.58	41	6.5	0.33	0.67	11.129
my_165	36.53952	-121.93207	5.69	0.50	42.5	0.51	120	8.6	0.98	1.10	11.075
my_166	36.53685	-121.92701	5.84	0.50	61.3	0.52	77	7.7	0.63	0.81	11.231
my_167	36.53673	-121.92723	5.07	0.50	52.2	0.51	83	7.1	0.68	0.85	11.207
my_168	36.53615	-121.92745	5.04	0.50	101.8	0.55	83	7.1	0.68	0.87	11.150
my_169	36.53350	-121.92790	2.62	0.50	0.0	0.50	144	6.2	1.17	1.28	10.931
my_170	36.53209	-121.92598	3.68	0.50	233.0	0.71	22	4.2	0.18	0.74	10.961
my_171	36.53305	-121.92671	4.29	0.50	118.5	0.56	37	5.2	0.30	0.64	10.980
my_172	36.53384	-121.92776	3.98	0.50	38.9	0.51	134	7.3	1.09	1.21	10.964
my_173	36.53162	-121.92658	2.81	0.80	0.0	0.80	93	5.1	0.76	1.10	10.887
my_177	36.52658	-121.92446	4.11	0.70	220.9	0.85	84	6.2	0.69	1.09	10.672
my_178	36.52724	-121.92498	5.26	0.70	134.3	0.76	41	6.3	0.33	0.83	10.684
my_179	36.52783	-121.92547	5.01	0.60	57.2	0.61	34	5.8	0.28	0.67	10.692
my_180	36.52835	-121.92571	4.95	0.50	30.3	0.50	56	6.3	0.46	0.68	10.713
my_181	36.52948	-121.92504	7.69	0.60	167.5	0.70	16	8.1	0.13	0.71	10.839
my_182	36.52762	-121.92528	5.48	0.60	84.7	0.63	25	6.1	0.20	0.66	10.690

Survey station	Latitude (WGS84)	Longitude (WGS84)	Meas. terrace height (m)	GPS vert. unc. 1σ (m)	Horiz. offset (m)	Meas. vert. unc. 1σ (m)	Dist. to inner edge (m)	Model terrace height (m)	Model unc. 1σ (m)	Total vert. unc. 1σ (m)	Dist. to SGHF (km)
my_187	36.50242	-121.93885	8.45	0.60	99.4	0.64	75	10.3	0.61	0.88	7.960
my_188	36.50272	-121.93799	8.16	0.70	122.8	0.75	17	8.6	0.14	0.76	8.041
my_189	36.50767	-121.93968	13.07	1.40	664.6	2.02	28	13.8	0.23	2.03	8.278
my_190	36.50003	-121.93527	10.40	1.10	278.2	1.26	102	12.9	0.83	1.51	8.035
my_191	36.49932	-121.93639	11.52	0.80	189.0	0.90	26	12.2	0.21	0.93	7.907
my_192	36.49979	-121.93666	10.09	0.70	245.6	0.88	13	10.4	0.11	0.89	7.923
my_193	36.49782	-121.93610	18.29	0.80	22.5	0.80	19	18.8	0.16	0.82	7.820
my_198	36.49298	-121.94237	7.76	0.80	53.3	0.81	40	8.7	0.33	0.87	7.045
my_199	36.49324	-121.94328	10.57	0.70	124.8	0.75	87	12.7	0.71	1.03	7.001
my_200	36.49346	-121.94340	9.29	0.70	137.5	0.76	93	11.6	0.76	1.08	7.008
my_201	36.49353	-121.94183	9.56	0.60	29.8	0.60	33	10.4	0.27	0.66	7.121
my_202	36.49374	-121.94161	10.82	0.60	58.7	0.61	46	12.0	0.38	0.72	7.151
my_203	36.48840	-121.94374	11.61	0.70	421.3	1.16	185	16.2	1.51	1.90	6.624
my_204	36.48833	-121.94374	12.16	0.90	426.5	1.29	193	16.9	1.57	2.04	6.618
my_205	36.48900	-121.94383	11.31	0.60	310.2	0.90	119	14.2	0.97	1.33	6.660
my_206	36.48212	-121.93843	8.83	0.60	132.6	0.67	160	12.8	1.31	1.47	6.538
my_207	36.48164	-121.93802	10.68	0.60	75.8	0.62	104	13.2	0.85	1.05	6.533
my_208	36.48219	-121.93964	10.62	0.80	238.1	0.95	261	17.1	2.13	2.33	6.461
my_210	36.47090	-121.93539	16.88	0.50	23.4	0.50	86	19.0	0.70	0.86	5.945
my_211	36.47074	-121.93501	14.38	0.50	62.3	0.52	88	16.5	0.72	0.89	5.960
my_212	36.47069	-121.93500	16.98	0.50	64.9	0.52	92	19.2	0.75	0.91	5.957
my_213	36.47060	-121.93501	12.94	0.50	69.8	0.52	101	15.4	0.82	0.98	5.950
my_214	36.47168	-121.93624	12.28	0.50	95.4	0.54	80	14.3	0.65	0.85	5.943
my_215	36.47122	-121.93580	11.68	0.50	31.4	0.51	83	13.7	0.68	0.84	5.941
my_216	36.46996	-121.93386	14.83	0.50	194.9	0.66	87	17.0	0.71	0.97	5.983
my_217	36.46956	-121.93360	12.76	0.50	240.9	0.73	85	14.9	0.69	1.00	5.973
my_229	36.46733	-121.93057	8.94	1.20	235.8	1.31	187	13.5	1.53	2.01	6.021
my_230	36.46803	-121.93177	8.09	1.20	102.8	1.22	120	11.0	0.98	1.57	5.989
my_231	36.46943	-121.93380	11.34	1.30	136.8	1.33	108	14.0	0.88	1.60	5.949
my_232	36.46928	-121.93393	8.18	1.40	135.0	1.43	126	11.3	1.03	1.76	5.929
my_233	36.46904	-121.93313	9.58	1.40	65.1	1.41	80	11.6	0.65	1.55	5.968
my_234	36.46518	-121.92931	8.63	1.10	132.9	1.14	302	16.0	2.42	2.68	5.954
my_235	36.46713	-121.92966	5.99	1.10	348.6	1.34	211	11.2	1.72	2.18	6.069
my_236	36.46675	-121.92941	5.90	1.10	302.5	1.28	243	11.9	1.98	2.36	6.059
my_237	36.46573	-121.92903	4.29	1.20	185.0	1.27	248	10.4	2.02	2.39	6.012
my_238	36.46548	-121.92900	4.59	1.20	157.3	1.25	260	11.0	2.12	2.46	5.996
my_239	36.46424	-121.92896	7.12	1.20	27.4	1.20	265	13.7	2.16	2.47	5.911
my_240	36.46386	-121.92868	9.59	1.30	24.8	1.30	237	15.4	1.93	2.33	5.902
my_241	36.46309	-121.92731	8.87	1.20	168.4	1.26	125	12.0	1.02	1.62	5.941
my_242	36.46270	-121.92739	9.29	1.20	195.1	1.27	142	12.8	1.16	1.72	5.908
my_243	36.46248	-121.92736	10.85	1.20	216.1	1.29	146	14.4	1.19	1.76	5.895
my_244	36.46156	-121.92668	11.26	1.10	334.7	1.32	137	14.6	1.12	1.73	5.876
my_245	36.46132	-121.92631	7.51	0.50	436.7	1.08	142	11.0	1.16	1.58	5.883
my_246	36.45855	-121.92534	9.97	0.50	119.0	0.56	191	14.7	1.56	1.66	5.753
my_247	36.45807	-121.92532	9.79	0.50	65.7	0.52	216	15.1	1.76	1.84	5.719
my_248	36.45719	-121.92515	13.27	0.50	33.1	0.51	234	19.0	1.91	1.97	5.668
my_249	36.45616	-121.92512	12.48	0.60	146.5	0.68	229	18.1	1.87	1.99	5.597
my_250	36.45605	-121.92553	10.73	0.60	161.6	0.70	267	17.3	2.18	2.29	5.560
my_251	36.45542	-121.92566	8.76	0.20	46.2	0.22	294	16.0	2.40	2.41	5.507
my_252	36.45605	-121.92579	9.62	0.20	27.1	0.21	290	16.8	2.37	2.37	5.543
my_253	36.45588	-121.92630	7.56	0.20	42.0	0.22	338	15.6	2.43	2.44	5.495
my_254	36.45384	-121.92495	13.87	0.20	233.0	0.55	174	18.2	1.42	1.52	5.443
my_255	36.45404	-121.92443	14.68	0.20	233.3	0.55	158	18.6	1.29	1.40	5.493
my_256	36.45391	-121.92536	13.00	0.20	215.2	0.51	170	17.2	1.39	1.48	5.419
my_257	36.45359	-121.92640	16.76	0.20	251.2	0.58	99	19.2	0.81	1.00	5.326
my_258	36.45284	-121.92703	12.53	0.20	347.0	0.78	8	12.7	0.07	0.79	5.228
my_259	36.45246	-121.92765	15.34	0.20	406.0	0.91	9	15.6	0.07	0.91	5.159
my_260	36.45355	-121.92975	11.50	0.20	431.0	0.96	205	16.6	1.67	1.93	5.093
my_261	36.45299	-121.92912	10.78	0.20	430.0	0.96	121	13.8	0.99	1.38	5.096
my_262	36.45660	-121.92501	12.12	0.20	114.9	0.32	219	17.5	1.79	1.82	5.636
my_263	36.45846	-121.92518	9.41	0.20	299.8	0.68	183	13.9	1.49	1.64	5.757
my_264	36.45607	-121.92578	9.84	0.20	29.1	0.21	289	17.0	2.36	2.37	5.545
my_265	36.45507	-121.92559	9.70	0.50	13.6	0.50	278	16.6	2.27	2.32	5.487
my_266	36.45518	-121.92536	10.38	0.50	18.4	0.50	280	17.3	2.28	2.34	5.511
my_267	36.45507	-121.92525	10.84	0.50	31.2	0.51	277	17.7	2.26	2.32	5.510
my_268	36.45486	-121.92501	12.42	0.50	62.1	0.52	253	18.7	2.06	2.13	5.511
my_269	36.45469	-121.92498	12.38	0.40	75.8	0.43	243	18.4	1.98	2.03	5.501

Survey station	Latitude (WGS84)	Longitude (WGS84)	Meas. terrace height (m)	GPS vert. unc. 1σ (m)	Horiz. offset (m)	Meas. vert. unc. 1σ (m)	Dist. to inner edge (m)	Model terrace height (m)	Model unc. 1σ (m)	Total vert. unc. 1σ (m)	Dist. to SGHF (km)
my_270	36.45427	-121.92481	12.44	0.50	122.3	0.57	200	17.4	1.63	1.73	5.483
my_271	36.45394	-121.92485	13.60	0.50	153.3	0.60	175	17.9	1.43	1.55	5.457
my_272	36.44749	-121.92658	8.96	4.70	160.8	4.71	93	11.3	0.76	4.77	4.877
my_273	36.44818	-121.92680	11.37	4.70	102.9	4.71	75	13.2	0.61	4.75	4.912
my_274	36.44703	-121.92631	12.44	4.80	214.5	4.82	99	14.9	0.81	4.89	4.863
my_275	36.44822	-121.92678	13.69	4.80	102.9	4.81	73	15.5	0.60	4.84	4.916
my_276	36.44858	-121.92734	10.70	4.80	50.3	4.80	109	13.4	0.89	4.88	4.903
my_277	36.44848	-121.92877	13.06	4.70	79.0	4.70	191	17.8	1.56	4.95	4.798
my_278	36.44875	-121.92813	16.05	4.70	36.7	4.70	137	19.4	1.12	4.83	4.861
my_279	36.44867	-121.92851	14.06	4.60	59.8	4.60	161	18.0	1.31	4.79	4.829
my_280	36.44855	-121.92786	17.22	4.60	8.2	4.60	146	20.8	1.19	4.75	4.865
my_281	36.44835	-121.92875	6.82	3.90	77.5	3.90	203	11.8	1.66	4.24	4.790
my_282	36.44845	-121.92820	7.61	3.80	26.2	3.80	169	11.8	1.38	4.04	4.835
my_283	36.44835	-121.92789	10.54	3.70	12.2	3.70	164	14.6	1.34	3.93	4.849
my_290	36.44884	-121.92907	14.44	1.10	38.6	1.10	171	18.7	1.40	1.78	4.802
my_291	36.44849	-121.92909	15.12	1.10	0.0	1.10	204	20.1	1.66	2.00	4.776
my_292	36.44939	-121.92877	12.09	1.60	32.4	1.60	108	14.8	0.88	1.83	4.862
my_293	36.45064	-121.92852	14.20	1.60	170.6	1.64	22	14.7	0.18	1.65	4.969
my_294	36.45240	-121.92842	10.31	1.60	365.0	1.79	33	11.1	0.27	1.81	5.102
my_295	36.45313	-121.92857	12.86	1.50	444.0	1.79	100	15.3	0.82	1.96	5.143
my_296	36.44033	-121.92294	8.94	0.50	30.6	0.50	144	12.5	1.17	1.28	4.615
my_297	36.44004	-121.92276	8.84	0.50	12.6	0.50	150	12.5	1.22	1.32	4.607
my_298	36.44002	-121.92287	8.18	0.50	5.0	0.50	159	12.1	1.30	1.39	4.598
my_302	36.44077	-121.92305	13.86	0.60	48.7	0.61	133	17.1	1.09	1.24	4.639
my_303	36.44262	-121.92317	15.75	0.70	231.5	0.86	43	16.8	0.35	0.93	4.763
my_304	36.44163	-121.92272	17.27	0.70	115.2	0.74	75	19.1	0.61	0.96	4.723
my_305	36.44088	-121.92301	11.80	0.90	63.8	0.91	126	14.9	1.03	1.37	4.650
my_306	36.44069	-121.92333	11.97	1.10	86.1	1.12	159	15.9	1.30	1.71	4.614
my_310	36.43828	-121.92149	18.19	0.50	92.1	0.54	171	22.4	1.40	1.50	4.568
my_311	36.43872	-121.92170	12.96	0.50	40.7	0.51	168	17.1	1.37	1.46	4.586
my_312	36.43923	-121.92218	17.11	0.50	43.6	0.51	154	20.9	1.26	1.36	4.590
my_313	36.43771	-121.92063	18.14	0.50	322.4	0.86	95	20.5	0.78	1.16	4.587
my_314	36.43706	-121.92011	11.68	0.60	236.7	0.79	59	13.1	0.48	0.93	4.576
my_315	36.43665	-121.91963	15.97	0.50	177.8	0.63	28	16.7	0.23	0.67	4.580
my_316	36.43162	-121.91782	19.37	0.60	132.6	0.67	37	20.3	0.30	0.73	4.344
my_317	36.43090	-121.91747	18.34	0.60	216.1	0.76	7	18.5	0.06	0.77	4.317
my_318	36.43080	-121.91790	17.30	0.60	210.3	0.76	32	18.1	0.26	0.80	4.281
my_319	36.43771	-121.91992	18.62	0.60	579.0	1.40	33	19.4	0.27	1.42	4.635
my_320	36.41270	-121.91479	13.71	0.60	157.7	0.69	108	16.4	0.88	1.12	3.201
my_321	36.41418	-121.91526	14.50	0.60	327.1	0.93	129	17.7	1.05	1.41	3.275
my_322	36.41304	-121.91493	17.01	0.60	198.1	0.74	140	20.5	1.14	1.36	3.216
my_324	36.41174	-121.91527	11.76	0.60	85.9	0.63	102	14.3	0.83	1.04	3.100
my_325	36.41187	-121.91565	9.87	0.50	122.8	0.57	140	13.3	1.14	1.28	3.083
my_328	36.40636	-121.91242	12.38	1.40	100.5	1.42	213	17.6	1.74	2.24	2.911
my_329	36.40631	-121.91251	12.51	1.20	110.5	1.22	223	18.0	1.82	2.19	2.901
my_330	36.40717	-121.91326	11.04	1.00	171.1	1.07	202	16.0	1.65	1.96	2.911
my_331	36.40115	-121.91061	15.77	0.20	79.8	0.27	177	20.1	1.44	1.47	2.663
my_332	36.40066	-121.91012	13.43	0.20	132.6	0.35	236	19.2	1.93	1.96	2.662
my_333	36.40039	-121.90963	11.82	0.20	184.8	0.45	266	18.4	2.17	2.22	2.676
my_334	36.40058	-121.90968	11.59	0.20	172.1	0.43	247	17.7	2.01	2.06	2.686
my_335	36.40011	-121.90835	12.49	0.20	302.4	0.69	244	18.5	1.99	2.11	2.744
my_336	36.40096	-121.91110	12.63	0.20	38.6	0.22	194	17.4	1.58	1.60	2.616
my_337	36.39968	-121.90679	14.95	0.20	450.7	1.00	175	19.3	1.43	1.75	2.820
my_338	36.39786	-121.90404	19.57	0.20	758.9	1.67	150	23.3	1.22	2.07	2.879
my_339	36.39840	-121.90474	20.84	0.20	675.9	1.49	197	25.7	1.61	2.19	2.870
my_340	36.40010	-121.90836	12.36	0.20	302.4	0.69	246	18.4	2.01	2.12	2.742
my_345	36.39313	-121.90331	16.23	0.70	171.5	0.79	110	18.9	0.90	1.20	2.591
my_346	36.39297	-121.90349	17.56	0.60	185.6	0.72	123	20.6	1.00	1.24	2.568
my_347	36.39236	-121.90351	20.28	0.60	253.3	0.82	134	23.6	1.09	1.36	2.522
my_348	36.39041	-121.90389	18.79	0.50	468.6	1.14	199	23.7	1.62	1.98	2.357
my_349	36.39540	-121.90390	32.80	0.50	86.3	0.53	135	36.1	1.10	1.22	2.713
my_351	36.39624	-121.90547	18.11	0.40	0.0	0.40	270	24.8	2.20	2.24	2.665
my_352	36.39650	-121.90530	17.41	0.40	33.3	0.41	256	23.7	2.09	2.13	2.695
my_353	36.39721	-121.90539	18.17	0.40	108.2	0.46	269	24.8	2.19	2.24	2.740
my_354	36.39950	-121.90630	18.35	0.40	370.0	0.90	157	22.2	1.28	1.57	2.841
my_355	36.39940	-121.90624	17.01	0.40	357.0	0.88	163	21.0	1.33	1.59	2.838
my_356	36.39991	-121.90733	13.07	0.40	441.0	1.04	192	17.8	1.57	1.88	2.800

Survey station	Latitude (WGS84)	Longitude (WGS84)	Meas. terrace height (m)	GPS vert. unc. 1σ (m)	Horiz. offset (m)	Meas. vert. unc. 1σ (m)	Dist. to inner edge (m)	Model terrace height (m)	Model unc. 1σ (m)	Total vert. unc. 1σ (m)	Dist. to SGHF (km)
my_357	36.40042	-121.90810	13.15	0.40	521.0	1.21	205	18.2	1.67	2.06	2.783
my_359	36.39602	-121.90558	17.66	0.40	9.8	0.40	279	24.5	2.28	2.31	2.642
my_360	36.38996	-121.90384	19.41	0.30	84.8	0.35	198	24.3	1.62	1.65	2.329
my_361	36.39037	-121.90428	19.02	0.30	31.7	0.31	234	24.8	1.91	1.93	2.327
my_362	36.39070	-121.90428	18.03	0.30	48.9	0.32	229	23.7	1.87	1.90	2.351
my_363	36.39042	-121.90471	16.80	0.30	8.8	0.30	271	23.5	2.21	2.23	2.301
my_364	36.39167	-121.90413	18.32	0.30	150.9	0.45	201	23.3	1.64	1.70	2.431
my_365	36.38187	-121.90156	24.84	0.40	197.1	0.59	228	30.5	1.86	1.95	1.908
my_366	36.38201	-121.90131	23.65	0.40	216.6	0.62	202	28.6	1.65	1.76	1.935
my_367	36.38297	-121.90146	26.78	0.40	319.5	0.80	170	31.0	1.39	1.60	1.993
my_368	36.38091	-121.90155	31.12	0.40	93.4	0.45	208	36.2	1.70	1.76	1.840
my_369	36.38074	-121.90146	32.34	0.40	78.6	0.44	196	37.2	1.60	1.66	1.833
my_370	36.38057	-121.90148	33.47	0.30	64.0	0.33	192	38.2	1.57	1.60	1.821
my_371	36.38022	-121.90190	38.56	0.40	8.9	0.40	177	42.9	1.44	1.50	1.766
my_372	36.38001	-121.90220	35.76	0.40	25.7	0.40	150	39.5	1.22	1.29	1.730
my_373	36.38060	-121.90148	32.56	0.30	97.3	0.37	193	37.3	1.57	1.62	1.822
my_374	36.37987	-121.90224	35.99	0.30	279.9	0.68	134	39.3	1.09	1.29	1.718
my_375	36.37812	-121.90404	60.61	0.40	30.2	0.41	32	61.4	0.26	0.48	1.469
my_376	36.37801	-121.90435	59.92	0.40	0.0	0.40	58	61.4	0.47	0.62	1.440
my_379	36.37787	-121.90454	60.75	0.30	0.0	0.30	71	62.5	0.58	0.65	1.417
my_380	36.37329	-121.90531	65.43	0.50	200.4	0.66	56	66.8	0.46	0.81	1.037
my_381	36.37327	-121.90623	64.02	0.60	231.2	0.78	135	67.3	1.10	1.35	0.973
my_382	36.37319	-121.90550	66.52	0.60	215.3	0.76	76	68.4	0.62	0.98	1.017
my_385	36.37268	-121.90437	75.57	0.50	0.0	0.50	49	76.8	0.40	0.64	1.059
my_386	36.37256	-121.90476	71.60	0.50	37.7	0.51	82	73.6	0.67	0.84	1.023
my_387	36.37268	-121.90366	75.86	0.50	63.1	0.52	20	76.4	0.16	0.54	1.106
my_388	36.37242	-121.90325	75.27	0.50	104.5	0.55	29	76.0	0.24	0.60	1.117
my_389	36.37051	-121.90145	76.53	0.50	356.0	0.92	18	77.0	0.15	0.94	1.104
my_390	36.36947	-121.90179	71.41	0.50	425.0	1.05	4	71.5	0.03	1.05	1.006
my_391	36.36923	-121.90195	71.19	0.50	440.0	1.08	15	71.6	0.12	1.09	0.978
my_392	36.36947	-121.90178	72.13	0.50	425.0	1.05	4	72.2	0.03	1.05	1.007
my_393	36.35676	-121.90543	58.70	0.80	451.9	1.27	115	61.5	0.94	1.58	-0.154
my_394	36.35694	-121.90438	58.00	0.70	402.3	1.12	20	58.5	0.16	1.13	-0.070
my_395	36.35397	-121.90381	39.58	0.60	192.7	0.73	73	41.4	0.60	0.94	-0.246
my_396	36.36056	-121.90295	65.92	0.50	333.0	0.88	140	69.4	1.14	1.44	0.288
my_397	36.36119	-121.90346	67.77	0.50	380.0	0.97	222	73.2	1.81	2.05	0.300
my_398	36.35840	-121.90396	68.29	0.50	86.4	0.53	7	68.5	0.06	0.54	0.063
my_399	36.35709	-121.90441	57.92	0.50	96.9	0.54	17	58.3	0.14	0.56	-0.061
my_400	36.35728	-121.90541	57.62	0.50	94.3	0.54	100	60.1	0.82	0.98	-0.115
my_401	36.35726	-121.90580	57.72	0.50	120.9	0.57	135	61.0	1.10	1.24	-0.143
my_402	36.35686	-121.90680	35.12	0.50	0.0	0.50	232	40.8	1.89	1.96	-0.240
my_403	36.35732	-121.90618	39.17	0.50	75.8	0.53	167	43.3	1.36	1.46	-0.164
my_404	36.35712	-121.90676	36.07	0.50	28.4	0.50	223	41.6	1.82	1.89	-0.219
my_405	36.35664	-121.90645	36.29	0.50	40.4	0.51	206	41.4	1.68	1.76	-0.232
my_409	36.35449	-121.90456	30.66	0.60	315.0	0.91	116	33.5	0.95	1.31	-0.259
my_410	36.35362	-121.90279	33.19	0.60	494.0	1.23	36	34.1	0.29	1.27	-0.202
my_411	36.35447	-121.90355	37.37	0.50	380.0	0.97	30	38.1	0.25	1.00	-0.192
my_412	36.35670	-121.90667	36.20	0.50	7.7	0.50	225	41.7	1.84	1.90	-0.243
sc_1	37.11563	-122.30539	21.42	1.30	56.1	1.31	525	31.4	2.50	2.82	-0.455
sc_2	37.11573	-122.30540	19.63	1.60	48.0	1.60	521	29.6	2.50	2.97	-0.452
sc_3	37.11843	-122.31401	15.67	0.90	157.9	0.96	1020	30.1	3.15	3.30	-0.993
sc_4	37.11835	-122.31450	16.91	0.30	198.8	0.53	1063	31.8	3.23	3.28	-1.036
sc_5	37.11785	-122.31431	16.69	0.40	183.6	0.57	1067	31.6	3.24	3.29	-1.047
sc_6	37.11749	-122.31489	18.17	0.30	242.9	0.61	1130	33.6	3.37	3.43	-1.111
sc_7	37.11699	-122.31500	16.37	0.30	273.6	0.67	1162	32.1	3.44	3.50	-1.145
sc_8	37.11804	-122.31441	16.54	0.30	189.9	0.51	1067	31.4	3.24	3.28	-1.044
sc_9	37.11687	-122.31516	15.04	0.30	350.0	0.82	1180	31.0	3.48	3.57	-1.163
sc_10	37.11721	-122.31547	15.65	0.30	232.0	0.59	1190	31.7	3.50	3.55	-1.171
sc_11	37.11729	-122.31744	13.47	0.30	230.5	0.59	1349	30.9	3.86	3.90	-1.322
sc_12	37.11637	-122.31968	10.57	0.30	151.3	0.45	1571	30.0	4.40	4.42	-1.546
sc_13	37.11464	-122.30344	21.74	0.40	88.4	0.44	434	30.9	2.47	2.51	-0.352
sc_14	37.11438	-122.30309	21.30	0.90	133.9	0.95	413	30.3	2.46	2.64	-0.337
sc_15	37.11456	-122.30327	20.17	0.70	176.4	0.80	422	29.2	2.47	2.59	-0.343
sc_16	37.11387	-122.30221	21.12	0.40	15.8	0.40	366	29.6	2.45	2.49	-0.294
sc_17	37.11418	-122.30266	22.97	0.30	31.1	0.31	387	31.7	2.46	2.48	-0.314
sc_18	37.11428	-122.30286	21.37	0.30	13.3	0.30	398	30.2	2.46	2.48	-0.324
sc_19	37.11384	-122.30225	21.16	0.30	82.9	0.35	371	29.7	2.46	2.48	-0.299

Survey station	Latitude (WGS84)	Longitude (WGS84)	Meas. terrace height (m)	GPS vert. unc. 1σ (m)	Horiz. offset (m)	Meas. vert. unc. 1σ (m)	Dist. to inner edge (m)	Model terrace height (m)	Model unc. 1σ (m)	Total vert. unc. 1σ (m)	Dist. to SGHF (km)
sc_20	37.11391	-122.30236	20.63	0.50	22.5	0.50	376	29.3	2.46	2.51	-0.304
sc_21	37.11360	-122.30183	21.04	0.40	21.4	0.40	351	29.3	2.44	2.47	-0.277
sc_22	37.11351	-122.30152	21.89	0.40	13.2	0.40	334	29.8	2.43	2.46	-0.258
sc_23	37.11335	-122.30132	21.02	0.50	32.2	0.51	327	28.8	2.43	2.48	-0.250
sc_24	37.10819	-122.29370	35.54	0.50	83.3	0.53	57	36.9	0.47	0.71	0.089
sc_25	37.10859	-122.29403	35.25	0.50	119.8	0.56	43	36.3	0.35	0.66	0.083
sc_26	37.11205	-122.29908	18.39	0.60	50.1	0.61	226	24.0	1.84	1.94	-0.140
sc_27	37.11368	-122.30158	21.10	0.90	277.0	1.08	340	29.1	2.43	2.67	-0.266
sc_28	37.11238	-122.29959	21.60	1.20	52.7	1.21	246	27.7	2.01	2.34	-0.163
sc_29	37.08736	-122.27354	29.57	1.00	60.4	1.01	270	36.2	2.20	2.42	0.620
sc_30	37.08699	-122.27288	31.81	0.70	98.2	0.73	247	37.9	2.01	2.14	0.653
sc_31	37.08615	-122.27145	30.33	0.70	241.1	0.88	191	35.0	1.56	1.79	0.723
sc_32	37.08562	-122.27076	26.13	0.80	105.0	0.83	201	31.1	1.64	1.84	0.750
sc_33	37.08611	-122.27146	26.04	1.00	49.5	1.01	195	30.8	1.59	1.88	0.720
sc_34	37.08307	-122.26853	29.23	0.50	37.3	0.51	182	33.7	1.48	1.57	0.797
sc_35	37.08385	-122.26872	26.77	0.40	93.9	0.45	165	30.8	1.35	1.42	0.822
sc_36	37.08392	-122.26875	26.86	0.40	101.0	0.46	168	31.0	1.37	1.44	0.822
sc_37	37.08567	-122.27027	28.33	0.50	320.0	0.86	173	32.6	1.41	1.65	0.791
sc_38	37.08268	-122.26859	29.80	0.80	42.4	0.81	210	35.0	1.71	1.89	0.773
sc_39	37.08229	-122.26826	30.39	0.40	43.2	0.41	213	35.6	1.74	1.79	0.779
sc_40	37.08181	-122.26774	28.14	0.80	75.2	0.82	202	33.1	1.65	1.84	0.795
sc_41	37.08124	-122.26734	28.28	0.70	137.8	0.76	205	33.3	1.67	1.84	0.798
sc_42	37.08205	-122.26849	3.60	0.50	237.0	0.72	245	9.6	2.00	2.12	0.748
sc_43	37.07982	-122.26745	26.80	0.30	54.6	0.32	289	33.9	2.36	2.38	0.716
sc_44	37.07932	-122.26718	26.55	0.30	62.1	0.33	293	33.8	2.39	2.41	0.713
sc_45	37.07300	-122.26158	37.92	0.70	134.3	0.76	109	40.6	0.89	1.17	0.834
sc_46	37.07349	-122.26208	36.61	0.40	76.4	0.43	111	39.3	0.91	1.00	0.819
sc_47	37.07003	-122.25923	38.77	0.40	509.0	1.18	104	41.3	0.85	1.45	0.868
sc_48	37.07510	-122.26210	38.34	0.40	185.4	0.57	45	39.4	0.37	0.68	0.899
sc_49	37.07531	-122.26228	40.14	0.60	203.1	0.75	34	41.0	0.28	0.80	0.895
sc_50	37.07369	-122.26249	34.16	0.70	45.3	0.71	125	37.2	1.02	1.24	0.797
sc_51	37.07612	-122.26288	39.64	0.20	73.6	0.26	44	40.7	0.36	0.44	0.889
sc_52	37.07716	-122.26299	40.76	0.20	102.8	0.30	33	41.6	0.27	0.40	0.934
sc_53	37.07782	-122.26330	40.51	0.20	162.7	0.41	38	41.4	0.31	0.51	0.943
sc_54	37.07824	-122.26411	38.74	0.20	129.9	0.35	93	41.0	0.76	0.83	0.901
sc_55	37.07882	-122.26469	37.53	0.20	84.1	0.27	127	40.7	1.04	1.07	0.884
sc_56	37.07906	-122.26528	35.90	0.30	71.3	0.34	161	39.9	1.31	1.36	0.850
sc_57	37.07913	-122.26543	30.76	0.20	74.0	0.26	172	35.0	1.40	1.43	0.841
sc_58	37.07919	-122.26578	27.44	0.20	84.8	0.27	197	32.3	1.61	1.63	0.817
sc_59	37.07920	-122.26598	25.66	0.30	69.7	0.34	213	30.9	1.74	1.77	0.801
sc_60	37.06991	-122.25927	40.87	0.40	180.6	0.56	110	43.6	0.90	1.06	0.859
sc_61	37.07188	-122.25976	50.62	0.40	84.6	0.44	49	51.8	0.40	0.60	0.920
sc_62	37.06402	-122.25447	38.10	0.60	37.2	0.61	78	40.0	0.64	0.88	0.992
sc_63	37.06533	-122.25558	38.33	0.60	212.2	0.76	81	40.3	0.66	1.01	0.959
sc_64	37.06372	-122.25420	34.71	0.60	8.3	0.60	86	36.8	0.70	0.92	1.002
sc_65	37.06379	-122.25419	38.75	0.70	370.0	1.07	79	40.7	0.64	1.25	1.005
sc_66	37.05774	-122.24966	34.59	0.10	101.9	0.24	143	38.1	1.17	1.19	1.111
sc_67	37.05600	-122.24639	39.09	0.10	451.0	0.99	47	40.2	0.38	1.06	1.302
sc_68	37.05542	-122.24597	41.99	0.20	519.0	1.15	61	43.5	0.50	1.25	1.311
sc_69	37.05838	-122.25082	34.31	0.40	20.9	0.40	196	39.1	1.60	1.65	1.044
sc_70	37.05972	-122.25222	34.83	0.50	186.5	0.65	198	39.7	1.62	1.74	0.988
sc_71	37.05400	-122.24435	45.86	0.30	129.1	0.41	44	46.9	0.36	0.55	1.381
sc_72	37.05251	-122.24286	45.72	0.70	340.0	1.02	31	46.5	0.25	1.05	1.438
sc_73	37.05193	-122.24256	42.79	0.50	406.0	1.02	21	43.3	0.17	1.03	1.437
sc_74	37.05507	-122.24572	43.91	0.10	40.9	0.13	55	45.3	0.45	0.47	1.316
sc_75	37.05747	-122.24765	38.33	0.10	356.0	0.78	33	39.1	0.27	0.83	1.263
sc_76	37.05779	-122.24910	34.93	0.10	466.0	1.02	100	37.4	0.82	1.31	1.158
sc_77	37.04735	-122.23743	43.54	0.30	125.2	0.41	34	44.4	0.28	0.49	1.655
sc_78	37.04817	-122.23799	41.86	0.30	30.9	0.31	16	42.3	0.13	0.33	1.646
sc_79	37.04551	-122.23591	40.89	0.70	366.0	1.06	52	42.2	0.42	1.14	1.699
sc_80	37.04389	-122.23363	30.70	0.30	271.0	0.66	95	33.0	0.78	1.02	1.814
sc_81	37.04539	-122.23581	34.38	0.40	17.0	0.40	56	35.8	0.46	0.61	1.702
sc_82	37.04506	-122.23494	33.56	0.40	250.0	0.68	42	34.6	0.34	0.76	1.759
sc_83	37.04503	-122.23490	34.33	0.40	245.0	0.67	43	35.4	0.35	0.75	1.761
sc_84	37.04288	-122.23304	28.83	0.10	56.7	0.16	192	33.6	1.57	1.57	1.820
sc_85	37.04367	-122.23334	30.49	0.10	97.2	0.23	108	33.1	0.88	0.91	1.829
sc_86	37.04425	-122.23397	34.04	0.10	161.1	0.37	85	36.1	0.69	0.78	1.804

Survey station	Latitude (WGS84)	Longitude (WGS84)	Meas. terrace height (m)	GPS vert. unc. 1σ (m)	Horiz. offset (m)	Meas. vert. unc. 1σ (m)	Dist. to inner edge (m)	Model terrace height (m)	Model unc. 1σ (m)	Total vert. unc. 1σ (m)	Dist. to SGHF (km)
sc_87	37.04499	-122.23502	34.00	0.20	-	0.20	52	35.3	0.42	0.47	1.750
sc_88	37.04528	-122.23554	35.22	0.20	270.0	0.62	57	36.6	0.47	0.78	1.720
sc_89	37.03279	-122.22717	17.76	0.60	192.0	0.73	636	28.8	2.59	2.69	1.857
sc_90	37.03340	-122.22710	18.05	0.60	43.6	0.61	601	28.7	2.56	2.63	1.890
sc_91	37.03316	-122.22722	17.71	0.40	69.1	0.43	622	28.6	2.57	2.61	1.870
sc_92	37.03431	-122.22724	18.85	0.50	43.6	0.51	576	29.3	2.54	2.59	1.919
sc_93	37.03505	-122.22756	18.12	0.80	84.4	0.82	586	28.7	2.54	2.67	1.925
sc_94	37.03562	-122.22764	19.26	0.50	38.6	0.51	569	29.7	2.53	2.58	1.944
sc_95	37.02514	-122.22130	12.74	1.00	89.4	1.02	770	25.0	2.74	2.92	2.003
sc_96	37.02526	-122.21972	17.76	1.40	270.0	1.52	679	29.1	2.63	3.04	2.137
sc_97	37.02515	-122.21864	20.08	1.30	138.1	1.33	636	31.1	2.59	2.91	2.221
sc_98	37.02506	-122.21757	20.09	0.80	53.0	0.81	604	30.8	2.56	2.68	2.305
sc_99	37.02283	-122.21510	16.20	1.20	75.0	1.21	618	27.0	2.57	2.84	2.409
sc_100	37.02239	-122.21471	17.87	1.00	359.0	1.27	649	29.0	2.60	2.89	2.397
sc_101	37.02025	-122.21072	21.26	0.20	359.0	0.81	475	30.8	2.48	2.61	2.654
sc_102	37.02071	-122.21138	20.83	0.20	202.0	0.48	509	30.7	2.50	2.54	2.621
sc_103	37.02084	-122.21230	20.94	0.10	135.0	0.31	570	31.3	2.53	2.55	2.551
sc_104	37.02122	-122.21304	20.62	0.10	55.2	0.16	604	31.3	2.56	2.56	2.507
sc_105	37.02154	-122.21372	21.41	0.10	54.2	0.16	621	32.3	2.57	2.58	2.466
sc_106	37.01310	-122.20041	22.37	0.60	114.5	0.65	349	30.6	2.44	2.53	3.185
sc_107	37.01282	-122.19987	24.55	0.50	33.0	0.51	331	32.4	2.43	2.48	3.217
sc_108	37.01152	-122.19807	23.29	0.40	87.6	0.44	310	30.8	2.42	2.46	3.308
sc_109	37.01122	-122.19790	24.58	0.40	301.0	0.77	317	32.2	2.43	2.54	3.309
sc_110	37.01380	-122.20377	20.63	0.30	333.5	0.79	527	30.6	2.51	2.63	2.941
sc_111	37.01363	-122.20255	21.28	0.30	244.3	0.61	475	30.8	2.48	2.55	3.033
sc_112	37.01382	-122.20148	23.82	0.20	135.9	0.36	388	32.6	2.46	2.49	3.129
sc_113	37.01002	-122.19576	24.04	0.20	75.7	0.26	306	31.5	2.42	2.44	3.431
sc_114	37.00957	-122.19618	18.73	0.40	49.2	0.41	366	27.2	2.45	2.49	3.377
sc_115	37.01006	-122.19520	25.10	0.40	102.6	0.46	291	32.3	2.37	2.42	3.478
sc_116	37.00729	-122.19206	23.59	0.30	432.0	0.99	357	31.9	2.45	2.64	3.614
sc_117	37.01102	-122.19744	23.23	0.30	415.0	0.95	302	30.6	2.42	2.60	3.337
sc_118	37.01002	-122.19654	23.76	0.30	146.4	0.44	334	31.7	2.43	2.47	3.367
sc_119	37.00295	-122.18524	23.09	0.20	10.3	0.20	336	31.1	2.43	2.44	3.982
sc_120	37.00345	-122.18498	24.41	0.20	171.4	0.42	289	31.5	2.36	2.40	4.026
sc_121	37.00422	-122.18631	23.74	0.30	133.6	0.42	307	31.2	2.42	2.46	3.950
sc_122	37.00454	-122.18834	21.28	0.30	39.4	0.31	436	30.5	2.47	2.49	3.798
sc_123	37.00400	-122.18690	23.14	0.30	160.3	0.46	362	31.6	2.45	2.49	3.892
sc_124	36.98520	-122.15709	20.17	0.40	18.6	0.40	356	28.5	2.45	2.48	5.499
sc_125	36.98523	-122.15952	17.90	0.60	90.1	0.63	454	27.2	2.47	2.55	5.318
sc_126	36.98593	-122.16062	18.44	0.60	124.9	0.66	463	27.9	2.48	2.56	5.245
sc_127	36.98632	-122.16079	18.15	0.60	27.4	0.60	436	27.3	2.47	2.54	5.248
sc_128	36.98699	-122.16152	18.70	0.60	25.3	0.60	367	27.2	2.45	2.53	5.254
sc_129	36.98841	-122.16291	17.24	0.80	123.0	0.84	344	25.3	2.44	2.58	5.168
sc_130	36.98839	-122.16445	15.71	1.10	44.5	1.10	394	24.5	2.46	2.70	5.042
sc_131	36.98892	-122.16431	21.51	0.40	213.4	0.61	357	29.8	2.45	2.52	5.077
sc_132	36.98857	-122.16255	19.71	0.40	74.9	0.43	329	27.6	2.43	2.47	5.202
sc_133	36.98772	-122.16190	19.16	0.40	177.1	0.56	338	27.2	2.43	2.50	5.237
sc_134	36.98662	-122.16175	19.04	0.30	239.1	0.60	381	27.7	2.46	2.53	5.261
sc_135	36.98880	-122.16877	16.96	1.40	305.0	1.55	517	26.9	2.50	2.94	4.709
sc_136	36.98889	-122.16804	17.91	1.30	200.0	1.37	467	27.4	2.48	2.83	4.773
sc_137	36.98858	-122.16686	18.22	0.70	138.0	0.76	443	27.5	2.47	2.59	4.854
sc_138	36.98814	-122.16681	18.73	0.80	29.4	0.80	457	28.1	2.47	2.60	4.869
sc_139	36.99009	-122.16864	19.22	1.40	130.3	1.43	397	28.0	2.46	2.85	4.794
sc_140	36.99072	-122.16864	22.35	1.10	36.3	1.10	350	30.6	2.44	2.68	4.822
sc_141	36.99155	-122.16964	21.59	0.90	48.1	0.91	332	29.5	2.43	2.59	4.810
sc_142	36.99166	-122.16990	22.43	1.30	174.5	1.36	340	30.5	2.43	2.79	4.791
sc_143	36.99329	-122.17142	24.04	0.80	199.0	0.91	366	32.5	2.45	2.62	4.720
sc_144	36.99323	-122.17181	23.85	0.80	187.3	0.90	395	32.7	2.46	2.62	4.681
sc_145	36.99232	-122.17003	22.03	0.70	212.3	0.84	361	30.4	2.45	2.59	4.762
sc_146	36.99419	-122.17336	20.42	0.60	26.0	0.60	404	29.3	2.46	2.54	4.572
sc_147	36.99430	-122.17268	22.17	0.60	166.1	0.70	346	30.3	2.44	2.54	4.652
sc_148	36.99379	-122.17189	21.86	0.60	119.7	0.65	378	30.5	2.46	2.55	4.674
sc_149	36.99481	-122.17492	22.09	0.70	29.4	0.70	368	30.6	2.46	2.55	4.471
sc_150	36.99444	-122.17418	19.72	0.90	77.4	0.92	388	28.5	2.46	2.63	4.515
sc_151	36.99628	-122.17672	23.37	0.40	9.9	0.40	323	31.1	2.43	2.46	4.389
sc_152	36.99693	-122.17774	23.59	0.40	31.3	0.41	323	31.3	2.43	2.46	4.336
sc_153	36.99684	-122.17825	23.77	0.40	146.2	0.51	349	32.0	2.44	2.49	4.301

Survey station	Latitude (WGS84)	Longitude (WGS84)	Meas. terrace height (m)	GPS vert. unc. 1σ (m)	Horiz. offset (m)	Meas. vert. unc. 1σ (m)	Dist. to inner edge (m)	Model terrace height (m)	Model unc. 1σ (m)	Total vert. unc. 1σ (m)	Dist. to SGHF (km)
sc_154	36.99718	-122.18066	21.29	0.40	178.8	0.56	469	30.8	2.48	2.54	4.126
sc_155	36.99800	-122.18155	19.58	1.00	391.0	1.31	502	29.4	2.49	2.82	4.068
sc_156	36.99748	-122.18120	19.37	0.70	23.5	0.70	481	29.0	2.48	2.58	4.104
sc_157	36.99930	-122.18314	19.59	0.80	58.7	0.81	485	29.2	2.48	2.61	3.995
sc_158	37.00159	-122.18377	24.63	0.70	10.7	0.70	297	32.0	2.42	2.52	4.065
sc_159	37.00106	-122.18427	23.54	0.70	267.5	0.91	365	32.0	2.45	2.62	3.993
sc_160	37.00109	-122.18521	21.93	0.80	227.0	0.94	449	31.2	2.47	2.65	3.901
sc_161	37.00098	-122.18592	20.55	0.80	277.8	1.00	450	29.9	2.47	2.67	3.894
sc_162	36.97896	-122.15557	17.54	0.30	316.9	0.75	715	29.2	2.67	2.78	5.426
sc_163	36.97796	-122.15420	15.03	0.30	286.0	0.69	771	27.2	2.74	2.83	5.441
sc_164	36.97722	-122.15341	15.02	0.30	121.3	0.40	845	27.9	2.85	2.88	5.443
sc_165	36.97790	-122.15397	15.42	0.30	14.3	0.30	773	27.7	2.74	2.76	5.461
sc_166	36.97663	-122.15172	15.72	0.60	102.2	0.64	840	28.6	2.84	2.91	5.554
sc_167	36.97699	-122.14879	13.24	0.60	61.5	0.62	741	25.2	2.70	2.77	5.809
sc_168	36.97672	-122.14971	15.05	0.50	52.4	0.51	785	27.4	2.76	2.81	5.722
sc_169	36.97664	-122.14925	15.94	1.30	48.7	1.30	785	28.3	2.76	3.05	5.757
sc_170	36.97822	-122.14685	15.94	0.70	7.6	0.70	554	26.2	2.52	2.62	6.022
sc_171	36.97764	-122.14783	19.35	0.60	113.1	0.65	646	30.4	2.60	2.68	5.917
sc_172	36.97688	-122.14467	13.51	0.60	230.0	0.78	628	24.4	2.58	2.70	6.140
sc_173	36.97654	-122.14340	12.92	0.60	300.0	0.89	571	23.3	2.53	2.68	6.258
sc_174	36.97572	-122.14096	14.53	0.70	269.6	0.91	610	25.3	2.56	2.72	6.390
sc_175	36.97549	-122.14069	14.35	0.70	34.8	0.70	613	25.1	2.57	2.66	6.402
sc_176	36.97398	-122.13881	12.61	0.60	11.4	0.60	633	23.6	2.58	2.65	6.488
sc_177	36.97223	-122.13697	12.20	0.60	11.4	0.60	618	23.0	2.57	2.64	6.560
sc_178	36.97116	-122.13688	11.07	0.90	20.8	0.90	657	22.3	2.61	2.76	6.572
sc_179	36.97177	-122.13576	13.24	0.60	103.6	0.64	579	23.7	2.54	2.62	6.638
sc_180	36.96922	-122.13758	11.67	1.00	101.6	1.02	803	24.2	2.79	2.97	6.536
sc_181	36.96929	-122.13732	10.97	0.80	326.0	1.07	777	23.2	2.75	2.95	6.560
sc_182	36.96937	-122.13704	10.20	0.70	314.0	0.98	750	22.2	2.71	2.89	6.587
sc_183	36.96882	-122.13496	12.47	0.90	303.0	1.12	822	25.1	2.81	3.03	6.572
sc_184	36.96809	-122.13288	10.52	1.80	76.0	1.81	817	23.1	2.81	3.34	6.708
sc_185	36.96706	-122.13230	10.94	1.30	23.3	1.30	849	23.9	2.85	3.14	6.771
sc_186	36.96742	-122.13136	10.49	0.90	123.2	0.94	829	23.2	2.82	2.98	6.803
sc_187	36.96603	-122.12922	11.11	1.10	141.5	1.14	894	24.4	2.93	3.14	6.961
sc_188	36.96516	-122.12936	9.47	0.80	139.3	0.86	971	23.5	3.06	3.18	6.968
sc_189	36.96522	-122.12745	11.20	1.30	230.1	1.39	988	25.4	3.09	3.39	7.023
sc_190	36.96497	-122.12698	11.21	1.40	53.7	1.41	1005	25.5	3.12	3.42	7.065
sc_191	36.96616	-122.12618	14.52	0.60	20.8	0.60	870	27.6	2.89	2.95	7.186
sc_192	36.96673	-122.12554	14.64	0.60	122.9	0.66	761	26.8	2.73	2.81	7.269
sc_193	36.96674	-122.12161	16.72	0.60	196.6	0.74	591	27.3	2.55	2.65	7.567
sc_194	36.96472	-122.12043	16.74	0.60	455.0	1.16	736	28.6	2.70	2.94	7.573
sc_195	36.96550	-122.12134	17.61	0.70	521.0	1.34	661	28.8	2.61	2.93	7.557
sc_196	36.96471	-122.12043	16.98	0.80	121.3	0.84	737	28.9	2.70	2.83	7.572
sc_197	36.96453	-122.12041	17.46	0.60	4.3	0.60	755	29.5	2.72	2.79	7.566
sc_198	36.96318	-122.12035	14.89	0.80	20.5	0.80	833	27.7	2.83	2.94	7.594
sc_199	36.96265	-122.11737	14.62	0.80	155.8	0.87	800	27.1	2.78	2.91	7.730
sc_200	36.96249	-122.11783	16.78	0.60	27.5	0.60	836	29.6	2.84	2.90	7.685
sc_201	36.96216	-122.11473	14.82	0.70	19.0	0.70	713	26.5	2.67	2.76	7.954
sc_202	36.96221	-122.11391	17.52	0.60	150.2	0.68	722	29.3	2.68	2.77	7.992
sc_203	36.96021	-122.11312	15.89	0.50	20.8	0.50	845	28.8	2.85	2.89	8.052
sc_204	36.95957	-122.11053	16.22	0.40	323.3	0.81	784	28.6	2.76	2.88	8.150
sc_205	36.95885	-122.10974	16.22	0.40	25.5	0.40	756	28.3	2.72	2.75	8.221
sc_206	36.95803	-122.10994	15.78	0.40	84.3	0.44	794	28.2	2.77	2.81	8.228
sc_207	36.95776	-122.10976	14.72	0.50	164.0	0.62	811	27.3	2.80	2.86	8.226
sc_208	36.95751	-122.10766	14.35	0.40	196.6	0.59	791	26.7	2.77	2.83	8.292
sc_209	36.95691	-122.10703	14.38	0.40	34.7	0.41	795	26.8	2.78	2.80	8.345
sc_210	36.95646	-122.10471	15.16	0.50	65.1	0.52	782	27.5	2.76	2.81	8.485
sc_211	36.95590	-122.10356	14.72	0.50	37.1	0.51	788	27.1	2.77	2.81	8.563
sc_212	36.95591	-122.10151	13.96	0.30	154.7	0.45	776	26.2	2.75	2.79	8.722
sc_213	36.95605	-122.10311	18.57	0.30	143.0	0.43	787	30.9	2.76	2.80	8.598
sc_214	36.95545	-122.10100	14.00	0.30	281.0	0.68	818	26.6	2.81	2.89	8.743
sc_215	36.95511	-122.09972	12.56	0.80	199.4	0.91	812	25.1	2.80	2.94	8.833
sc_216	36.95578	-122.09930	14.59	0.60	7.0	0.60	766	26.8	2.74	2.80	8.883
sc_217	36.95562	-122.09865	14.48	0.80	855.9	2.03	750	26.5	2.71	3.39	8.934
sc_218	36.95568	-122.09746	12.92	0.60	115.2	0.65	723	24.7	2.68	2.76	9.026
sc_219	36.95507	-122.09478	13.27	0.30	216.0	0.56	731	25.1	2.69	2.75	9.233
sc_220	36.95490	-122.09373	13.55	0.30	100.5	0.37	744	25.5	2.71	2.73	9.311

Survey station	Latitude (WGS84)	Longitude (WGS84)	Meas. terrace height (m)	GPS vert. unc. 1σ (m)	Horiz. offset (m)	Meas. vert. unc. 1σ (m)	Dist. to inner edge (m)	Model terrace height (m)	Model unc. 1σ (m)	Total vert. unc. 1σ (m)	Dist. to SGHF (km)
sc_221	36.95492	-122.09259	13.04	0.30	8.8	0.30	745	25.0	2.71	2.72	9.405
sc_222	36.95413	-122.09224	12.68	0.30	96.6	0.37	801	25.2	2.78	2.81	9.429
sc_223	36.95463	-122.09046	14.98	0.70	156.4	0.78	816	27.6	2.81	2.91	9.565
sc_224	36.95421	-122.08969	14.39	0.50	21.3	0.50	881	27.6	2.91	2.95	9.610
sc_225	36.95417	-122.08885	13.88	0.50	95.8	0.54	913	27.4	2.96	3.01	9.677
sc_226	36.95404	-122.08786	12.99	0.40	73.8	0.43	965	27.0	3.05	3.08	9.752
sc_227	36.95490	-122.08724	12.79	0.60	16.8	0.60	925	26.4	2.98	3.04	9.843
sc_228	36.95316	-122.08738	12.95	0.50	116.0	0.56	1056	27.7	3.22	3.27	9.793
sc_229	36.95247	-122.08734	12.32	0.50	117.1	0.56	1139	27.9	3.39	3.44	9.802
sc_230	36.95252	-122.08582	13.36	0.40	188.5	0.57	1196	29.4	3.51	3.56	9.850
sc_231	36.95336	-122.08468	13.97	0.60	15.2	0.60	1102	29.2	3.31	3.37	9.969
sc_232	36.95255	-122.08351	13.07	0.50	125.9	0.57	1167	28.9	3.45	3.50	10.034
sc_233	36.95330	-122.08348	13.81	0.60	202.3	0.75	1102	29.0	3.31	3.40	10.055
sc_234	36.95254	-122.08168	13.97	0.60	216.2	0.76	1144	29.6	3.40	3.48	10.210
sc_235	36.95215	-122.08219	13.56	0.50	36.2	0.51	1195	29.6	3.51	3.55	10.129
sc_236	36.95096	-122.07625	12.19	0.50	22.1	0.50	1301	29.2	3.75	3.78	10.583
sc_237	36.95044	-122.07570	12.30	0.70	63.3	0.71	1361	29.9	3.89	3.95	10.582
sc_238	36.95021	-122.07499	11.97	0.30	14.1	0.30	1373	29.6	3.91	3.93	10.630
sc_239	36.94944	-122.07407	10.71	0.30	68.4	0.34	1445	29.0	4.09	4.10	10.671
sc_240	36.95027	-122.07452	11.07	0.20	183.2	0.45	1359	28.6	3.88	3.91	10.671
sc_241	36.95042	-122.07242	10.62	0.20	55.3	0.23	1326	27.9	3.80	3.81	10.849
sc_242	36.94977	-122.07223	10.44	0.20	103.6	0.30	1398	28.3	3.97	3.99	10.836
sc_243	36.94980	-122.07119	10.85	0.20	108.9	0.31	1384	28.6	3.94	3.95	10.922
sc_244	36.94927	-122.07078	10.86	0.20	40.9	0.22	1410	28.9	4.00	4.01	10.967
sc_245	36.94851	-122.07053	10.67	0.20	105.9	0.31	1462	29.1	4.13	4.14	10.988
sc_246	36.94868	-122.06799	12.34	1.90	187.1	1.94	1447	30.7	4.09	4.53	11.144
sc_247	36.94900	-122.06895	14.58	1.00	23.8	1.00	1436	32.8	4.07	4.19	11.069
sc_248	36.94904	-122.06630	14.03	2.00	84.9	2.01	1416	32.1	4.02	4.49	11.286
sc_249	36.94848	-122.06630	12.93	1.50	119.7	1.52	1479	31.6	4.17	4.44	11.261
sc_250	36.94793	-122.06634	15.51	1.10	124.5	1.13	1490	34.2	4.20	4.35	11.281
sc_251	36.94873	-122.06540	9.52	0.40	152.6	0.52	1453	27.9	4.11	4.14	11.346
sc_252	36.94913	-122.06355	10.15	0.40	209.8	0.61	1419	28.2	4.02	4.07	11.515
sc_253	36.94913	-122.06347	9.77	0.40	43.3	0.41	1419	27.9	4.02	4.05	11.521
sc_254	36.94897	-122.06308	9.31	0.40	37.1	0.41	1434	27.5	4.06	4.08	11.546
sc_255	36.95066	-122.05959	11.18	0.30	9.0	0.30	1272	27.9	3.68	3.69	11.852
sc_256	36.94952	-122.05682	9.10	0.40	287.8	0.74	1345	26.5	3.85	3.92	12.081
sc_257	36.94947	-122.05633	8.98	0.40	13.5	0.40	1367	26.6	3.90	3.92	12.118
sc_258	36.94943	-122.05507	9.44	0.60	183.0	0.72	1367	27.0	3.90	3.97	12.220
sc_259	36.94910	-122.05435	8.36	0.50	73.0	0.53	1410	26.4	4.00	4.04	12.263
sc_260	36.94958	-122.05327	8.34	0.50	10.8	0.50	1370	26.0	3.91	3.94	12.373
sc_261	36.94973	-122.05225	9.26	0.50	58.2	0.52	1373	26.9	3.91	3.95	12.463
sc_262	36.94901	-122.04974	9.81	0.50	149.0	0.60	1500	28.6	4.22	4.26	12.635
sc_263	36.94967	-122.05012	12.42	0.60	103.3	0.64	1421	30.5	4.03	4.08	12.634
sc_264	36.94988	-122.04688	6.78	0.40	52.6	0.42	1492	25.5	4.20	4.22	12.908
sc_265	36.94956	-122.04881	7.82	0.40	123.4	0.48	1464	26.3	4.13	4.16	12.736
sc_266	36.94985	-122.04796	7.95	0.40	55.1	0.42	1459	26.4	4.12	4.14	12.818
sc_267	36.95008	-122.04546	8.05	0.50	27.4	0.50	1515	27.0	4.26	4.29	13.032
sc_268	36.95018	-122.04554	12.94	0.50	13.9	0.50	1503	31.8	4.23	4.26	13.030
sc_269	36.95009	-122.04601	6.58	0.60	0.0	0.60	1501	25.4	4.23	4.27	12.988
sc_270	36.95258	-122.04210	8.67	0.60	43.5	0.61	1399	26.6	3.98	4.02	13.424
sc_271	36.95292	-122.04112	7.86	0.90	81.5	0.92	1389	25.7	3.95	4.06	13.513
sc_272	36.95311	-122.04071	7.90	0.60	19.3	0.60	1391	25.7	3.96	4.00	13.555
sc_273	36.95348	-122.03895	7.02	0.60	39.1	0.61	1488	25.7	4.19	4.24	13.701
sc_274	36.95207	-122.03475	6.16	0.40	199.1	0.59	1806	27.7	5.01	5.05	13.994
sc_275	36.95189	-122.03425	7.36	0.40	50.2	0.42	1851	29.4	5.13	5.15	14.028
sc_276	36.95270	-122.03681	7.80	0.40	99.2	0.46	1632	27.8	4.56	4.58	13.854
sc_277	36.95191	-122.03388	7.99	0.20	147.0	0.38	1872	30.2	5.19	5.20	14.058
sc_278	36.95197	-122.03306	8.30	0.30	74.6	0.34	1920	30.9	5.32	5.33	14.128
sc_279	36.95168	-122.03145	7.51	0.30	6.7	0.30	2046	31.3	5.66	5.67	14.247
sc_280	36.95189	-122.02800	7.17	0.40	148.0	0.51	2265	32.9	6.27	6.29	14.537
sc_281	36.95186	-122.02995	6.59	0.40	95.1	0.45	2134	31.1	5.90	5.92	14.376
sc_282	36.95146	-122.02705	7.27	0.30	85.4	0.35	2362	33.9	6.54	6.55	14.595
sc_283	36.95465	-122.02469	8.55	0.50	39.6	0.51	2322	34.8	6.43	6.45	14.930
sc_284	36.95432	-122.02495	6.81	0.50	127.0	0.57	2324	33.1	6.43	6.46	14.893
sc_285	36.95309	-122.02519	6.89	0.50	84.7	0.53	2384	33.7	6.60	6.62	14.820
sc_286	36.95280	-122.02535	7.50	0.40	14.2	0.40	2390	34.4	6.62	6.63	14.793
sc_287	36.95584	-122.02432	9.93	0.30	44.0	0.32	2278	35.8	6.30	6.31	15.012

Survey station	Latitude (WGS84)	Longitude (WGS84)	Meas. terrace height (m)	GPS vert. unc. 1σ (m)	Horiz. offset (m)	Meas. vert. unc. 1σ (m)	Dist. to inner edge (m)	Model terrace height (m)	Model unc. 1σ (m)	Total vert. unc. 1σ (m)	Dist. to SGHF (km)
sc_288	36.95608	-122.02454	10.29	0.30	67.7	0.33	2247	35.9	6.22	6.23	15.005
sc_289	36.95715	-122.02527	11.70	0.30	35.2	0.31	2132	36.2	5.90	5.90	14.993
sc_290	36.95968	-122.02572	11.66	0.30	75.8	0.34	1973	34.8	5.46	5.47	15.070
sc_291	36.95759	-122.02546	11.54	0.30	356.0	0.83	2094	35.7	5.79	5.85	14.998
sc_292	36.96081	-122.02520	11.18	0.50	81.7	0.53	1973	34.3	5.46	5.49	15.163
sc_293	36.95985	-122.02534	11.28	0.80	105.2	0.83	1997	34.6	5.53	5.59	15.108
sc_294	36.96022	-122.02542	9.67	0.40	82.7	0.44	1976	32.8	5.47	5.49	15.118
sc_295	36.96077	-122.02524	10.43	0.50	44.9	0.51	1971	33.5	5.45	5.48	15.157
sc_296	36.96094	-122.02504	10.76	0.80	21.8	0.80	1981	33.9	5.48	5.54	15.181
sc_297	36.96349	-122.01204	9.79	0.60	43.8	0.61	2531	37.9	7.02	7.05	16.355
sc_298	36.96405	-122.01208	9.60	0.70	45.9	0.71	2488	37.4	6.90	6.93	16.376
sc_299	36.96474	-122.01210	11.56	0.50	91.9	0.54	2437	38.9	6.75	6.77	16.405
sc_300	36.96519	-122.01213	9.32	0.60	60.6	0.61	2402	36.3	6.65	6.68	16.423
sc_301	36.96417	-122.01205	9.49	0.60	81.3	0.63	2482	37.2	6.88	6.91	16.384
sc_302	36.96340	-122.01202	9.82	0.60	84.9	0.63	2539	38.0	7.04	7.07	16.352
sc_303	36.96406	-122.00975	8.11	1.40	95.3	1.42	2645	37.3	7.35	7.48	16.567
sc_304	36.96417	-122.01010	9.45	1.10	143.5	1.14	2613	38.3	7.26	7.34	16.544
sc_305	36.96384	-122.00655	8.53	0.50	113.0	0.56	2883	39.9	8.03	8.05	16.818
sc_306	36.96373	-122.00602	8.07	0.50	33.7	0.51	2929	39.8	8.17	8.18	16.856
sc_307	36.96376	-122.00753	7.83	0.60	82.9	0.63	2800	38.4	7.79	7.82	16.736
sc_308	36.96022	-121.98921	7.96	0.50	43.7	0.51	3478	44.7	9.78	9.79	18.071
sc_309	36.96059	-121.98907	8.95	0.50	74.3	0.53	3438	45.3	9.66	9.67	18.099
sc_310	36.96044	-121.98984	7.67	0.50	93.8	0.54	3452	44.2	9.70	9.72	18.030
sc_311	36.96028	-121.98803	10.36	1.70	27.4	1.70	3471	47.0	9.76	9.90	18.170
sc_312	36.96050	-121.98727	11.34	0.50	5.6	0.50	3447	47.8	9.69	9.70	18.242
sc_313	36.95753	-121.98107	7.48	0.50	76.8	0.53	3824	47.3	10.80	10.81	18.616
sc_314	36.95807	-121.98200	8.30	0.50	11.8	0.50	3752	47.5	10.59	10.60	18.564
sc_315	36.95818	-121.98222	8.20	0.60	10.0	0.60	3737	47.3	10.54	10.56	18.551
sc_316	36.95607	-121.97128	4.50	0.40	14.2	0.40	3771	43.9	10.64	10.65	19.349
sc_317	36.95629	-121.97122	4.72	0.40	15.7	0.40	3746	43.9	10.57	10.58	19.364
sc_318	36.95550	-121.97158	4.30	0.30	19.3	0.30	3838	44.3	10.84	10.85	19.299
sc_319	36.95721	-121.97010	5.72	0.50	67.7	0.52	3629	43.8	10.22	10.24	19.496
sc_320	36.95748	-121.96944	5.15	0.50	65.8	0.52	3590	42.9	10.11	10.12	19.562
sc_321	36.95825	-121.96831	4.59	0.60	131.4	0.67	3492	41.4	9.82	9.84	19.689
sc_322	36.95863	-121.96770	5.73	0.60	89.7	0.63	3444	42.1	9.68	9.70	19.755
sc_323	36.95888	-121.96692	7.69	0.90	21.6	0.90	3410	43.8	9.58	9.62	19.830
sc_324	36.96064	-121.96397	8.04	0.60	32.0	0.60	3200	42.2	8.96	8.98	20.148
sc_325	36.96064	-121.96404	7.61	0.60	124.9	0.66	3200	41.8	8.96	8.98	20.143
sc_326	36.96513	-121.96062	10.97	0.50	120.2	0.57	2706	40.7	7.52	7.54	20.622
sc_327	36.96464	-121.96102	10.62	0.50	10.5	0.50	2758	40.8	7.67	7.69	20.568
sc_328	36.96427	-121.96099	10.96	0.50	71.5	0.52	2799	41.5	7.79	7.81	20.553
sc_329	36.96550	-121.96026	10.78	0.40	105.7	0.46	2667	40.2	7.41	7.42	20.667
sc_330	36.96594	-121.95944	11.57	0.40	47.4	0.41	2626	40.6	7.29	7.30	20.754
sc_331	36.96515	-121.96046	13.77	0.50	32.0	0.51	2705	43.5	7.52	7.54	20.636
sc_332	36.96632	-121.95835	12.21	0.60	260.0	0.83	2578	40.8	7.15	7.20	20.867
sc_333	36.96604	-121.95910	11.34	0.70	234.0	0.87	2617	40.3	7.27	7.32	20.787
sc_334	36.96883	-121.95653	13.91	0.60	162.4	0.70	2312	40.1	6.40	6.44	21.119
sc_335	36.96831	-121.95701	15.08	0.70	91.7	0.73	2397	42.0	6.64	6.68	21.049
sc_336	36.97006	-121.95546	14.72	0.50	164.0	0.62	2158	39.5	5.97	6.00	21.262
sc_337	36.96974	-121.95555	15.27	0.50	40.9	0.51	2194	40.4	6.07	6.09	21.240
sc_338	36.97074	-121.95468	15.45	0.40	32.6	0.41	2069	39.4	5.72	5.74	21.355
sc_339	36.97239	-121.94900	17.25	1.20	13.2	1.20	1833	39.1	5.08	5.22	21.892
sc_340	36.97249	-121.94876	17.40	1.30	59.1	1.31	1822	39.1	5.05	5.22	21.916
sc_341	36.97212	-121.94952	17.40	0.70	81.3	0.72	1863	39.5	5.16	5.21	21.838
sc_342	36.97211	-121.94975	17.82	0.60	18.0	0.60	1864	39.9	5.17	5.20	21.819
sc_343	36.96022	-121.96459	7.49	0.50	20.1	0.50	3249	42.1	9.10	9.12	20.080
sc_344	36.96047	-121.96433	10.40	0.80	44.8	0.81	3220	44.8	9.02	9.05	20.112
sc_345	36.96057	-121.96420	7.48	0.50	14.3	0.50	3209	41.8	8.99	9.00	20.127
sc_346	36.96063	-121.96395	8.02	0.50	14.4	0.50	3201	42.2	8.96	8.98	20.149
sc_347	36.96075	-121.96383	7.41	1.30	29.1	1.30	3188	41.5	8.92	9.02	20.165
sc_348	36.96089	-121.96357	7.75	1.20	12.1	1.20	3171	41.7	8.87	8.96	20.193
sc_349	36.96095	-121.96343	7.18	0.50	18.8	0.50	3164	41.1	8.85	8.87	20.206
sc_350	36.96111	-121.96329	7.86	0.60	10.7	0.60	3146	41.6	8.80	8.82	20.225
sc_351	36.96143	-121.96325	8.30	0.50	30.0	0.50	3111	41.7	8.70	8.71	20.242
sc_352	36.96177	-121.96309	9.15	0.60	24.6	0.60	3072	42.2	8.59	8.61	20.271
sc_353	36.96218	-121.96300	9.29	0.90	62.2	0.91	3027	41.9	8.45	8.50	20.296
sc_354	36.96277	-121.96277	12.48	1.10	10.5	1.10	2961	44.5	8.26	8.33	20.331

Survey station	Latitude (WGS84)	Longitude (WGS84)	Meas. terrace height (m)	GPS vert. unc. 1σ (m)	Horiz. offset (m)	Meas. vert. unc. 1σ (m)	Dist. to inner edge (m)	Model terrace height (m)	Model unc. 1σ (m)	Total vert. unc. 1σ (m)	Dist. to SGHF (km)
sc_355	36.96319	-121.96216	10.71	4.10	80.7	4.10	2899	42.2	8.08	9.06	20.409
sc_356	36.96335	-121.96163	14.37	0.80	143.6	0.86	2878	45.7	8.02	8.07	20.455
sc_357	36.96353	-121.96130	13.89	1.20	184.7	1.27	2855	45.0	7.95	8.05	20.501
sc_358	36.95893	-121.96682	7.33	1.10	218.0	1.20	3404	43.4	9.56	9.63	19.840
sc_359	36.95881	-121.96740	4.41	0.60	105.1	0.64	3422	40.6	9.61	9.63	19.788
sc_360	36.95841	-121.96838	3.69	0.50	158.0	0.61	3475	40.4	9.77	9.79	19.690
sc_361	36.97301	-121.94759	15.60	0.50	258.0	0.75	1771	36.9	4.92	4.98	22.034
sc_362	36.97288	-121.94795	16.49	0.60	39.7	0.61	1782	37.9	4.95	4.98	22.000
sc_363	36.97301	-121.94756	15.65	0.60	16.6	0.60	1771	36.9	4.92	4.95	22.037
sc_364	36.97326	-121.94711	11.28	0.90	26.1	0.90	1746	32.3	4.85	4.94	22.085
sc_365	36.97256	-121.94864	16.97	1.70	69.5	1.71	1815	38.6	5.03	5.32	21.929
sc_366	36.97269	-121.94832	16.98	1.90	21.2	1.90	1802	38.5	5.00	5.35	21.961
sc_367	36.97230	-121.94919	17.18	0.60	27.9	0.60	1843	39.1	5.11	5.14	21.872
sc_368	36.97225	-121.94920	16.42	0.60	69.8	0.62	1848	38.4	5.12	5.16	21.869
sc_369	36.97271	-121.94823	16.82	0.70	72.8	0.72	1799	38.3	4.99	5.04	21.969
sc_370	36.97544	-121.94363	25.08	1.10	-	1.10	1547	44.3	4.34	4.48	22.446
sc_371	36.97687	-121.94220	24.53	0.70	260.0	0.90	1410	42.5	4.00	4.10	22.646
sc_372	36.97656	-121.94254	21.40	0.70	67.7	0.72	1438	39.7	4.07	4.13	22.605
sc_373	36.97708	-121.94153	23.82	0.60	107.2	0.64	1400	41.7	3.98	4.03	22.710
sc_374	36.97689	-121.94221	24.07	0.70	17.9	0.70	1408	42.1	4.00	4.06	22.645
sc_375	36.97724	-121.94126	24.68	3.10	67.1	3.10	1389	42.5	3.95	5.03	22.739
sc_376	36.97753	-121.94073	20.21	1.00	39.5	1.00	1371	37.9	3.91	4.04	22.795
sc_377	36.97786	-121.94020	22.17	0.80	94.2	0.83	1351	39.6	3.86	3.95	22.853
sc_378	36.97808	-121.93991	20.22	0.80	?	0.80	1338	37.6	3.83	3.91	22.886
sc_379	36.97825	-121.93968	21.51	0.80	19.7	0.80	1328	38.8	3.81	3.89	22.912
sc_380	36.97898	-121.93696	31.62	0.80	30.0	0.80	1367	49.2	3.90	3.98	23.167
sc_381	36.97890	-121.93531	24.29	1.10	55.7	1.11	1389	42.1	3.95	4.10	23.298
sc_382	36.97876	-121.93415	22.54	0.90	42.4	0.91	1355	40.0	3.87	3.98	23.386
sc_383	36.97854	-121.93211	23.32	0.80	37.6	0.80	1304	40.4	3.75	3.84	23.543
sc_384	36.97790	-121.92890	17.94	1.20	51.0	1.21	1274	34.7	3.68	3.88	23.776
sc_385	36.97797	-121.92902	18.80	1.10	39.5	1.10	1271	35.5	3.68	3.84	23.769
sc_386	36.97833	-121.93040	22.56	1.70	40.6	1.70	1268	39.3	3.67	4.05	23.673
sc_387	36.97720	-121.92589	31.75	0.30	69.3	0.34	1226	48.1	3.58	3.59	23.991
sc_388	36.97705	-121.92500	34.05	0.30	74.3	0.34	1211	50.2	3.54	3.56	24.057
sc_389	36.97725	-121.92550	34.85	0.30	108.3	0.38	1207	51.0	3.54	3.56	24.024
sc_390	36.97696	-121.92468	35.12	0.30	85.9	0.35	1207	51.3	3.54	3.55	24.079
sc_391	36.97737	-121.92500	36.47	0.30	80.8	0.35	1213	52.7	3.55	3.57	24.041
sc_392	36.97665	-121.92381	34.97	0.40	124.0	0.48	1194	51.0	3.51	3.54	24.136
sc_393	36.97623	-121.92267	30.14	0.50	77.2	0.53	1180	46.1	3.48	3.52	24.211
sc_394	36.97585	-121.92165	30.49	1.80	76.8	1.81	1170	46.3	3.46	3.90	24.277
sc_395	36.97215	-121.91217	25.20	0.50	60.0	0.52	1106	40.5	3.32	3.36	24.886
sc_396	36.97186	-121.91191	24.47	0.50	68.9	0.52	1126	39.9	3.36	3.40	24.894
sc_397	36.97197	-121.91205	26.74	0.50	49.5	0.51	1120	42.1	3.35	3.39	24.888
sc_398	36.97047	-121.90835	23.09	0.40	53.4	0.42	1188	39.1	3.49	3.52	25.123
sc_399	36.97060	-121.90893	22.96	0.60	82.3	0.63	1182	38.9	3.48	3.54	25.081
sc_400	36.97051	-121.90862	24.06	0.40	47.7	0.41	1187	40.0	3.49	3.52	25.103
sc_401	36.97000	-121.90757	23.98	0.30	62.4	0.33	1233	40.4	3.59	3.61	25.165
sc_402	36.97012	-121.90789	24.42	0.30	56.9	0.33	1222	40.7	3.57	3.58	25.145
sc_403	36.97048	-121.90816	24.25	0.30	46.9	0.32	1185	40.2	3.49	3.50	25.139
sc_404	36.96786	-121.90319	23.45	1.40	81.2	1.41	1173	39.3	3.46	3.74	25.428
sc_405	36.96803	-121.90328	22.13	1.00	25.7	1.00	1176	38.0	3.47	3.61	25.428
sc_406	36.96703	-121.90127	24.51	0.50	40.3	0.51	1043	39.2	3.20	3.24	25.548
sc_407	36.96717	-121.90125	33.89	0.60	60.0	0.61	1036	48.5	3.18	3.24	25.555
sc_408	36.96598	-121.89967	25.11	0.50	76.0	0.53	973	39.2	3.06	3.11	25.632
sc_409	36.96611	-121.89960	40.30	0.50	52.4	0.51	960	54.2	3.04	3.08	25.644